



# City Research Online

## City, University of London Institutional Repository

---

**Citation:** Basara, B. (1993). A numerical study into the effects of turbulent flows around full-scale buildings. (Unpublished Doctoral thesis, City University London)

This is the accepted version of the paper.

This version of the publication may differ from the final published version.

---

**Permanent repository link:** <https://openaccess.city.ac.uk/id/eprint/8267/>

**Link to published version:**

**Copyright:** City Research Online aims to make research outputs of City, University of London available to a wider audience. Copyright and Moral Rights remain with the author(s) and/or copyright holders. URLs from City Research Online may be freely distributed and linked to.

**Reuse:** Copies of full items can be used for personal research or study, educational, or not-for-profit purposes without prior permission or charge. Provided that the authors, title and full bibliographic details are credited, a hyperlink and/or URL is given for the original metadata page and the content is not changed in any way.

**A NUMERICAL STUDY INTO THE EFFECTS  
OF TURBULENT FLOWS AROUND  
FULL-SCALE BUILDINGS**

**Branislav Basara  
B.Sc. (Eng.)**

**Thesis submitted for the degree of  
Doctor of Philosophy  
in the School of Engineering  
City University**

**Hydraulics Division  
Department of Civil Engineering  
City University  
Northampton Square  
London EC1V 0HB**

**October 1993**

## Abstract

This thesis describes the development and application of a numerical predictive procedure for turbulent flows around full-scale buildings.

Two different turbulence models were considered: a complete Reynolds-stress model with two alternative proposals for the pressure-strain correlations and a  $k-\epsilon$  model used in conjunction with both linear and non-linear stress-strain relationships.

The governing differential equations were discretized using finite-volume techniques and a co-located variable-storage arrangement. A multigrid method was introduced and was found to reduce the computational time by nearly a factor of ten. Both the Reynolds-stress transport model and the non-linear  $k-\epsilon$  model were implemented in a form suitable for use with body-fitted coordinates on a co-located grid. When using the Reynolds-stress models, a number of techniques were utilized to stabilize the solution process and attain rapid convergence.

The atmospheric boundary layer at inlet to the computation domain, traditionally specified from empirical correlations, was simulated here using a full Reynolds-stress model in conjunction with a marching integration procedure. Due account was taken of the terrain roughness which matched that for the full-scale tests. The outcome of those simulations consisted of profiles of mean velocity and turbulence quantities that were self sustaining and in close accord with the few full-scale measurements available.

The turbulence models' performance was assessed first through detailed comparisons with various benchmark flows including the backward-facing step in both straight and divergent channel, the two-dimensional rib, the circular cylinder and the three-dimensional cube. Detailed model verification was then carried out by comparisons with full-scale measurements on various structures including a single-span low-rise building, a semi-cylindrical greenhouse and a multi-span glasshouse. It was found that the Reynolds-stress models consistently produced more accurate simulations than the  $k-\epsilon$  models. Moreover, it was demonstrated that a recently proposed model for the pressure-strain correlations yields very satisfactory results without the use of wall-reflection terms.

Parametric studies were performed to determine the sensitivity of the average pressure loading to various design parameters such as the height and width of the building, the eaves geometry (sharp or curved) and the height and location of a solid windbreak placed upstream of the building.

Finally, a method is proposed for representing the unsteady nature of the flow around full-scale buildings. The unsteady pressure loading is recovered and so is the peak loading which far exceeds the steady-state value. The method utilizes classical turbulence modelling techniques and is shown to yield results that are in qualitative accord with the field measurements.

## **Acknowledgements**

**I am very grateful to my Supervisor, Dr B.A.Younis, for his continuos interest, guidance, encouragement and support during this study.**

**I wish to thank Prof I. Demirdzic, who made arrangements for my study at City University and whose helpful advices I greatly appreciate.**

**I wish also to thank Prof M. Ivanovic, who introduced me to computational fluid dynamics.**

**Thanks to my colleagues Dr D. Cokljat, Mr Vlado Przulj and Mr Jakirlic Suad for their support, interest and helpful comments, which are greatly appreciated.**

**I acknowledge the financial assistance provided by Agriculture and Food Research Council - Engineering Institute, Silsoe (grant LRG 169).**

**Dedicated to my wife Amira and our daughter Sara, in gratitude for their support and sacrifices.**

## Contents

|   | <b>PAGE</b> |
|---|-------------|
| <b>Abstract</b>                                       | i           |
| <b>Acknowledgements</b>                               | ii          |
| <b>Contents</b>                                       | iii         |
| <b>Nomenclature</b>                                   | vi          |
| <b>List of figures</b>                                | ix          |
| <br>  |             |
| <b>CHAPTER 1 INTRODUCTION</b>                         | <b>1</b>    |
| <br>  |             |
| <b>1.1 Background</b>                                 | 1           |
| <b>1.2 The present approach and its justification</b> | 4           |
| <b>1.3 Previous related studies</b>                   | 6           |
| <b>1.4 Objectives</b>                                 | 8           |
| <b>1.5 Contents of thesis</b>                         | 9           |
| <br>  |             |
| <b>CHAPTER 2 MATHEMATICAL FORMULATION</b>             | <b>12</b>   |
| <br>  |             |
| <b>2.1 Introduction</b>                               | 12          |
| <b>2.2 Mean-flow equations</b>                        | 13          |
| <b>2.2 The k-<math>\epsilon</math> model</b>          | 15          |
| <b>2.4 Reynolds-stress transport modelling</b>        | 22          |
| <b>2.5 Closure</b>                                    | 32          |
| <br>  |             |
| <b>CHAPTER 3 SOLUTION PROCEDURE</b>                   | <b>33</b>   |
| <br>  |             |
| <b>3.1 Introduction</b>                               | 33          |
| <b>3.2 The discretization procedure</b>               | 34          |
| <b>3.3 Interpolation practices</b>                    | 41          |
| <b>3.3.1 Central differencing schemes</b>             | 41          |
| <b>3.3.2 Upwind differencing schemes</b>              | 42          |
| <b>3.3.3 'Power-law' differencing schemes</b>         | 43          |
| <b>3.3.4 Linear-upwind differencing schemes</b>       | 44          |
| <b>3.3.5 Hybrid differencing schemes</b>              | 45          |
| <b>3.4 Pressure-velocity coupling</b>                 | 46          |
| <b>3.5 Pressure-stress-velocity coupling</b>          | 49          |
| <b>3.6 Boundary conditions</b>                        | 53          |

|   |            |
|---|------------|
| <b>3.6.1 Inlet boundaries</b>                                     | <b>54</b>  |
| <b>3.6.2 Outlet boundaries</b>                                    | <b>54</b>  |
| <b>3.6.3 Symmetry boundaries</b>                                  | <b>54</b>  |
| <b>3.6.4 Fixed pressure boundaries</b>                            | <b>55</b>  |
| <b>3.6.5 Wall boundaries</b>                                      | <b>57</b>  |
| <b>3.7 Solution algorithm and convergence criterion</b>           | <b>59</b>  |
| <b>3.8 A multigrid method</b>                                     | <b>60</b>  |
| <b>3.8.a Multigrid V cycle</b>                                    | <b>61</b>  |
| <b>3.8.b Coarse-grid equations</b>                                | <b>62</b>  |
| <b>3.8.c Restriction and extrapolation</b>                        | <b>63</b>  |
| <b>3.8.d Boundary conditions</b>                                  | <b>65</b>  |
| <b>3.8.1 Solution algorithm</b>                                   | <b>65</b>  |
| <b>3.8.2 Verification tests</b>                                   | <b>68</b>  |
| <b>3.9 Closure</b>  | <b>69</b>  |
| <b>CHAPTER 4 PRELIMINARY VERIFICATION OF COMPUTATIONAL METHOD</b> | <b>73</b>  |
| <b>4.1 Introduction</b>   | <b>73</b>  |
| <b>4.2 Backward-facing step</b>                                   | <b>74</b>  |
| <b>4.3 Two-dimensional square rib</b>                             | <b>77</b>  |
| <b>4.4 Backward-facing step in divergent channel</b>              | <b>78</b>  |
| <b>4.5 Circular cylinder</b>                                      | <b>81</b>  |
| <b>4.6 Cube</b>   | <b>83</b>  |
| <b>4.7 Closure</b>  | <b>86</b>  |
| <b>CHAPTER 5 COMPUTATION OF FULL-SCALE FLOWS</b>                  | <b>114</b> |
| <b>5.1 Introduction</b>   | <b>114</b> |
| <b>5.2 Simulation of the atmospheric boundary layer</b>           | <b>115</b> |
| <b>5.2.1 Empirical correlations</b>                               | <b>117</b> |
| <b>5.2.2 Reynolds-stress transport modelling</b>                  | <b>119</b> |
| <b>5.2.3 Effects of inlet profiles</b>                            | <b>121</b> |
| <b>5.3 Results for building FB16</b>                              | <b>122</b> |
| <b>5.4 Results for building FB17</b>                              | <b>129</b> |
| <b>5.5 Results for building G07</b>                               | <b>131</b> |
| <b>5.6 Parametric studies</b>                                     | <b>132</b> |
| <b>5.6.1 Effects of geometry</b>                                  | <b>133</b> |
| <b>5.6.2 Effects of eaves shapes</b>                              | <b>134</b> |

|  |                |
|--|----------------|
| <b>5.6.3 Effects of windbreaks</b>         | <b>135</b>     |
| <b>5.7 Simulation of peak loads</b>        | <b>136</b>     |
| <b>5.8 Closure</b>                         | <b>139</b>     |
| <br><b>CHAPTER 6 CLOSURE</b>               | <br><b>191</b> |
| <b>6.1 Introduction</b>                    | <b>191</b>     |
| <b>6.2 Fulfillment of objectives</b>       | <b>192</b>     |
| <b>6.3 Recommendations for future work</b> | <b>195</b>     |
| <br><b>REFERENCES</b>                      | <br><b>197</b> |

## NOMENCLATURE

| Symbol                           | Meaning  |
|----------------------------------|--|
| $A_{nb}$                         | Coefficients in discretized equation                       |
| $A$                              | Area   |
| $a_{ij}$                         | Anisotropy tensor  |
| $C_D, C_E$                       | Coefficients in nonlinear stress-strain relationship       |
| $C_f,$                           | Wall skin-friction coefficient                             |
| $C_s$                            | Coefficient in model for triple correlation                |
| $C_P$                            | Coefficient of pressure                                    |
| $C_\epsilon$                     | Coefficient in model for diffusion of $\epsilon$           |
| $C_{\epsilon_1}, C_{\epsilon_2}$ | Coefficient in model for sources of $\epsilon$             |
| $C_\mu$                          | Coefficient in formulation for eddy-viscosity              |
| $C_1$                            | Coefficient in model for $\Phi_{ij,1}$                     |
| $C_2$                            | Coefficient in model for $\Phi_{ij,2}$                     |
| $C'_1, C'_2$                     | Coefficients in model for $\Phi_{ij,w}$                    |
| $D_{ij}$                         | Rate of diffusion $\bar{u_i u_j}$ term                     |
| $\overline{D}_{ij}$              | Main rate of strain tensor                                 |
| $\overset{\circ}{D}_{ij}$        | Oldroyd derivative   |
| $E$                              | Logarithmic law constant                                   |
| $f$                              | Wall-dumping function                                      |
| $F$                              | Mass flux  |
| $\hat{F}_i, F_i$                 | Instantaneous and time-averaged value of body forces       |
| $G_{ij}$                         | Tensor in model for $\Phi_{ij,2}$ term                     |
| $J$                              | Jacobian of coordinate transformation                      |
| $k$                              | Turbulence kinetic energy                                  |
| $L$                              | Turbulence length scale                                    |
| $p$                              | Time-averaged value of pressure                            |
| $p'$                             | Fluctuating value of pressure and also pressure correction |
| $\hat{p}$                        | Instantaneous value of pressure                            |
| $P_{ij}$                         | Rate of production of $\bar{u_i u_j}$                      |

|  |  |
|--|--|
| $P_e$  | Pecklet number   |
| $P_k$  | Production of turbulent kinetic energy                     |
| $R$  | Residual   |
| $q$  | Dynamic pressure   |
| $q_m$  | Diffusive flux   |
| $Re$   | Reynolds number  |
| $S_1, S_2, S_3$                                  | Coefficients in formulation for design wind speed          |
| $S_{ij}$   | Mean strain tensor   |
| $S_\Phi$   | Source term of variable $\Phi$                             |
| $t$  | Time   |
| $T_{mi}$   | Stress tensor  |
| $U_\tau$   | Friction velocity  |
| $U_i, u_i$                                       | Time-averaged and fluctuating velocity                     |
| $\hat{U}_i$                                      | Instantaneous value of velocity                            |
| $\overline{u_i u_j}$                             | Reynolds-stress tensor                                     |
| $\overline{u_i u_j u_k}$                         | Triple velocity correlation                                |
| $V$  | Volume   |
| $V_b$  | Basic wind speed   |
| $V_s$  | Design wind speed  |
| $u, v, w$  | Fluctuating velocity components in x, y and z directions   |
| $U, V, W$  | Time-averaged velocity components in x, y and z directions |
| $\overline{u^2}, \overline{v^2}, \overline{w^2}$ | Normal-stress components in x, y and z directions          |
| $\overline{uv}, \overline{uw}, \overline{vw}$    | Shear-stress components                                    |
| $W_{ij}$   | Mean vorticity tensor                                      |
| $x, y, z$  | Cartesian coordinates                                      |
| $x^1, x^2, x^3$                                  | Coordinates of general system                              |
| $y_0$  | Ground roughness   |
| $y^1, y^2, y^3$                                  | Cartesian coordinates                                      |
| $y^+$  | Non-dimensional distance from the wall                     |

### Greek Symbols

$\alpha, \beta, \gamma,$       Coefficients in expression for  $\Phi_{ij,2}$

|   |   |
|---|---|
| $\beta_i^j$                             | Coordinate transformation factor                          |
| $\Gamma_\Phi$                           | Diffusivity coefficient                                   |
| $\delta$                                | Boundary-layer thickness                                  |
| $\delta_{ij}$                           | Kronecker delta   |
| $\epsilon$                              | Dissipation of turbulent kinetic energy                   |
| $\epsilon_{ij}$                         | Dissipation rate of $\bar{u}_i \bar{u}_j$                 |
| $\kappa$                                | Von Karman constant                                       |
| $\mu$                                   | Molecular viscosity                                       |
| $\mu_t$                                 | Turbulent viscosity                                       |
| $\nu$                                   | Molecular kinematic viscosity                             |
| $\nu_t$                                 | Turbulent kinematic viscosity                             |
| $\rho$                                  | Density   |
| $\hat{\rho}$                            | Instantaneous density                                     |
| $\sigma_k, \sigma_\epsilon$             | Coefficients of turbulent diffusion of $k$ and $\epsilon$ |
| $\tau_{ij}$                             | Shear-stress tensor                                       |
| $\tau_w$                                | Wall shear-stress   |
| $\Phi$                                  | Symbol which denotes any variable                         |
| $\hat{\Phi}, \Phi'$                     | Instantaneous and fluctuated value of variable $\Phi$     |
| $\Phi_{ij,1}, \Phi_{ij,2}, \Phi_{ij,w}$ | Terms in modelled pressure-strain correlations            |

## Abbreviations

|             |  |
|-------------|--|
| <b>CFD</b>  | Computational fluid dynamics   |
| <b>DNS</b>  | Direct numerical simulation  |
| <b>EKE</b>  | Irrotational-strain modification of $\epsilon$ equation                        |
| <b>LES</b>  | Large-eddy simulation  |
| <b>LKE</b>  | Linear $k-\epsilon$ model  |
| <b>NKE</b>  | Non-linear $k-\epsilon$ model  |
| <b>RSM</b>  | Reynolds-stress model  |
| <b>RSM0</b> | Pressure-strain correlations proposed by<br>Launder, Reece and Rodi (1975)     |
| <b>RSM1</b> | Pressure-strain correlations proposed by<br>Speziale, Sarkar and Gatski (1990) |

## List of Figures

| Number | Title   | Page |
|--------|---|------|
| 1.1    | Map of the U.K. showing "basic" wind speed in m\s<br>(British Standards Institution, 1991).                             | 2    |
| 3.1    | Three-dimensional control volume.   | 36   |
| 3.2    | Area projections for two-dimensional control volume.  | 38   |
| 3.3    | Notation for fixed-pressure boundary.   | 56   |
| 3.4    | Multigrid V cycle.  | 61   |
| 3.5    | Restriction-extrapolation scheme.   | 64   |
| 3.6    | Flowchart of solution algorithm.  | 64   |
| 3.7    | Backward-facing step coordinates and geometry.  | 70   |
| 3.8    | Predicted and measured cross-stream profiles of mean velocity for different grid sizes.                                 | 70   |
| 3.9    | The nodal absolute relative error on different grids<br>a) 42x17, b) 82x62 and c) 162x62.                               | 71   |
| 3.10   | Multigrid convergence rates for the laminar flow over backward-facing step.   | 72   |
| 4.1    | Backward-facing step coordinates and geometry.  | 88   |
| 4.2    | Backward-facing step. Predicted mean-velocity vectors by LKE.   | 88   |
| 4.3    | Backward-facing step. Predicted streamlines by LKE<br>(a), EKE (b), NKE (c), RSM0 (d) and RSM1 (e).                     | 89   |
| 4.4    | Backward-facing step. Distribution of wall pressure coefficient predicted by LKE, EKE, NKE (a) and LKE, RSM0, RSM1 (b). | 90   |
| 4.5    | Backward-facing step. The mean-velocity profiles as obtained by LKE, EKE, NKE (a) and LKE, RSM0, RSM1 (b).              | 91   |
| 4.6    | Backward-facing step. The turbulence intensity profiles as obtained by LKE, EKE, NKE (a) and LKE, RSM0, RSM1 (b).       | 92   |
| 4.7    | Backward-facing step. The shear stress profiles as obtained by LKE, EKE, NKE (a) and LKE, RSM0, RSM1 (b).               | 93   |
| 4.8    | Two-dimensional rib coordinates and geometry.   | 94   |

| Number | Title   | Page |
|--------|---|------|
| 4.9    | Two-dimensional rib. Distribution of wall pressure coefficient predicted by LKE, EKE, NKE (a) and LKE, RSM0, RSM1 (b).          | 94   |
| 4.10   | Two-dimensional rib. The mean-velocity profiles as obtained by LKE, EKE, NKE (a) and LKE, RSM0, RSM1 (b).                       | 95   |
| 4.11   | Two-dimensional rib. The turbulence intensity profiles as obtained by LKE, EKE, NKE (a) and LKE, RSM0, RSM1 (b).                | 96   |
| 4.12   | Backward-facing step (in divergent channel) coordinates and geometry.   | 97   |
| 4.13   | Grid size 185x82: (a) 0 degree and (b) 6 degree.  | 97   |
| 4.14   | Backward-facing step: (a) 0 degree and (b) 6 degree. Predicted streamlines by RSM0 and RSM1.                                    | 98   |
| 4.15   | Backward-facing step: (a) 0 degree and (b) 6 degree. Distribution of wall skin friction coefficient predicted by RSM0 and RSM1. | 99   |
| 4.16   | Backward-facing step: (a) 0 degree and (b) 6 degree. Distribution of wall pressure coefficient predicted by RSM0 and RSM1.      | 100  |
| 4.17   | Backward-facing step: (a) 0 degree and (b) 6 degree. The mean-velocity profiles as obtained by RSM0 and RSM1.                   | 101  |
| 4.18   | Backward-facing step: (a) 0 degree and (b) 6 degree. The shear-stress profiles ( $\bar{uv}$ ) as obtained by RSM0 and RSM1.     | 102  |
| 4.19   | Backward-facing step: (a) 0 degree and (b) 6 degree. The normal stress profiles ( $\bar{u^2}$ ) as obtained by RSM0 and RSM1.   | 103  |
| 4.20   | Backward-facing step: (a) 0 degree and (b) 6 degree. The normal stress profiles ( $\bar{v^2}$ ) as obtained by RSM0 and RSM1.   | 104  |
| 4.21   | The smoothness of grid lines.   | 82   |
| 4.22   | Circular cylinder. Grid size 109X67.  | 105  |
| 4.23   | Circular cylinder. Distribution of wall pressure coefficient predicted by LKE and RSM1.   | 106  |

| Number | Title   | Page |
|--------|---|------|
| 4.24   | Inflow boundary conditions: velocity U (a),<br>turbulence kinetic energy k (b) and length scale l<br>(c), non-dimensionalized by $U_H$ and H, measured<br>in the wind tunnel.                                   | 107  |
| 4.25   | Cube. Computational domain.   | 107  |
| 4.26   | Cube. Vertical cross section: 44x28x21 (a), 55x33x28<br>(b) and 70x48x41 (c).   | 108  |
| 4.27   | Cube. Velocity vectors as obtained by measurements a)<br>and predicted by LKE using the grids A (b) and C (c).  | 109  |
| 4.28   | Cube. Velocity vectors predicted by LKE (a), NKE (b)<br>and EKE (c) (grid C and LUDS scheme).   | 110  |
| 4.29   | Cube. Turbulence kinetic energy as obtained by<br>measurements (a), and predicted by LKE using the<br>grids A (b) and C (c).  | 111  |
| 4.30   | Cube. Turbulence kinetic energy predicted by LKE (a),<br>NKE (b) and EKE (c) (grid C and LUDS scheme).  | 112  |
| 4.31   | Cube. Comparison of surface pressure coefficients at<br>vertical and horizontal plane ( $y=H/2$ ).  | 113  |
| 5.1    | Figure from Hoxey and Richards (1991) showing<br>measured velocity profiles for the roughness a)<br>$y_0 = 40\text{mm}$ and b) $y_0 = 10 \text{ mm}$ (N.B:<br>z above correspond to y in the present notation). | 116  |
| 5.2    | Predicted and measured wall static pressure<br>coefficients for boundary layer thickness $\delta=H$ ,<br>$3H$ , $5H$ , $7H$ (FB16).   | 142  |
| 5.3    | Predicted and measured wall static pressure<br>coefficients for $\delta= 55H$ and 'power-law'<br>distribution at inlet (FB16).  | 142  |
| 5.4    | The physical a) and transformed b) coordinate<br>system.  | 120  |
| 5.5    | The streamwise velocity, turbulence intensity and<br>dissipation rate profiles as obtained by the Harris<br>and Deaves correlations and by the Reynolds-stress<br>model.  | 143  |
| 5.6    | Turbulence intensity profiles as obtained by the<br>Harris and Deaves correlations and by the Reynolds-<br>stress model. Roughness (a) $y_0 = 20\text{mm}$ and (b)<br>$y_0 = 40\text{mm}$ .                     | 144  |

| Number | Title   | Page |
|--------|---|------|
| 5.7    | <b>Measured and predicted velocity profile by the Harris and Deaves correlations and by Reynolds-stress model. Roughness (a) <math>y_0 = 10\text{mm}</math> and (b) <math>y_0 = 40\text{mm}</math>.</b> | 144  |
| 5.8    | <b>Predicted wall static pressure coefficient for the inlet profiles obtained by Harris and Deaves correlations and by the Reynolds-stress model.</b>   | 145  |
| 5.9    | <b>Dimensions of the building FB16 (From Richards, 1989).</b>   | 146  |
| 5.10   | <b>Flow visualization on roof of FB16 (From Richards, 1989).</b>  | 146  |
| 5.11   | <b>Smoke observations on the roof of the building (a) and snow tracks in front of the building (b).</b>   | 147  |
| 5.12   | <b>FB16. a: Grid 108x100, b: predicted stream lines, c: velocity vectors (LKE).</b>   | 148  |
| 5.13   | <b>FB16. a: Grid 142x110, b: predicted stream lines, c: velocity vectors (LKE).</b>   | 149  |
| 5.14   | <b>FB16. Distribution of wall pressure coefficient obtained with the upwind and the power-law differencing schemes.</b>   | 150  |
| 5.15   | <b>FB16. Predicted streamlines for roughness lengths <math>y_0 = 0</math> (a) and for <math>y_0 = 40\text{mm}</math> (b).</b>   | 151  |
| 5.16   | <b>FB16. LKE and NKE results for wall static-pressure distribution.</b>   | 152  |
| 5.17   | <b>FB16. Distribution of wall pressure coefficient predicted by LKE and EKE.</b>  | 152  |
| 5.18   | <b>FB16. EKE results for streamlines (a) and velocity vectors (b).</b>  | 153  |
| 5.19   | <b>FB16. Turbulence kinetic energy contours as obtained by LKE (a) and EKE (b).</b>   | 154  |
| 5.20   | <b>FB16. Predicted streamlines by RSM0 (a) and RSM1 (b).</b>  | 155  |
| 5.21   | <b>FB16. Distribution of wall pressure coefficient predicted by LKE, RSM0 (a), and RSM1 (b).</b>  | 156  |
| 5.22   | <b>FB16. Predicted turbulence kinetic energy by RSM0 and RSM1.</b>  | 157  |
| 5.23   | <b>FB16. Computational domain (height = 300m) covered with grid 38x29.</b>  | 158  |

| Number | Title   | Page |
|--------|---|------|
| 5.24   | "New" domain (height = 15m) covered with the grids<br>37x20 (a), 75x38 (b) and 142x74 (c).                              | 159  |
| 5.25   | Predicted streamlines for different grids (a), (b) and (c)<br>of Fig. 5.24.   | 160  |
| 5.26   | <b>FB16.</b> Grid levels 37x29 (a), 72x56 (b) and 142x110 (c)<br>used for the multigrid method.                         | 161  |
| 5.27   | <b>FB16.</b> The convergence rate obtained with the<br>multigrid and the single-grid methods.                           | 162  |
| 5.28   | Dimensions of Greenhouse FB17 (From Richardson, 1991).  | 163  |
| 5.29   | Grid 216x123 used for FB17.   | 163  |
| 5.30   | <b>FB17.</b> Wall skin-friction coefficient predicted by LKE,<br>RSM0 and RSM1.   | 164  |
| 5.31   | <b>FB17.</b> Predicted streamlines by LKE (a), RSM0 (b),<br>and RSM1 (c).   | 165  |
| 5.32   | <b>FB17.</b> Distribution of wall pressure coefficient<br>predicted by LKE, RSM0 and RSM1 (FB17).                       | 166  |
| 5.33   | <b>FB17.</b> Predicted pressure contours by LKE (a) and<br>RSM1 (b).  | 167  |
| 5.34   | <b>FB17.</b> Predicted turbulence kinetic energy by LKE (a),<br>RSM0 (b) and RSM1 (c).                                  | 168  |
| 5.35   | Dimensions of multispan structure G07 (From Hoxey<br>and Moran, 1991)   | 169  |
| 5.36   | <b>G07.</b> Predicted coefficient of wall pressure<br>distribution.   | 170  |
| 5.37   | <b>G07.</b> Predicted streamlines by EKE (a) and RSM1 (b).  | 171  |
| 5.38   | <b>G07.</b> Predicted turbulence kinetic energy by EKE (a)<br>and RSM1 (b).   | 172  |
| 5.39   | <b>G07.</b> Grid levels 63x29 (a), 124x56 (b) and 256x110 (c)<br>used for the multigrid method.                         | 173  |
| 5.40   | <b>G07.</b> The convergence rate obtained with the multigrid<br>and single-grid methods.                                | 174  |
| 5.41   | Grid distribution for buildings of same width W but<br>different heights. H = 3m (a), 4.5m (b), 5.5m (c) and<br>7m (d). | 175  |
| 5.42   | Predicted streamlines for heights H = 3m (a), 4.5m (b),<br>5.5m c) and 7m d).   | 176  |

| Number | Title   | Page |
|--------|---|------|
| 5.43   | <b>Predicted average pressure coefficients for buildings of different heights, on the windward (a), roof (b) and leeward (c) sides.</b>   | 177  |
| 5.44   | <b>Computation domains for the buildings with the same height and different widths <math>W = 5\text{m}</math> (a), <math>6.7\text{m}</math> (b), <math>8.6\text{m}</math> (c) and <math>10\text{ m}</math> (d).</b> | 178  |
| 5.45   | <b>Predicted streamlines for the different widths <math>W = 5\text{m}</math> a), <math>6.7\text{m}</math> b), <math>8.6\text{m}</math> c) and <math>10\text{m}</math> d).</b>                                       | 179  |
| 5.46   | <b>Predicted pressure coefficients for the buildings with different widths on the windward a), roof b) and leeward c) side of building.</b>   | 180  |
| 5.47   | <b>Dimensions of building FB19 (From Robertson, 1989). Grids for sharp (b) and curved (c) eaves.</b>  | 181  |
| 5.48   | <b>Predicted streamlines for sharp eaves a) and curved eaves b).</b>  | 182  |
| 5.49   | <b>Flow visualization around curved eaves. (From Robertson, 1989).</b>  | 182  |
| 5.50   | <b>Velocity vectors for sharp (a) and curved (b) eaves.</b>   | 183  |
| 5.51   | <b>Predicted pressure coefficients over roof for sharp and curved eaves.</b>  | 183  |
| 5.52   | <b>Effects of windbreaks. (a) Notation. (b) streamlines for <math>H=2.18</math> and <math>X=5\text{m}</math> (b).</b>   | 184  |
| 5.53   | <b>Predicted average pressure coefficients for the windward a), roof b) and leeward (c) sides.</b>  | 185  |
| 5.54   | <b>Typical records of wind mean velocity and surface pressure (From Part 2 Code of Practice, 1991)</b>  | 186  |
| 5.55   | <b>Unsteady results for the drag coefficient <math>C_d</math>.</b>  | 186  |
| 5.56   | <b>Evolution of mean-flow streamlines with time.</b>  | 187  |
| 5.57   | <b>Perturbation of velocity at inlet as a function of time and amplitude.</b>   | 188  |
| 5.58   | <b>Predicted pressure coefficient on building roof.</b>   | 188  |
| 5.59   | <b>Field measurements of wind velocity at reference height.</b>   | 189  |
| 5.60   | <b>Predicted pressure coefficient on building roof.</b>   | 189  |
| 5.61   | <b>Predicted spectra of roof pressure coefficient.</b>  | 190  |

# Chapter 1

## INTRODUCTION

### 1.1 BACKGROUND

The structural design analysis for full-scale buildings requires knowledge of the pressures exerted on their sides by the turbulent wind flows around them. Those pressures are traditionally obtained from Codes of Practice which utilize the basic definition for the Coefficient of Pressure ( $C_p$ ) thus:

$$\Delta p = C_p q \quad (1.1)$$

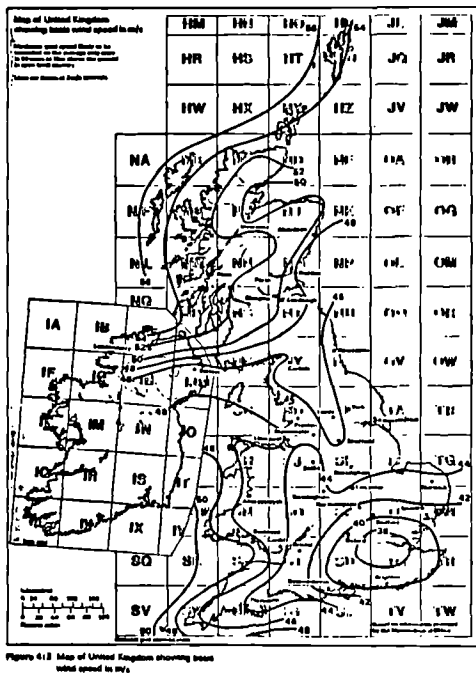
The value of  $C_p$ , which is taken to depend on the building shape and on the flow conditions that prevail at the chosen site, is given in tabulated form.  $q$  is the dynamic pressure defined as:

$$q = \frac{1}{2} \rho V_s^2 \quad (1.2)$$

In the expression above,  $V_s$  is not the flow velocity usually used in the definition of pressure coefficient but, rather, it is the "design" wind speed which is obtained from the relation:

$$V_s = S_1 S_2 S_3 V_b \quad (1.3)$$

Three empirical correction factors are involved:  $S_1$  which is introduced to take account of local topographic influences (e.g. hilly terrain),  $S_2$  which is needed to account for the combined effects of surface roughness, gust duration and the height of the structure and  $S_3$  which is related to the design life of the building.  $V_b$  is the true (or "basic") wind speed, defined in the UK Code as the 3-second gust speed at 10m height in open level country likely to be exceeded on average once in 50 years. Its values are reported by the Meteorological Office which employs a wide-spread system of anemographs (continuously-recording wind-speed measuring instruments) to create maps of wind speeds (Fig. 1.1) which are then used for design purposes.



mined from measurements on either full-scale buildings on open sites or on scaled-down models in wind tunnels.

Data collected from full-scale buildings are probably the most appropriate for design purposes but they are very scarce and are in the main limited to very few building geometries. They are also influenced by the random behaviour of the weather which, together with the costs involved, make parametric investigations rather impractical. In contrast, the flow conditions can be precisely controlled in a wind-tunnel and data obtained here tend to be more reproducible. The difficulty here is in the simulation of the atmospheric boundary layer that develops upstream of the real building. Geometric similarity requires the equality in the real and the model building of at least one (but preferably both) of the following scale ratios:  $L/y_0$  and  $L/\delta$  where  $L$  is a characteristic buildings dimension,  $y_0$  is the effective roughness height and  $\delta$  is the boundary-layer thickness. Boundary layer turbulence is produced by blocks placed upstream of the test section and those rarely succeed in reproducing the appropriate roughness characteristics of the real flow. Moreover, the simulated boundary-layer thickness is rarely thick enough compared to the height of the model since wind-tunnels of sufficient length to produce this are not always available. Real winds are, of course, never steady and there are many practical difficulties which prevent the reproduction of the observed gustiness in a wind tunnel. Not surprisingly, therefore, difference between the modelled and the 'real' flow conditions remain and those decrease the significance of wind-tunnel experiments for the determination of dynamic wind loading.

Computational fluid dynamics (CFD) models offer an alternative, but as yet untested, approach to problems related to the wind environment. This approach has developed quite rapidly in recent years due to advances in computer technology and in the provision of turbulence models and numerical algorithms suitable for complex-flow applications. The main requirement now is for a systematic validation and testing of this approach to determine its capabilities and limitations for real wind engineering flows. For only then will CFD be accepted by the wind engineering community and its results used as input to the Codes of Practice, alongside those from full-scale and wind-tunnel tests.

## 1.2 THE PRESENT APPROACH AND ITS JUSTIFICATION

The first issue to be addressed in the simulation of flows around buildings is the choice of the strategy for solving the Navier-Stokes equations of motion. Direct Numerical Simulation methods (DNS) attempt to simulate directly all the dynamically important scales of turbulent flows and, as such, they require a very large number of grid nodes to resolve all the scales present. This requirement easily exceeds the capacity of modern computers and this in turn limits the validity of this approach to some very simple flows, at low Reynolds numbers. The approach is therefore not appropriate to wind engineering applications and is unlikely to become so in the foreseeable future. In Large-Eddy Simulations (LES), the three-dimensional time-dependent Navier-Stokes equations are again solved numerically but now only motions of scales larger than the mesh size are resolved. The effects of the small-scale dissipative motions are modelled. This approach is now producing some very promising results, but it remains far too expensive to be used as an everyday engineering design tool.

At present, the only viable prospect for practical engineering calculations lies in the solution of the time-averaged Navier-Stokes equations together with a turbulence model for approximating the resulting unknown Reynolds stresses. Most turbulence models in current engineering practice are of the eddy-viscosity type in which the turbulent stresses are related to the local velocity gradients through a suitably-defined "eddy viscosity". Depending on the number of additional equations solved, zero-, one- and two-equation models may be used. The most popular of the two-equation closure methods is the  $k-\epsilon$  model in which the eddy viscosity is obtained from a relationship in terms of the turbulence kinetic energy ( $k$ ) and  $\epsilon$ , its dissipation rate. Often, this model has to be modified to give satisfactory results for different applications and some examples of these modifications will be tested in this study.

The Reynolds-stress model (RSM) account for non-local effects by solving differential transport equations for the Reynolds stresses. In three-dimensional flows, all components of the Reynolds-stress tensor are finite and hence the complete model involves the solution of a differential

transport equation for each stress together with an additional one for a turbulence length-scale related quantity. Such models may not therefore be suited to everyday use, particularly for complicated geometries, though their ability to produce very accurate results has been amply demonstrated in recent years (Speziale, 1991).

The turbulence models chosen for this study are the  $k-\epsilon$  model in both its standard and modified forms and a complete Reynolds-stress transport model. The purpose was to determine the minimum level of closure needed to reproduce the correct wind loads on the various building structures investigated. Various modifications to the  $k-\epsilon$  model were tested, including the use of a novel non-linear stress-strain relationship. For the Reynolds-stress model, alternative closure assumptions were investigated and a new model for the pressure-strain correlations, proposed by Speziale, Sarkar and Gatski (1991), was assessed in detail for the first time.

Another important issue to be addressed is related to the specification of the atmospheric boundary layer upstream of the buildings. The velocity profiles, together with those for the turbulence kinetic energy, the dissipation rate and (for RSM simulations) the Reynolds stresses, are needed as inlet boundary conditions for the wind-loading simulations. The choice of those inlet profiles may strongly influence the quality of the simulations. Various possibilities are examined, including the use of empirical relations and numerical simulations.

The quality of the wind-load predictions is also influenced by the choice of the numerical method used for solving the governing equations and hence issues of stability, accuracy and economy of the numerical method have to be addressed as well. Full-scale buildings are rarely amenable to analysis with simple orthogonal coordinates (e.g. cartesian) and this often also applies to the surrounding terrain. There is therefore a need to abandon the orthogonal formulation in favour of arbitrary, body-fitted coordinates. The present approach allows for this in the context of a finite-volume method with a co-located grid-storage arrangement. Obtaining a numerically-accurate solution to the governing equations with the minimum of computational effort remains the ultimate goal for the computational modeller. However, the two requirements are difficult to reconcile: accurate solutions are only possible by using 'higher order'

discretization schemes or by refining the grid, both options leading to an increase in computational effort. In this study, consideration is given to the multi-grid technique which reduces the computational effort involved in obtaining numerically-accurate solutions on fine grids.

It is hoped that the combination of an appropriate turbulence model with an efficient numerical method, together with modern graphics postprocessors to present results, and the validation of the whole package against experimental data will provide a practical tool to study building-related flow problems.

### 1.3 PREVIOUS RELATED STUDIES

Several attempts at modelling the effects of turbulent wind flows around buildings have been reported in the literature, both for two-dimensional (2D) and three-dimensional (3D) geometries and for both simple and complex shapes. Typically, two-dimensional simulations are performed to test the turbulence models and the numerical methods in isolation of complicating three-dimensional effects. Hanson, Summers, and Wilson (1984) used a random vortex method to depict the flow evolution over a 2D hypothetical building. No turbulence model was used and there were no comparisons with experiments. Mathews and Meyer (1987) applied a  $k-\epsilon$  model to calculate the flow over a semi-circular building. At inlet to the solution domain, the velocity were obtained from a power law with exponent of 0.15, while the turbulence intensity and length scale were prescribed empirically. Their calculations are open to criticism on many counts (see Richards and Younis, 1990). The inlet profiles used were inappropriate in that they were not self sustaining: this means that their calculations were dependent on the position of the inlet plane. Moreover, the computational grid used was inadequate for the purpose: being orthogonal, based on potential flow solution, leading to bad resolution of the area around the base of the building. Interestingly, a similar grid-generation method was used by Mathews, Crosby, Visser and Meyer (1988) for a multispan structure also leading to an inadequate grid and poor overall agreement with measurements. Selvam (1992) used a  $k-\epsilon$  model to simulate the experiments carried out at Texas-Tech University

for flows around a full-scale building. The results were not satisfactory leading to the somewhat obvious conclusion that the use of a 2D representation of a 3D building is questionable. Crosby, Mathews and Plessis (1990) also used a  $k-\epsilon$  model to investigate the effects of windbreaks placed upstream of buildings. Qualitatively, the results were quite realistic in that they showed the reduction in wind loading due to the presence of the windbreaks but quantitative comparisons with the data without windbreaks were again not satisfactory. The effects of eaves geometry on pressure distribution over a full-scale building were investigated by Richards (1989) who used the PHOENICS package in conjunction with the standard  $k-\epsilon$  model. Body-fitted coordinates were used. The Harris and Deaves (1981) formulae were used to prescribe the profiles of the atmospheric boundary layer at inlet and the terrain was assumed to be rough with a specified effect roughness height. His predictions showed that, on the windward side of the roof, the flow remained attached when curved eaves were used and became detached with sharp eaves, as indicated by smoke observations. Both 2D and 3D simulations were carried out, the latter generally closer to the measured pressure distributions though this quantity was still grossly overpredicted over both the windward and leeward sides of the roof. Haagvist and Taesler (1989) also used the PHOENICS to simulate wind tunnel experiments for a single house and for the same house surrounded by several identical ones. Cartesian coordinates were used even though the structures had sloping roofs. The inlet conditions were taken from the measurements. Where several houses were modelled, the boundary conditions were cyclic, such that the outlet conditions from one run were used as the inlet conditions for the next. The results for the single house showed the calculated pressure coefficient systematically higher than measured, with agreement being particularly bad on the leeward side of the roof. For the multiple houses, the calculated pressure coefficients were again generally higher than those from experiment. Paterson and Holmes (1991) reported predictions of the mean and peak wind pressures on arched-roof buildings. The  $k-\epsilon$  model was used, and results were presented for both wind-tunnel flows and the full-scale data from the Texas Tech building. The root mean square pressure coefficients were calculated from algebraic expression to which the steady-flow solutions were an input. Large disagreement for the pressure coefficients on the all sides of the building were reported, due probably to the fairly coarse grid employed (26x29x14).

Turbulent flows around cubes are frequently used as test cases for 3D model validation. Paterson and Apelt (1986) used a linear  $k-\epsilon$  model and underpredicted the extent of the separated zones on the sides and on the top of the cube. The pressures were also underpredicted in those areas. Similar results were obtained with the same model when used by Paterson and Apelt (1990), Murakami and Moshida (1989) and Richards and Hoxey (1991). Murakami and Moshida (1989) made some serious grid independence checks but the problems remained. Somewhat better results were obtained by Baskaran and Stathopoulos (1989) who modified the model for streamline curvature effects along the lines suggested by Leschziner and Rodi (1981). Murakami, Mochida and Hayashi (1990) reported some Large-Eddy Simulations for the cube which showed improved predictions of the pressure distribution and the turbulence kinetic energy. Comparisons were reported for the predicted and measured turbulence kinetic energy and its production rate and those were used to explain the reasons for defects observed with the  $k-\epsilon$  model. Large-Eddy Simulations for the same flow were later reported by Murakami, Mochida, Hayashi and Sakamoto (1992) who compared the results with the algebraic-stress model. The latter gave poor results for the pressure distribution especially for the top surface of the cube. The shape of the spectrum of fluctuating surface pressure predicted by LES agreed fairly well with that measured but at the expense of computing time, 50 times greater than for the  $k-\epsilon$  model (Murakami, private communication).

## 1.4 OBJECTIVES

The objectives of the present study were:

1. To develop and validate a practical computational method for predicting the patterns of turbulent flows around buildings and the associated pressure loading. The aim is to meet an identifiable requirement of the engineering community for a method which is reliable, cost-effective and of known capabilities and limitations.
2. To investigate the suitability of different turbulence models for use for flows around buildings. This will be achieved by comparing the

performance of two very different turbulence models: a  $k-\epsilon$  model, in both standard and modified forms, and a full Reynolds-stress-transport model of turbulence. The benchmark flows chosen for this comparison include the backward-facing step in both straight and divergent channels, the 2D rib, the circular cylinder and the 3D cube.

3. To simulate, using a full Reynolds-stress model, the properties of the atmospheric boundary layers that develop upstream of the full-scale structures and to use the results as input to the flow-solving method.
4. To verify the predictive procedure against the full-scale data from the Silsoe Research Institute (U.K.). A low-rise building, a semi-cylindrical greenhouse and a multi-span structure will be considered.
5. To conduct parametric studies aimed at quantifying the influences of geometrical parameters on the patterns of wind flow and pressure loading on selected full-scale structures.
6. To advance an appropriate method for the prediction of unsteady wind loading using conventional turbulence modelling techniques.
7. To implement and test a multigrid procedure suited to non orthogonal body-fitted coordinates with a co-located grid arrangement and to apply the method to the calculation of full-scale flows.

## 1.5 CONTENTS OF THESIS

This thesis is written in six chapters of which this is the first. The mathematical basis for the present study will be presented in Chapter 2. There, the mean flow equations will be given and the need for time-averaging will be described. Alternative, linear and non-linear, relationships for linking the unknown turbulent stresses with the local rates of strain will then be presented together with the equations for the turbulence kinetic energy and its rate of dissipation. Those will form the basis of the  $k-\epsilon$  model used in this study. The transport equations that constitute the Reynolds-stress model will then be presented, together with the various

assumptions needed to close them. Two very different models for the pressure-strain correlations are described.

Details of the finite-volume methodology used here to solve the governing differential equations are presented in Chapter 3. Emphasis is placed on the techniques used for obtaining solutions with non-orthogonal, body-fitted coordinates. The SIMPLE algorithm for the pressure-velocity coupling will be presented together with details of the interpolation practice used to avoid numerical oscillations. Details of the method employed to achieve the turbulent-stress/velocity coupling will also be given. The solution algorithm and the convergence criterion are described. Also presented in this chapter are the details of the multigrid technique used to accelerate the solution of the governing equations on fine meshes. The method's results for a laminar flow over a backward-facing step will be presented in this chapter while the outcome of the application of this technique to the highly turbulent flows around full-scale buildings are presented in Chapter 5.

Chapter 4 is concerned with a preliminary assessment of the turbulence models against data from a number of established benchmark flows. Results will be presented here for the  $k-\epsilon$  model with both linear and non-linear stress-strain relationships. Some modifications to the  $\epsilon$ -equation were considered and the outcome will be reported here. The Reynolds-stress model results will also be presented and the predictions obtained with two versions of pressure-strain correlations compared.

The main results of the present work are reported in Chapter 5 which compares the performance of the various turbulence models for the experimental data from the full-scale buildings. Details of the methods used for simulating the approach atmospheric boundary layer will be presented here. The computed profiles (obtained by using a Reynolds-stress model in conjunction with a marching-integration method) will be compared with established empirical relations and with open-filed measurements of the atmospheric boundary layer. The procedure for treating ground roughness will be presented. The chapter will also report the outcome of tests performed to establish the sensitivity of the computed solutions to the size of the computational grid and to the choice of the differencing scheme. Parametric studies aimed at quantifying the effects on the pressure distribution over a full-scale building of changes in the height or

width of the building, the shape of the eaves (i.e. sharp or curved) and the placement of windbreaks upstream of the building will be reported. Optimization of the position of windbreak with no porosity against the building is presented for two different heights of windbreak. Finally, the procedure developed here for simulating the effects of unsteady wind loading will be explained and some results presented for a full-scale building.

The main conclusions arrived at from this study will be summarized in Chapter 6 and suggestions for future research will be made.

Some of the results presented in this thesis have been documented in Basara and Younis (1992 a, b), Basara, Przulj and Younis (1992), Hoxey, Robertson, Basara and Younis (1992), Basara and Younis (1993) and Basara, Cokljat and Younis (1993).

# Chapter 2

## MATHEMATICAL FORMULATION

### 2.1 INTRODUCTION

This chapter presents the basic equations governing fluid motion and considers the various alternative models used later in this thesis to close the time-averaged equations. The problems associated with modelling of turbulent separated flows are, of course, not confined to flows around buildings and there are, at present, many proposals aimed at improving the performance of those models. Some of those proposals will be presented here and their performance verified later in Chapter 4 against some well documented experiments.

Section 2.2 lists the instantaneous and time-averaged equations of motion. In Section 2.3, the manner in which the unknown turbulent stresses are related to the mean rates of strain is explained and options for both linear and non-linear relations discussed. This section will also provide the basis of the  $k-\epsilon$  model used in this study. The Reynolds-stress model equations are presented in Section 2.4 where the approximations used for the various unknown terms will be presented, focusing in particular on two alternative approaches for handling the pressure-strain correlations. Closure and summary of this chapter are contained in Section 2.5.

## 2.2 MEAN-FLOW EQUATIONS

It is generally accepted that the continuity equation together with the Navier-Stokes equations provide a complete description of fluid flows including turbulent ones.

The continuity equation describes the conservation of mass and may be written as:

$$\frac{\partial \hat{\rho}}{\partial t} + \frac{\partial(\hat{\rho}\hat{U}_j)}{\partial x_j} = 0 \quad (2.1)$$

The Navier-Stokes equations express the conservation of momentum and may be written as:

$$\frac{\partial(\hat{\rho}\hat{U}_i)}{\partial t} + \frac{\partial(\hat{\rho}\hat{U}_j\hat{U}_i)}{\partial x_j} = \frac{\partial}{\partial x_j} \left[ \mu \left( \frac{\partial \hat{U}_i}{\partial x_j} + \frac{\partial \hat{U}_j}{\partial x_i} \right) \right] + \hat{F}_i - \frac{\partial \hat{p}}{\partial x_i} \quad (2.2)$$

In the above equations, the cartesian tensor notation is used wherein repeated indices imply summation. Symbols with " ^ " refer to the instantaneous value of that particular variable.

In most engineering problems, the details of the instantaneous flow field are not of particular use or interest and it is more useful to construct models based on averaged quantities. The equations for averaged quantities can be obtained by first de-composing the instantaneous values into mean and fluctuating parts, thus:

$$\hat{\Phi} = \Phi + \Phi' \quad (2.3)$$

where  $\Phi$  denotes an averaged value and  $\Phi'$  denotes the fluctuations about the mean value.

In general, the time-averaged value, at a single point, is defined by

$$\Phi = \lim_{\tau \rightarrow \infty} \frac{1}{\tau} \int_0^\tau \hat{\Phi} dt$$

where  $\tau$  is the time interval for which the averaged value is to be defined. By substitution of the instantaneous values in the equations (2.1) and (2.2), and by using certain properties of averaged and fluctuating values (Hinze, 1959), we obtain the time-averaged equations which for an incompressible fluid of constant property may be written as:

### Continuity equation

$$\frac{\partial \bar{U}_j}{\partial x_j} = 0 \quad (2.4)$$

### Momentum equations

$$\rho \frac{\partial \bar{U}_i}{\partial t} + \rho \bar{U}_j \frac{\partial \bar{U}_i}{\partial x_j} = \frac{\partial}{\partial x_j} \left( \mu \frac{\partial \bar{U}_i}{\partial x_j} - \rho \bar{u}_i \bar{u}_j \right) + \bar{F}_i - \frac{\partial \bar{P}}{\partial x_i} \quad (2.5)$$

The time-averaging of the Navier-Stokes equations has given rise to some unknown correlations ( $\bar{u}_i \bar{u}_j$ ), known as Reynolds stresses, which have to be determined somehow before equation (2.5) may be solved.

An exact transport equation for  $\bar{u}_i \bar{u}_j$  is obtained from the Navier-Stokes equations by multiplying the equations for the fluctuating components  $u_i$  and  $u_j$  by  $u_j$  and  $u_i$  respectively, then summing these equations and time-averaging the result. The resulting equations for constant-density flows with no body forces are given as:

$$\begin{aligned} \frac{\partial \bar{u}_i \bar{u}_j}{\partial t} + U_k \frac{\partial \bar{u}_i \bar{u}_j}{\partial x_k} &= - \left( \bar{u}_i \bar{u}_k \frac{\partial \bar{U}_j}{\partial x_k} + \bar{u}_j \bar{u}_k \frac{\partial \bar{U}_i}{\partial x_k} \right) \\ &- \frac{\partial}{\partial x_k} \left[ \bar{u}_i \bar{u}_j \bar{u}_k + \overline{\frac{p'}{\rho} (\delta_{jk} u_i + \delta_{ik} u_j)} - \nu \frac{\partial \bar{u}_i \bar{u}_j}{\partial x_k} \right] \\ &+ \overline{\frac{p'}{\rho} \left( \frac{\partial u_i}{\partial x_j} + \frac{\partial u_j}{\partial x_i} \right)} - 2\nu \overline{\left( \frac{\partial u_i}{\partial x_k} \frac{\partial u_j}{\partial x_k} \right)} \end{aligned} \quad (2.6)$$

The first term appearing on the left-hand side of equation (2.6) represents the rate of change of  $\bar{u}_i \bar{u}_j$  with respect to time. This term vanishes

in steady flows and will therefore be discarded from further consideration. The second term on the left represents the rate at which  $\bar{u}_i \bar{u}_j$  is transported (convected) by the mean flow. The terms on the right-side of equation (2.6) denote respectively the rates of: production of  $\bar{u}_i \bar{u}_j$  by mean shear, diffusion of  $\bar{u}_i \bar{u}_j$  by various agencies, redistribution of the turbulence kinetic energy amongst the fluctuating components, and, finally, dissipation by viscous processes.

Equation (2.6) does not by itself constitute a turbulence model since it, too, contains some unknowns that will first need to be modelled. The manner in which this is done here will be presented in Section 2.4; the next section considers how  $\bar{u}_i \bar{u}_j$  is traditionally obtained from an algebraic constitutive relationship.

### 2.3 THE $k-\epsilon$ MODEL

The  $k-\epsilon$  model of turbulence is based on Boussinesq's (1877) proposal in which the turbulent stresses are assumed to vary linearly with the local mean rates of strain. The proposal is thus simply an extension, to turbulent flows, of Stoke's Law for laminar flows, and may be written as:

$$-\rho \bar{u}_i \bar{u}_j = \mu_t \left( \frac{\partial U_i}{\partial x_j} + \frac{\partial U_j}{\partial x_i} \right) - \frac{2}{3} \rho \delta_{ij} k \quad (2.7)$$

Equation (2.7) defines the eddy-viscosity  $\mu_t$  which, unlike its laminar counterpart, depends on the flow rather than on the fluid. The kinematic eddy-viscosity is defined, for later use, as  $\nu_t = \mu_t / \rho$ . The second term in equation (2.7) was not present in Boussinesq's original proposal but was added later to ensure that the sum of the normal Reynolds-stresses yields the identity:

$$k \equiv \frac{1}{2} (\bar{u}^2 + \bar{v}^2 + \bar{w}^2) \quad (2.8)$$

where  $k$  is the turbulence kinetic energy.

The eddy-viscosity  $\mu_t$  is assumed to be proportional to a velocity scale and a length scale characterizing the turbulence motion, which, in the context of the  $k-\epsilon$  model, are taken to be  $k^{\frac{1}{2}}$  and  $k^{\frac{3}{2}}/\epsilon$ , respectively. This then gives:

$$\mu_t = \rho C_\mu \frac{k^2}{\epsilon} \quad (2.9)$$

where  $\epsilon$  is the dissipation rate of turbulence kinetic energy.

Boussinesq's linear stress-strain relationship is known to give an adequate representation of the turbulence field in boundary-layer flows, where flow reversal is absent and the normal stresses do not appear in the governing equations. In other types of flow, however, the terms  $\partial \bar{u}^2 / \partial x$ ,  $\partial \bar{v}^2 / \partial y$  etc. can form a significant contribution to the momentum balance and it is in those cases that Boussinesq's relation turns out to be a major source of error in the calculations. Separated flows fall in this category: the turbulence anisotropy at the point of flow separation is known to exert a significant influence on the subsequent development of the separated layer and hence the large inaccuracies observed in the prediction of those flows. Since anisotropy is badly represented by a linear relationship, it is logical to consider alternative stress-strain relationships for the prediction of separated flows. A number of alternative proposals have been reported in the literature, here the proposal of Speziale (1987) is adopted in which, by analogy between Newtonian turbulent flows and laminar, non-Newtonian, flows, the Reynolds stresses are written as:

$$\begin{aligned} -\bar{u}_i \bar{u}_j &= -\frac{2}{3} k \delta_{ij} + 2 C_\mu \frac{k^2}{\epsilon} \bar{D}_{ij} \\ &+ 4 C_D C_\mu^2 \frac{k^3}{\epsilon^2} (\bar{D}_{im} \bar{D}_{mj} - \frac{1}{3} \bar{D}_{mn} \bar{D}_{mn} \delta_{ij}) \\ &+ 4 C_E C_\mu^2 \frac{k^3}{\epsilon^2} (\bar{D}_{ij}^o - \frac{1}{3} \bar{D}_{mm}^o \delta_{ij}) \end{aligned} \quad (2.10)$$

where the mean rate of strain tensor can be expressed as:

$$\bar{D}_{ij} = \frac{1}{2} \left( \frac{\partial U_i}{\partial x_j} + \frac{\partial U_j}{\partial x_i} \right) \quad (2.11)$$

and the Oldroyd derivative of the mean rate of strain as:

$$\overset{\circ}{D}_{ij} = \frac{\partial \overline{D}_{ij}}{\partial t} + U_m \frac{\partial \overline{D}_{ij}}{\partial x_m} - \frac{\partial U_i}{\partial x_m} \overline{D}_{mj} - \frac{\partial U_j}{\partial x_m} \overline{D}_{mi} \quad (2.12)$$

The first line in equation (2.10) corresponds to Boussinesq, the remaining two lines may be considered as corrections to it imparting a non-linear dependence on the strain rate. Two new constants are now involved:  $C_D$  and  $C_E$ . Both are assigned the value of 1.68, deduced by the model's originator from comparisons with normal-stress data from turbulent channel flow. The model does not appear to be very sensitive to the choice of values for the new coefficients: Speziale showed that even a 15% change in their values results in only a small change in the computed results.

For the purpose of completeness, the models equations appropriate to two-dimensional flows are given below in expanded form:

$$\begin{aligned} -\overline{u^2} &= -\frac{2}{3}k + 2\nu_t \frac{\partial U}{\partial x} + \frac{1}{3}L \left[ (C_D - 2C_E) \left( \frac{\partial U}{\partial x} \right)^2 \right. \\ &\quad + \left( \frac{1}{4}C_D - 2C_E \right) \left( \frac{\partial U}{\partial y} \right)^2 + \left( \frac{1}{2}C_D - C_E \right) \left( \frac{\partial U}{\partial y} \frac{\partial V}{\partial x} \right) \\ &\quad \left. + \left( \frac{1}{4}C_D + C_E \right) \left( \frac{\partial V}{\partial x} \right)^2 \right] + LC_E \left( U \frac{\partial^2 U}{\partial x^2} - V \frac{\partial^2 V}{\partial y^2} \right) \end{aligned} \quad (2.13)$$

$$\begin{aligned} -\overline{v^2} &= -\frac{2}{3}k + 2\nu_t \frac{\partial V}{\partial y} + \frac{1}{3}L \left[ (C_D - 2C_E) \left( \frac{\partial V}{\partial y} \right)^2 \right. \\ &\quad + \left( \frac{1}{4}C_D - 2C_E \right) \left( \frac{\partial V}{\partial x} \right)^2 + \left( \frac{1}{2}C_D - C_E \right) \left( \frac{\partial U}{\partial y} \frac{\partial V}{\partial x} \right) \\ &\quad \left. + \left( \frac{1}{4}C_D + C_E \right) \left( \frac{\partial U}{\partial y} \right)^2 \right] + LC_E \left( V \frac{\partial^2 V}{\partial y^2} - U \frac{\partial^2 U}{\partial x^2} \right) \end{aligned} \quad (2.14)$$

$$\begin{aligned} -\overline{uv} &= \nu_t \left( \frac{\partial U}{\partial y} + \frac{\partial V}{\partial x} \right) - LC_E \left( \frac{\partial U}{\partial y} \frac{\partial V}{\partial y} + \frac{\partial U}{\partial x} \frac{\partial V}{\partial x} \right) \\ &\quad + \frac{1}{2}LC_E \left[ U \left( \frac{\partial^2 V}{\partial x^2} - \frac{\partial^2 V}{\partial y^2} \right) + V \left( \frac{\partial^2 U}{\partial y^2} - \frac{\partial^2 U}{\partial x^2} \right) \right] \end{aligned} \quad (2.15)$$

where L is defined as:

$$L = 4C_\mu^2 \frac{k^3}{\epsilon^2} \quad (2.16)$$

It is clear from the above that the new stress-strain relationship is far more complicated than Boussinesq, not only because it involves more terms but, also, because it contains terms (quadratic in the velocity gradients) that can be difficult to implement in finite-difference schemes. Whether or not this added complexity is justified will be seen from the comparisons in subsequent chapters.

In addition to the stress-strain relationship, the complete turbulence model involves the solution of differential transport equations for the turbulence kinetic energy ( $k$ ) and its rate of dissipation ( $\epsilon$ ). The  $k$ -equation can be derived by contraction of the indices in equation (2.6), thus:

$$\overbrace{\frac{\partial k}{\partial t} + U_j \frac{\partial k}{\partial x_j}}^a - \overbrace{\bar{u}_i \bar{u}_j \left( \frac{\partial U_i}{\partial x_j} \right)}^b - \overbrace{\frac{\partial}{\partial x_j} \left( \overbrace{\bar{u}_j k' + \frac{1}{\rho} \bar{u}_j p'}^d - \nu \frac{\partial k}{\partial x_j} \right)}^c - \nu \overbrace{\left( \frac{\partial u_i}{\partial x_j} \right)^2}^e \quad (2.17)$$

The pressure-strain term does not appear in the  $k$ -equation since the role of this term is to redistribute the turbulence energy among its components without affecting the overall level of turbulent kinetic energy in the flow.

Terms (a), (b) and (c) (representing temporal and spatial rates of change and the production rate  $P_k$ ) are exact in the sense that they contain quantities that are themselves the dependent variable of equations to be solved. Term (d) is the total diffusion of  $k$ . The viscous part is negligible at high Reynolds numbers, the pressure diffusion is neglected following standard practice and the turbulent diffusion is modelled by the gradient transport hypothesis thus:

$$-\bar{u}_j k' = \frac{\nu_t}{\sigma_k} \frac{\partial k}{\partial x_j} \quad (2.18)$$

Term (e) is the dissipation rate of turbulence kinetic energy, hitherto denoted as  $\epsilon$ .

The modelled equation for  $k$  therefore takes the form:

$$\frac{\partial k}{\partial t} + U_j \frac{\partial k}{\partial x_j} = \frac{\partial}{\partial x_j} \left( \frac{\nu_t}{\sigma_k} \frac{\partial k}{\partial x_j} \right) + P_k - \epsilon \quad (2.19)$$

A transport equation for  $\epsilon$  can be obtained by differentiating the equation for the fluctuating velocity  $u_i$  with respect to  $x_l$ , multiplying the result by  $2\nu(\partial u_i / \partial x_l)$  and then time averaging, thus:

$$\begin{aligned} \overbrace{\frac{\partial \epsilon}{\partial t}}^a + \overbrace{U_j \frac{\partial \epsilon}{\partial x_j}}^b &= - \frac{\partial}{\partial x_j} \left( \overbrace{u_j \epsilon'}^{c_1} + \frac{2\nu}{\rho} \overbrace{\frac{\partial p}{\partial x_l} \frac{\partial u_j}{\partial x_l}}^{c_2} - \nu \overbrace{\frac{\partial \epsilon}{\partial x_j}}^{c_3} \right) \\ &- \overbrace{2\nu \left( \frac{\partial u_i}{\partial x_l} \frac{\partial u_j}{\partial x_l} + \frac{\partial u_l}{\partial x_i} \frac{\partial u_l}{\partial x_j} \right) \frac{\partial U_i}{\partial x_j}}^d - \overbrace{2\nu u_j \frac{\partial u_i}{\partial x_l} \frac{\partial^2 U_i}{\partial x_j \partial x_l}}^e \\ &- \overbrace{2\nu \frac{\partial u_i}{\partial x_j} \frac{\partial u_i}{\partial x_l} \frac{\partial u_j}{\partial x_l}}^f - \overbrace{2 \left( \nu \frac{\partial^2 u_i}{\partial x_j \partial x_l} \right)^2}^g \end{aligned} \quad (2.20)$$

Reynolds source

In the limit of high turbulence numbers only two terms remain: term (f) which expresses the generation rate of vorticity fluctuations through the self-stretching action of turbulence and term (g) which expresses the decay of the dissipation rate (Hanjalic, 1984). It is usual to model the difference between terms (f) and (g) collectively as:

$$-2\nu \frac{\partial u_i}{\partial x_j} \frac{\partial u_i}{\partial x_l} \frac{\partial u_j}{\partial x_l} - 2 \left( \nu \frac{\partial^2 u_i}{\partial x_j \partial x_l} \right)^2 = C_{\epsilon_1} \frac{\epsilon}{k} P_k - C_{\epsilon_2} \frac{\epsilon^2}{k} \quad (2.21)$$

Term ( $c_1$ ) in equation (2.20) represents diffusion of  $\epsilon$  by turbulent fluctuations and, like its counterpart in the  $k$ -equation, it is modelled by gradient-transport hypothesis, thus:

$$-\overline{u_j \epsilon'} = \frac{\nu_t}{\sigma_\epsilon} \frac{\partial \epsilon}{\partial x_j} \quad (2.22)$$

The final modelled equation for  $\epsilon$  takes the form:

$$\frac{\partial \epsilon}{\partial t} + U_j \frac{\partial \epsilon}{\partial x_j} = \frac{\partial}{\partial x_j} \left( \frac{\nu_t}{\sigma_\epsilon} \frac{\partial \epsilon}{\partial x_j} \right) + C_{\epsilon 1} \frac{\epsilon}{k} P_k - C_{\epsilon 2} \frac{\epsilon^2}{k} \quad (2.23)$$

Note that the form of the equations for the  $k$  and  $\epsilon$  remains unaltered irrespective of whether the linear or the non-linear stress-strain relationship is used. The complete model then entails the solution of the momentum equations (2.5) and of equations (2.19) and (2.23) for  $k$  and  $\epsilon$  respectively. The mean-flow and turbulence variables being linked via the eddy viscosity as defined in equation (2.7). The constants of this model are assigned the values in Table 2.1.

| $C_\mu$ | $\sigma_k$ | $\sigma_\epsilon$ | $C_{\epsilon 1}$ | $C_{\epsilon 2}$ | $C_E$ | $C_D$ |
|---------|------------|-------------------|------------------|------------------|-------|-------|
| 0.09    | 1.0        | 1.3               | 1.44             | 1.9              | 1.68  | 1.68  |

Table 2.1 Constants for the  $k$ - $\epsilon$  model

The  $k$ - $\epsilon$  model is very widely used in practical calculations yet it is known not to be valid to a wide number of flows unless modified in some way. Usually, the  $\epsilon$ -equation is modified to affect the level of the energy dissipation rate and indirectly, the eddy viscosity.

Most modifications are applied to the source terms of  $\epsilon$  which are given by:

$$S_\epsilon = C_{\epsilon 1} \frac{\epsilon}{k} P_k - C_{\epsilon 2} \frac{\epsilon^2}{k} \quad (2.24)$$

Hanjalic and Launder (1980) argued that the irrotational strain rates are more influential in the production of  $\epsilon$  than the rotational (shear) strains. Mathematically, their proposal for 'sensitizing' the dissipation rate to irrotational strains amounts to splitting the  $P_k$  term in equation (2.24) into two parts, one representing production-by-shear and another representing production-by-irrotational strains, and then multiplying the second

part by a coefficient greater than that multiplying the first. Details of this model adaptation and its justification can be found in the original reference. Here, only the final form of the  $\epsilon$ -sources is relevant and this (for two-dimensional flows) may be written as:

$$\begin{aligned} S_\epsilon = & \frac{\epsilon}{k} \left[ -C_{\epsilon 1} \bar{u}\bar{v} \left( \frac{\partial U}{\partial y} + \frac{\partial V}{\partial x} \right) - C'_{\epsilon 1} (\bar{u}^2 - \bar{v}^2) \frac{\partial U}{\partial x} \right. \\ & \left. + 4(C'_{\epsilon 1} - C_{\epsilon 1}) \nu_t \frac{\partial U}{\partial y} \frac{\partial V}{\partial x} \right] - C_{\epsilon 2} \frac{\epsilon^2}{k} \end{aligned} \quad (2.25)$$

In thin shear layers (where  $\partial U / \partial y \gg \partial V / \partial x$ ), this can be simplified to the following:

$$S_\epsilon = -C_{\epsilon 1} \bar{u}\bar{v} \frac{\partial U}{\partial y} \frac{\epsilon}{k} - C'_{\epsilon 1} (\bar{u}^2 - \bar{v}^2) \frac{\partial U}{\partial x} \frac{\epsilon}{k} - C_{\epsilon 2} \frac{\epsilon^2}{k} \quad (2.26)$$

Hanjalic and Launder proposed that  $C_{\epsilon 1}$  be kept at its original value of 1.44 and  $C'_{\epsilon 1}$  assigned the value of 4.44. Later work by Johnston (1984), in connection with boundary-layer flows in adverse pressure gradient, suggested that a lower value for  $C'_{\epsilon 1}$  may be more appropriate; the value of 2.5 was recommended and this will be adopted in the present work.

For later convenience, the following shorthand notation will be used to identify the various model adaptations:

**LKE** denotes the standard, linear,  $k-\epsilon$  model;

**NKE** denotes the model when used with Speziale's non-linear stress-strain relationship;

**EKE** denotes the standard model with irrotational-strain modification to the  $\epsilon$ -equation.

## 2.4 REYNOLDS-STRESS TRANSPORT MODELLING

Equation (2.6) for the transport of  $\overline{u_i u_j}$  may be written in the symbolic form:

$$U_k \frac{\partial \overline{u_i u_j}}{\partial x_k} = \widehat{P_{ij}} + \widehat{D_{ij}} + \widehat{\Phi_{ij}} - \widehat{\epsilon_{ij}} \quad (2.27)$$

The production rate of  $\overline{u_i u_j}$  is given as:

$$P_{ij} = - \left( \overline{u_i u_k} \frac{\partial U_j}{\partial x_k} + \overline{u_j u_k} \frac{\partial U_i}{\partial x_k} \right) \quad (2.28)$$

Clearly, this term requires no modelling as it is formed of quantities that are the dependent variables of equations to be solved.

The diffusion term  $D_{ij}$  represents the rate of transport of  $\overline{u_i u_j}$  by turbulent fluctuations, molecular diffusion and pressure fluctuations and this term is expressed in the form:

$$D_{ij} = - \frac{\partial}{\partial x_k} \left[ \overline{u_i u_j u_k} - \nu \frac{\partial \overline{u_i u_j}}{\partial x_k} + \frac{p'}{\rho} (\delta_{jk} u_i + \delta_{ik} u_j) \right] \quad (2.29)$$

The viscous-diffusion term is small in all regions of the flow except very close to the walls. At any rate, it is exact and is retained without change. Almost nothing is known about the pressure-diffusion term and hence this term is dropped following the usual practice. In an extension to gradient-transport hypothesis, Daly and Harlow (1970) proposed that the diffusion of  $\overline{u_i u_j}$  is proportional to its spatial gradients to write:

$$D_{ij} = C_s \frac{k}{\epsilon} \overline{u_k u_l} \frac{\partial \overline{u_i u_j}}{\partial x_l} \quad (2.30)$$

where the multiplier  $k/\epsilon$  may be interpreted as a characteristic time-scale

of the energy-containing eddies and  $C_s$  is a constant. Hanjalic and Launder (1972), from consideration of the exact transport equation for  $\overline{u_i u_j u_k}$ , proposed an alternative model which is written as:

$$-\overline{u_i u_j u_k} = C_s \frac{k}{\epsilon} \left[ \overline{u_i u_l} \frac{\partial \overline{u_j u_k}}{\partial x_l} + \overline{u_j u_l} \frac{\partial \overline{u_k u_i}}{\partial x_l} + \overline{u_k u_l} \frac{\partial \overline{u_i u_j}}{\partial x_l} \right] \quad (2.31)$$

Note that Daly and Harlow's model is represented by the last term in above expression. There is no evidence that the adoption of the more complete expression leads to improved predictions in complex shear flows. Therefore, and following the example of Launder, Reece and Rodi (1975), Gibson and Launder (1978) and Gibson and Younis (1982), the simpler model of Daly and Harlow was used throughout this work.

The pressure-strain term  $\Phi_{ij}$  is given by:

$$\overline{\Phi_{ij}} = \frac{p'}{\rho} \left( \frac{\partial u_i}{\partial x_j} + \frac{\partial u_j}{\partial x_i} \right) \quad (2.32)$$

Chou (1945) derived an analytical solution to the Poisson equation for the fluctuating pressure correlations from which it was obvious that those correlations may be modelled as the sum of three separate contributions, thus:

$$\Phi_{ij} = \Phi_{ij,1} + \Phi_{ij,2} + \Phi_{ij,w} \quad (2.33)$$

The first term represents interactions between turbulence quantities, the second term represents interactions between the turbulence field with the mean rate of strain and the third term accounts for the effects of a wall on the turbulent field in its vicinity.

In non-isotropic homogeneous flow with small or zero mean rate of strain, only the term  $\Phi_{ij,1}$  is significant; its role being to redistribute the turbulence energy amongst its components and to diminish the shear stresses. Rotta (1951) proposed the following model:

$$\Phi_{ij,1} = -C_1 \epsilon a_{ij} \quad (2.34)$$

where  $C_1$  is a coefficient and  $a_{ij}$  is the normalized anisotropy tensor given by:

$$a_{ij} = \frac{\bar{u}_i \bar{u}_j}{k} - \frac{2}{3} \delta_{ij} \quad (2.35)$$

Launder, Reece and Rodi (1975) proposed that the second term  $\Phi_{ij,2}$  may be modelled as:

$$\Phi_{ij,2} = \alpha \left( P_{ij} - \frac{2}{3} \delta_{ij} P_k \right) + \beta k \left( \frac{\partial U_i}{\partial x_j} + \frac{\partial U_j}{\partial x_i} \right) + \gamma \left( G_{ij} - \frac{2}{3} \delta_{ij} P_k \right) \quad (2.36)$$

where

$$G_{ij} = - \left( \bar{u}_i \bar{u}_k \frac{\partial U_k}{\partial x_j} + \bar{u}_j \bar{u}_k \frac{\partial U_k}{\partial x_i} \right) \quad (2.37)$$

and  $\alpha$ ,  $\beta$  and  $\gamma$  are constants.

Launder et al. (1975) also found that the first term in equation (2.36) is the dominant one and suggested that it, alone, can also be used as a complete model for  $\Phi_{ij,2}$ , thus:

$$\Phi_{ij,2} = -C_2 \left( P_{ij} - \frac{2}{3} \delta_{ij} P_k \right) \quad (2.38)$$

Obviously,  $C_2$  will need to assume a different value from that of  $\alpha$  to compensate for the absence of the additional terms in the simplified expression.

The complete model for the pressure-strain term has to account for wall-proximity effects which act to reduce the level of the fluctuating velocity component normal to the wall and increase the components parallel to it. On the assumption that both  $\Phi_{ij,1}$  and  $\Phi_{ij,2}$  are influenced by the presence of the wall,  $\Phi_{ij,w}$  (see equation, 2.33) may be modelled in two parts as:

$$\Phi_{ij,w} = \Phi'_{ij,1} + \Phi'_{ij,2} \quad (2.39)$$

Shir's (1973) proposals for  $\Phi'_{ij,1}$  are widely accepted and may be written as:

$$\Phi'_{ij,1} = C'_1 \frac{\epsilon}{k} \left( \overline{u_k u_m} n_k n_m \delta_{ij} - \frac{3}{2} \overline{u_k u_i} n_k n_j - \frac{3}{2} \overline{u_k u_j} n_k n_i \right) f \left( \frac{L}{x_n} \right) \quad (2.40)$$

where  $L$  represents a typical length scale of the energy containing eddies,  $n_i$  is a unit vector normal to the wall and  $x_n$  is the normal distance to the wall.

Gibson and Launder (1978) extended Shir's proposal to include a correction for  $\Phi_{ij,2}$ , thus:

$$\Phi'_{ij,2} = C'_2 \left( \Phi_{km,2} n_k n_m \delta_{ij} - \frac{3}{2} \Phi_{ki,2} n_k n_j - \frac{3}{2} \Phi_{kj,2} n_k n_i \right) f \left( \frac{L}{x_n} \right) \quad (2.41)$$

Attention is now turned to consideration of the wall-damping function  $f$ : the ratio of a typical length scale of the energy-containing eddies to the normal distance from the wall. The turbulence length scale is usually taken to be proportional  $k^{3/2}/\epsilon$  and therefore  $f$  can be expressed as:

$$f = \alpha \frac{k^{3/2}}{x_n \epsilon} \quad (2.42)$$

Some authors prefer  $(-\overline{uv})^{3/2}/\epsilon$  but the two definitions are broadly equivalent since the ratio  $-\overline{uv}/k$  is constant in the near-wall region. The proportionality coefficient  $\alpha$  is taken as  $C_\mu^{3/4}/\kappa$  where  $\kappa$  is the von Karman constant.

With the assumption that the small-scale motions responsible for viscous dissipation are isotropic at high turbulence Reynolds number, the last term in equation (2.27), which represents the dissipation of  $\overline{u_i u_j}$ , may be related to the dissipation of  $k$ , thus:

$$\epsilon_{ij} = 2\nu \frac{\overline{\partial u_i / \partial x_k \partial u_j / \partial x_k}}{} = \frac{2}{3} \delta_{ij} \epsilon \quad (2.43)$$

This implies that energy is dissipated by molecular effects from the three normal stresses in equal proportions. This, of course, would not be valid in the viscous-dominated regions very close to the walls but certain boundary conditions may be adopted there to remove the need for carrying out the computations in that region.

The full modelled Reynolds-stress transport equations adopted for this study are:

$$\begin{aligned}
 U_k \frac{\partial \bar{u}_i \bar{u}_j}{\partial x_k} &= \frac{\partial}{\partial x_k} \left( C_s \frac{k}{\epsilon} \bar{u}_k \bar{u}_l \frac{\partial \bar{u}_i \bar{u}_j}{\partial x_l} \right) - \left( \bar{u}_i \bar{u}_k \frac{\partial U_j}{\partial x_k} + \bar{u}_j \bar{u}_k \frac{\partial U_i}{\partial x_k} \right) \\
 &- C_1 \frac{\epsilon}{k} \left( \bar{u}_i \bar{u}_j - \frac{2}{3} \delta_{ij} k \right) - C_2 \left( P_{ij} - \frac{2}{3} \delta_{ij} P_k \right) \\
 &+ C'_1 \frac{\epsilon}{k} \left( \bar{u}_k \bar{u}_m n_k n_m \delta_{ij} - \frac{3}{2} \bar{u}_k \bar{u}_i n_k n_j - \frac{3}{2} \bar{u}_k \bar{u}_j n_k n_i \right) f \left( \frac{L}{x_n} \right) \\
 &+ C'_2 \left( \Phi_{km,2} n_k n_m \delta_{ij} - \frac{3}{2} \Phi_{ki,2} n_k n_j - \frac{3}{2} \Phi_{kj,2} n_k n_i \right) f \left( \frac{L}{x_n} \right) \\
 &- \frac{2}{3} \delta_{ij} \epsilon
 \end{aligned} \tag{2.44}$$

For two-dimensional flows, the equations for the Reynolds stresses can be written as:

$$\begin{aligned}
 U \frac{\partial \bar{u}^2}{\partial x} + V \frac{\partial \bar{u}^2}{\partial y} &= \frac{\partial}{\partial x} \left[ C_s \frac{k}{\epsilon} \left( \bar{u}^2 \frac{\partial \bar{u}^2}{\partial x} + \bar{u}\bar{v} \frac{\partial \bar{u}^2}{\partial y} \right) \right] \\
 &+ \frac{\partial}{\partial y} \left[ C_s \frac{k}{\epsilon} \left( \bar{u}\bar{v} \frac{\partial \bar{u}^2}{\partial x} + \bar{v}^2 \frac{\partial \bar{u}^2}{\partial y} \right) \right] \\
 &+ P_{11} - C_1 \frac{\epsilon}{k} \left( \bar{u}^2 - \frac{2}{3} k \right) - C_2 \left( P_{11} - \frac{2}{3} P_k \right) \\
 &- 2C'_1 \frac{\epsilon}{k} \bar{u}^2 f_x + 2C'_2 \left( P_{11} - \frac{2}{3} P_k \right) f_x \\
 &+ C'_1 \frac{\epsilon}{k} \bar{v}^2 f_y - C'_2 \left( P_{22} - \frac{2}{3} P_k \right) f_y - \frac{2}{3} \epsilon
 \end{aligned} \tag{2.45}$$

$$\begin{aligned}
 U \frac{\partial \bar{v}^2}{\partial x} + V \frac{\partial \bar{v}^2}{\partial y} &= \frac{\partial}{\partial x} \left[ C_s \frac{k}{\epsilon} \left( \bar{u}^2 \frac{\partial \bar{v}^2}{\partial x} + \bar{u}\bar{v} \frac{\partial \bar{v}^2}{\partial y} \right) \right] \\
 &+ \frac{\partial}{\partial y} \left[ C_s \frac{k}{\epsilon} \left( \bar{u}\bar{v} \frac{\partial \bar{v}^2}{\partial x} + \bar{v}^2 \frac{\partial \bar{v}^2}{\partial y} \right) \right]
 \end{aligned}$$

$$\begin{aligned}
& + P_{22} - C_1 \frac{\epsilon}{k} \left( \bar{v}^2 - \frac{2}{3} k \right) - C_2 \left( P_{22} - \frac{2}{3} P_k \right) \\
& + C'_1 \frac{\epsilon}{k} \bar{u}^2 f_x - C'_2 \left( P_{11} - \frac{2}{3} P_k \right) f_x \\
& - 2C'_1 \frac{\epsilon}{k} \bar{v}^2 f_y + 2C'_2 \left( P_{22} - \frac{2}{3} P_k \right) f_y - \frac{2}{3} \epsilon
\end{aligned} \quad (2.46)$$

$$\begin{aligned}
U \frac{\partial \bar{w}^2}{\partial x} + V \frac{\partial \bar{w}^2}{\partial y} &= \frac{\partial}{\partial x} \left[ C_s \frac{k}{\epsilon} \left( \bar{u}^2 \frac{\partial \bar{w}^2}{\partial x} + \bar{u}\bar{v} \frac{\partial \bar{w}^2}{\partial y} \right) \right] \\
&+ \frac{\partial}{\partial y} \left( C_s \frac{k}{\epsilon} \left[ \bar{u}\bar{v} \frac{\partial \bar{w}^2}{\partial x} + \bar{v}^2 \frac{\partial \bar{w}^2}{\partial y} \right] \right) \\
&- C_1 \frac{\epsilon}{k} \left( \bar{w}^2 - \frac{2}{3} k \right) + \frac{2}{3} C_2 P_k \\
&+ C'_1 \frac{\epsilon}{k} \bar{u}^2 f_x - C'_2 \left( P_{11} - \frac{2}{3} P_k \right) f_x \\
&+ C'_1 \frac{\epsilon}{k} \bar{v}^2 f_y - C'_2 \left( P_{22} - \frac{2}{3} P_k \right) f_y
\end{aligned} \quad (2.47)$$

$$\begin{aligned}
U \frac{\partial \bar{u}\bar{v}}{\partial x} + V \frac{\partial \bar{u}\bar{v}}{\partial y} &= \frac{\partial}{\partial x} \left[ C_s \frac{k}{\epsilon} \left( \bar{u}^2 \frac{\partial \bar{u}\bar{v}}{\partial x} + \bar{u}\bar{v} \frac{\partial \bar{u}\bar{v}}{\partial y} \right) \right] \\
&+ \frac{\partial}{\partial y} \left[ C_s \frac{k}{\epsilon} \left( \bar{u}\bar{v} \frac{\partial \bar{u}\bar{v}}{\partial x} + \bar{v}^2 \frac{\partial \bar{u}\bar{v}}{\partial y} \right) \right] \\
&+ P_{12} - C_1 \frac{\epsilon}{k} \bar{u}\bar{v} - C_2 P_{12} \\
&- \frac{3}{2} C'_1 \frac{\epsilon}{k} \bar{u}\bar{v} f_x + \frac{3}{2} C'_2 P_{12} f_x \\
&- \frac{3}{2} C'_1 \frac{\epsilon}{k} \bar{u}\bar{v} f_y + \frac{3}{2} C'_2 P_{12} f_y - \frac{2}{3} \epsilon
\end{aligned} \quad (2.48)$$

where  $f_x$  and  $f_y$  are the wall-damping functions, and  $P_{11}$ ,  $P_{22}$  and  $P_{12}$  are the rates of production terms given by:

$$\begin{aligned}
P_{11} &= -2\bar{u}^2 \frac{\partial U}{\partial x} - 2\bar{u}\bar{v} \frac{\partial U}{\partial y} \\
P_{22} &= -2\bar{v}^2 \frac{\partial V}{\partial y} - 2\bar{u}\bar{v} \frac{\partial V}{\partial x} \\
P_{12} &= -\bar{u}^2 \frac{\partial V}{\partial x} - \bar{v}^2 \frac{\partial U}{\partial y}
\end{aligned} \quad (2.49)$$

The equation for  $\epsilon$  used in conjunction with the Reynolds-stress model is the same as before (see equation, 2.27) except that the diffusion term (term  $c_1$  in equation 2.20) is modelled in a manner analogous to its counterpart in the stress equations, thus:

$$-\overline{u_j \epsilon'} = \left( C_\epsilon \frac{k}{\epsilon} \overline{u_j u_l} \frac{\partial \epsilon}{\partial x_l} \right) \quad (2.50)$$

The final form of  $\epsilon$ -equation for the Reynolds-stress model is therefore:

$$\frac{\partial \epsilon}{\partial t} + U_j \frac{\partial \epsilon}{\partial x_j} = \frac{\partial}{\partial x_j} \left( C_\epsilon \frac{k}{\epsilon} \overline{u_j u_l} \frac{\partial \epsilon}{\partial x_l} \right) + C_{\epsilon 1} \frac{\epsilon}{k} P_k - C_{\epsilon 2} \frac{\epsilon^2}{k} \quad (2.51)$$

$P_k$  is now calculated by using the stresses obtained from their own equations.

The complete model thus entails solving the set of momentum equations (2.5), together with equations (2.44) for the Reynolds stresses and equation (2.51) for  $\epsilon$ . A number of coefficients appear in the model and those are assigned the values shown in Table 2.2 below.

| $C_1$ | $C_2$ | $C'_1$ | $C'_2$ | $C_s$ | $C_\epsilon$ | $C_{\epsilon 1}$ | $C_{\epsilon 2}$ |
|-------|-------|--------|--------|-------|--------------|------------------|------------------|
| 1.8   | 0.6   | 0.5    | 0.18   | 0.22  | 0.18         | 1.44             | 1.90             |

Table 2.2 Coefficients used for the Reynolds-stress model

The main obstacle to the use of complete Reynolds-stress-transport models of turbulence in practical engineering calculations arguably lies in the use of the wall-damping term  $\Phi_{ijw}$  in such models. In simple, unidirectional, flows bounded by a single wall, this quantity can be defined without too much ambiguity: the turbulence length scale is taken to be proportional  $k^{3/2}/\epsilon$  and the normal distance from the wall is readily available from the computational grid. The situation for flows in complex domains is very different. Thus, for example, two (or three) walls may intersect to form a corner and the question then arises as to the

best practice for specifying the wall damping function in the corner region: sometimes a linear additive approach is used (wherein the walls are assumed to act separately from each other) while in other applications an integral, averaged, approach is preferred. The function is sometimes taken to vary linearly with distance from the walls and, at other times, quadratically. There are no rules or guidelines as to be the best practice to employ for a particular geometry; that has to be determined by trial and error and, even then, not without discontinuities appearing in the predicted distributions of wall pressure and shear stresses. When the fluid is bounded by curved surfaces requiring the use of body-fitted coordinates that may be non-orthogonal, an added difficulty arises, namely that the normal distances from the walls are not readily available but must be evaluated from geometric considerations. Those can be costly, in terms of time- and storage requirements, and may also become entirely impractical when several such complex boundaries are simultaneously present.

Clearly, then, the ability to abandon the cumbersome wall-reflections term without compromising the validity of the complete closure model must be viewed as an important prerequisite to the wider acceptance and use of the Reynolds-stress-transport models for practical engineering calculations.

Recently, Speziale, Sarkar and Gatski (1991) proposed a new model for the complete pressure-strain correlations which is written as:

$$\begin{aligned}\Phi_{ij} = & - (C_1 \epsilon + C_1^* P_k) b_{ij} + C_2 \epsilon (b_{ik} b_{kj} - \frac{1}{3} b_{mn} b_{mn} \delta_{ij}) \\ & + [C_3 - C_3^* (b_{mn} b_{mn})^{\frac{1}{2}}] k S_{ij} + C_4 k (b_{ik} S_{jk} + b_{jk} S_{ik} - \frac{2}{3} b_{mn} S_{mn} \delta_{ij}) \\ & + C_5 k (b_{ik} W_{jk} + b_{jk} W_{ik})\end{aligned}\quad (2.52)$$

where  $b_{ij}$  is the anisotropy tensor,  $W_{ij}$  is the mean vorticity tensor and  $S_{ij}$  is the mean rate of strain tensor, quantities defined as:

$$b_{ij} = \frac{\bar{u}_i \bar{u}_j}{2k} - \frac{1}{3} \delta_{ij} \quad (2.53)$$

$$W_{ij} = \frac{1}{2} \left( \frac{\partial U_i}{\partial x_j} - \frac{\partial U_j}{\partial x_i} \right) \quad (2.54)$$

$$S_{ij} = \frac{1}{2} \left( \frac{\partial U_i}{\partial x_j} + \frac{\partial U_j}{\partial x_i} \right) \quad (2.55)$$

The new model differs from that of Launder, Reece and Rodi in being quadratic in the Reynolds-stresses and, as such, potentially more capable of representing the complex interactions between the mean flow and the turbulence fields. Indeed, the Launder et al. model can be recovered by simply setting the coefficient  $C_1^*$ ,  $C_2$  and  $C_3^*$  to zero. The originators also excluded some data sets for homogeneous free shear flows from its calibration,\*with the result that the new model obtains the correct relative stress levels in both free and wall-bounded flows , the latter without contribution from a wall-reflections term. When this model was first considered in the present work, no assessment of its performance had been carried out anywhere and hence its suitability to complex, separated, flows was yet to be determined. The present study thus forms the first attempt at a detailed assessment of this model in practically-relevant flows. The full set of model equations for two-dimensional flows are listed below for completeness:

$$\begin{aligned} U \frac{\partial \bar{u}^2}{\partial x} + V \frac{\partial \bar{u}^2}{\partial y} &= \frac{\partial}{\partial x} \left[ C_s \frac{k}{\epsilon} \left( \bar{u}^2 \frac{\partial \bar{u}^2}{\partial x} + \bar{u}\bar{v} \frac{\partial \bar{u}^2}{\partial y} \right) \right] \\ &\quad + \frac{\partial}{\partial y} \left[ C_s \frac{k}{\epsilon} \left( \bar{u}\bar{v} \frac{\partial \bar{u}^2}{\partial x} + \bar{v}^2 \frac{\partial \bar{u}^2}{\partial y} \right) \right] \\ &\quad + P_{11} - (C_1 \epsilon + C_1^* P_k) b_{11} \\ &\quad + C_2 \epsilon \left( b_{11}^2 + b_{12}^2 - \frac{A_2}{3} \right) + (C_3 - C_3^* \sqrt{A_2}) k S_{11} \\ &\quad + C_4 k \left( \frac{4}{3} b_{11} S_{11} + \frac{2}{3} b_{12} S_{12} - \frac{2}{3} b_{22} S_{22} \right) \\ &\quad + 2C_5 k b_{12} W_{12} - \frac{2}{3} \epsilon \end{aligned} \quad (2.56)$$
  

$$\begin{aligned} U \frac{\partial \bar{v}^2}{\partial x} + V \frac{\partial \bar{v}^2}{\partial y} &= \frac{\partial}{\partial x} \left[ C_s \frac{k}{\epsilon} \left( \bar{u}^2 \frac{\partial \bar{v}^2}{\partial x} + \bar{u}\bar{v} \frac{\partial \bar{v}^2}{\partial y} \right) \right] \\ &\quad + \frac{\partial}{\partial y} \left[ C_s \frac{k}{\epsilon} \left( \bar{u}\bar{v} \frac{\partial \bar{v}^2}{\partial x} + \bar{v}^2 \frac{\partial \bar{v}^2}{\partial y} \right) \right] \\ &\quad + P_{22} - (C_1 \epsilon + C_1^* P_k) b_{22} \\ &\quad + C_2 \epsilon \left( b_{22}^2 + b_{12}^2 - \frac{A_2}{3} \right) + (C_3 - C_3^* \sqrt{A_2}) k S_{22} \end{aligned}$$

$$\begin{aligned}
& + C_4 k \left( \frac{4}{3} b_{22} S_{22} + \frac{2}{3} b_{12} S_{12} - \frac{2}{3} b_{11} S_{11} \right) \\
& - 2C_5 k b_{12} W_{12} - \frac{2}{3} \epsilon
\end{aligned} \tag{2.57}$$

$$\begin{aligned}
U \frac{\partial \bar{w}^2}{\partial x} + V \frac{\partial \bar{w}^2}{\partial y} &= \frac{\partial}{\partial x} \left[ C_s \frac{k}{\epsilon} \left( \bar{u}^2 \frac{\partial \bar{w}^2}{\partial x} + \bar{u}\bar{v} \frac{\partial \bar{w}^2}{\partial y} \right) \right] \\
&+ \frac{\partial}{\partial y} \left[ C_s \frac{k}{\epsilon} \left( \bar{u}\bar{v} \frac{\partial \bar{w}^2}{\partial x} + \bar{v}^2 \frac{\partial \bar{w}^2}{\partial y} \right) \right] \\
&- (C_1 \epsilon + C_1^* P_k) b_{33} + C_2 \epsilon \left( b_{33}^2 - \frac{A_2}{3} \right) \\
&+ C_4 k \left( -\frac{2}{3} b_{11} S_{11} - \frac{4}{3} b_{12} S_{12} - \frac{2}{3} b_{22} S_{22} \right) - \frac{2}{3} \epsilon
\end{aligned} \tag{2.58}$$

$$\begin{aligned}
U \frac{\partial \bar{u}\bar{v}}{\partial x} + V \frac{\partial \bar{u}\bar{v}}{\partial y} &= \frac{\partial}{\partial x} \left[ C_s \frac{k}{\epsilon} \left( \bar{u}^2 \frac{\partial \bar{u}\bar{v}}{\partial x} + \bar{u}\bar{v} \frac{\partial \bar{u}\bar{v}}{\partial y} \right) \right] \\
&+ \frac{\partial}{\partial y} \left[ C_s \frac{k}{\epsilon} \left( \bar{u}\bar{v} \frac{\partial \bar{u}\bar{v}}{\partial x} + \bar{v}^2 \frac{\partial \bar{u}\bar{v}}{\partial y} \right) \right] \\
&+ P_{12} - (C_1 \epsilon + C_1^* P_k) b_{12} \\
&+ C_2 \epsilon (b_{11} b_{12} + b_{22} b_{12}) + (C_3 - C_3^* \sqrt{A_2}) k S_{12} \\
&+ C_4 k (b_{11} S_{12} + b_{22} S_{12} + b_{21} S_{11} + b_{21} S_{22}) \\
&+ C_5 k (b_{22} - b_{11}) W_{12} - \frac{2}{3} \epsilon
\end{aligned} \tag{2.59}$$

where

$$A_2 = b_{11}^2 + b_{22}^2 + b_{33}^2 + 2b_{12}^2 \tag{2.60}$$

The coefficients used here are those recommended by the model originators and are given in Table 2.3.

| $C_1$ | $C_2$ | $C_1^*$ | $C_3$ | $C_3^*$ | $C_4$ | $C_5$ | $C_{\epsilon_1}$ | $C_{\epsilon_2}$ |
|-------|-------|---------|-------|---------|-------|-------|------------------|------------------|
| 3.4   | 4.2   | 1.8     | 0.8   | 1.3     | 1.25  | 0.4   | 1.44             | 1.83             |

Table 2.3. Coefficients for the Speziale, Sarkar and Gatski model

The following labels are adopted to identify the alternative treatments for the pressure-strain correlations:

RSM0 the model of Launder et al. (1975) plus the wall-damping models of equations ( $\Phi'_{ij,1}$  of Shir, 1973, and,  $\Phi'_{ij,2}$  of Gibson & Launder, 1978).

RSM1 the model of Speziale et al. (1991).

## 2.5 CLOSURE

This chapter was concerned with presenting the mathematical basis of the  $k-\epsilon$  model and the Reynolds-stress closure. Two extensions to the 'standard'  $k-\epsilon$  model were considered and adopted for further testing: the first is Speziale's non-linear stress-strain relationship which should hopefully correct some of the defects associated with Boussinesq's linear approximation and the second is the irrotational-strain modification which has lead to some improvements in boundary-layer flows and may still be of benefit in separated flows.

Closure proposals for the Reynolds-stress equations were reviewed and some selected for the present application. In particular, two alternative proposals for the influential pressure-strain correlations are to be assessed: the first is a very well established one but requires a wall-damping function while the second is recently proposed, as yet untested, but potentially quite useful for practical computations as it does not appear to require a wall-damping function.

The implementation of the non-linear stress-strain relations and the complete Reynolds-stress closure in a general, non-orthogonal, flow solver utilizing a co-located storage arrangement is quite a challenging task, as will be demonstrated in the next chapter.

# Chapter 3

## SOLUTION PROCEDURE

### 3.1 INTRODUCTION

This chapter considers various aspects of the solution of the differential equations formulated in Chapter 2. A finite-volume method is used, derived from one advanced originally by Peric (1985) to calculate turbulent flows in complex domains. The method utilizes a co-located grid arrangement, whereby all the dependent variables are stored at the same location, and employs the Cartesian components for the dependent variables thus avoiding the troublesome 'curvature terms' associated with alternative methods. The method was extended here by the inclusion of the non-linear  $k-\epsilon$  model and the Reynolds-stress model. Efforts were directed towards the advancement of a predictive procedure which is both economical and reliable for use by practicing engineers. To this end, an algorithm for Reynolds-stress model simulations is proposed and its performance compared with alternative proposals. Section 3.2 presents the governing differential equations in general coordinate system and outlines the basis of discretization procedure for non-orthogonal body-fitted coordinates (Peric, 1985, Demirdzic and Peric, 1988). The differencing schemes used are briefly presented in Section 3.3. Those include the central, upwind, hybrid, power-law and linear-upwind differencing schemes.

The iterative SIMPLE algorithm of Patankar and Spalding (1972) used to couple the pressure and velocity calculations is introduced in Section 3.4, together with details of the special interpolation practice required to obtain stable solutions on a co-located grid. Section 3.5 considers the implementation of the Reynolds-stress model and gives details of the special practices required to obtain coupled velocity-stress solutions on a co-located grid. The boundary conditions are treated in Section 3.6 and details of the solution algorithm and convergence criterion provided in Section 3.7. A multigrid method was implemented in the code to accelerate the attainment of accurate results on fine meshes. Details of this method, and the results of its validation for some laminar-flow cases, are given in Section 3.8. The chapter is concluded in Section 3.9 with a summary of its main points.

### 3.2 THE DISCRETIZATION PROCEDURE

For the derivations that follow, it is more convenient to use the compact forms of the continuity and momentum equations proposed by Demirdzic (1982) and Peric (1985) which, for steady flows, are written as:

$$\frac{1}{J} \frac{\partial}{\partial x^j} (\rho U_m \beta_m^j) = 0 \quad (3.1)$$

$$\frac{1}{J} \frac{\partial}{\partial x^j} [(\rho U_m U_i - T_{mi}) \beta_m^j] = S_{U_i} \quad (3.2)$$

where the system ( $x^1, x^2, x^3$ ) is a general coordinate system and ( $y^1, y^2, y^3$ ) is the reference Cartesian coordinate system. The  $\beta_j^i$  represent the cofactor of  $\partial y^j / \partial x^i$  in the Jacobian of the coordinate transformation  $y^j = y^j(x^i)$  given as:

$$J = \begin{vmatrix} \frac{\partial y^1}{\partial x^1} & \frac{\partial y^2}{\partial x^1} & \frac{\partial y^3}{\partial x^1} \\ \frac{\partial y^1}{\partial x^2} & \frac{\partial y^2}{\partial x^2} & \frac{\partial y^3}{\partial x^2} \\ \frac{\partial y^1}{\partial x^3} & \frac{\partial y^2}{\partial x^3} & \frac{\partial y^3}{\partial x^3} \end{vmatrix} \quad (3.3)$$

The generalized equation for a representative variable ( $\Phi$ ) can be written as:

$$\frac{1}{J} \frac{\partial}{\partial x^j} [(\rho U_m \Phi - q_m) \beta_m^j] = S_\Phi \quad (3.4)$$

where  $\Phi$  represents any of the variables  $U_1, U_2, k, \epsilon, \bar{u^2}, \bar{v^2}$  and so on.

The diffusive flux  $q_m$  may be defined by gradient-transport hypothesis as:

$$q_m = \Gamma_\Phi \frac{\partial \Phi}{\partial x^n} \frac{1}{J} \beta_m^n \quad (3.5)$$

The diffusive flux in the momentum equations (3.2) is the stress tensor which can be written as:

$$T_{mi} = \frac{1}{J} \mu \left( \frac{\partial U_i}{\partial x_n} \beta_m^n + \frac{\partial U_m}{\partial x_i} \beta_i^l \right) - \rho \bar{u_m u_i} \quad (3.6)$$

Again, gradient-transport hypothesis (here Boussinesq's stress-strain relationship) can be used to obtain the equation below:

$$T_{mi} = \frac{1}{J} \mu_{eff} \left( \frac{\partial U_i}{\partial x_n} \beta_m^n + \frac{\partial U_m}{\partial x_i} \beta_i^l \right) \quad (3.7)$$

where  $\mu_{eff}$  is the sum of molecular and turbulent viscosity. When the non-linear stress-strain relationship is used, then the stress tensor can be derived from equation (2.10) by using the following transformed expressions

$$\overline{D}_{mi} = \frac{1}{2J} \left( \frac{\partial U_i}{\partial x_n} \beta_m^n + \frac{\partial U_m}{\partial x_i} \beta_i^l \right) \quad (3.8)$$

and

$$\overset{\circ}{D}_{mi} = U_k \frac{\partial \overline{D}_{mi}}{\partial x_n} \beta_k^n - \overline{D}_{ki} \frac{\partial U_m}{\partial x_l} \beta_k^l - \overline{D}_{km} \frac{\partial U_i}{\partial x_j} \beta_k^j \quad (3.9)$$

When the Reynolds-stress model is used, each component of the Reynolds-stress tensor is obtained from its own equation (2.44). Those equations have the same form as equation (3.4) with sources that contain, among other terms, the production rate of  $\bar{u}_i \bar{u}_j$  which can now be expressed as:

$$P_{ij} = -\frac{1}{J}(\bar{u}_i \bar{u}_k \frac{\partial U_j}{\partial x_m} \beta_k^m + \bar{u}_j \bar{u}_k \frac{\partial U_i}{\partial x_m} \beta_k^m) \quad (3.10)$$

In finite-volume methods, the governing equations are integrated, term-by-term, over control volumes such as the one shown in Fig. 3.1. All the dependent variables are stored at the control-volumes centers.

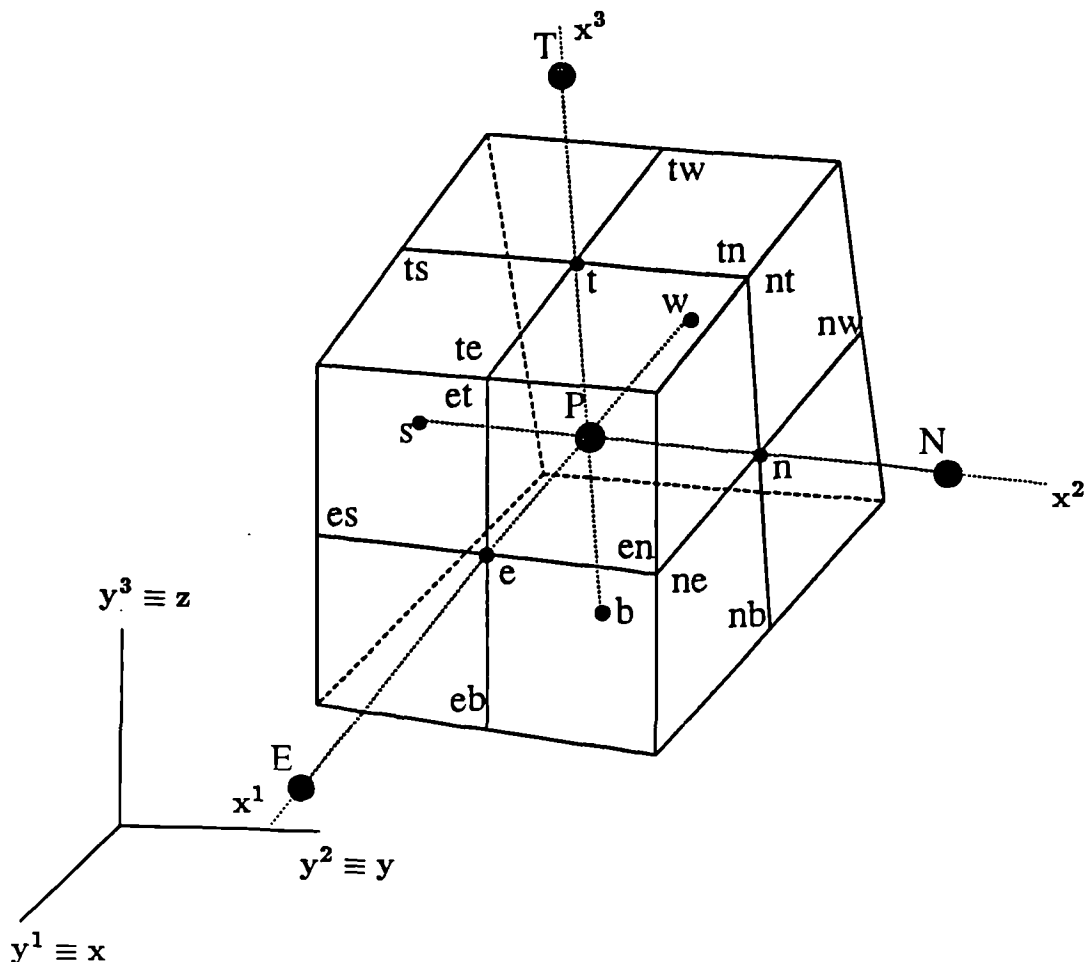


Fig. 3.1 Three-dimensional control volume.

In carrying out the integrations, Gauss' theorem is used to convert the volume integral into a surface one:

$$\int_V \operatorname{div} \vec{f} = \oint_A \vec{f} \cdot d\vec{A} \quad (3.11)$$

Thus, for the control volume in Fig.3.1, we have

$$\begin{aligned} \int_V \operatorname{div} \vec{f} &= \int_{A_e} f_e dA - \int_{A_w} f_w dA + \int_{A_n} f_n dA - \int_{A_s} f_s dA \\ &+ \int_{A_t} f_t dA - \int_{A_b} f_b dA \end{aligned} \quad , \quad (3.12)$$

The resulting balance equation for each control volume and variable  $\Phi$  may now be expressed as:

$$I_e - I_w + I_n - I_s + I_t - I_b = \int_{\Delta V} S_\Phi dV \quad (3.13)$$

Each of these terms is made up of two distinct parts, namely a convection contribution C and a diffusion contribution D. The latter is also in two parts: a normal  $D^N$  part and a cross-derivative part  $D^C$ .

The numerical evaluation of the terms in the last equation requires the calculation of various geometric parameters. Those include the quantity  $\beta_j^i$  which can be expressed in terms of the projection area of the control volume as:

$$\beta_j^i = \frac{b_j^i \Delta x_i}{\Delta x_1 \Delta x_2 \Delta x_3} \quad (3.14)$$

where  $b_j^i$  are the projection areas shown, for two-dimensional cases, in Fig. 3.2 (see next page). The cell volume  $\Delta V$  is evaluated from:

$$\Delta V = J \Delta x_1 \Delta x_2 \Delta x_3 \quad (3.15)$$

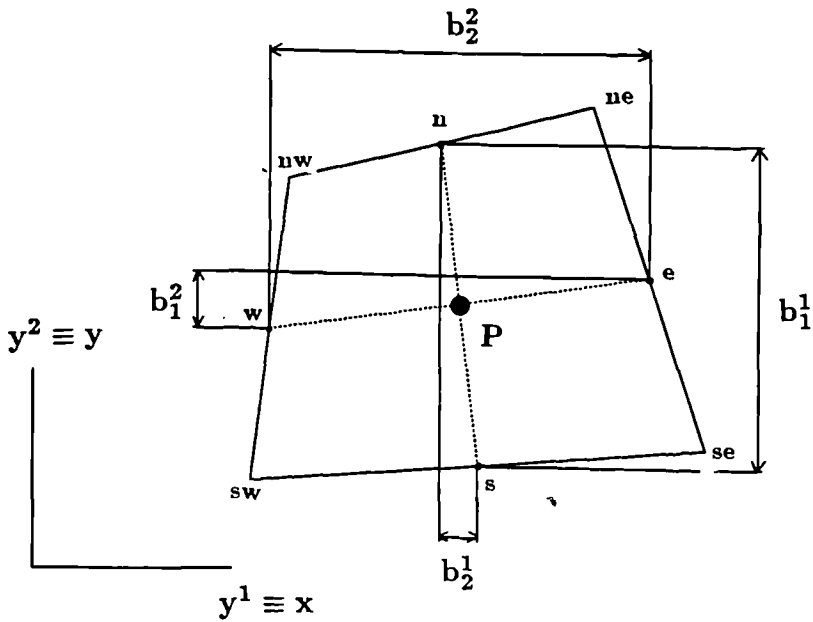


**Fig. 3.2 Area projections for two-dimensional control volume.**

The mass flux entering the control volume through its east face can be evaluated as:

$$\begin{aligned}
 F_e &= \rho_e(U_1 b_1^1 + U_2 b_2^1 + U_3 b_3^1)_e \\
 &= \rho_e \{ U_{1e} [(y_{ne} - y_{se})(z_{te} - z_{be}) - (y_{te} - y_{be})(z_{ne} - z_{se})] \\
 &\quad + U_{2e} [(x_{te} - x_{be})(z_{ne} - z_{se}) - (x_{ne} - x_{se})(z_{te} - z_{be})] \\
 &\quad + U_{3e} [(x_{ne} - x_{se})(y_{te} - y_{be}) - (x_{te} - x_{be})(y_{ne} - y_{se})] \} \quad (3.16)
 \end{aligned}$$

The mass fluxes through the other faces are calculated from similar expressions. The integral form of the continuity equation (3.1) for three-dimensional flow can now be written as:

$$F_e - F_w + F_n - F_s + F_t - F_b = 0 \quad (3.17)$$

The integrated mass fluxes are used in evaluating the convective fluxes of  $\Phi$  in equation (3.4). Thus convection contribution through the east cell face can now be written as:

$$C_e = \rho_e (U_1 b_1^1 + U_2 b_2^1 + U_3 b_3^1)_e \Phi_e = F_e \Phi_e \quad (3.18)$$

The diffusive flux (equations 3.4 and 3.5) through the east face is obtained after integration as:

$$\begin{aligned} D_e &= D_e^N + D_e^C \\ &= - \left( \frac{\Gamma_\Phi}{\text{Vol.}} \right)_e [(b_1^1 b_1^1 + b_2^1 b_2^1 + b_3^1 b_3^1)_e (\Phi_E - \Phi_P) \\ &\quad - (b_1^2 b_1^1 + b_2^2 b_2^1 + b_3^2 b_3^1)_e (\Phi_{ne} - \Phi_{se}) \\ &\quad - (b_1^3 b_1^1 + b_2^3 b_2^1 + b_3^3 b_3^1)_e (\Phi_{te} - \Phi_{be})] \end{aligned} \quad (3.19)$$

Note the emergence of terms containing values of  $\Phi$  other than at E or P. Those are "cross-diffusion" terms ( $D_e^C$ ) which are only <sup>non-zero</sup> for non-orthogonal grids. The geometrical factors appearing above are obtained from:

$$\begin{aligned} b_{2e}^1 &= (z_E - z_P)(y_{te} - y_{be}) - (z_{te} - z_{be})(y_E - y_P) \\ b_{2e}^2 &= (x_E - x_P)(z_{te} - z_{be}) - (x_{te} - x_{be})(z_E - z_P) \\ b_{2e}^3 &= (x_{te} - x_{be})(y_E - y_P) - (x_E - x_P)(y_{te} - y_{be}) \\ b_{3e}^1 &= (y_E - y_P)(z_{ne} - z_{se}) - (y_{ne} - y_{se})(z_E - z_P) \\ b_{3e}^2 &= (x_{ne} - x_{se})(z_E - z_P) - (x_E - x_P)(z_{ne} - z_{se}) \\ b_{3e}^3 &= (x_E - x_P)(y_{ne} - y_{se}) - (x_{ne} - x_{se})(y_E - y_P) \end{aligned} \quad (3.20)$$

Finally, the source term  $S_\Phi$  is assumed to be uniform over the whole control volume and hence the term, after integration, can be expressed as:

$$S_\Phi = \int_V s_\Phi dV \approx (s_\Phi)_P Vol. \quad (3.21)$$

Thus, for example, the pressure-gradient term in the  $U_1$ -component equation, integrated over the control volume, is obtained as:

$$S_{U_1} = -(p_e - p_w)b_{1P}^1 - (p_n - p_s)b_{1P}^2 - (p_t - p_b)b_{1P}^3 \quad (3.22)$$

The geometric factors  $b_{1P}^1$ ,  $b_{1P}^2$  and  $b_{1P}^3$  now relate to the central point P rather than to the cell faces; they are evaluated from:

$$\begin{aligned} b_{1P}^1 &= (y_n - y_s)(z_t - z_b) - (y_t - y_b)(z_n - z_s) \\ b_{1P}^2 &= (y_t - y_b)(z_e - z_w) - (y_e - y_w)(z_t - z_b) \\ b_{1P}^3 &= (y_e - y_w)(z_n - z_s) - (y_n - y_s)(z_e - z_w) \end{aligned} \quad (3.23)$$

Following the usual practice, and to enhance the stability of the solution process, the integrated source term may be linearized in the following form:

$$S_\Phi = S'_\Phi - S''_\Phi \Phi_P \quad (3.24)$$

where  $S''_\Phi$  must be positive.

The above procedure apply to both the mean-flow and the turbulence-model equations with some additional treatments required for the latter. When the non-linear  $k-\epsilon$  model is used, additional terms arise and those are incorporated as source terms in the appropriate momentum equation. The various terms of the Reynolds-stress equations are treated in the same way as in the scalar equation (3.4). The diffusion coefficient in those equations  $\Gamma_\Phi$  is now evaluated from the Daly and Harlow model as

the product of  $C_s k/\epsilon$  with the appropriate Reynolds stress.

The outcome of the discretization procedure is a set of algebraic equations which can be written in the form:

$$A_P \Phi_P = \sum_{nb} A_{nb} \Phi_{nb} + S'_\Phi \quad (3.25)$$

where

$$A_P = \sum_{nb} A_{nb} + S''_\Phi$$

and

$$nb = E, W, N, S, T, B$$

where  $S''_\Phi$  is the linearized source term from equation (3.22) and  $A_{nb}$  are coefficients containing convective and diffusive contributions.

The set of algebraic equations (3.25) is solved by the strongly implicit procedure of Stone (1968).

### 3.3 INTERPOLATION PRACTICES

An interpolation scheme is required to obtain the value of a dependent variable on the cell face from knowledge of the values at surrounding grid nodes. The choice of interpolation scheme has a profound influence on the stability of the numerical algorithm and the accuracy of the computed solutions. This choice is governed by various requirements which include robustness, economy and accuracy for a given grid density. Various schemes were tried in the course of this study. Below is an outline of their main features.

#### 3.3.1 Central differencing scheme

In this scheme, the value of  $\Phi$  at the east cell face is obtained from the

expression:

$$\Phi_e = \Phi_E f_{1P} + \Phi_P (1 - f_{1P}) \quad (3.26)$$

where  $f_{1P}$  is an interpolation factor given by

$$f_{1P} = \frac{\bar{Pe}}{\bar{Pe} + \bar{eE}} \quad (3.27)$$

$\bar{Pe}$  is the distance between the central point  $P$  and point  $e$  in the center of the east cell face and  $\bar{eE}$  is the distance between  $e$  and point  $E$  at the centre of the east neighboring volume (see Fig. 3.1).

If this scheme is used to evaluate the convective parts of the coefficients  $A_{nb}$  then that results in:

$$A_E^C = -F_{1e} f_{1P}$$

and, for the west side:

$$A_W^C = F_{1w} (1 - f_{1W}) \quad (3.28)$$

It is clear from the above that the convective part of the coefficients may become large and negative leading to the whole coefficient  $A_{nb}$  to become negative with undesirable consequences to the stability of the solution process. For this reason, and for flows dominated by convection, this scheme is usually abandoned in favour of one of the following below.

### 3.3.2 Upwind differencing scheme

In this scheme, the cell-face values are obtained from the following expressions:

$$\Phi_e = \Phi_P \text{ if } F_{le} > 0$$

$$\Phi_e = \Phi_E \text{ if } F_{le} < 0 \quad (3.29)$$

If a new operator is defined by  $\text{MAX}[a,b]$  to denote the greater of  $a$  and  $b$ , the convective parts of the coefficient  $A_{nb}$  can be written as:

$$A_E^C = \text{MAX}[0, -F_{le}]$$

or, for the west face, as:

$$A_W^C = \text{MAX}[0, F_{lw}] \quad (3.30)$$

This scheme is formally only first-order accurate thus requiring relatively fine grids for accurate solutions. On the other hand it is also stable, since it does not allow for the coefficients to become negative.

### 3.3.3 Power-law differencing scheme

The power-law scheme was proposed by Patankar (1980) to operate on both the diffusion and convection fluxes, thus:

$$A_E = D_e \text{MAX} \left[ 0, \left( 1 - \frac{0.1 |F_e|}{D_e} \right)^5 \right] + \text{MAX}[0, -F_e] \quad (3.31)$$

or, for the west side:

$$A_W = D_w \text{MAX} \left[ 0, \left( 1 - \frac{0.1 |F_w|}{D_w} \right)^5 \right] + \text{MAX}[0, -F_w] \quad (3.32)$$

This scheme, like the central-differencing scheme, is second-order accurate. It is also stable since it guarantees the positivity of the coefficients.

### 3.3.4 Linear-upwind differencing scheme

In this scheme, the value at the cell-face is obtained by linear extrapolation of the values at the two nodes upwind of it, thus:

$$\begin{aligned}\Phi_e &= \Phi_P + (\Phi_P - \Phi_W)(1 - f_{1w}) \quad \text{if } F_{1e} > 0 \\ \Phi_e &= \Phi_E + (\Phi_E - \Phi_{EE})(1 - f_{1E}) \quad \text{if } F_{1e} < 0\end{aligned}\quad (3.33)$$

With this definition, the convective parts of the coefficients  $A_{nb}$  may be written for the east face as:

$$\begin{aligned}A_E^C &= \text{MAX}[0, -F_{1e}](1 + f_{1E}) + \text{MAX}[0, -F_{1w}]f_{1P} \\ A_{EE}^C &= -\text{MAX}[0, -F_{1e}]f_{1E}\end{aligned}$$

and, for the west face as:

$$\begin{aligned}A_W^C &= \text{MAX}[0, F_{1w}](2 - f_{1ww}) + \text{MAX}[0, F_{1e}](1 - f_{1w}) \\ A_{WW}^C &= -\text{MAX}[0, F_{1w}](1 - f_{1ww})\end{aligned}\quad (3.34)$$

In this scheme, therefore, the coefficient  $A_p$  in equation (3.25) now contains additional contributions from nodes lying beyond the ones immediately surrounding it, thus:

$$A_P^C = \sum_{nb} A_{nb}^C \quad nb = E, W, N, S, T, B, EE, WW, NN, SS, TT, BB \quad (3.35)$$

This scheme is second-order accurate but it is also unbounded which means that the interpolated values may take on values greater or less than those at the domain boundaries.

Peric (1985) suggested a 'flux-blending' method to enable the use of higher-order schemes with guaranteed bounded solutions. In this method, the flux is re-interpreted as the combination of two different contributions, weighted in some arbitrary manner, thus

$$\mathbf{I} = \mathbf{I}_B + \alpha(\mathbf{I}_U - \mathbf{I}_B) \quad (3.36)$$

where it can be seen that  $\mathbf{I}$ , the resultant flux, is formed from contributions from the unbounded, higher-order, scheme (subscript U) and from the bounded scheme (subscript B) which is usually the upwind differencing scheme. The coefficient  $\alpha$  is the weighting factor which can either be specified within the calculation process or, more usually, set once and for all at the start of calculations.

### 3.3.5 Hybrid differencing scheme

One scheme which can be formulated using the flux-blending method is the well-known hybrid differencing scheme introduced originally to combine the merits of the central- and upwind-differencing schemes. Here, the former becomes the U scheme and the latter the B scheme.  $\alpha$  (see equation 3.36) is a control parameter whose values are set as follows:

$$\alpha = 0 \text{ for } |P_e| \leq 2$$

$$\alpha = 1 \text{ for } |P_e| > 2$$

where  $P_e$  is the Pecklet number defined as:

$$P_e = \frac{F_e}{D_e} \quad (3.37)$$

It can be seen that for highly-convective flows, i.e. for  $P_e > 2$ ,  $\alpha$  will be equal zero and hence the fluxes will be evaluated entirely from the upwind

scheme. In flows where diffusion and convection are in approximate balance,  $\alpha$  will be unity and the second-order accurate central-differencing scheme will be used.

### 3.4 PRESSURE-VELOCITY COUPLING

The coupling of the pressure and velocity calculations is achieved by the well known SIMPLE algorithm (Patankar and Spalding, 1972). In this algorithm, a pressure-correction equation is derived from the discretized equations for momentum and continuity. Details of this derivation may be found in the original reference. Here, the focus will be placed on the special adaptation of this technique for co-located grid storage.

The discretized  $U_1$ -momentum equation (3.25) for node P can be written as:

$$\begin{aligned} U_{1P}^* = & \frac{\sum_{nb} A_{nb} U_{1nb}^* + S_u^*}{A_P} \\ & + \frac{1}{A_P} \{ - (p_e^* - p_w^*) [(y_n - y_s)(z_t - z_b) - (y_t - y_b)(z_n - z_s)] \\ & - (p_n^* - p_s^*) [(y_t - y_b)(z_e - z_w) - (y_e - y_w)(z_t - z_b)] \\ & - (p_t^* - p_b^*) [(y_e - y_w)(z_n - z_s) - (y_n - y_s)(z_e - z_w)] \} \end{aligned} \quad (3.38)$$

where the pressure gradient term is treated separately from the sources  $S_u$ . This equation can be re-written as:

$$\begin{aligned} U_{1P}^* = & \left[ \frac{\sum_{nb} A_{nb} U_{1nb}^* + S_u^* - (p_n^* - p_s^*) [(y_t - y_b)(z_e - z_w) - (y_e - y_w)(z_t - z_b)]}{A_P} \right. \\ & \left. + \frac{-(p_t^* - p_b^*) [(y_e - y_w)(z_n - z_s) - (y_n - y_s)(z_e - z_w)]}{A_P} \right] \\ & - d_P (p_e^* - p_w^*) \end{aligned} \quad (3.39)$$

where

$$d_P = \frac{1}{A_P} [(y_n - y_s)(z_t - z_b) - (y_t - y_b)(z_n - z_s)] \quad (3.40)$$

The cell-face velocities are now obtained not from simple linear interpolation of the grid-node values but by interpolation of the equation above (see Rhie and Chow, 1982 and Peric, 1985). Thus, for the east face, for example,  $U_{1e}^*$  is now obtained from:

$$\begin{aligned} U_{1e}^* = & \left[ \frac{\sum_{nb} A_{nb} U_{1nb}^* + S_u^* - (p_n^* - p_s^*)[(y_t - y_b)(z_e - z_w) - (y_e - y_w)(z_t - z_b)]}{A_P} \right. \\ & + \left. \frac{-(p_t^* - p_b^*)[(y_e - y_w)(z_n - z_s) - (y_n - y_s)(z_e - z_w)]}{A_P} \right] \\ & - \bar{d}_e(p_E^* - p_P^*) \end{aligned} \quad (3.41)$$

where the overbars signify terms calculated by linear interpolation from nodes P and E while the pressure differences are evaluated from their nodal values.

By starting from a guessed pressure field, the calculated velocities do not necessarily satisfy the continuity equation and so a correction has to be introduced to those velocities in order to ensure this. The role of this correction can be seen from considering the discretized form of the continuity equation, expressed in terms of mass fluxes as:

$$F_e^* - F_w^* + F_n^* - F_s^* + F_t^* - F_b^* = S_m \quad (3.42)$$

The quantity  $S_m$  represents a false mass source which should disappear when a converged solution is attained. It can be shown that the velocity correction needed to enforce continuity is given by:

$$U'_{1e} = -\bar{d}_e(p'_E - p'_P) \quad (3.43)$$

where the term  $d_e$  is as defined above and is obtained by linear interpolation.

By substituting for the velocities by their corrections, mass-flux corrections  $\mathbf{F}'$  are obtained and those are then used to obtain the corrected fluxes, thus:

$$\mathbf{F}^{**} = \mathbf{F}^* + \mathbf{F}' \quad (3.44)$$

Manipulation of the above now gives:

$$\mathbf{F}'_e - \mathbf{F}'_w + \mathbf{F}'_n - \mathbf{F}'_s + \mathbf{F}'_t - \mathbf{F}'_b + \mathbf{S}_m = 0 \quad (3.45)$$

which, when combined with the equations for the velocity corrections (see equation, 3.43) yields the pressure-correction equation:

$$A_P p'_P = \sum_{nb} A_{nb} p'_{nb} - S_m \quad (3.46)$$

Solution of this equation yields the pressure corrections  $p'$ , which are now used to evaluate the velocity corrections from equation (3.43) and obtain new field values, thus:

$$\mathbf{U}_1^{**} = \mathbf{U}_1^* + \mathbf{U}'_1 \quad (3.47)$$

$$\mathbf{U}_2^{**} = \mathbf{U}_2^* + \mathbf{U}'_2 \quad (3.48)$$

$$\mathbf{U}_3^{**} = \mathbf{U}_3^* + \mathbf{U}'_3 \quad (3.49)$$

$$p^{**} = p^* + \alpha p' \quad (3.50)$$

where  $\alpha$  is an underrelaxation factor (Peric, 1985)

The newly-corrected values are then used in the solution of the momentum and pressure-correction equations until convergence is attained.

### 3.5 PRESSURE-STRESS-VELOCITY COUPLING

When using the Reynolds-stress transport models, there are certain benefits to be gained from treating the gradients of Reynolds stresses in the momentum equations as sources to those equations rather than as diffusion terms. One implication of this is that the expressions for the cell-face velocities, listed in the previous section, can now be re-formulated to account for the additional sources. In this work, the equivalent expression to equation (3.38) is obtained as:

$$U_{1P}^* = \left[ \frac{\sum_{nb} A_{nb} U_{1nb}^* + S_u^*}{A_P} \right] - d_P [(p_e^* - p_w^*) + (\rho \bar{u^2}_e - \rho \bar{u^2}_w)] \quad (3.51)$$

From this, and similar expressions at neighboring nodes, cell-face values are obtained by Rhie and Chow interpolation as:

$$U_{1e}^* = \left[ \frac{\sum_{nb} A_{nb} U_{1nb}^* + S_u^*}{A_P} \right]_e - \bar{d}_e [(p_E^* - p_P^*) + (\rho \bar{u_E^2} - \rho \bar{u_P^2})] \quad (3.52)$$

where overbars again denote linear interpolation and, as was the case with the pressure, the normal-stress differences are evaluated from nodal values.

Note in the above equations that the stress-gradient terms have been split into two parts, one of which has gradients in the same direction as the pressure (i.e.  $\partial/\partial x$ ) and is therefore included explicitly in the equation while the other part contains gradients in the other directions (i.e.  $\partial/\partial y$  and  $\partial/\partial z$ ) and is therefore included in  $S_u^*$ . Similar expressions may be obtained for the all components of velocity at the various cell faces.

Another consequence of treating the stress-gradient terms as sources is rather more undesirable; namely that the calculation of velocities and stresses may become uncoupled. The velocities and the Reynolds stresses, it should be remembered, are linked via their gradients and hence the potential for uncoupled solutions when the two are stored at the same grid location. The basic question which needs to be answered here, then,

is how best to incorporate the stress-gradient terms into the source-terms of the momentum equations without giving rise to oscillatory solutions. The answer lies in the way in which the values of the Reynolds stresses at the cell faces are obtained.

The most obvious way for obtaining those cell-face values is by linear interpolation of the stress values at the nodes. This approach was the first to be tried here and it was found to be satisfactory in some cases (e.g. flows in straight channels). In other cases, for example in some of the full-scale non-orthogonal geometries, this approach proved inadequate either because it produced oscillatory profiles (where positive and negative velocities occurred alternately) or because of very slow convergence. This approach was therefore abandoned in favour of one having its origins in the Rhie and Chow interpolation.

The discussion that follows uses the stress-components  $\bar{u^2}$  and  $\bar{uv}$  as examples; the approach is valid for all other components. The finite-difference equations for those two components (for two-dimensional and orthogonal grids) are:

$$\begin{aligned}\bar{u_P^2} &= \left[ \frac{\sum_{nb} A_{nb} \bar{u_{nb}^2} + S_{\bar{u^2}}}{A_P} \right] \\ &- \frac{1}{A_P} \left[ -2 + \frac{4}{3} C_2 - \frac{8}{3} C'_2 f_x - \frac{2}{3} C'_2 f_y \right] \rho \bar{u^2} \frac{\partial U}{\partial x} \quad (3.53)\end{aligned}$$

$$\begin{aligned}\bar{uv_P} &= \left[ \frac{\sum_{nb} A_{nb} \bar{uv}_{nb} + S_{\bar{uv}}}{A_P} \right] \\ &- \frac{1}{A_P} \left[ -1 + C_2 - \frac{3}{2} C'_2 f_x - \frac{3}{2} C'_2 f_y \right] \rho \bar{v^2} \frac{\partial U}{\partial y} \quad (3.54)\end{aligned}$$

The  $\bar{u^2}$  component appears in the U-momentum equation as  $\partial \bar{u^2} / \partial x$  and, for this reason, terms containing  $\partial U / \partial x$  have been grouped together in the way shown above. Similarly,  $\bar{uv}$  appears in the same equation as  $\partial \bar{uv} / \partial y$  and hence the grouping together of terms in  $\partial U / \partial y$ .

Now, in order to obtain the cell-face values of those stress-components, the following relations are used:

$$\begin{aligned}\overline{u_e^2} &= \left[ \frac{\sum_{nb} A_{nb} \overline{u_{nb}^2} + S_{u^2}}{A_P} \right] \\ &- \frac{1}{A_P} \left[ -2 + \frac{4}{3} C_2 - \frac{8}{3} C'_2 f_x - \frac{2}{3} C'_2 f_y \right] \overline{u^2} \left( \frac{U_E - U_P}{x_E - x_P} \right) \quad (3.55)\end{aligned}$$

$$\begin{aligned}\overline{uv_n} &= \left[ \frac{\sum_{nb} A_{nb} \overline{uv_{nb}} + S_{uv}}{A_P} \right] \\ &- \frac{1}{A_P} \left[ -1 + C_2 - \frac{3}{2} C'_2 f_x - \frac{3}{2} C'_2 f_y \right] \overline{v^2} \left( \frac{U_N - U_P}{y_N - y_P} \right) \quad (3.56)\end{aligned}$$

Here, again, overbars denote linear interpolation. Note, however, the treatment of the velocity gradients that were grouped together above: those are now evaluated from differences of mean velocity values at the grid nodes and it is this feature of the treatment that ensures that the stresses respond to the velocities themselves and this ensures that the solution process remains coupled.

Alternative methods for treating the diffusion terms in the momentum equations are available and some were used in this work to determine the optimum one. For the sake of later comparisons, the method details above will be referred to as **METHOD 1**: it consists of extracting the whole of the stress-gradient terms out of momentum diffusion and treating them as sources. In this method, then, diffusion of momentum, in the context of the difference equations, is purely by molecular agencies.

**METHOD 2** is one advocated by Obi, Peric and Scheuerer (1989) and by Lien and Leschziner (1991). In this method, part of the turbulent-diffusion term is restored to the difference equations by extracting from the terms multiplying the velocity gradients in equations (3.55 and 3.56) those that are unconditionally positive and treating them as 'apparent' or pseudo-viscosities.

In **METHOD 3**, which was advanced in the course of this work, a turbulent diffusion term, identical to the one appropriate to the  $k-\epsilon$  model, was added to the difference equations for momentum via their diffusion coefficients and taken away from the same equations via their sources.

Meanwhile, the stress-gradient terms were treated in exactly the same way as in METHOD 1.

Those methods were applied to a number of simple benchmark flows in order to assess their relative merits. In those tests, the RSM1 variant was used. For completeness, the stresses in this model are given by:

$$\begin{aligned} \bar{u_e^2} &= \left[ \frac{\sum_{nb} A_{nb} \bar{u_{nb}^2} + S_{\bar{u^2}}}{A_P} \right] \\ &- \frac{1}{A_P} [-2\bar{u^2} + C'_1 \bar{u_2} b_{11} + (C_3 - C'_3 \sqrt{A_2}) k] \\ &+ \frac{4/3 C_4 k b_{11}}{x_E - x_P} \left( \frac{U_E - U_P}{x_E - x_P} \right) \end{aligned} \quad (3.57)$$

$$\begin{aligned} \bar{uv_n} &= \left[ \frac{\sum_{nb} A_{nb} \bar{uv}_{nb} + S_{\bar{uv}}}{A_P} \right] \\ &- \frac{1}{A_P} [v^2 + C'_1 \bar{uv} b_{12} + (C_3 - C'_3 \sqrt{A_2}) k / 2] \\ &+ \frac{1/2 C_4 k (b_{11} + b_{22}) + 1/2 C_5 k (b_{22} - b_{11})}{y_N - y_P} \left( \frac{U_N - U_P}{y_N - y_P} \right) \end{aligned} \quad (3.58)$$

The performances of the various methods, in terms of CPU time required to attain the same level of convergence, are compared below for the 2D channel flow and the backward-facing step.

For the channel (whose length to width ratio was 25), 105x22 nodes were used and the results obtained with the various methods are shown in Table 3.1 (RES in that table denotes the maximum value of the normalized residuals of pressures or velocities). The relative performance of each method is clear. It should be emphasised that all the methods were started from the same initial fields ( $k-\epsilon$  converged solutions were used to speed-up convergence) and that identical solutions were obtained by each method.

| <b>method</b> | <b>RES</b>                  | <b>Number of iterations</b> | <b>CPU time required</b> |
|---------------|-----------------------------|-----------------------------|--------------------------|
| <b>1</b>      | <b><math>10^{-5}</math></b> | <b>428</b>                  | <b>2837.6</b>            |
| <b>2</b>      | <b><math>10^{-5}</math></b> | <b>414</b>                  | <b>2745.3</b>            |
| <b>3</b>      | <b><math>10^{-5}</math></b> | <b>375</b>                  | <b>2346.4</b>            |

**Table 3.1 CPU time needed by METHODS 1, 2 and 3 for 2D channel flow.**

The results obtained for the backward-facing step are shown in Table 3.2. Here, 185x69 nodes were used. The precise flow conditions are described later in section 5.4.

| <b>method</b> | <b>RES</b>                  | <b>Number of iterations</b> | <b>CPU time required</b> |
|---------------|-----------------------------|-----------------------------|--------------------------|
| <b>1</b>      | <b><math>10^{-4}</math></b> | <b>2104</b>                 | <b>72237.6</b>           |
| <b>2</b>      | <b><math>10^{-4}</math></b> | <b>1615</b>                 | <b>55234.8</b>           |
| <b>3</b>      | <b><math>10^{-4}</math></b> | <b>792</b>                  | <b>27421.4</b>           |

**Table 3.2 CPU time needed by METHODS 1, 2 and 3 for the backward-facing step.**

Clearly, then, METHOD 3 seems to provide the best option for the treatment of the diffusion terms in the momentum equations and for this reason this method will be used throughout this study.

### **3.6 BOUNDARY CONDITIONS**

The types of boundaries employed in this study, namely inlet, outlet, symmetry and wall are presented below.

### 3.6.1 Inlet boundaries

The values of the dependent variables at inlet to the solution domain are usually known from experiments and can therefore be used to provide the boundary conditions. In the absence of experimental data, those profiles may be obtained from some empirical relations. In all cases, profiles of turbulence dissipation rate ( $\epsilon$ ) are obtained either from the measured turbulence kinetic energy (using  $\epsilon \propto k^{3/2}/l$  where  $l$  is distribution of length scale) or from assumption of local equilibrium. For the cases of turbulent flows around buildings, the inlet boundary conditions were specified by carrying out simulations of the atmospheric boundary layers that develop upstream of the solution domain. A Reynolds-stress model was used for this purpose, details are given later in Chapter 5.

From the numerical point of view, the treatment of the inlet boundary is very simple: the mass- and momentum convective fluxes at inlet are calculated in the usual way and those then act to convect the pre-specified values into the flow domain. The inlet mass flux is also used to correct the mass flux at exit from the solution domain in order to ensure the satisfaction of mass balance for the whole domain.

### 3.6.2 Outlet boundaries

The flow at exit from the solution domain is assumed to be parallel, or fully-developed, which is true only if the exit plane is sufficiently removed from the regions where the flow undergoes some perturbation. Numerically, this condition is achieved by setting to zero the appropriate coefficient in the finite-difference equation (3.25).

### 3.6.3 Symmetry boundaries

When the flow is bounded by a plane of symmetry, the velocity com-

ponent normal to this plane is set equal to zero while the gradients of all the remaining variables normal to the plane are set to zero. When a symmetry boundary condition is used in the absence of a natural plane of symmetry, care should be taken in placing this boundary at a location where the above conditions apply. For turbulent flows around buildings, for example, the top of the solution domain is treated as a plane of symmetry and is therefore located at a distance from the building so as to exert no effect on the calculated flow around it. This approach can be rather wasteful of computer resources and may not therefore be suitable for practical calculations. An alternative approach adopted and developed in this work is described below.

### 3.6.4 Fixed pressure boundaries

If the top boundary (in the example of a flow around a building) is not to be a plane of symmetry, then a method has to be found for calculating the flow across it. This can be done by adopting a 'pressure boundary conditions' as was done here.

The approach is based on the use of an initial solution for the whole flow domain, obtained on a fairly coarse grid. The calculated values of pressure at a certain height within the solution domain, and below the top boundary, are stored for later use. The calculations are then repeated, only this time in a domain which extends only as far as the height at which pressure values were stored. The grid nodes are now distributed in a smaller domain, leading to a greater mesh density. The pressure is again stored at a certain height, below the top boundary, and used in a repeat calculation over a yet smaller domain. The pressure gradients across the last row of cells are always calculated from values appropriate to the previous (coarser) grid and used for the determination of the 'entrainment' velocities there. Thus, for example, if the velocity component  $V$  is required at point  $P$  in Fig. 3.3, then that will be obtained from the following expression:

$$V_P = \left[ \frac{\sum_{nb} A_{nb} V_{nb} + S_v}{A_P} \right]_{S-SS} - \bar{d}_{PS-SS}(p_P - p_S) \quad (3.59)$$

The pressure-difference term above is evaluated from the previous, coarser, grid. The terms with overbars are unknown at point P and will need to be calculated. This is done, following Demirdzic (1991, private communication) by extrapolation of the two equivalent terms in the finite-difference equations appropriate to points S and SS. The latter may be written as:

$$\left[ \frac{\sum_{nb} A_{nb} V_{nb} + S_v}{A_p} \right]_S = V_S^* + d_S(p_n - p_s)_S \quad (3.60)$$

and

$$\left[ \frac{\sum_{nb} A_{nb} V_{nb} + S_v}{A_p} \right]_{SS} = V_{SS}^* + d_{SS}(p_n - p_s)_{SS} \quad (3.61)$$

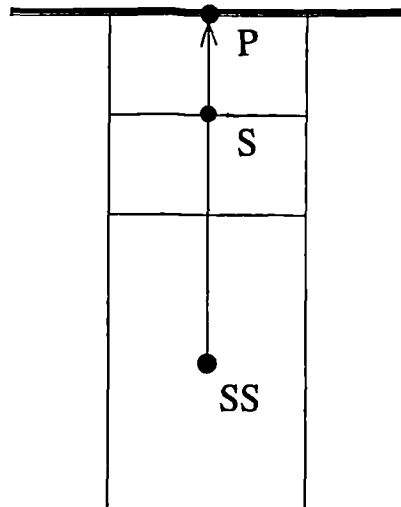


Fig. 3.3 Notation for fixed-pressure boundary

The velocities thus calculated serve to provide the boundary condition for the velocity. The values of  $k$  and  $\epsilon$  from the previous grid are used as fixed-value boundary conditions for those parameters.

### 3.6.5 Wall boundaries

In laminar flows, the boundary conditions used at the wall are simply that the velocities there are zero. In turbulent flows, the computational grid does not normally extend into the viscous sub-layer but only to a point outside it, in the fully-turbulent region of the flow. The boundary conditions are not different from before. For the velocity components parallel to the wall, a flux boundary condition is used. The momentum flux at the wall, the wall shear stress, is obtained from the log.-law:

$$U_P = \frac{U_\tau}{\kappa} \ln(Ey_P^+) \quad (3.62)$$

where  $U_\tau$  is the friction velocity  $\sqrt{\tau_w/\rho}$ ,  $U_P$  is the velocity component parallel to the wall and  $y^+$  is the normal distance in wall coordinates, defined as:

$$y^+ = \frac{\rho U_\tau \delta n}{\mu} \quad (3.63)$$

$E$  is a constant whose value depends on the wall roughness (for smooth walls,  $E$  is taken to be equal 9) and von Karman's constant  $\kappa$  is equal 0.41.

The wall shear stress may be expressed as:

$$\vec{\tau}_w = -\lambda_w \vec{U}_P \quad (3.64)$$

where  $\lambda_w$  is a coefficient evaluated differently depending on whether the computational point lies in the laminar or fully-turbulent parts of the flow. Thus:

$$\lambda_w = \frac{\mu}{\delta n} \quad \text{if } y^+ < 11.63 \text{ (laminar sublayer)} \quad (3.65)$$

$$\lambda_w = \frac{\rho U_\tau \kappa}{\ln(Ey^+)} \quad \text{if } y^+ > 11.63 \text{ (turbulent layer)} \quad (3.66)$$

The flux of  $k$ , the turbulence kinetic energy, at the wall is taken to be zero; a condition simply enforced by setting the appropriate finite-difference coefficient to zero. The value of  $k$  at the node closest to the wall is therefore obtained from the solution of its equation there. A single modification to the standard equation is required: it concerns the way in which the rate of production of  $k$  is evaluated at the grid node closest to the wall. Thus with the assumption of a constant-stress region close to the wall, the production rate of  $k$  there is given by:

$$P_k = \tau_w \frac{\partial U_p}{\partial n} \quad (3.67)$$

where  $n$  is the normal distance from the wall. Moreover, in this expression, the velocity gradient is evaluated from the log.-law relation, thus:

$$\frac{\partial U_p}{\partial n} = \frac{U_\tau}{\kappa \delta n} \quad (3.68)$$

The value of the dissipation rate  $\epsilon$  is fixed for the node closest to the wall by assuming that the turbulence there is in local equilibrium, thus:

$$\epsilon = \frac{U_\tau^3}{\kappa \delta n} \quad (3.69)$$

There are two alternative methods for specifying the boundary conditions for the Reynolds stresses at the wall. In the first of those, the values of those quantities are fixed to levels appropriate to local-equilibrium flows over plane walls. Thus, for example, models RSM0, with wall-damping function  $f$  set to unity, yield:

$$\bar{u^2} = 1.098k \quad \bar{v^2} = 0.247k \quad \bar{w^2} = 0.653k \quad \bar{uv} = -0.255k \quad (3.70)$$

The above stresses are wall-oriented and, in the case of non-orthogonal geometries, should be transformed to Cartesian components, as discussed

in Lien and Leschziner (1991). This approach is rather too restrictive and occasionally quite unstable and was not therefore used here.

The second method, and the one used here, sets the fluxes of the Reynolds-stress components at the wall to zero and then determines those quantities from the solution of their equations. Here, again, the velocity gradients are evaluated from appropriate log.-law relations.

The boundary conditions appropriate to rough terrains are discussed in Section 5.2.

### 3.7 SOLUTION ALGORITHM AND CONVERGENCE CRITERION

The solution algorithm for the  $k-\epsilon$  model may be summarized as follows:

- (1) Provide the initial distributions of all the dependent variables.
- (2) Solve the equations for the velocity components (equations 3.2 and 3.7).
- (3) Solve the pressure correction equation (equation 3.46) and use outcome to correct the velocity components, pressure and mass fluxes (equations 3.47-3.50).
- (4) Calculate  $k$  and  $\epsilon$  from their equations (equations 2.19 and 2.23) and update the eddy viscosity (equation 2.9).
- (5) Repeat the procedure from step (2) until convergence is attained.

The solution algorithm for the Reynolds-stress model may be summarized as follows:

- (1) Read from file previously-obtained  $k-\epsilon$  model results and use those to initialize the Reynolds-stresses using Boussinesq's stress-strain relationship.
- (2) Solve the equations for the velocity components (equation 3.2 and 3.6) in which the diffusion terms and the cell-face Reynolds stresses are treated as proposed in Section 3.5.

- (3) Solve the pressure correction equation (equation 3.46) and use the outcome to correct the velocity components, pressure and mass fluxes (equations 3.47-3.50) as proposed in Sections 3.4 and 3.5.
- (4) Calculate the Reynolds stresses from their equations (for the RSM0 model equation 2.44) and solve for  $\epsilon$  from equation (2.51).
- (5) Repeat the above from step (2) until convergence is attained.

The convergence criterion adopted here is the usual one: the sum of the absolute values of the residuals for all variables, normalized by the appropriate inlet flux, should drop below a pre-specified level, or

$$\frac{\sum_k |R^k|}{S_n} \leq \eta \quad (3.71)$$

### 3.8 A MULTIGRID METHOD

There are two conflicting requirements in the computation of practical flows over large domains. The first requirement is accuracy of the numerical solutions, something usually attained by employing very fine computational meshes. The second is the minimization of the computational effort and this is more readily achieved by using coarse grids. Multigrid methods have been developed with the aim of satisfying both those requirements by, essentially, accelerating the convergence process on fine grids.

The first practical multigrid algorithm was proposed by Brandt (1977), though he did not use it in any calculations. Ghia, U., Ghia, K.N. and Shin (1982) demonstrated the method's potential for the driven cavity test case where a four-time reduction in computing time was obtained. Vanka (1986 a, b) obtained results for the driven cavity and for a three-dimensional sudden expansion flow which showed that the computing time with the multigrid method is directly proportional to the number of grid nodes used. Barcus, Peric and Scheuerer (1987) presented results for the driven cavity and the backward facing step showing a reduction in computing time by a factor of 220. Becker, Ferziger, Peric and Scheuerer (1989) extended the work of Barkus et al., again testing the method in

laminar flows only. This was also the case in the work of Rayner (1991) who reported a 94% saving in computing time compared to the single-grid method. Peric, Ruger and Scheuerer (1989) appear to have been the first to apply the method to turbulent flows. For a backward-facing step case, they reported a two orders of magnitude reduction in computing time compared to a single grid method. The prospects of achieving such reductions in the calculation of turbulent flows around buildings provide the main motivation for implementing and testing the multigrid method in this study.

There are four distinct aspects to any multigrid method. Those are:

#### a) Multigrid V cycle

The multigrid method is implemented as a fixed V-cycle (see Fig. 3.4) through the grid levels, the finest level chosen to yield grid-independence solutions. The V cycle starts with the transfer of the fine-grid solution to a coarser grid. A prescribed number of iterations is then performed on the coarse grid to obtain corrections. Those are then either interpolated (i.e. restricted) to a yet coarser grid or, if the coarsest grid is reached, they are extrapolated to a finer grid.

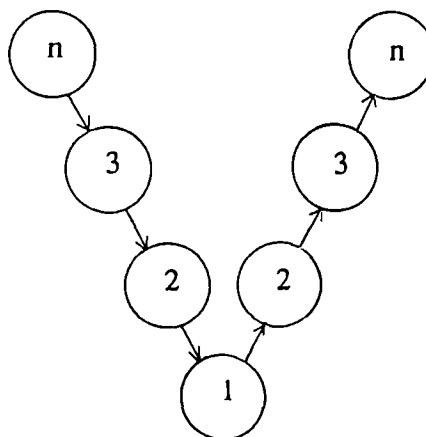


Fig. 3.4 Multigrid V cycle

There are two ways of switching the grid levels, one involves monitoring the convergence rate (e.g. Brandt, 1977) and the other, which is used here, is to set the number of iterations at each level and then proceed to the next one irrespective of whether or not convergence has been attained. Usually, more iterations are performed on the coarser grids.

In order to calculate corrections on the coarser grid, the coarse-grid error equation has to be derived and that is given below.

### b) Coarse-grid equations

The discretized equation for the finest grid  $M_k$  ( following equations 3.25) has the form:

$$\sum_{N_k} A_k(\Phi_k) \Phi_k = S(\Phi_k) \quad (3.72)$$

where  $N_k$  is the total number of nodes.

After some iterations, the solution  $\Phi_k^*$  will satisfy equation (3.72) up to residuals  $R$ :

$$\sum_{N_k} A_k(\Phi_k^*) \Phi_k^* = S(\Phi_k^*) - R_k \quad (3.73)$$

If a correction  $\Phi'_k$  to be added to  $\Phi_k^*$  is needed to reduce the residuals to zero, then we have:

$$\sum_{N_k} A_k(\Phi_k^* + \Phi'_k)(\Phi_k^* + \Phi'_k) = S(\Phi_k^* + \Phi'_k) \quad (3.74)$$

The last two equations may be combined into one as:

$$\begin{aligned} \sum_{N_k} A_k(\Phi_k^* + \Phi'_k)(\Phi_k^* + \Phi'_k) &= S(\Phi_k^* + \Phi'_k) + \sum_k A_k(\Phi_k^*) \Phi_k^* \\ &- S(\Phi_k^*) + R_k \end{aligned} \quad (3.75)$$

Equation (3.75) is represented on a coarser grid  $M_{k-1}$  in the following form:

$$\begin{aligned} \sum_{N_{k-1}} A_k (\Phi_{k-1}^* + \Phi'_{k-1}) (\Phi_{k-1}^* + \Phi'_{k-1}) &= S(\Phi_{k-1}^* + \Phi'_{k-1}) \\ + \sum_{N_{k-1}} \overset{\circ}{A}_{k-1} (\Phi_{k-1}^*) \overset{\circ}{\Phi}_{k-1}^* - \overset{\circ}{S} (\Phi_{k-1}^*) + \overset{\circ}{R}_{k-1} \end{aligned} \quad (3.76)$$

where  $\overset{\circ}{\Phi}_{k-1}$  denotes the restricted value of  $\Phi_k$  and can be written as:

$$\overset{\circ}{\Phi}_{k-1} = I_k^{k-1} \Phi_k \quad (3.77)$$

$I_k^{k-1}$  is an interpolation operator for the transfer of the variable values from fine ( $k$ ) to coarse ( $k-1$ ) grids. When the correction  $\Phi'_{k-1}$  is calculated on the coarse grid then a new approximation to the fine grid solution  $\Phi_k$  can be found from:

$$\Phi_k^{\text{new}} = \Phi_k^{\text{old}} + I_{k-1}^k \Phi'_{k-1} \quad (3.78)$$

The term  $I_{k-1}^k$  is an interpolation operator for the transfer of the variable values from coarse ( $k-1$ ) to fine ( $k$ ) grids. In the last equation, correction  $\Phi'_{k-1}$  is extrapolated to the finer grid and added to the old value  $\Phi_k^{\text{old}}$ .

The terms on right hand side of equation (3.76), which are restricted from the fine grid, do not change during iterations on the coarse grid.

### c) Restriction and extrapolation

Restriction refers to the process of interpolating on to the coarse grid the residuals and the field values obtained on the fine grid. Fig. 3.5 illustrates the coarse and fine-grid arrangements and defines some relevant fluxes.

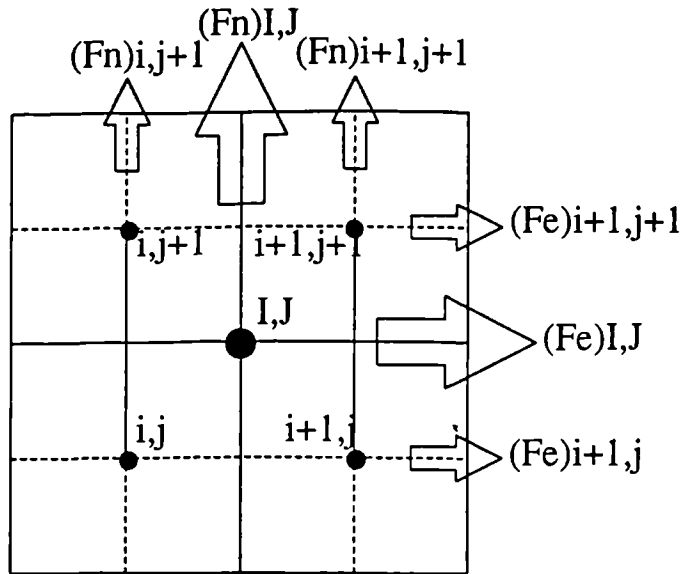


**Fig. 3.5 Restriction-extrapolation scheme**

Successively finer grids are obtained by dividing the coarser cell into four volumes.

Treatment of the residuals is straightforward: the residuals at a particular cell on the coarse grid are simply the sum of the residuals from the four surrounding cells on the fine grid, thus:

$$\overset{\circ}{R}_{k-1}^{I,J} = R_k^{i,j} + R_k^{i,j+1} + R_k^{i+1,j} + R_k^{i+1,j+1} \quad (3.79)$$

Different interpolation operators may be used to obtain the field values on the coarse grid from their values on the fine grid. Here, the simple linear interpolation is used, again using the values from the four surrounding nodes. When the sum of residuals  $R_k$  is zero, equation (3.76) has to ensure that the corrections made to the coarse-grid values are zero.

When restricting from fine to coarse grids, the convection and diffusion contributions of coefficients  $A_{k-1}^*$  are treated separately. The diffusion

fluxes are re-calculated on the coarse grid using restricted field values. The cell-face mass fluxes are initially set equal to the sum of the corresponding fluxes on the fine grids. After each iteration on the coarse grids, new velocities are obtained and those are then used to re-calculate the mass fluxes. The differences between the restricted mass fluxes and those obtained from restricted velocities are subsequently used to correct the mass fluxes. For consistency reasons the source terms  $\hat{S} (\Phi_{k-1}^*)$  are re-calculated on the coarse grid using restricted  $\Phi^*$  values.

After the coarsest grid has been reached, the coarse-grid corrections are extrapolated back to the next finer grid where they are added to the values there. Linear extrapolation is used. The fluxes are re-calculated on the finer grid using those extrapolated values.

#### d) Boundary conditions

The inlet-boundary values are taken as fixed and known and therefore do not require any correction. Care must be taken to ensure that the inlet fluxes for all variables remain the same across the whole boundary irrespective of the grid level used. Treatment of the symmetry and outlet boundaries is unaffected by the level of the grid.

At the walls, the wall-function method is applied in the same way as for a single grid. Note, however, that no corrections are applied to  $\epsilon$  but, rather, its value at the point nearest to the wall is obtained from the value of  $k$  there.

##### 3.8.1 Solution algorithm

The multigrid cycle starts on the coarsest grid where a converged solution is obtained. This is then extrapolated on the next finer grid where now a V-cycle is employed. If satisfactory convergence on that level is attained, then the solution is again extrapolated on the next finer grid

and so on. Usually, two or more V-cycles are repeated. The following steps are involved in a complete solution cycle:

- (1) Initialize the flow field on the coarsest grid.
- (2) Solve the appropriate difference equations using as many iterations as required until the absolute sum of residuals, normalized by the inlet fluxes, falls below a certain limit.
- (3) Extrapolate the coarse-grid results to the next finer grid.  
up to
- (4) Perform a pre-specified number of iterations on the fine grid.
- (5) Restrict the solution and residuals on the next coarser grid and again perform a pre-specified number of iterations.
- (6) After reaching the coarsest level, the calculated corrections are extrapolated and added to the values on the previous finer level.
- (7) Once the finest level in a particular V-cycle is reached, check for residuals and, if below a certain limit, proceed to the next V-cycle.

A flowchart of the solution algorithm is given in Fig. 3.6.

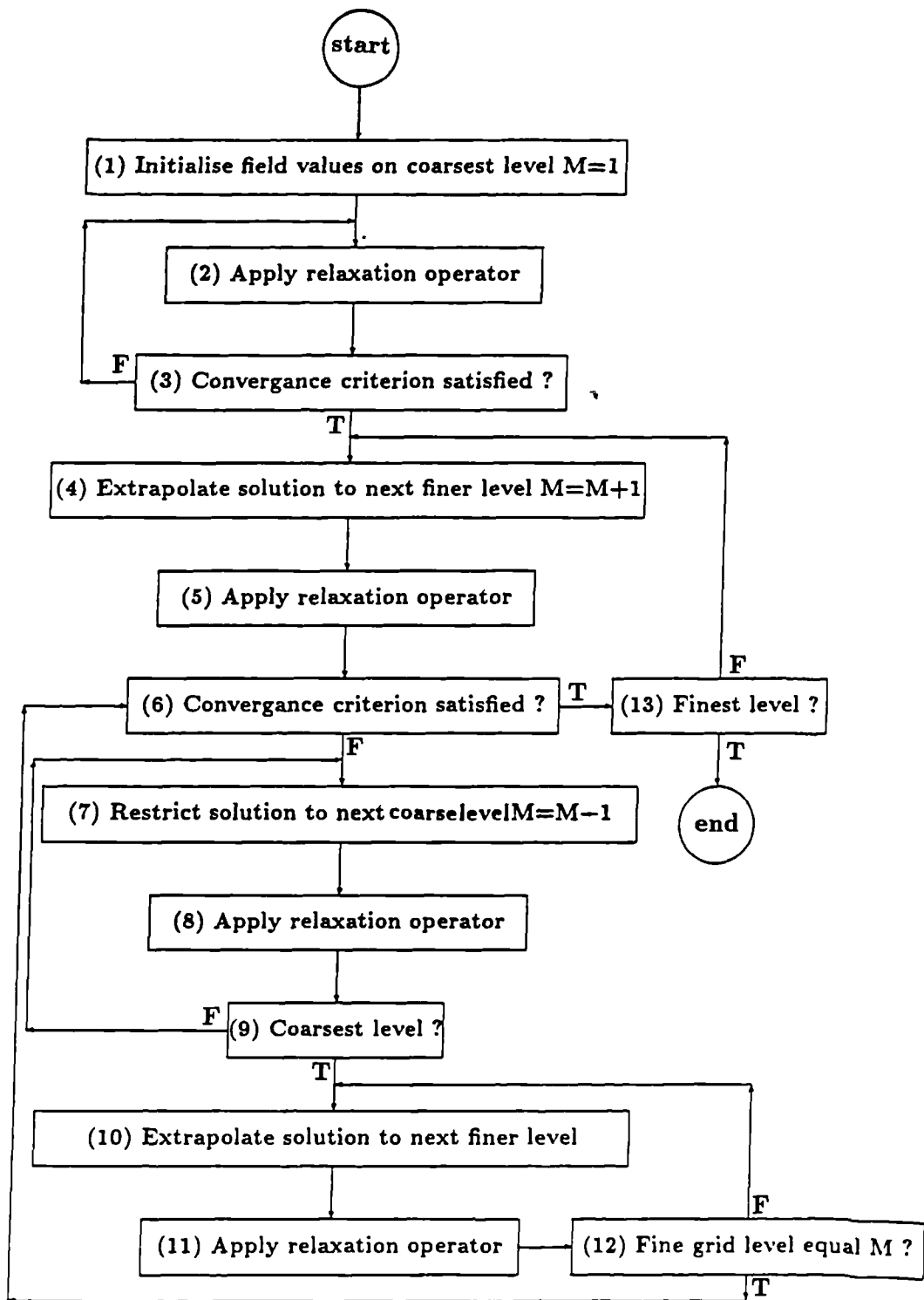


Fig. 3.6 Flowchart of solution algorithm

### 3.8.2 Verification tests

To assess the multigrid method, and to check its implementation, calculations were performed for the laminar flow over a backward-facing step at  $Re$  of 73 (based on a step height  $H$  of 0.015m and maximum velocity at inlet). This flow was documented experimentally by Denham and Patrick (1974). The calculation domain is shown in Fig. 3.7. The multigrid method was applied for four grid levels: 42x17, 82x32, 162x62, 322 x122.

The predicted and measured reattachment lengths for the different grid sizes are shown in Table 3.3.

| Grid size | 42x17 | 82x32 | 162x62 | 322x122 | experiment |
|-----------|-------|-------|--------|---------|------------|
|           | 3.35  | 4.11  | 4.54   | 4.7     | 4.7        |

**Table 3.3.** The predicted and measured reattachment lengths for different grid sizes.

Fig. 3.8 compares the predicted and measured velocity profiles. The predictions on the 322x122 grid are in very good agreement with the experiment. To quantify the grid effects, an additional parameter, the nodal absolute relative error, is defined as the difference between the results calculated with a particular grid and those obtained on the finest grid. The distribution of this parameter is shown in Fig. 3.9 for different grids. There, it can be seen that the maximum error occurs at the cells within the recirculation region and its maximum value is varies from 3% on the 162x62 grid to the 100% on the 42x17 grid. The Table 3.4 gives a summary of the CPU times (on the SUN SPARC station 1<sup>+</sup>), taken to obtain solutions by single-grid and by multigrid method. The convergence patterns for both the single- and multi-grid methods are compared in Fig. 3.10. The behaviour of the residuals for the single-grid case is similar to that reported by other authors (Rayner, 1991) and is due to the adoption of the maximum of the velocity or mass residuals at any

one time. Overall, the complete computational effort for the multigrid method is 8 times less than for the single-grid method.

| Grid size      | Number of grid levels | CPU time required |
|----------------|-----------------------|-------------------|
| <b>82x32</b>   | 1                     | <b>524.60</b>     |
|                | 2                     | <b>229.17</b>     |
| <b>162x62</b>  | 1                     | <b>4527.52</b>    |
|                | 3                     | <b>955.39</b>     |
| <b>322x122</b> | 1                     | <b>60986.67</b>   |
|                | 4                     | <b>7626.10</b>    |

**Table 3.4** The CPU times obtained by single-grid and multigrid methods.

### 3.9 CLOSURE

This chapter presented the discretization procedure used in conjunction with the body-fitted coordinates and considered the way in which the pressure-velocity coupling is effected to eliminate oscillations on a co-located grid. The method used in this work for the pressure-stress-velocity coupling was also explained. The alternative methods of treating the diffusion terms in the momentum equations, when using the Reynolds-stress model, were described and the new method was proposed.

A multigrid method was also introduced and was shown to reduce the computational effort for a laminar flow quite significantly. Its application to turbulent cases follows in Chapter 5.

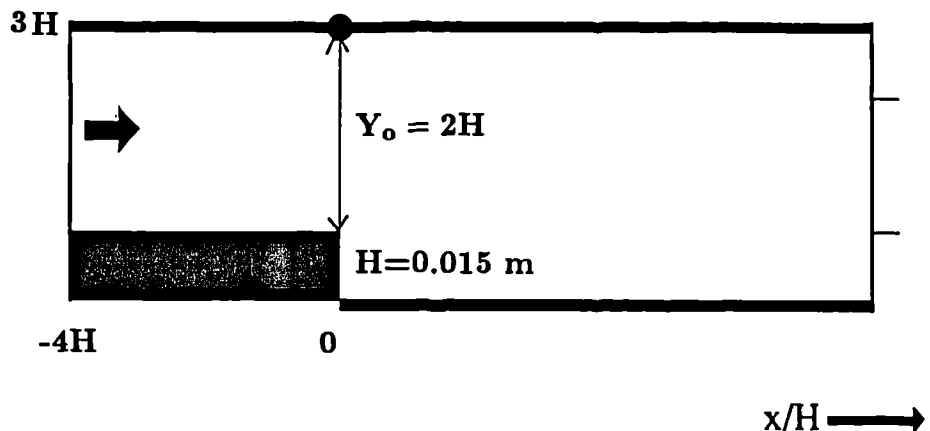


**Fig. 3.7 Backward-facing step coordinates and geometry.**

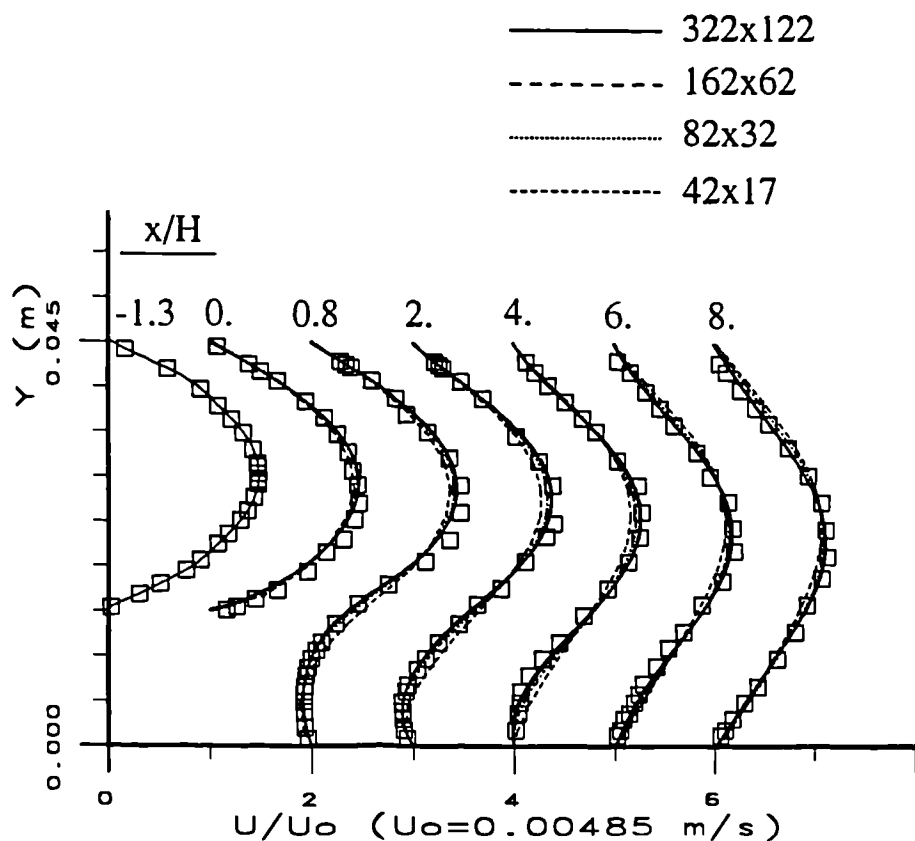


**Fig. 3.8 Predicted and measured cross-stream profiles of mean velocity for the different grid size.**

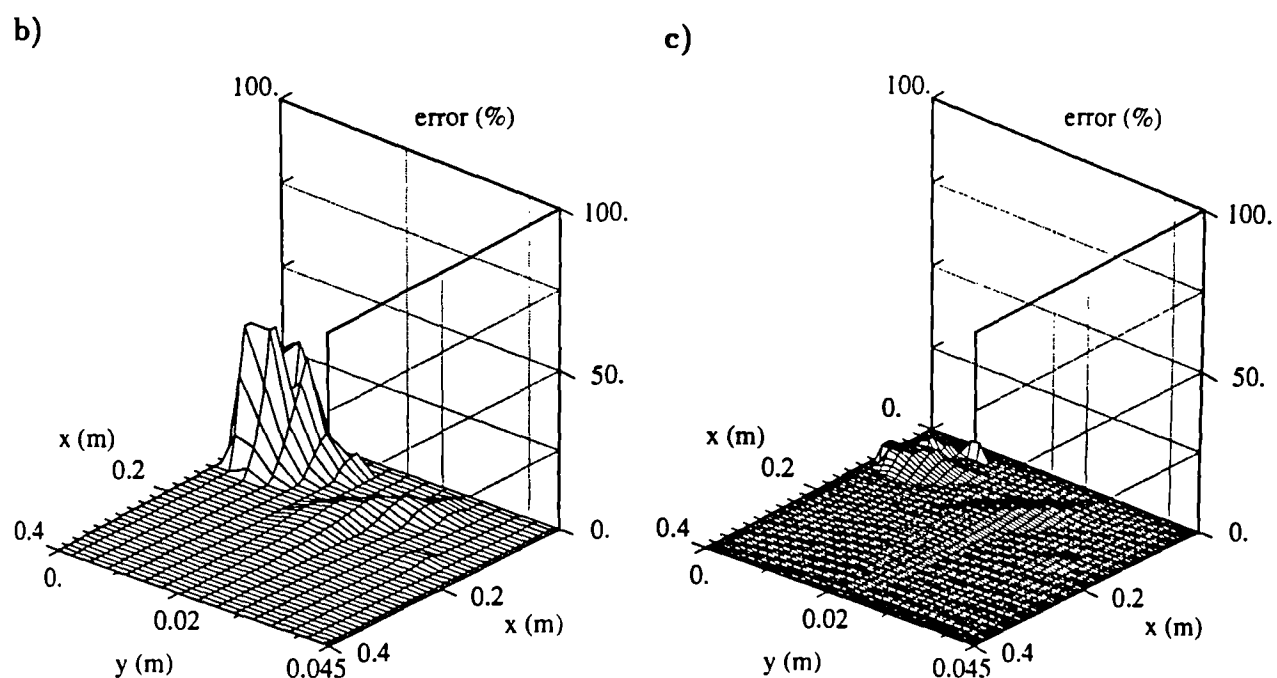
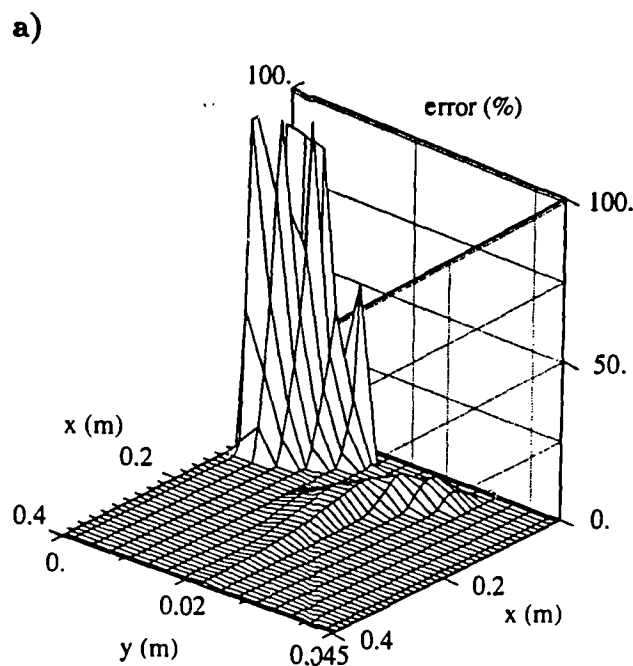


Fig. 3.9 The nodal absolute relative error on different grids a) 42x17, b) 82x62 and c) 162x62.

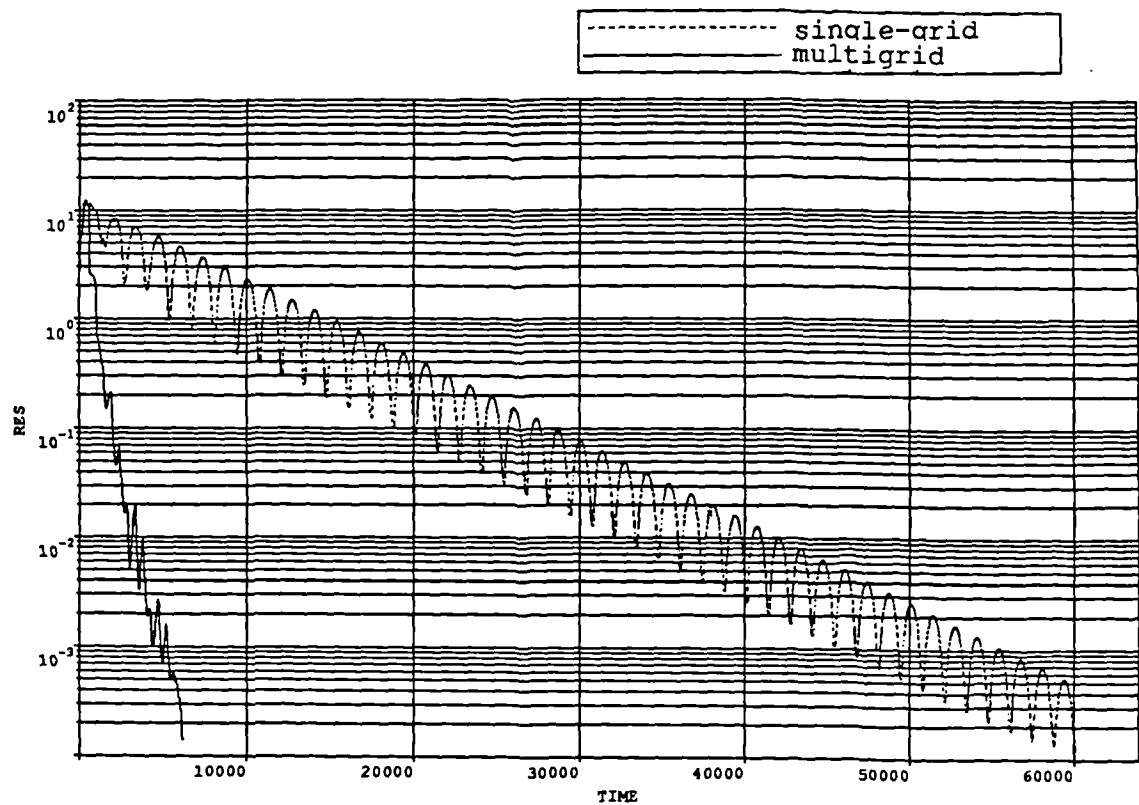


Fig. 3.10 Multigrid convergence rates for the laminar flow over backward-facing step

# Chapter 4

## PRELIMINARY VERIFICATION OF THE COMPUTATIONAL METHOD

### 4.1 INTRODUCTION

It is necessary to first check the complete computational method against some well-documented separated flows prior to its application to the study of flows over full-scale buildings. The test flows chosen for this purpose are universally accepted as being suited for the verification of turbulence models and solution methods. They are: the two-dimensional flow over backward-facing step (Section 4.2), the flow over a square rib (Section 4.3), the flow over backward-facing step in straight and divergent channels (Section 4.4), the flow over a circular cylinder in uniform stream (Section 4.5) and, finally, the three-dimensional flow around a cube (Section 4.6). The first two test cases were chosen to examine the behaviour of the non-linear stress-strain relationship and the new model for the pressure-strain correlations particularly with respect to their convergence properties and time requirements. The flow in the divergent channel checks the method's performance when a non-orthogonal grid is used and the implementation of the Reynolds-stress model in a non-orthogonal non-staggered code. This was also the motivation for choosing the circular cylinder which also required particular attention to be paid

to the generation of a smooth grid over the curved surface procedure. The flow around a cube, a classic test case in Wind Engineering (see Section 1.3), is studied here to determine the differences between the various modified forms of the  $k-\epsilon$  model.

As a reminder of the notation used to designate the various models, the standard "linear"  $k-\epsilon$  model is identified by LKE, the "non-linear" version by NKE and, when the irrotational strain modification is used, it is labeled EKE. The Reynolds-stress model with the pressure-strain correlation of Launder, Reece and Rodi (1975) is called RSM0 and, when Speziale, Sarkar and Gatski's proposal is used, it is labeled as RSM1.

## 4.2 BACKWARD-FACING STEP

The turbulent flow over a backward-facing step is now a generally-accepted test case for turbulence models assessment (e.g. 1980-81 AFOSR-HTTM-Stanford Conference on Complex Turbulent Flows, Comparison of Computation and Experiment). The flow is particularly suited for models testing because it is two-dimensional, occurring in an uncomplicated geometry and because the position of the separation point is fixed a priori. The standard test flow is that of Kim, Kline and Johnston (1980) with Reynolds number (based on the step height and maximum velocity at inlet) of  $10^5$ . The calculation domain is shown in Fig. 4.1.

A number of different grids were used and grid-independent results were obtained on the finest one which consisted of  $161 \times 62$  nodes, unevenly distributed. The predicted velocity vectors, plotted for clarity at selected streamwise locations, are shown in Fig. 4.2. The figure shows the evolution of an initially very thin boundary layer upstream of the step and the development of a new one on the upper surface of the tunnel. The predicted mean-flow streamlines are compared in Fig. 4.3 (a, b, c, d, e). It is immediately clear that both the Reynolds-stress models predict a primary recirculation zone greater in extent than that captured by the two-equation models. The non-linear model results are closest to those obtained by the Reynolds-stress models and it is interesting to note from Fig. 4.3 (c) that this model also captures a small, counter-rotating vor-

tex downstream of the step. A quantitative assessment is presented in Table 4.1 where the predicted and measured reattachment lengths are compared.

|  | $x_R/H$ |
|--|---------|
| Experiment<br>(Kim et al., 1980)       | 7.0     |
| Linear $k-\epsilon$ model              | 5.6     |
| Modified $\epsilon$ equation           | 5.87    |
| Non-linear $k-\epsilon$ model          | 6.3     |
| RSM0                                   | 6.46    |
| RSM1                                   | 6.43    |
| Obi, Peric and Scheuerer (1989) (RSM0) | 6.44    |
| Speziale and Ngo (1988) (NKE)          | 6.4     |

Table 4.1. The predicted and measured reattachment lengths for the backward-facing step.

Note that the present RSM results are almost identical and underpredict the measured value for re-attachment length by about 8%. The  $k-\epsilon$  models, in contrast, underpredict this quantity by about 20% with the standard model, reducing to about 10% when the non-linear formulation is used. The reasons for this discrepancy are not clear but have variously been attributed to uncertainty in specifying the inlet conditions, inadequate treatment of the wall region and, recently, to the inherently unsteady nature of this flow (Lasher and Taulbee, 1992).

The predicted wall static-pressure distributions are shown in Fig. 4.4 (a) for the  $k-\epsilon$  models and in Fig. 4.4 (b) for the Reynolds-stress models. The  $k-\epsilon$  models results are again different, though all consistently show a much more rapid pressure recovery than obtained in the measurements. The non-linear model is in overall better agreement with the data especially in the recovery region. The best agreement is achieved with the RSM0, although the RSM1 predictions are more accurate in the recirculation region.

The predicted and measured cross-stream distributions of mean velocity

at  $x/H$  of 2.67, 5.33 and 7.11 ( $x$  here measured from the obstacle) are compared in Fig. 4.5 (a, b). The NKE model results are better than those of the others though none succeeds in predicting the position of the dividing streamline. The Reynolds-stress models are much closer to the measurements though they exhibit an unrealistic rearward curvature of the velocity profiles at the first station downstream of re-attachment. This behaviour is more clearly apparent in the streamline plots already presented where it is clear that the minimum velocity in the re-attached flow occurs away from the wall. Similar behaviour is also evident in the predictions of Obi et al. (1989), attributed there to various agencies.

The axial turbulence intensity and the Reynolds shear stress are compared in Fig 4.6 (a, b) and Fig. 4.7 (a, b) at  $x/H$  of 7.667, 8.553 and 10.333. The Reynolds-stress models give the closest correspondence to the measurements. As for the two-equation models, the best agreement is obtained with the NKE which alone seems to capture the higher levels of the Reynolds stresses produced in the separated shear layer.

Turning now to some of the practical aspects of the present computations, it was mentioned earlier that the non-linear stress-strain relationship produces a large number of terms which are treated as additional sources in the momentum equations. Since those terms can be extremely large, it was feared that they may lead to slower convergence or even divergence of the solution cycle. Some special treatments were therefore introduced to avoid this. The velocity gradients at the nodes closest to the wall were calculated from the "log-law" relationship rather than from interpolation of field values. Furthermore, it was found best to initialize the dependent variables with the converged linear model results. Sometimes the additional momentum sources were added gradually, but this was not always found to be necessary. Consequently, the computing time required for the NKE model is approximatively twice that for the LKE model, which is similar to the result reported by Speziale and Ngo (1988).

This test case also confirmed that converged solutions for the Reynolds-stress models are only attainable by adopting the pressure-stress-velocity coupling procedure presented in Section 3.5. Failure to do this usually resulted in oscillatory solutions. As before, faster convergence was obtained by starting the calculations from converged  $k-\epsilon$  model results. The computing efforts involved in RSM1 and RSM0 are almost the same.

### **4.3 TWO-DIMENSIONAL SQUARE RIB**

The flow considered here is that obtained around a two-dimensional square rib, placed on a smooth flat plate, in a fully-developed turbulent boundary layer. The flow has some relevance to a number of practical problems such as flows around two-dimensional buildings and windbreaks. Here, as for the flows around buildings, flow reversal occurs upstream and downstream of the obstacle and the disturbed boundary layer relaxes to a new state downstream of the perturbation.

The calculations are compared with the measurements of Crabb, Durao and Whitelaw (1981). The calculation domain is shown in Fig. 4.8: it extends to 20 H (H is the rib height) downstream of the rib which is sufficient for the flow to relax to a new equilibrium state. The top boundary is a wall. Computations were carried out on grids of 60x37 and 101x50; the latter grid results are presented below.

The predicted and measured lengths of the downstream recirculation zones are compared in Table 4.2. The measurements obtain the reattachment length at around 12.3H. The  $k-\epsilon$  model results underestimate this quantity by about 13% which is similar to what was obtained for the backward-facing step. Note that here again, as for the previous case, the present linear-model result agrees very closely with results obtained by other workers with the same model. The irrotational-strain modification improves the predictions somewhat but it is the non-linear model which is seen here to yield the best agreement with the data. The two Reynolds-stress models overpredict the measured value by about 7% though it is again evident that the two model results are quite similar. Prediction of the flow in the similar conditions is reported in the work done by Obi, Peric and Scheuerer (1990) where reattachment length was also overpredicted.

The predicted and measured wall static-pressure distributions are compared in Fig. 4.9 (a, b). The measurements are quite well reproduced by all the models: the pressure minimum immediately behind the rib is accurately reproduced. Pressure recovery is also well reproduced. The closest agreement is achieved with the RSM0.

|  | $x_R/H$      |
|--|--------------|
| Experiment<br>(Crabb et al., 1981)                             | <b>12.3</b>  |
| Linear k- $\epsilon$ model<br>(Durao, McGuirk and Palma, 1982) | <b>10.7</b>  |
| Linear k- $\epsilon$ model<br>(present )                       | <b>10.7</b>  |
| Modified $\epsilon$ equation                                   | <b>11.2</b>  |
| Non-linear k- $\epsilon$ model                                 | <b>12.2</b>  |
| RSM0   | <b>13.02</b> |
| RSM1   | <b>13.1</b>  |

**Table 4.2. The predicted and measured reattachment lengths for the two-dimensional rib.**

The cross-stream profiles of mean velocity are presented in Fig. 4.10 (a, b). Focusing on the Reynolds-stress results, it is clear that the large distortion to the profiles introduced by the recirculation zones both upstream and downstream of the rib are gradually smoothed out with downstream development with the predicted profile shapes generally matching the measured ones. The exception to this appears to be the profile at the last measured station at 13 rib heights from the end of the rib where the data give a profile which appears to be in an advanced state of recovery while the Reynolds-stress models still obtain a small region of reversed flow. The cross-stream profiles of turbulence intensity are presented in Fig. 4.11 (a, b). All models underestimate this quantity at all stages of development, particularly at the last measurement station.

#### 4.4 BACKWARD-FACING STEP IN DIVERGENT CHANNEL

This experiment was featured in the Collaborative Testing of Turbulence Models exercise organized at Stanford University (Bradshaw, 1992). There, several models were applied with results that were in many cases very different from each other, even when the same turbulence model was

used! This lead to the conclusion (Bradshaw, 1992) that grid-independent solutions were yet to be obtained. Since the performance of the  $k-\epsilon$  model and its variants is already known for the backward-facing step (see Section 4.2), consideration in this section will be confined to the Reynolds-stress models only.

The flow configuration is shown in Fig. 4.12. Two angles of wall divergence are considered here, namely zero and six degree. The free-stream velocity was 44.2 m/s and the Reynolds number based on the momentum thickness was 5000. The inlet values were obtained from the experimental data which were tabulated and distributed to all participants in the Stanford exercise.

The grid used for the zero-angle case is shown in Fig. 4.13 (a). The effects of the grid sizes on the predicted reattachment length for this case are presented in Table 4.3.

| Grid size | LKE model | RSM0 model | RSM1 model |
|-----------|-----------|------------|------------|
| 95x42     | 4.1       | 4.3        | -          |
| 160x63    | 4.5       | 5.67       | -          |
| 185x69    | 4.74      | 5.45       | -          |
| 185x82    | 4.76      | 5.44       | 5.40       |

**Table 4.3.** The predicted reattachment lengths for the the zero-angle case for different grid sizes.

It is reasonable to assume that the results for the 185x82 grid are essentially grid-independent. Those results are therefore compared in Table 4.4 with the measurements of Driver and Seegmiller (1984) and with other predictions reported for the Stanford exercise. The model used by Leschziner is in fact the present RSM0 and it is therefore interesting to see the extent to which numerical diffusion acts to shorten the extent of the separated zone. The RSM1 is again almost identical to the RSM0.

| $\alpha = 0$ deg.     | Grid size | k- $\epsilon$ model | RSM0 | RSM1 | experiment |
|-----------------------|-----------|---------------------|------|------|------------|
| Driver and Seegmiller |           |                     |      |      | 6.26       |
| Present calc.         | 185x82    | 4.76                | 5.44 | 5.40 |            |
| Goulas                |           | 5.00                |      |      |            |
| Singhal               | 80x60     | 4.80                |      |      |            |
| Leschziner            | 85x45     | 4.60                | 4.80 |      |            |

Table 4.4. The predicted reattachment lengths for the zero-angle case

The grid used for the 6-degree case is shown in Fig. 4.13 (b). The finest grid from the previous test is again used here and the present results are compared with the measured value and the other predictions in Table 4.5.

| $\alpha = 6$ deg.     | Grid size | k- $\epsilon$ model | RSM0 | RSM1 | experiment |
|-----------------------|-----------|---------------------|------|------|------------|
| Driver and Seegmiller |           |                     |      |      | 8.21       |
| Present calc.         | 185x82    | 5.73                | 6.90 | 6.90 |            |
| Goulas                |           | 5.60                |      |      |            |
| Singhal               | 80x60     | 5.80                |      |      |            |
| Leschziner            | 85x45     | 5.30                | 6.10 |      |            |

Table 4.5. The predicted reattachment lengths for the six-angle case

In this flow, the RSM0 and RSM1 results for the reattachment length are exactly identical and underestimate the measured value quite substantially. Again, the same models (Leschziner's and the present RSM0) appear to give different results though this is not unexpected considering the different grids used.

The predicted and measured field values are compared in Figs. 4.14-4.20. All those figures are in the same format: the top part(s) for the zero-angle case and the bottom parts are for the 6-degree case. The mean-flow streamlines are shown in Fig. 4.14 (a, b). As mentioned before, dividing streamline is seen to curve backwards near the reattachment point

for reasons that remain unclear. The RSM1 appears to emphasizes this behaviour which suggests that the choice of pressure-strain model plays at least so role in shifting the location of minimum velocity away from the wall. Small contra-rotating vortices are captured downstream of the steps in all cases although they may be smaller than those obtained in the measurements. This can be inferred from the plots of skin-friction coefficient, presented in Fig. 4.15 (a, b). The predictions do not quite reproduce the measured minimum skin friction and later, in the recovery region, the measured  $C_f$  is overestimated.

The wall static-pressure distributions are compared in Fig. 4.16 (a, b). For the zero-degree case, this quantity is well reproduced by the predictions in the reattachment and recovery regions but is overestimated at distances greater than about  $15H$  from the obstacle. For the 6 degree test case,  $C_p$  is much more closely predicted throughout.

The axial-velocity profiles are presented in Fig. 4.17 (a, b) and show close correspondence between predictions and measurements. Profiles of the Reynolds stresses, at five axial locations downstream of the step, are shown in Fig. 4.18 (a, b) for  $\bar{uv}$ , in Fig. 4.19 (a, b) for  $\bar{u^2}$  and in Fig. 4.20 (a, b) for  $\bar{v^2}$ . The maxima of the  $\bar{u^2}$  and  $\bar{uv}$  stresses are well predicted though there is some shift in their locations. The  $\bar{v^2}$  normal-stress component is underpredicted for all the downstream positions. Here again, as before, RSM0 and RSM1 give essentially similar results which support the exclusion of the wall-damping function from the latter model.

#### 4.5 CIRCULAR CYLINDER

For the case of a flow over a circular cylinder, the boundary layer developing downstream of the stagnation point encounters increasingly more adverse pressure gradients till it eventually separates from the surface. Thus, in contrast to the cases above, the point at which the flow separates is not known *a priori* but has to be obtained by the model. This flow, therefore, provides a more exacting test for the closure method.

Achenbach (1968) obtained surface pressure measurements on a circular

cylinder placed normal to a uniform flow. Reynolds number was  $3.6 \times 10^6$ . The measurements were previously used by Majumdar and Rodi (1985) to validate a calculation method employing a  $k-\epsilon$  model on a cylindrical-polar mesh. The inlet conditions used by those workers are employed here: the inlet flow was assumed to be uniform with low relative turbulence intensity. The body-fitted mesh used here consisted of  $109 \times 67$  nodes. The flow was assumed to be steady and hence only one half of the whole domain was modelled. In order to prevent pressure discontinuities from appearing on the cylinder surface, it is necessary to generate a grid which is both closely packed as well as smooth close to the cylinder. This was achieved here by using a simple technique described by Peric (1985). The technique concerns the grid nodes lying next to the solid surface (e.g. nodes  $M_1$  and  $M_2$  straddling node  $M_0$ , as can be seen in Fig. 4.21).

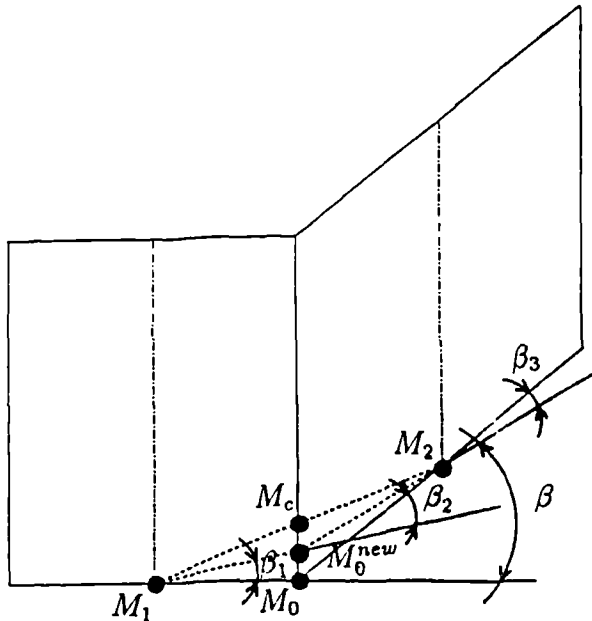


Fig. 4.21 The smoothness of grid lines.

A discontinuous grid will be generated but this can be made less discontinuous by moving node  $M_0$  a new position such that:

$$\beta_1 \simeq \beta_2 \simeq \beta_3 \simeq \frac{1}{3}\beta \quad (4.1)$$

This new position for the point  $M_0^{\text{new}}$  can be found by first finding the location of the cross point  $M_c$  and then placing the new point in the middle of the distance  $\overline{M_0 M_c}$ . This procedure can be repeated a number of times, with each result checked visually, till a satisfactory final distribution is obtained. A grid which has been generated using this procedure is shown in Fig. 4.22.

Achenbach (1968) only reported the wall static-pressure distribution and this is compared in Fig. 4.23 with results from LKE (NKE results are identical) and RSM1 (RSM0 results are identical). It is immediately obvious that the results of those very different models are essentially identical: they obtain the separation point at about  $128^\circ$  which is approximately  $13^\circ$  later than that measured. The pressure is well predicted up to the point of minimum value but the rate of pressure recovery from then on is badly reproduced. A similar result was obtained by Majumdar and Rodi who attributed it in part to the use of a steady-flow formulation to simulate a flow which may have been influenced by vortex shedding. Another explanation is that in the experiments, the boundary layer starts as laminar near the stagnation point and becomes turbulent somewhere downstream of it while in the computations the flow was assumed to be turbulent from the very start.

Nevertheless, the results presented above can be regarded as being quite satisfactory from the numerical point of view because of the good convergence rates achieved and the attainment of a smooth and continuous pressure field throughout the flow field. The CPU time needed by the Reynolds-stress models are approximately four times greater than for the  $k-\epsilon$  models.

#### 4.6 CUBE

The flow around a cube is the most often used test flow in wind engineering for the obvious similarities it shares with flows around sharp-edged buildings. The flow is rather complicated since it contains recirculation regions at the front, the back, the sides and the top of the model. In this

section, the aim is to examine the overall pattern of flow but with a particular focus on the region around the upstream corner of the cube which is known to exert a substantial influence on the downstream development of the flow. Simulations are carried out for experiments of Murakami and Moshida (1989) in which the Reynolds number (based on the velocity  $U_H$  and the height of the cube  $H$ ) was  $7 \times 10^4$ . The inlet profiles used in the computations are those obtained in the experiments, shown in Fig. 4.24 (a-c). The remaining velocity components  $V$  and  $W$  are set to zero while the dissipation rate is deduced from the measured length scale using the relation

$$\epsilon_y = \frac{C_D k_y^{\frac{3}{2}}}{l_y} \quad (4.2)$$

where constant  $C_D$  is equal 0.09.

The computational domain (Fig. 4.25) extends over  $15H$ ,  $8H$  and  $5H$  in the  $x$ -,  $y$ - and  $z$ -directions, respectively. Tests carried out here showed that this domain size is sufficient to ensure that the calculated pressure field on the cube was uninfluenced by the conditions imposed at the boundaries. Three different grids were used in order to check the sensitivity of the solutions: grid A consisting of  $44 \times 28 \times 21$  nodes, grid B with  $55 \times 33 \times 28$  nodes and grid C with  $70 \times 48 \times 41$  nodes. No symmetry was assumed in those tests. The grids were non-uniform, as can be seen in Fig. 4.26.

The effects of grid density can be seen in Fig. 4.27. Grid A (and also B which is not shown here) does not capture the region of reverse flow on the top of the model which is present in the data (Fig. 4.27). Grid A also underestimates the turbulence energy as can be seen from Fig. 4.29. Grid C gives somewhat better velocity field (Fig. 4.27 c) but that is much improved when the second-order accurate LUDS (Fig. 4.28 a) is used in place of the Upwind scheme. The results of grid C and LUDS are very similar to those obtained by Murakami, Mochida, Hayashi and Sakamoto (1991) using the same turbulence model on a grid of  $50 \times 49 \times 28$  and with the QUICK differencing scheme and hence grid C and LUDS will be used for the remainder of the present simulations. The turbulence kinetic energy distribution predicted by grid C and LUDS is shown in Fig. 4.30 (a). Clearly, some large discrepancies with the measurements are apparent and attention is now turned to the performance of the tur-

bulence model used.

In Fig. 4.28 , the predicted velocity vectors as obtained by the various  $k-\epsilon$  variants are presented. For the case of the linear model (LKE), a region of reversed flow is predicted near the top of the cube but its extent is smaller than that suggested by measurements. Somewhat longer recirculation zone is obtained with the non-linear model but that, too, is shorter than the measured length. The prediction of a too small recirculation zone is probably due to the overestimation of turbulence kinetic energy near the frontal corner (see Fig. 4.30): too high turbulence kinetic energy levels produce large eddy viscosities and the reverse flow is reduced by large turbulent mixing. It is not very surprising that the standard  $k-\epsilon$  model overestimates the levels of  $k$ . The reasons for this can be seen by comparing the ‘real’ production rate of  $k$ , which is obtained as:

$$G_k = \overbrace{-\bar{u}^2 \frac{\partial U}{\partial x} - \bar{v}^2 \frac{\partial V}{\partial y}}^{G_{k,n}} - \bar{uv} \left( \frac{\partial U}{\partial y} + \frac{\partial V}{\partial x} \right) \quad (4.3)$$

with the equivalent term used in the  $k-\epsilon$  formulation which is obtained with the use of Boussinesq as:

$$G_k = 2\nu_t \left( \overbrace{\frac{\partial U^2}{\partial x} + \frac{\partial V^2}{\partial y}}^{G_{k,n}} \right) + \nu_t \left( \frac{\partial U}{\partial y} + \frac{\partial V}{\partial x} \right)^2 \quad (4.4)$$

Inspection of equation 4.3 shows that, while production-by-shear is always positive (bar, perhaps, for a small region somewhere in the flow), production by normal strains may be positive or negative, depending on the signs of the  $\partial U/\partial x$  and  $\partial V/\partial y$ . In contrast, it is clear from equation 4.3 that all contributions to the production term are always positive and hence the total term is greater than its exact counterpart. Larger production rates normally produce larger levels of the quantity produced and hence the overestimation of  $k$  in regions where  $\partial U/\partial x$  or  $\partial V/\partial y$  (see equation 4.3) must surely be positive.

It is relatively straightforward, once the reasons for higher  $k$  are understood, to modify the model to take into account the limitations of Boussinesq. The focus is on the  $\epsilon$ -equation sources which can be expanded thus:

$$\begin{aligned}
S_\epsilon &= \frac{\epsilon}{k} (-C'_{\epsilon_1} (\bar{u}^2 - \bar{v}^2) \frac{\partial U}{\partial x} - C_{\epsilon_1} \bar{u}\bar{v} (\frac{\partial U}{\partial y} + \frac{\partial V}{\partial x})) \\
&\quad - C_{\epsilon_2} \frac{\epsilon^2}{k}
\end{aligned} \tag{4.5}$$

The separation of the production of  $k$  in the  $\epsilon$ -equation into generation by shearing and irrotational strains has already been discussed in Section 2.3. What has been done here, however, differs slightly from the original Hanjalic and Launder proposal in that a term involving  $(\partial U / \partial y)(\partial V / \partial x)$  has been dropped here since its sign cannot be guaranteed. The above argument has been focused, for simplicity, on two-dimensional flows. The case for three-dimensional flows is identical and there, again, all cross-gradient terms were dropped from the production of dissipation term.

With this modification, the model now predicts a separated zone on top of the cube which is in very close accord with measurements (Fig. 4.28 c). Also, the measured contours of  $k$  are much better predicted (Fig. 4.30 c) especially near the top corner where the predicted maximum-level contour is now much smaller in extent than before.

The capture of a recirculation zone of approximately the correct size leads to significant improvements in the calculated wall static-pressure coefficients, as can be seen in Fig. 4.31. The improvements obtained with the modified model (EKE) are not confined only to the roof but are also apparent in the region on the upstream face near the top corner. However, some differences with measurements are still apparent.

#### 4.7 CLOSURE

The results presented in this chapter serve to verify the implementation of the various turbulence models into a numerical procedure based on the use of body-fitted coordinates and a non-staggered grid arrangement. For the two-dimensional test cases, the advantages of using Reynolds-stress turbulence models became apparent: the predicted reattachment lengths were closer to the measured values and so were the predicted

wall-pressure distributions. The two alternative models for the pressure-strain correlations gave essentially identical results and this argues in favour of using the model of Speziale, Sarkar and Gatski (RSM1) which does not require wall-damping terms. For the  $k-\epsilon$  models, the non-linear relationship produced results for the backward-facing step and the 2D rib that are more accurate than the linear model results. Modification of the production of dissipation term produced the best results for the three-dimensional flow around a cube.

The circular-cylinder results were generally unsatisfactory, irrespective of the turbulence model used. This may well be due to the use here of a steady-flow method in a flow with possibly vortex shedding. Laminar-turbulent transitions may also have occurred in the experiments and that, too, was not accounted for here.

In the next chapter, the techniques and models developed and tested so far will be applied to flows around full-scale buildings.

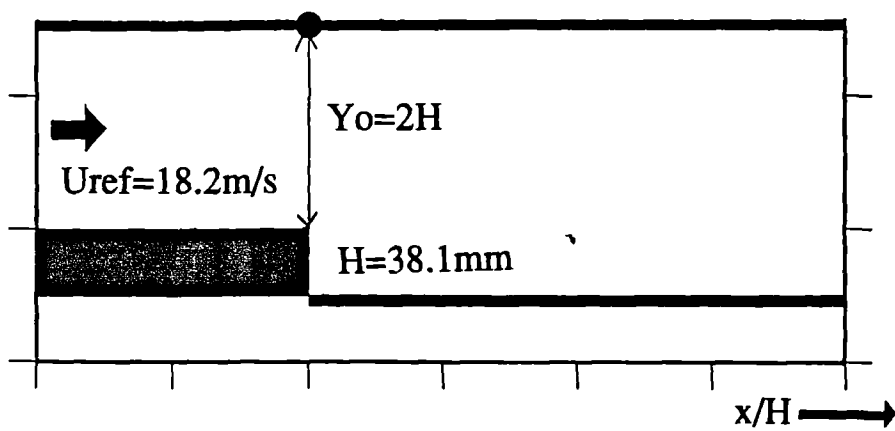


Fig. 4.1 Backward-facing step coordinates and geometry.

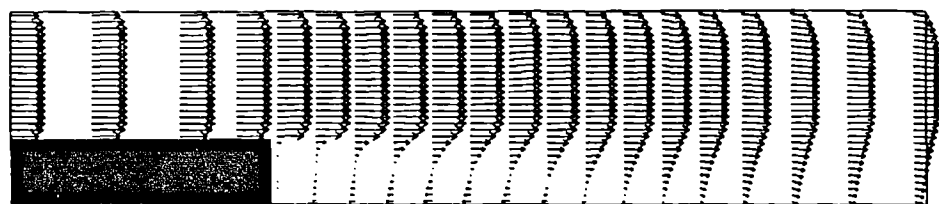
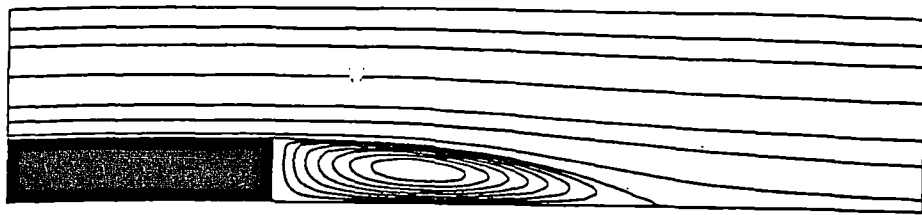
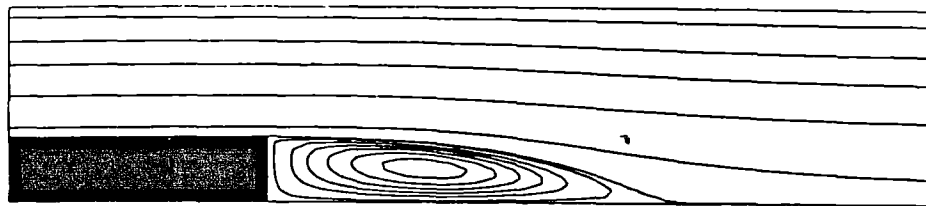


Fig. 4.2 Backward-facing step. Predicted mean-velocity vectors by LKE.

a)



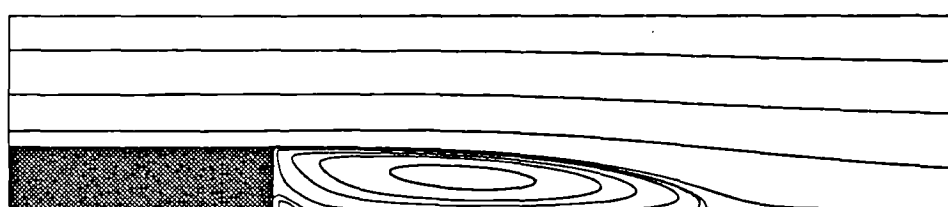
b)



c)



d)



e)

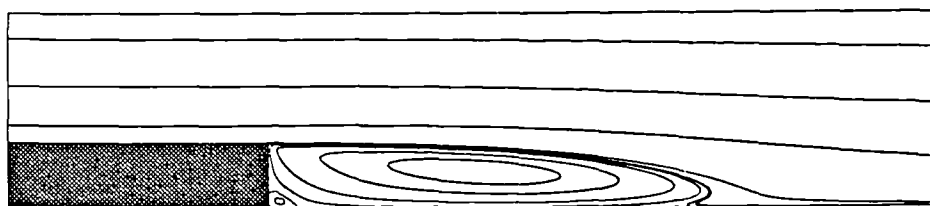


Fig. 4.3 Backward-facing step. Predicted streamlines by LKE (a), EKE (b), NKE (c), RSM0 (d) and RSM1 (e).

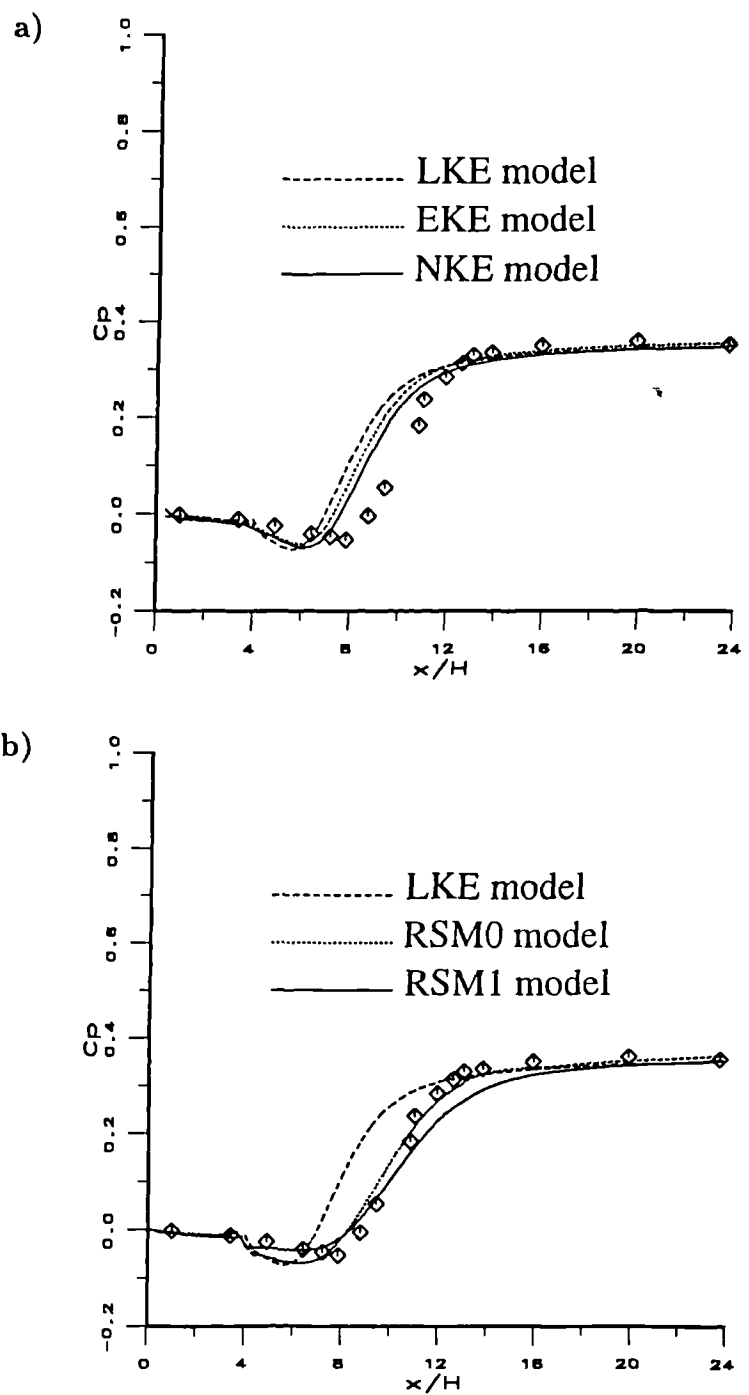


Fig. 4.4 Backward-facing step. Distribution of wall pressure coefficient predicted by LKE, EKE, NKE (a) and LKE, RSM0, RSM1 (b).

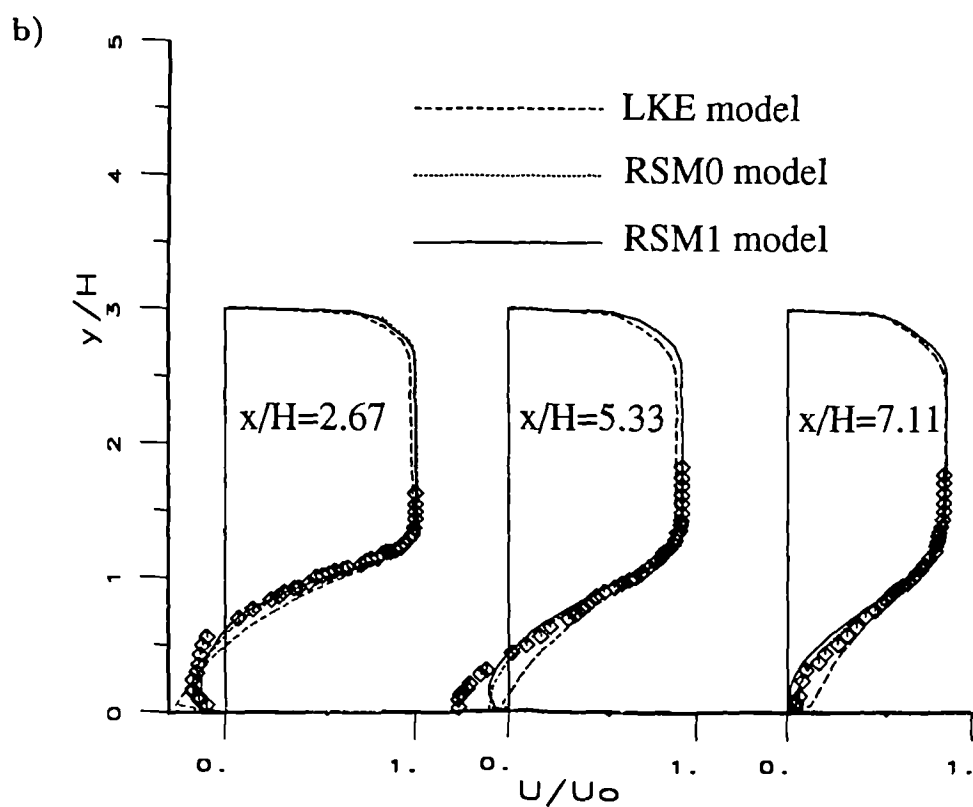
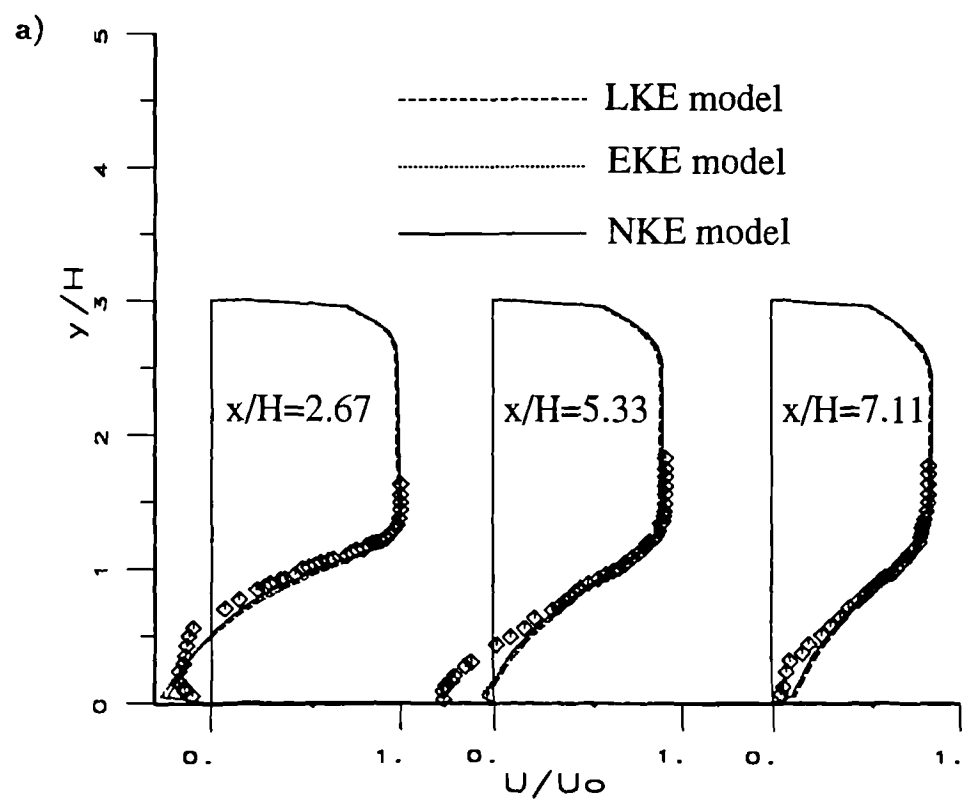


Fig. 4.5 Backward-facing step. The mean-velocity profiles as obtained by LKE, EKE, NKE (a) and LKE, RSM0, RSM1 (b).

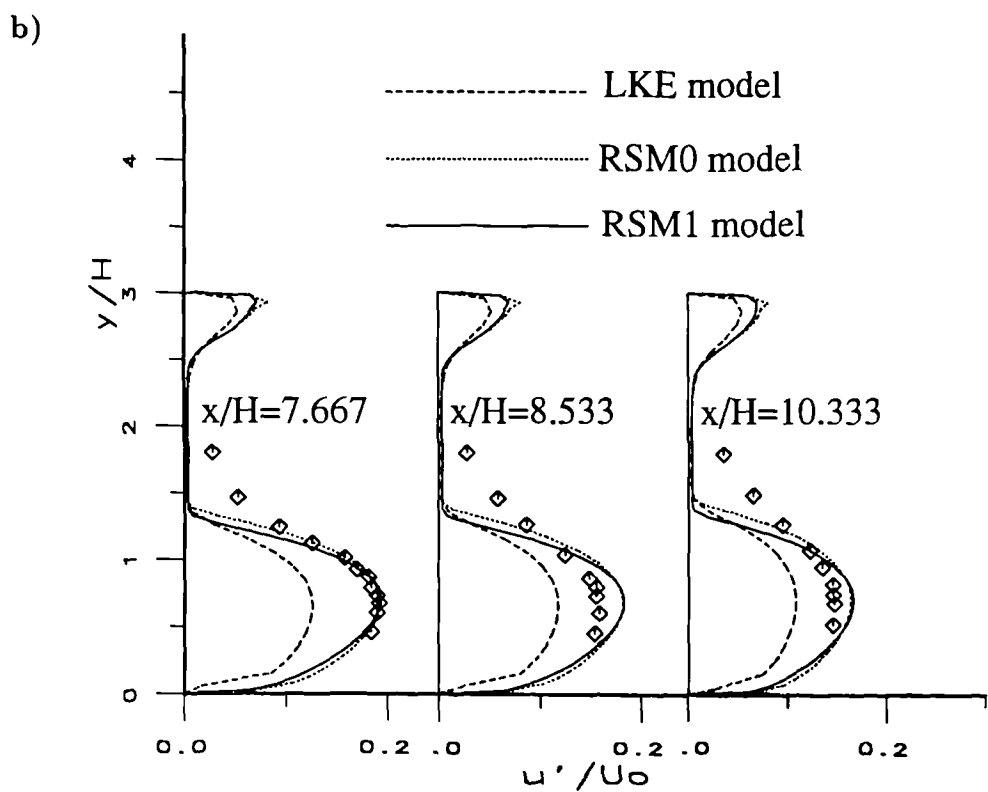
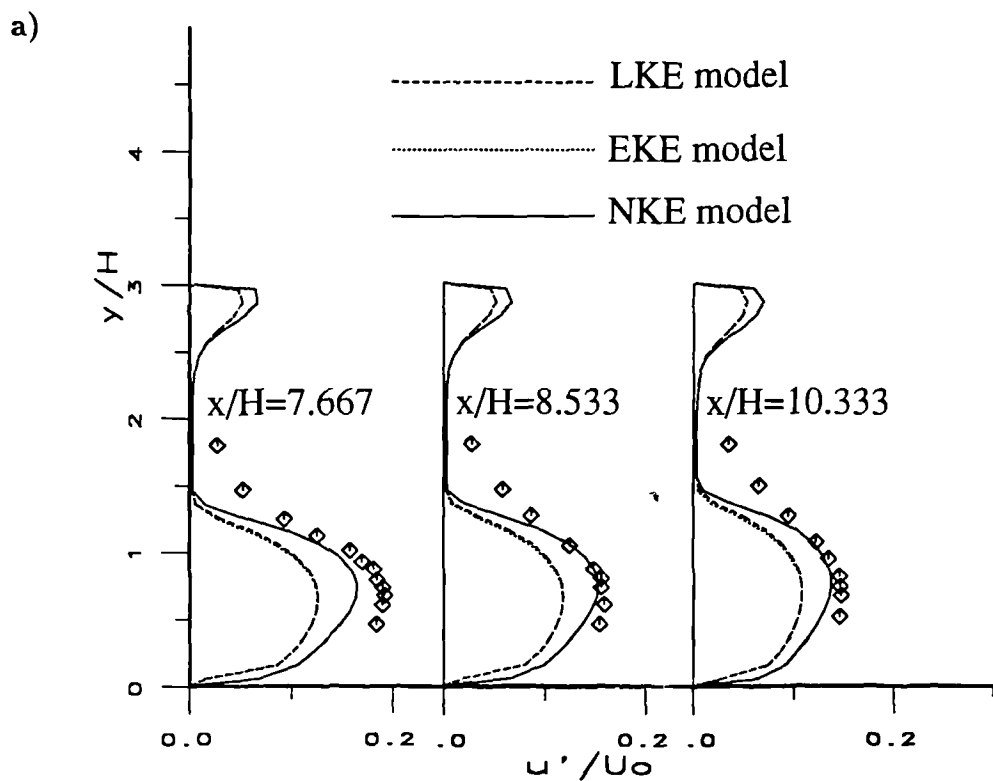


Fig. 4.6 Backward-facing step. The turbulence intensity profiles as obtained by LKE, EKE, NKE (a) and LKE, RSM0, RSM1 (b).

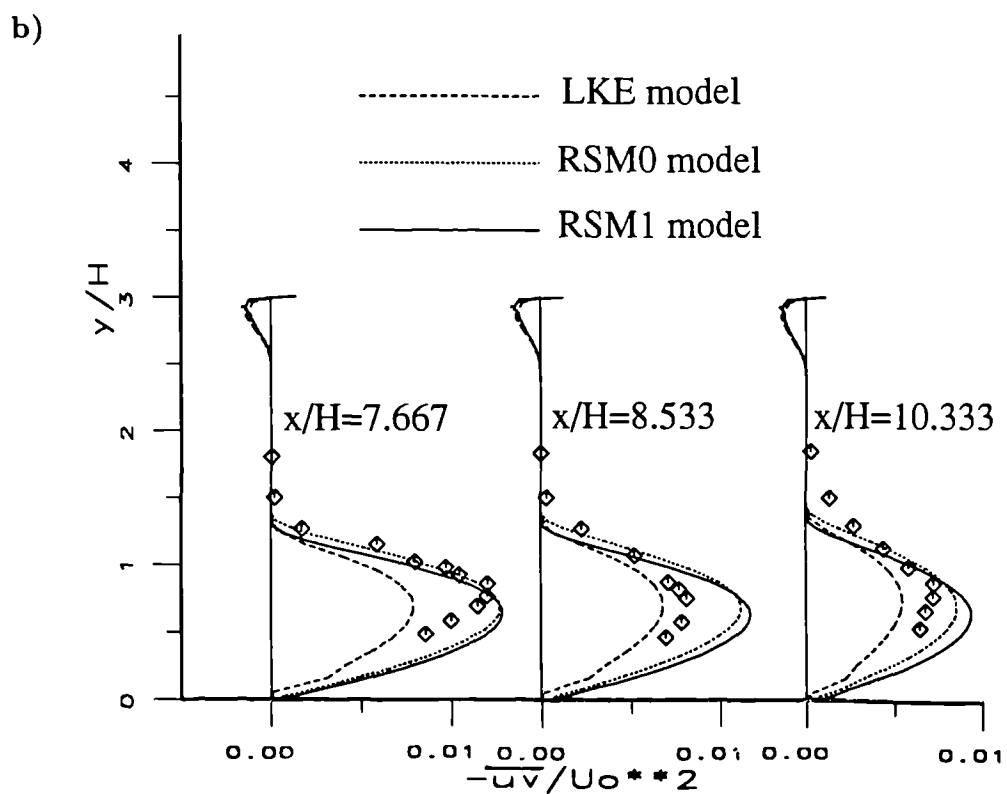
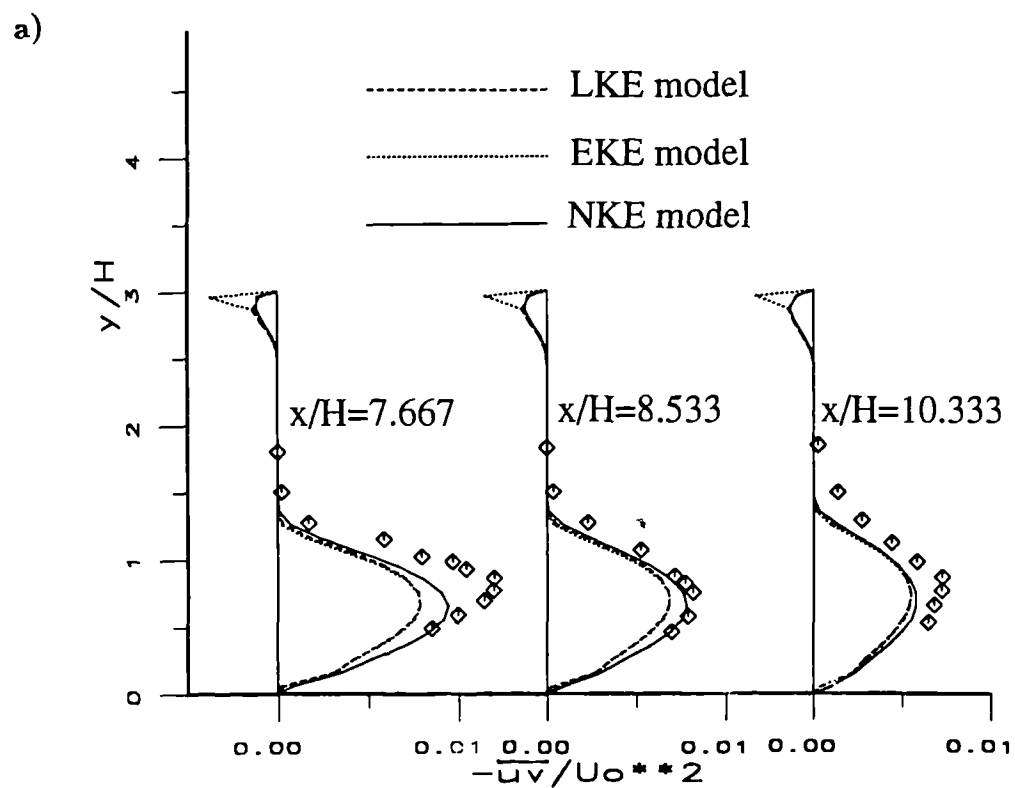


Fig. 4.7 Backward-facing step. The shear stress profiles as obtained by LKE, EKE, NKE (a) and LKE, RSM0, RSM1 (b).

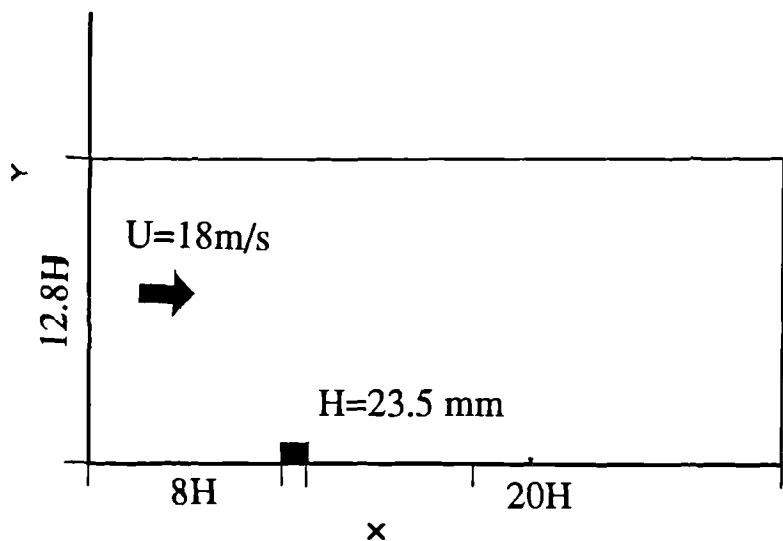


Fig. 4.8 Two-dimensional rib coordinates and geometry.

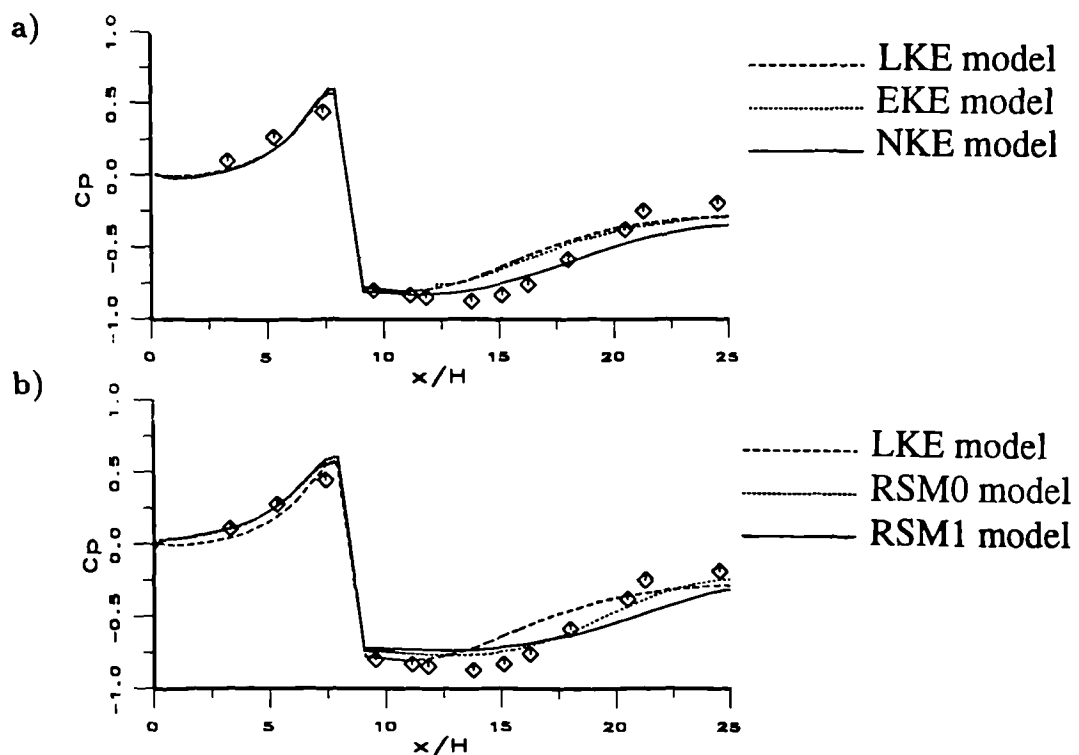


Fig. 4.9 Two-dimensional rib. Distribution of wall pressure coefficient predicted by LKE, EKE, NKE (a) and LKE, RSM0, RSM1 (b).

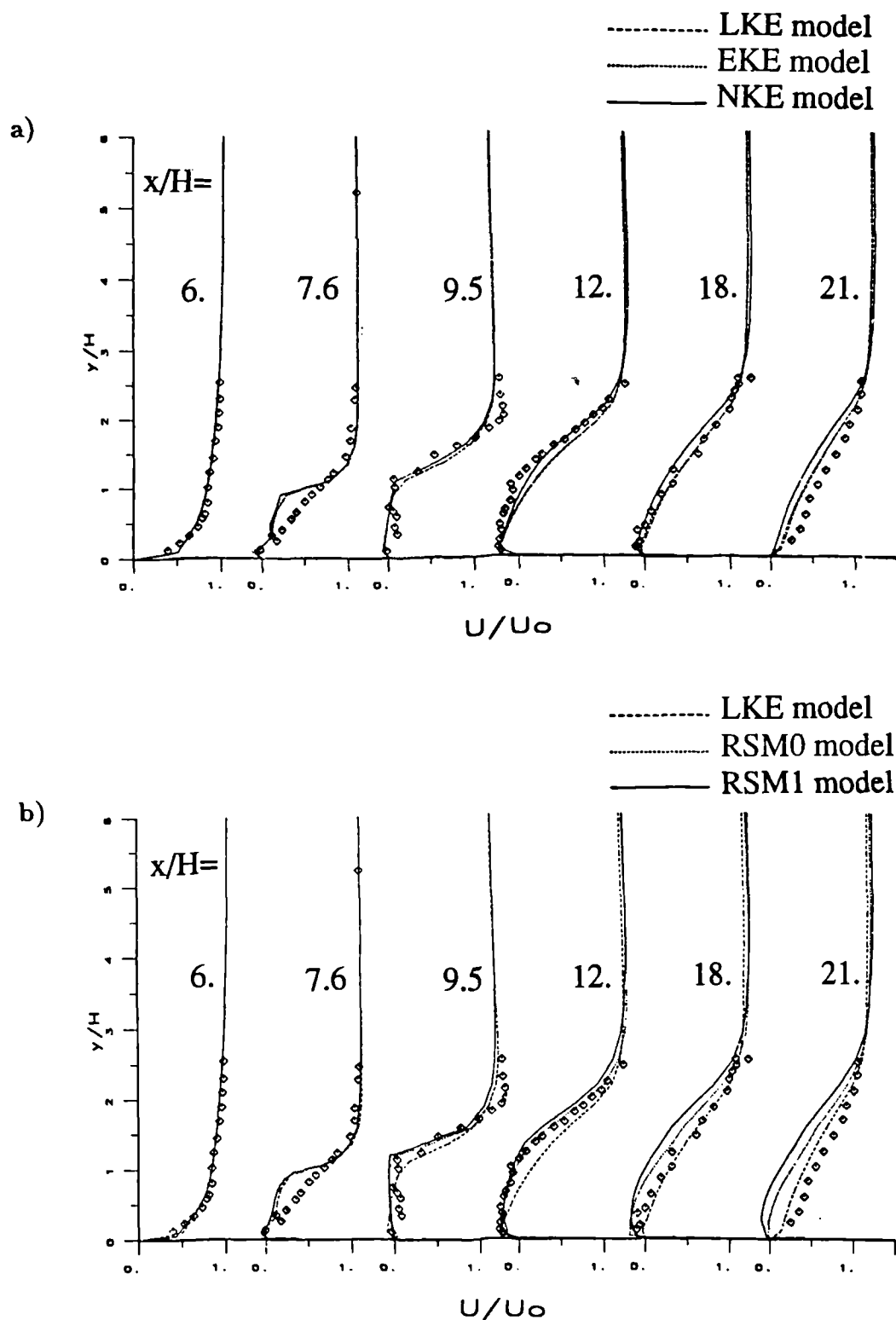


Fig. 4.10 Two-dimensional rib. The mean-velocity profiles as obtained by LKE, EKE, NKE (a) and LKE, RSM0, RSM1 (b).

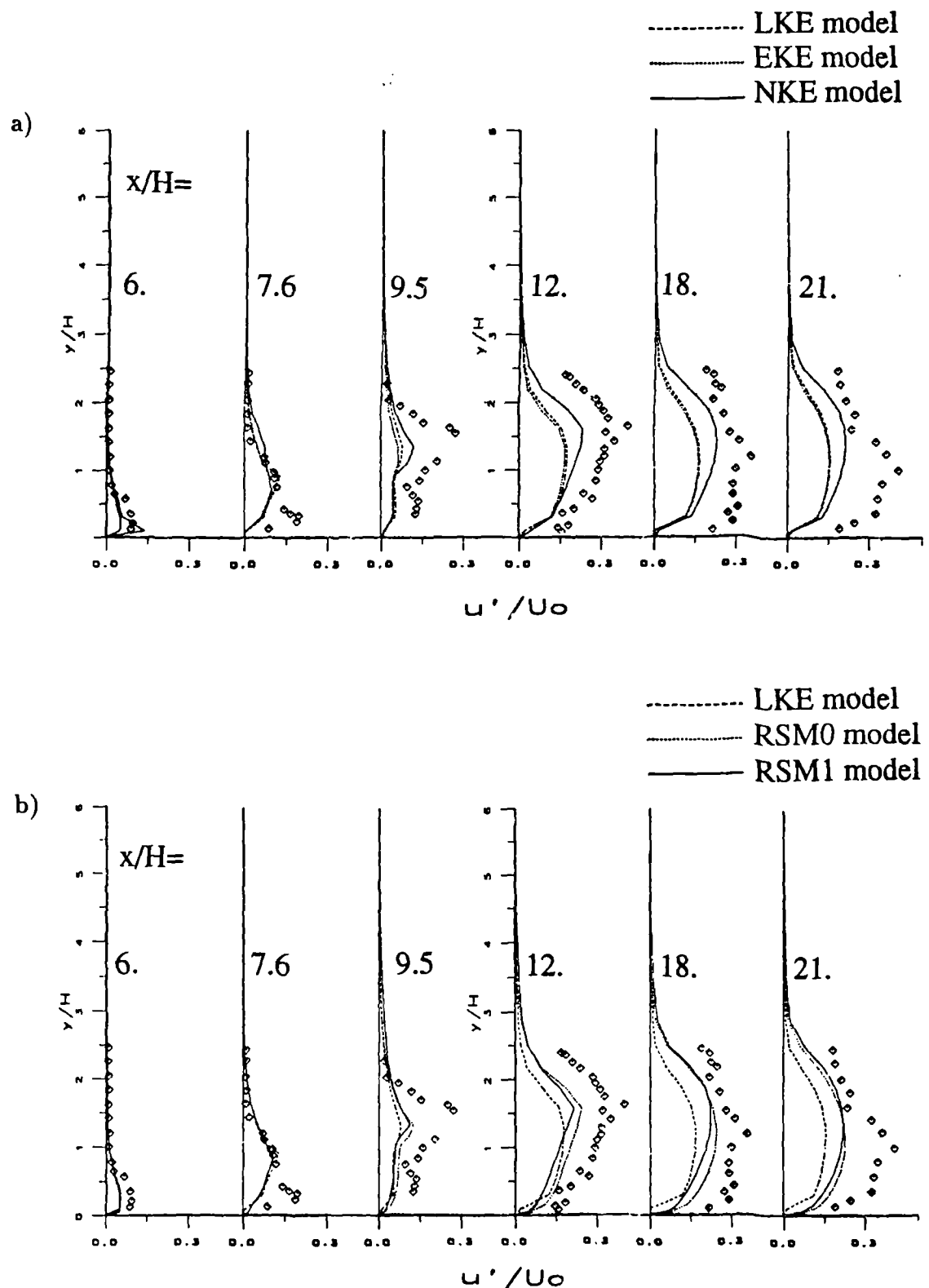
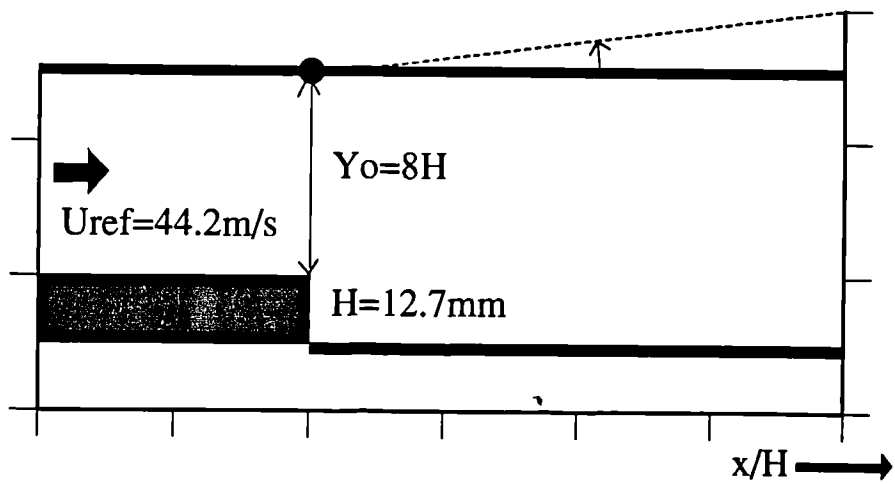
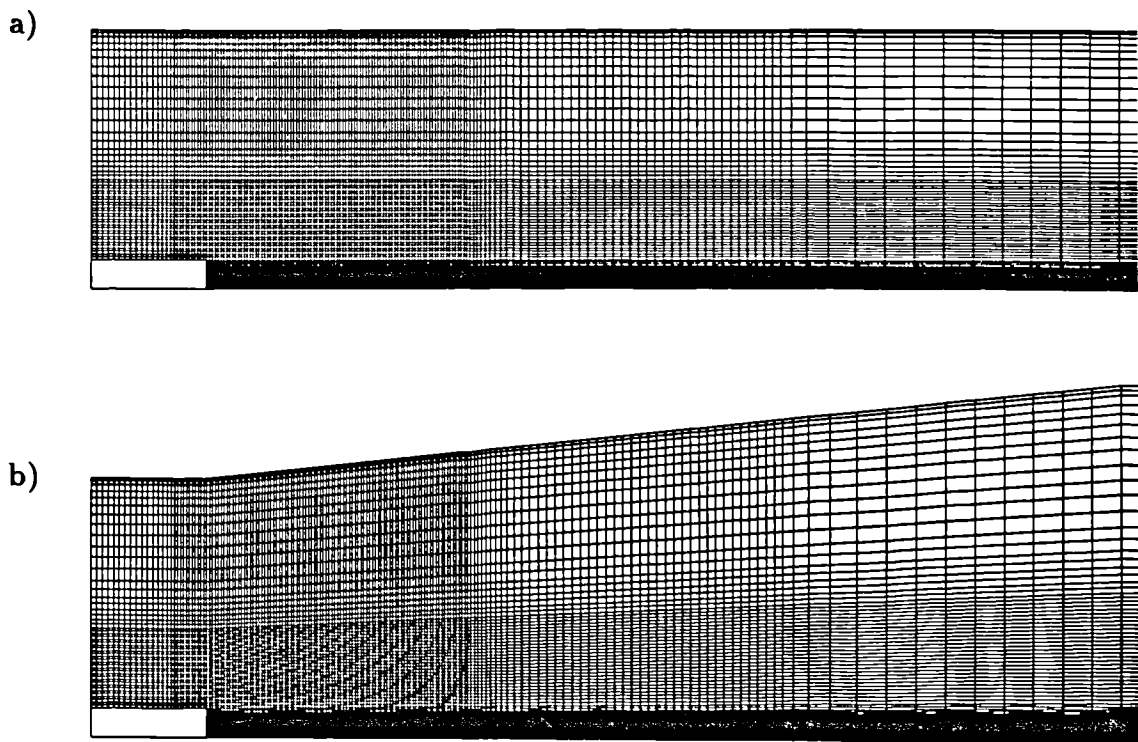


Fig. 4.11 Two-dimensional rib. The turbulence intensity profiles as obtained by LKE, EKE, NKE (a) and LKE, RSM0, RSM1 (b).



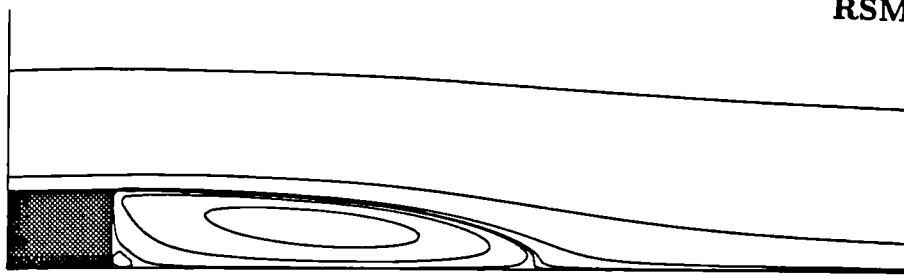
**Fig. 4.12 Backward-facing step (in divergent channel) coordinates and geometry.**



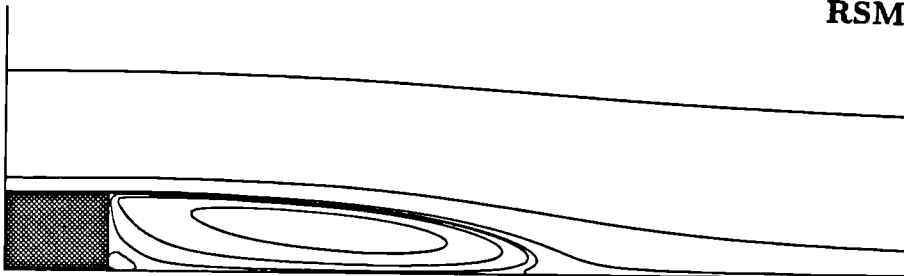
**Fig. 4.13 Grid size 185x82: (a) 0 degree and (b) 6 degree**

a)

RSM0 model



RSM1 model



b)

RSM0 model



RSM1 model

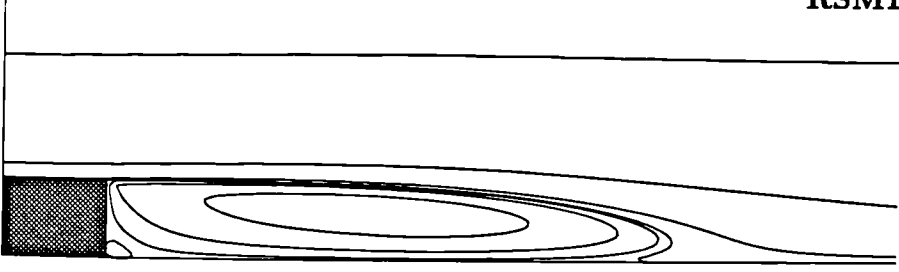


Fig. 4.14 Backward-facing step: (a) 0 degree and (b) 6 degree. Predicted streamlines by RSM0 and RSM1.

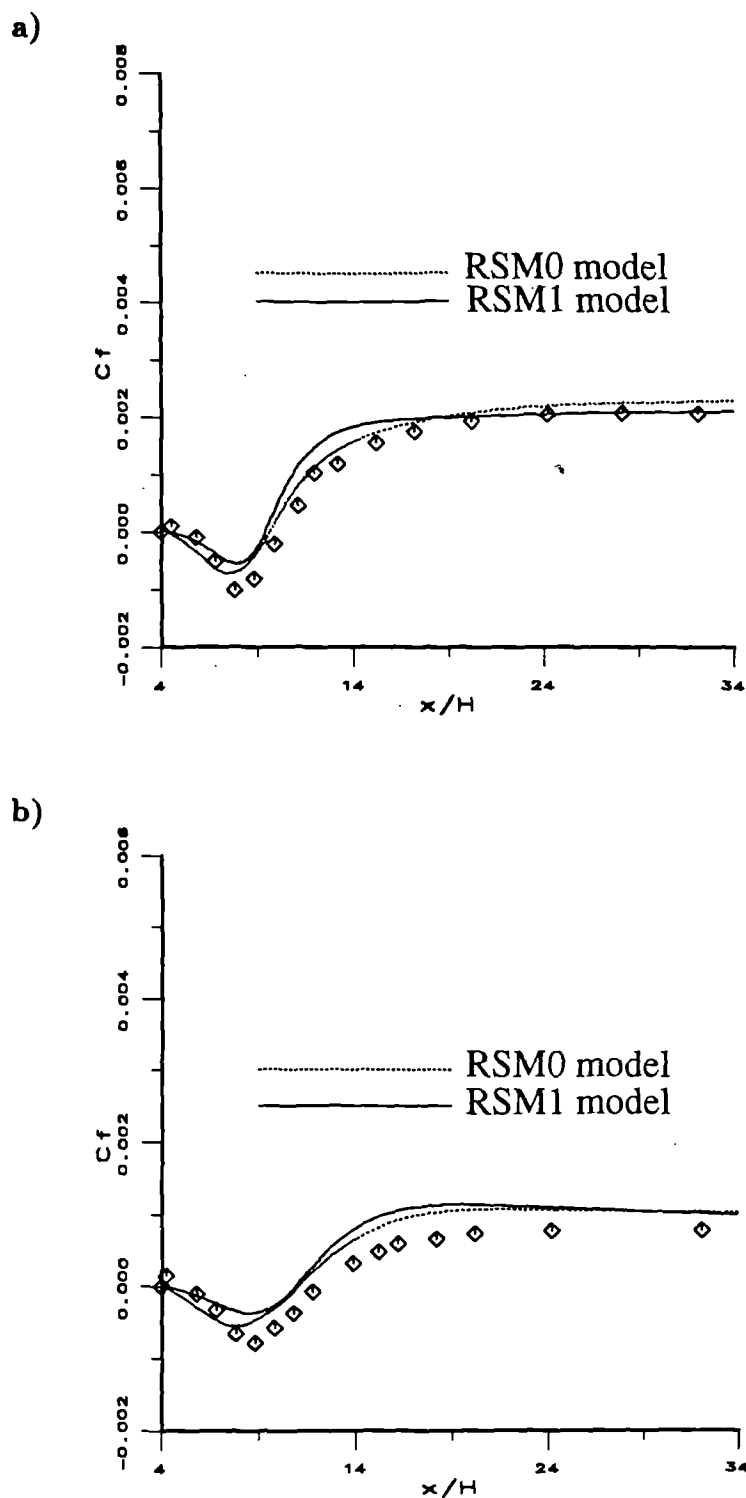


Fig. 4.15 Backward-facing step: (a) 0 degree and (b) 6 degree.  
 Distribution of wall skin friction coefficient  
 predicted by RSM0 and RSM1.

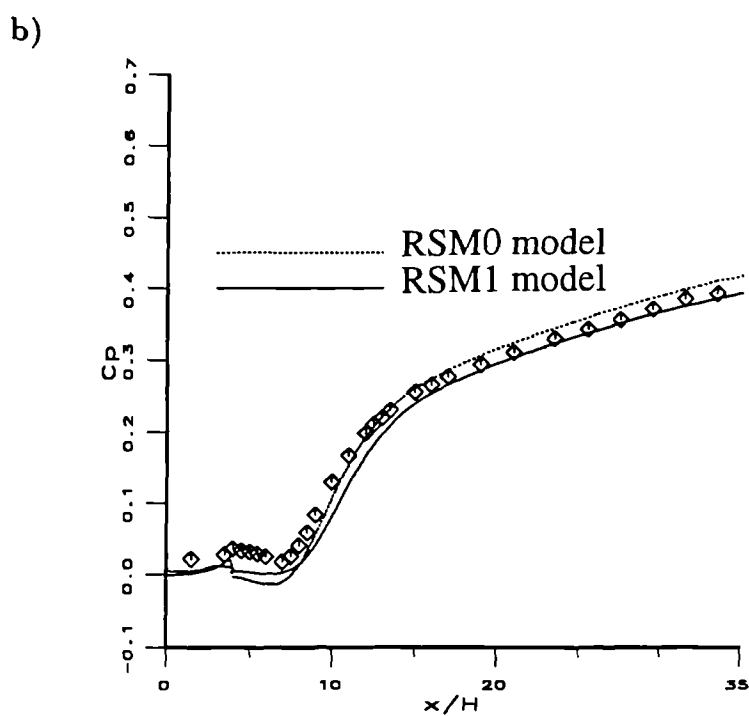
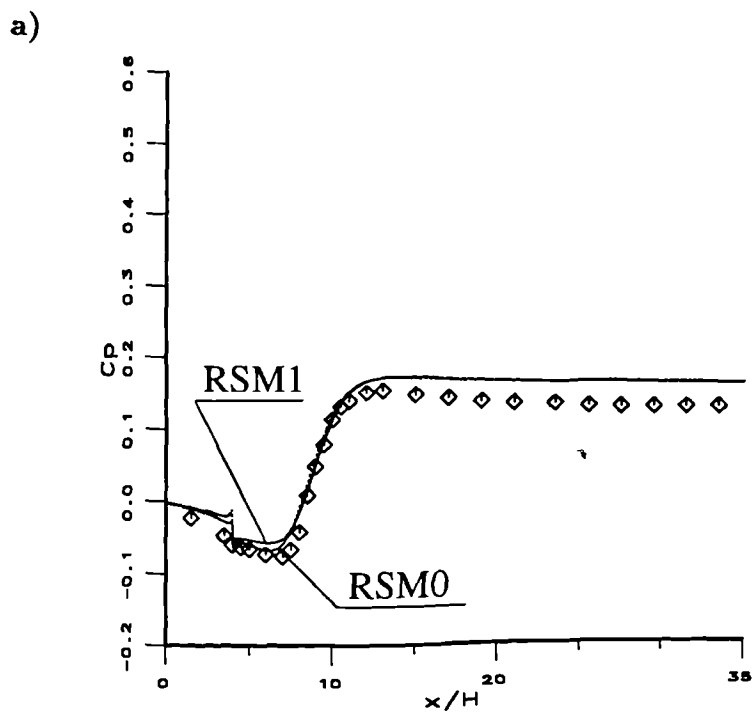


Fig. 4.16 Backward-facing step: (a) 0 degree and (b) 6 degree.  
Distribution of wall pressure coefficient predicted by  
RSM0 and RSM1.

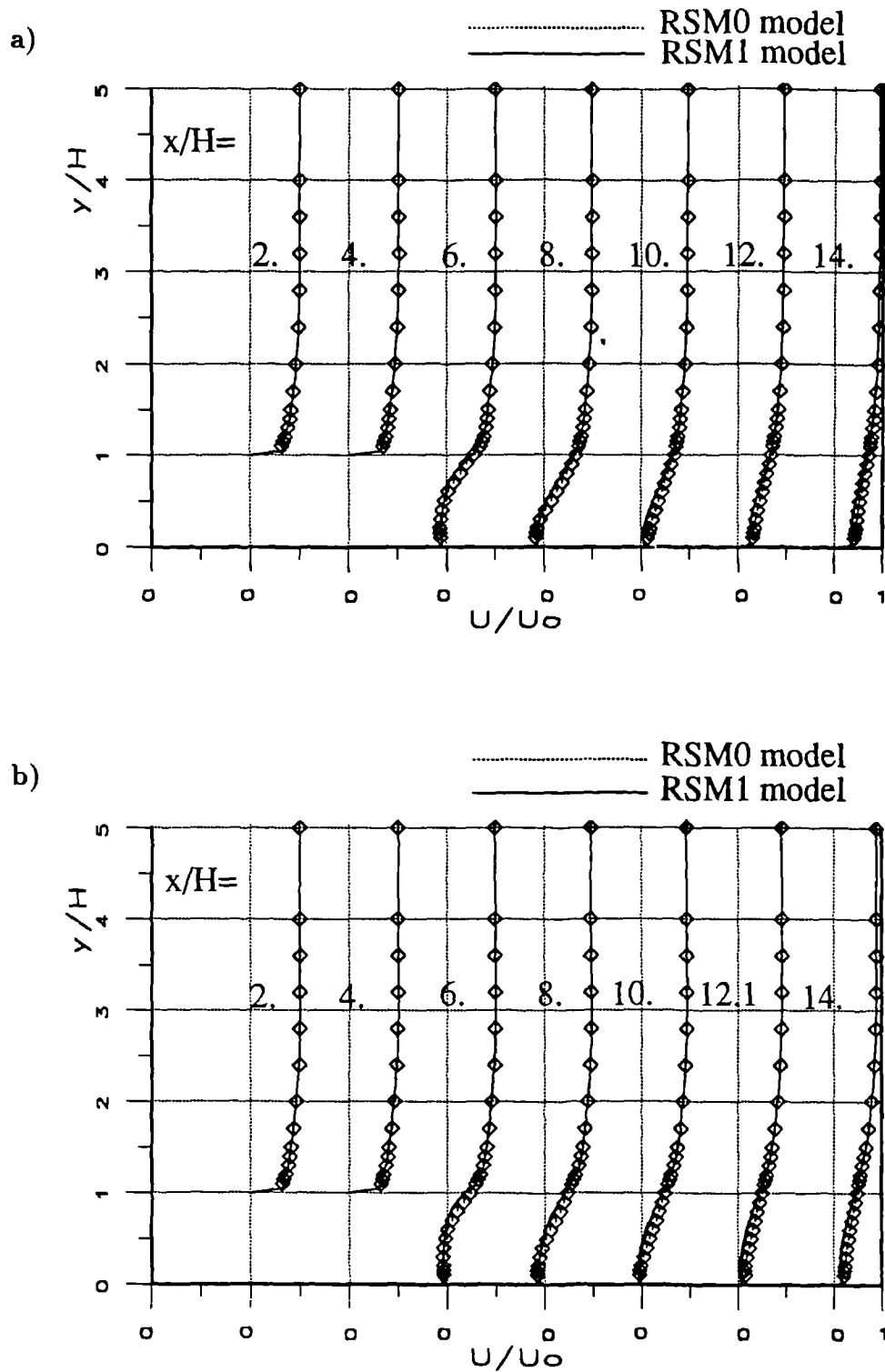


Fig. 4.17 Backward-facing step: (a) 0 degree and (b) 6 degree. The mean velocity profiles as obtained by RSM0 and RSM1.

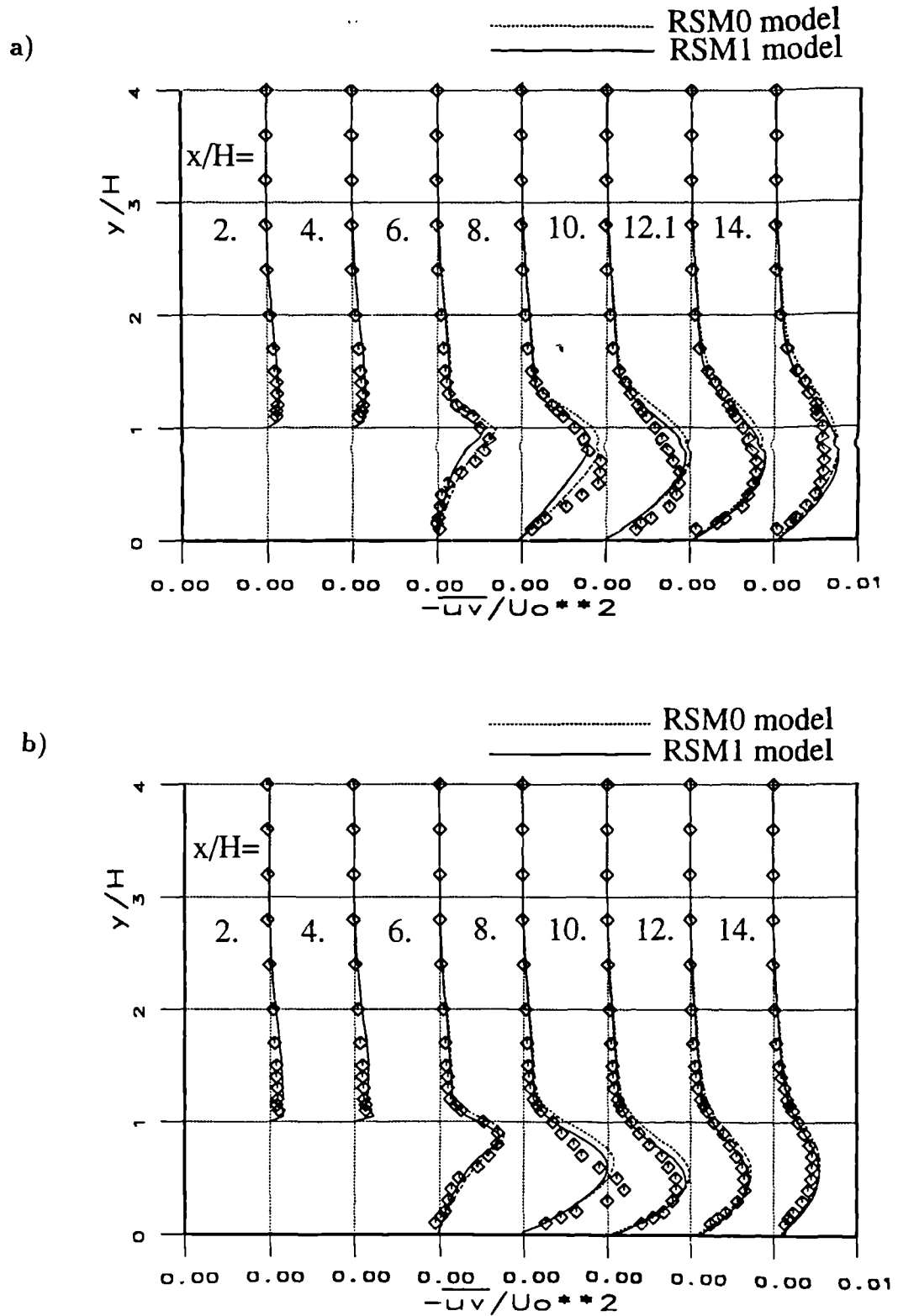


Fig. 4.18 Backward-facing step: (a) 0 degree and (b) 6 degree. The shear stress profiles ( $\bar{u}\bar{v}$ ) as obtained by RSM0 and RSM1.

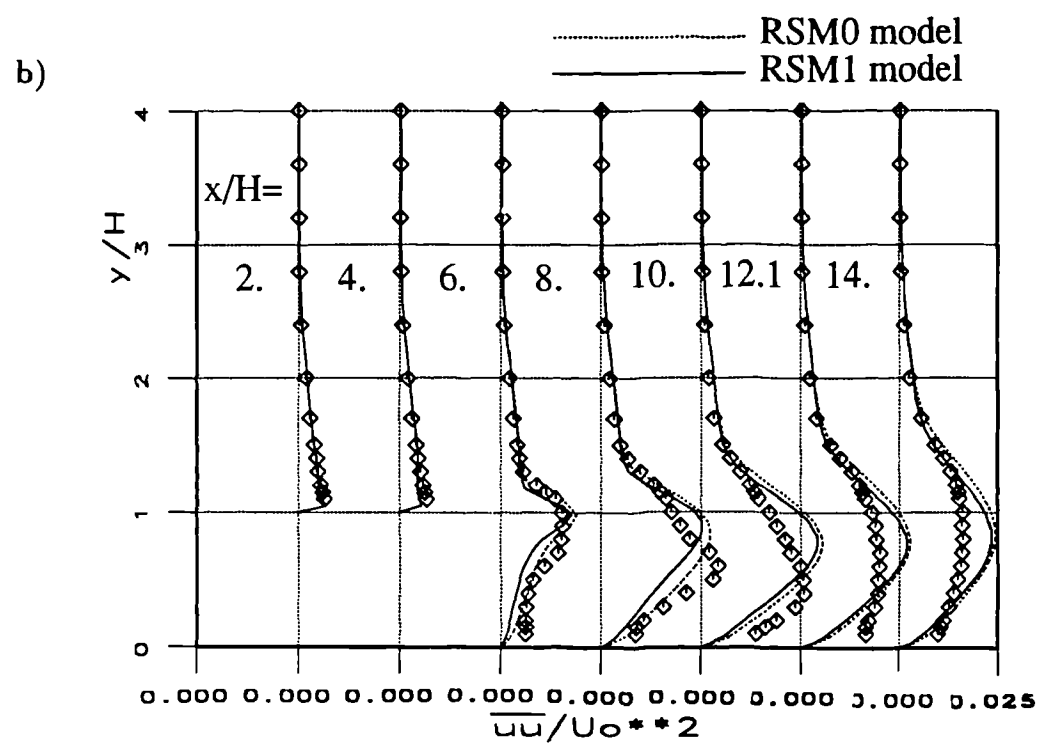
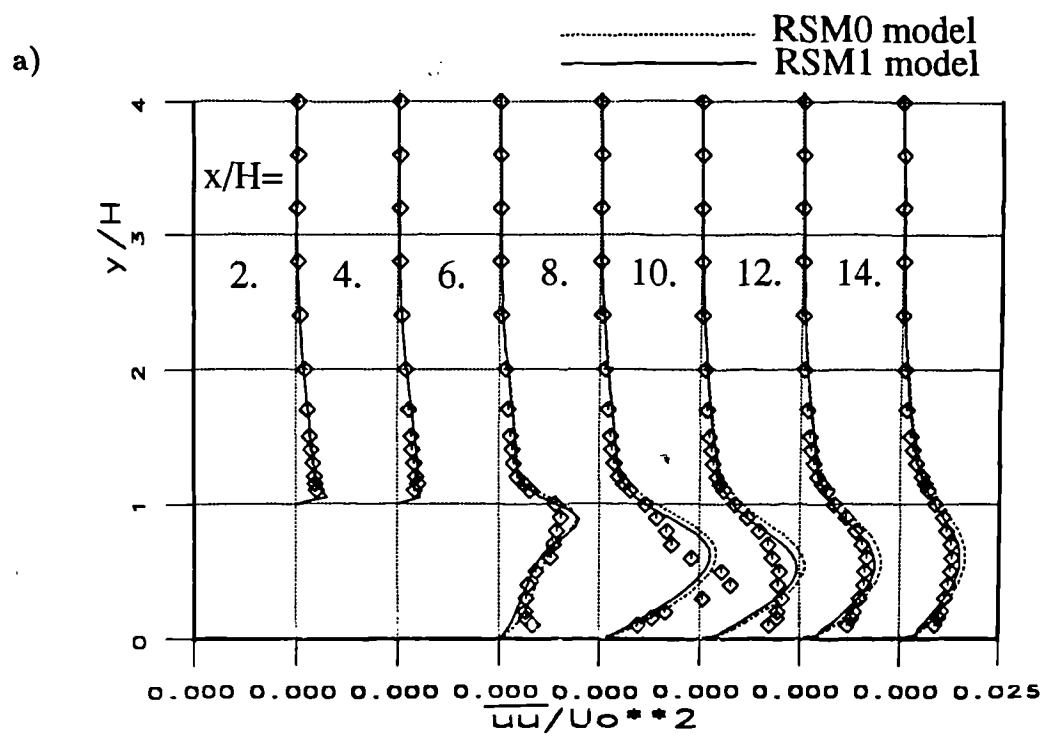


Fig. 4.19 Backward-facing step: (a) 0 degree and (b) 6 degree. The normal stress profiles ( $\bar{u}u^2$ ) as obtained by RSM0 and RSM1.

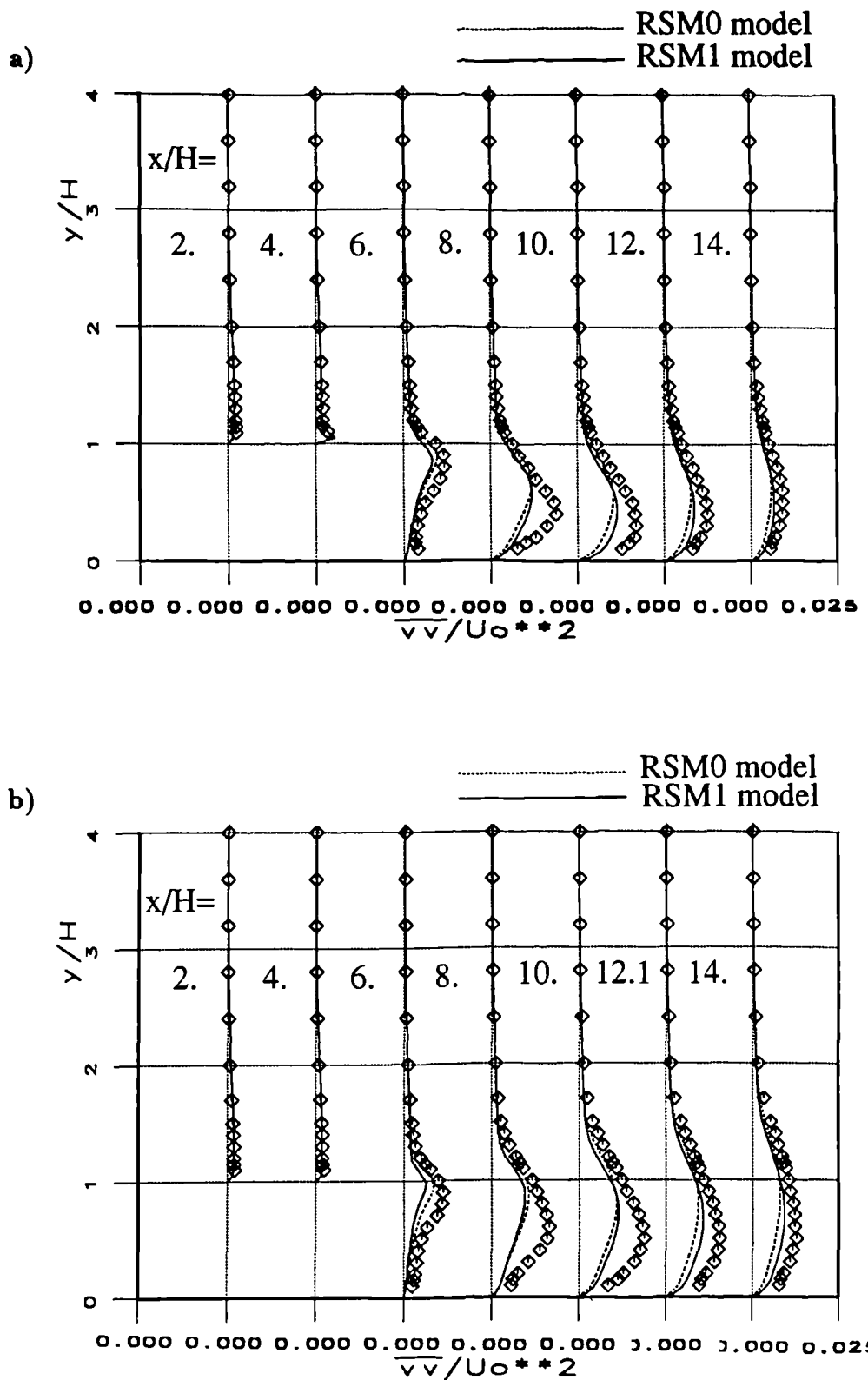
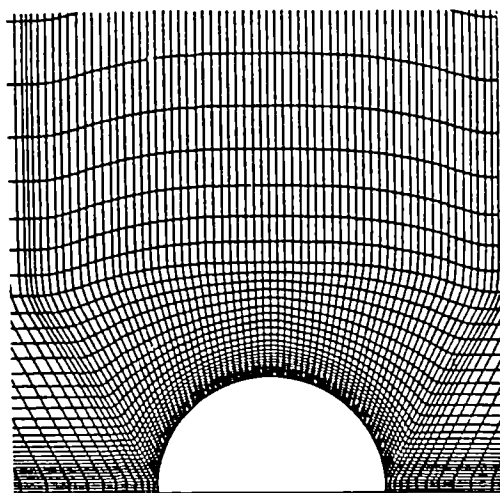
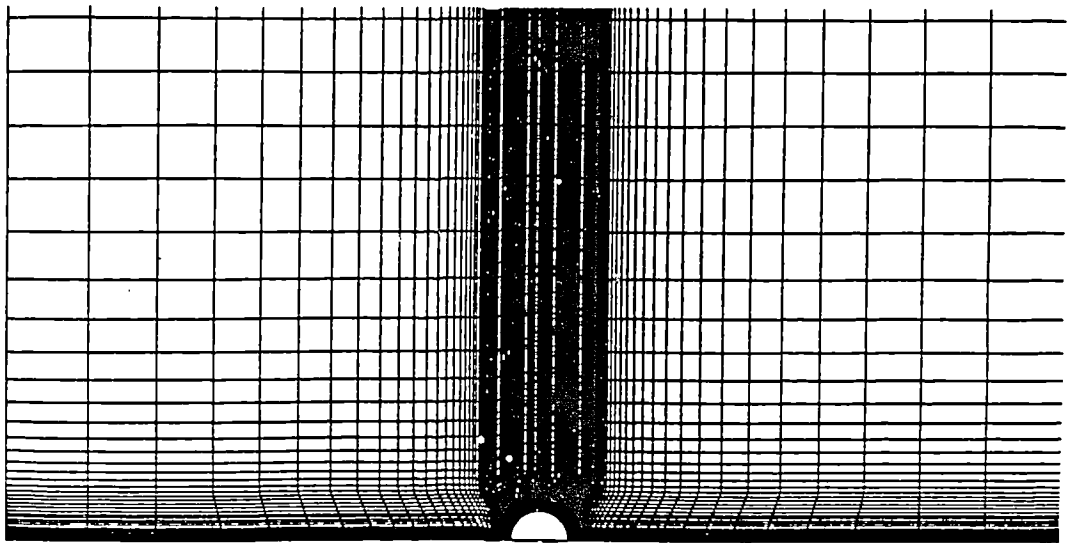


Fig. 4.20 Backward-facing step: (a) 0 degree and (b) 6 degree. The normal stress profiles ( $\bar{v}^2$ ) as obtained by RSM0 and RSM1.



**Fig. 4.22 Circular cylinder. Grid size 109X67.**

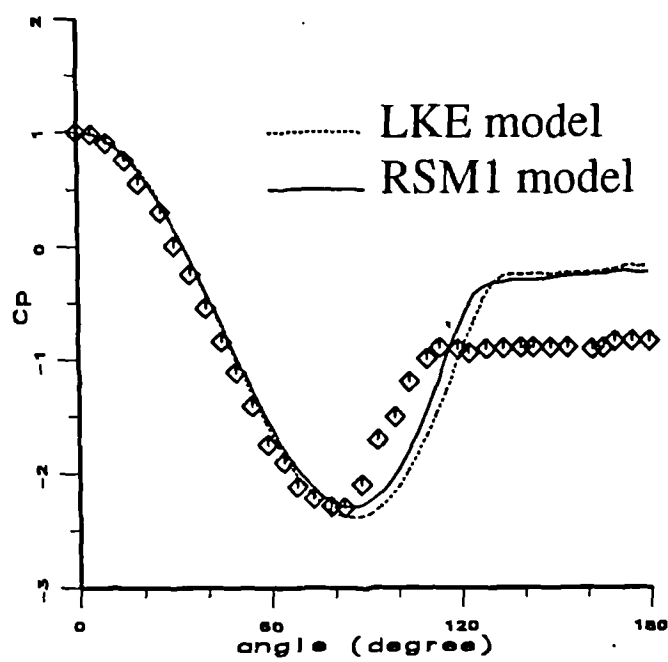
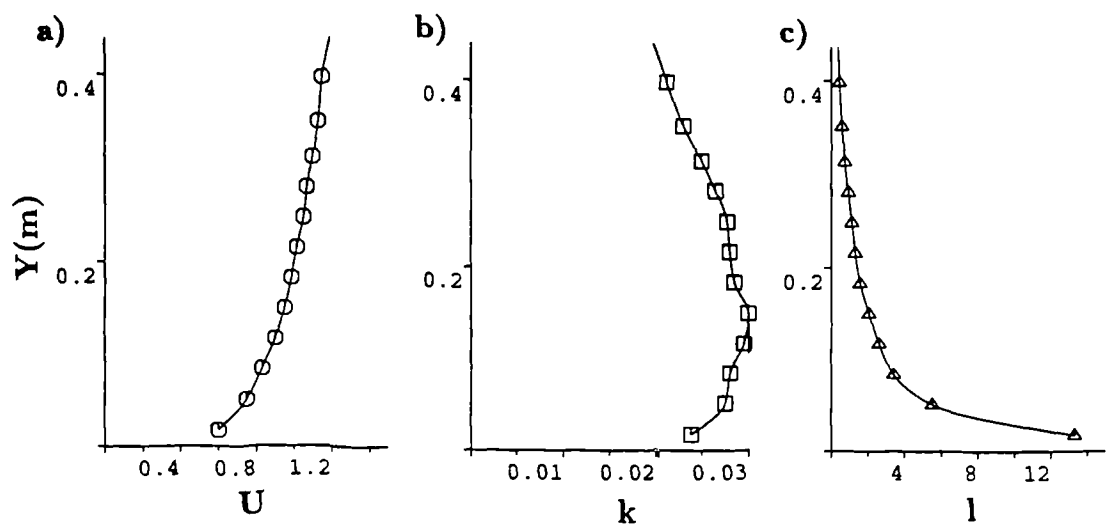
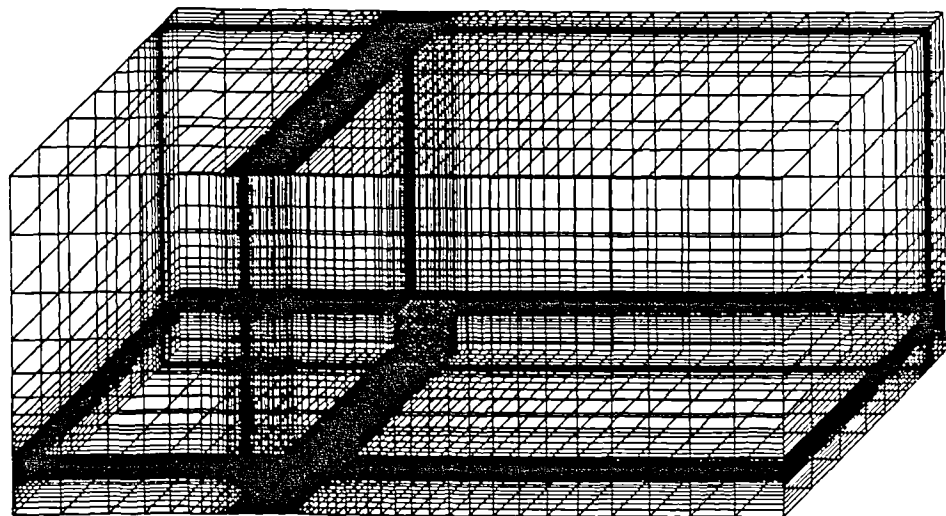


Fig. 4.23 Circular cylinder. Distribution of wall pressure coefficient predicted by LKE and RSM1.



**Fig. 4.24 Inflow boundary conditions: velocity  $U$  (a), turbulence kinetic energy  $k$  (b) and length scale  $l$  (c), non-dimensionalized by  $U_H$  and  $H$ , measured in the wind tunnel.**



**Fig. 4.25 Cube. Computational domain.**

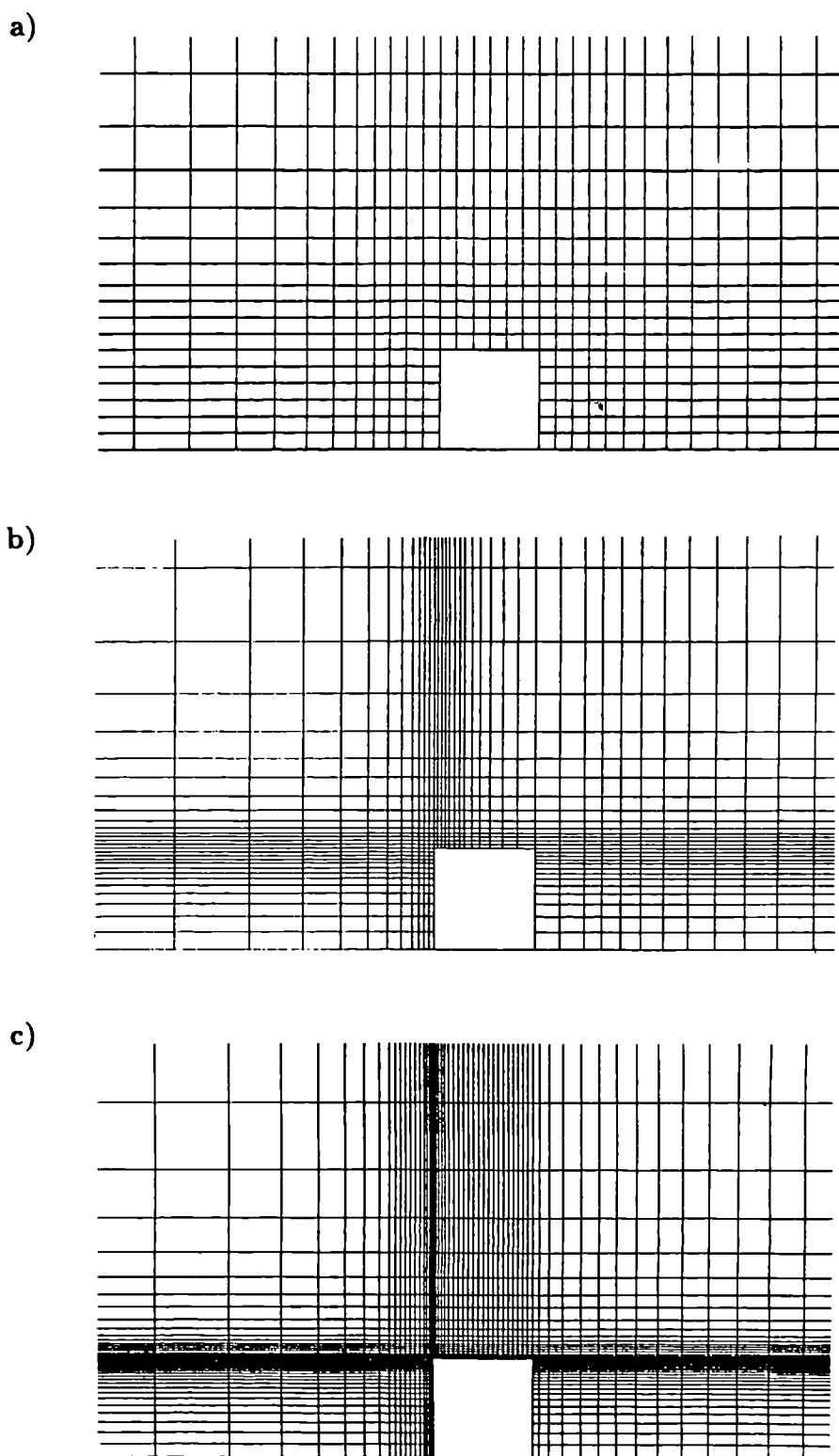
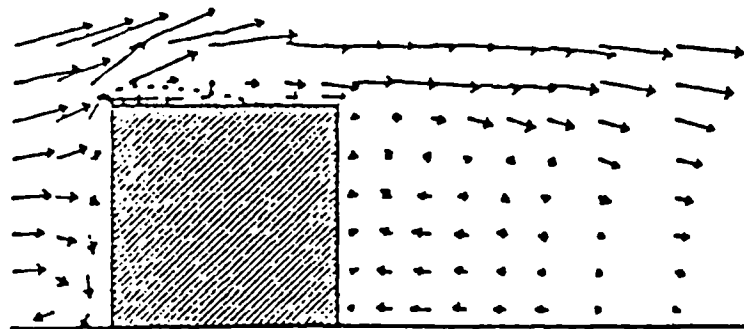
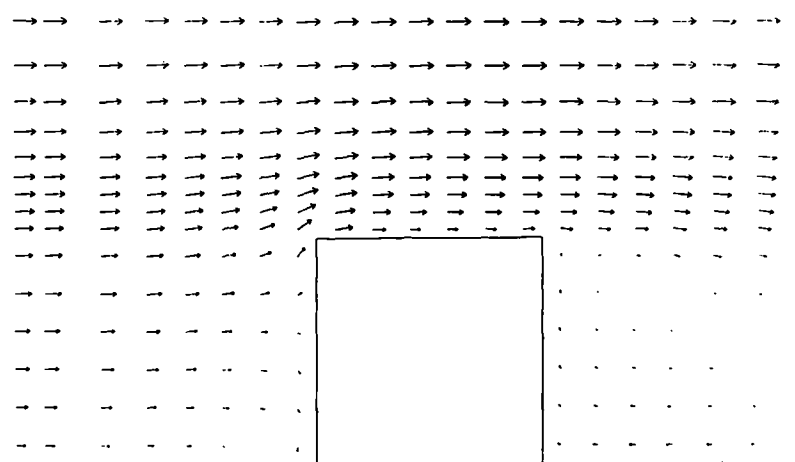


**Fig. 4.26 Cube. Vertical cross section: 44x28x21 (a), 55x33x28 (b) and 70x48x41 (c).**

a)



b)



c)

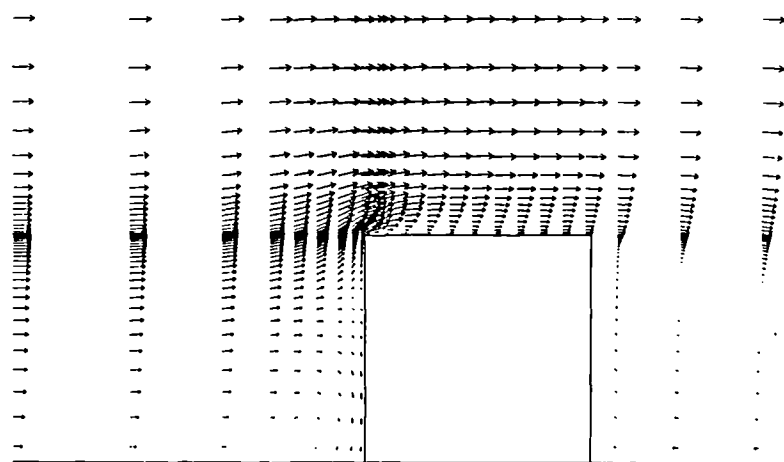


Fig. 4.27 Cube. Velocity vectors as obtained by measurements a) and predicted by LKE using the grids A (b) and C (c).

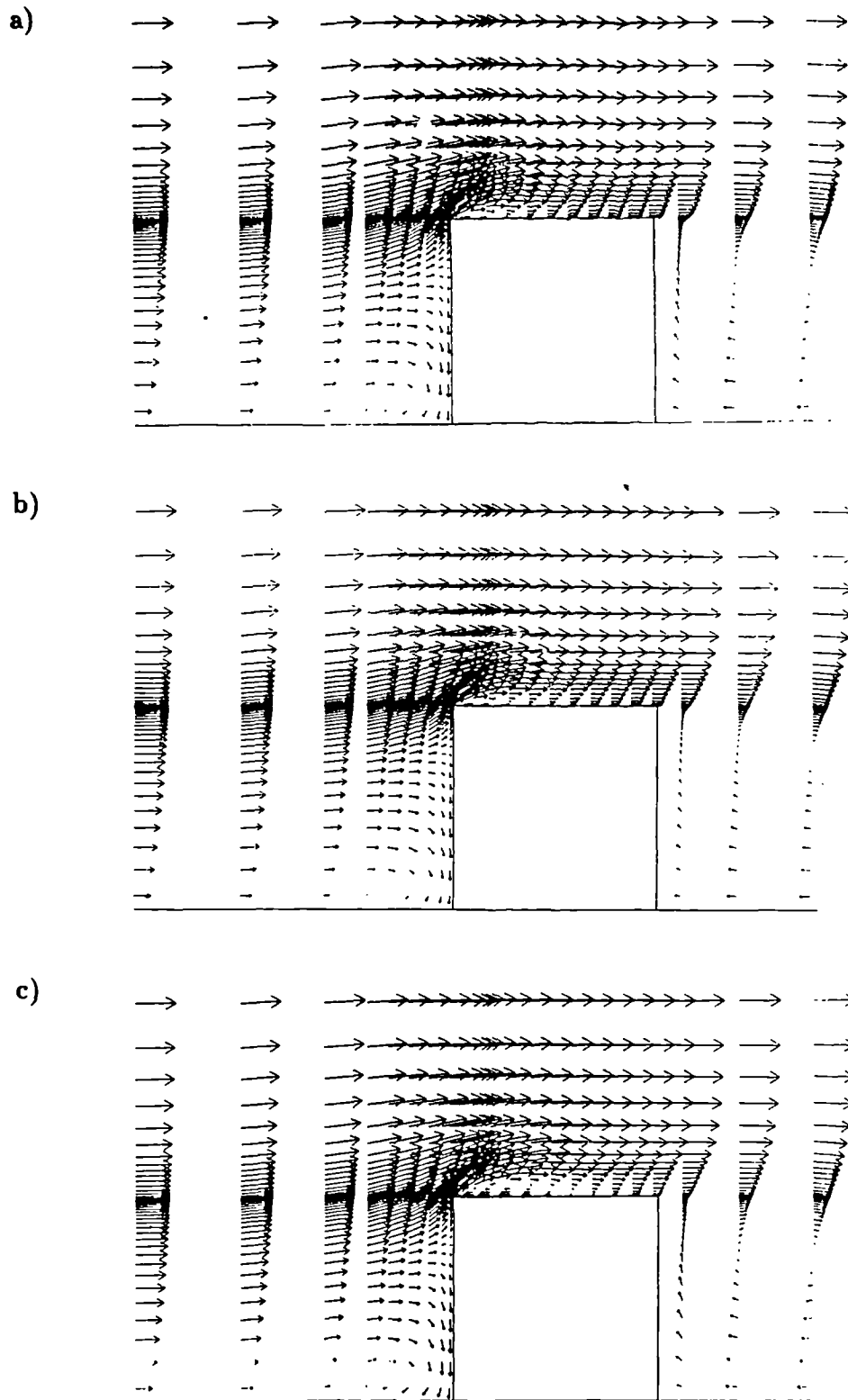


Fig. 4.28 Cube. Velocity vectors predicted by LKE (a), NKE (b) and EKE (c) (grid C and LUDS scheme).

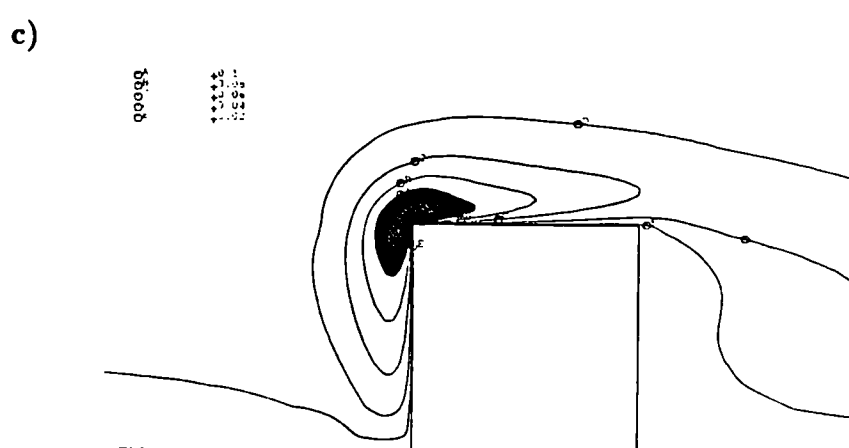
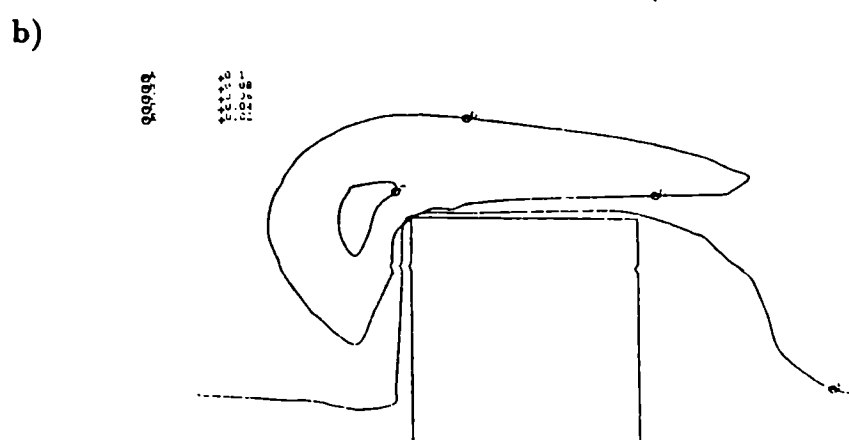
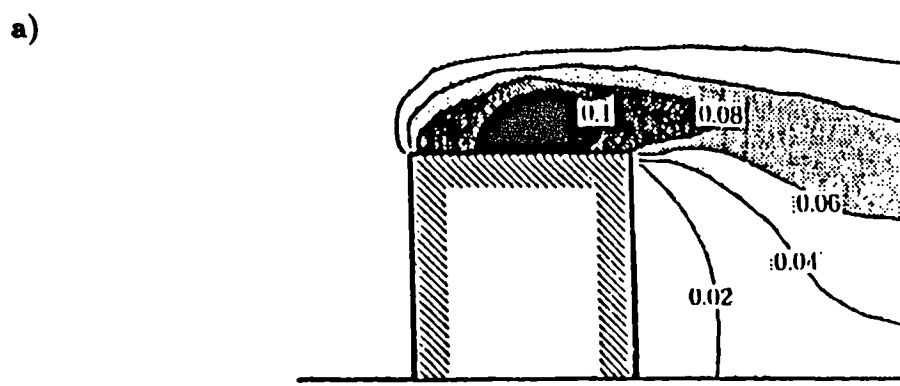
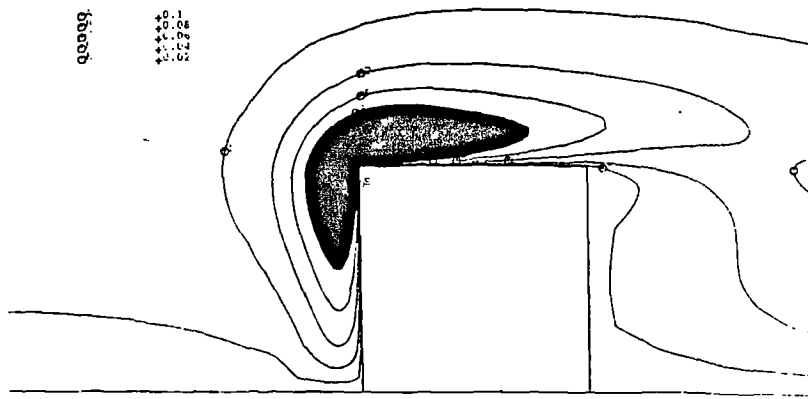
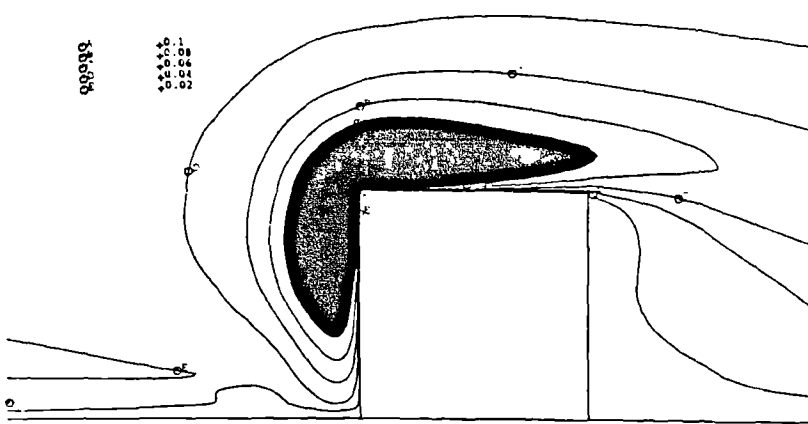


Fig. 4.29 Cube. Turbulence kinetic energy as obtained by measurements (a), and predicted by LKE using the grids A (b) and C (c).

a)



b)



c)

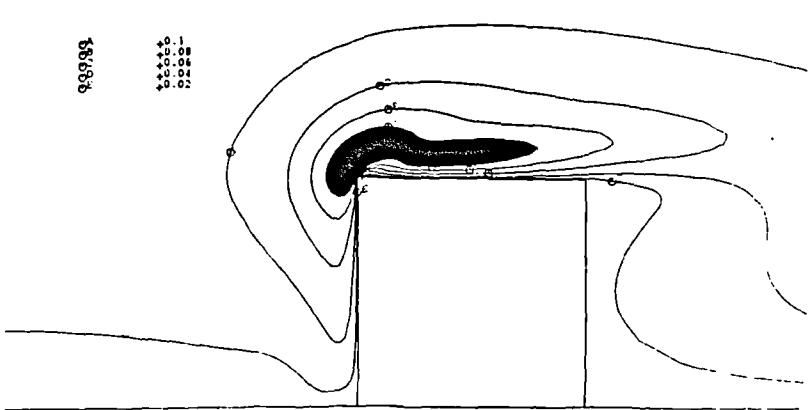


Fig. 4.30 Cube. Turbulence kinetic energy predicted by LKE (a), NKE (b) and EKE (c) (grid C and LUDS scheme).

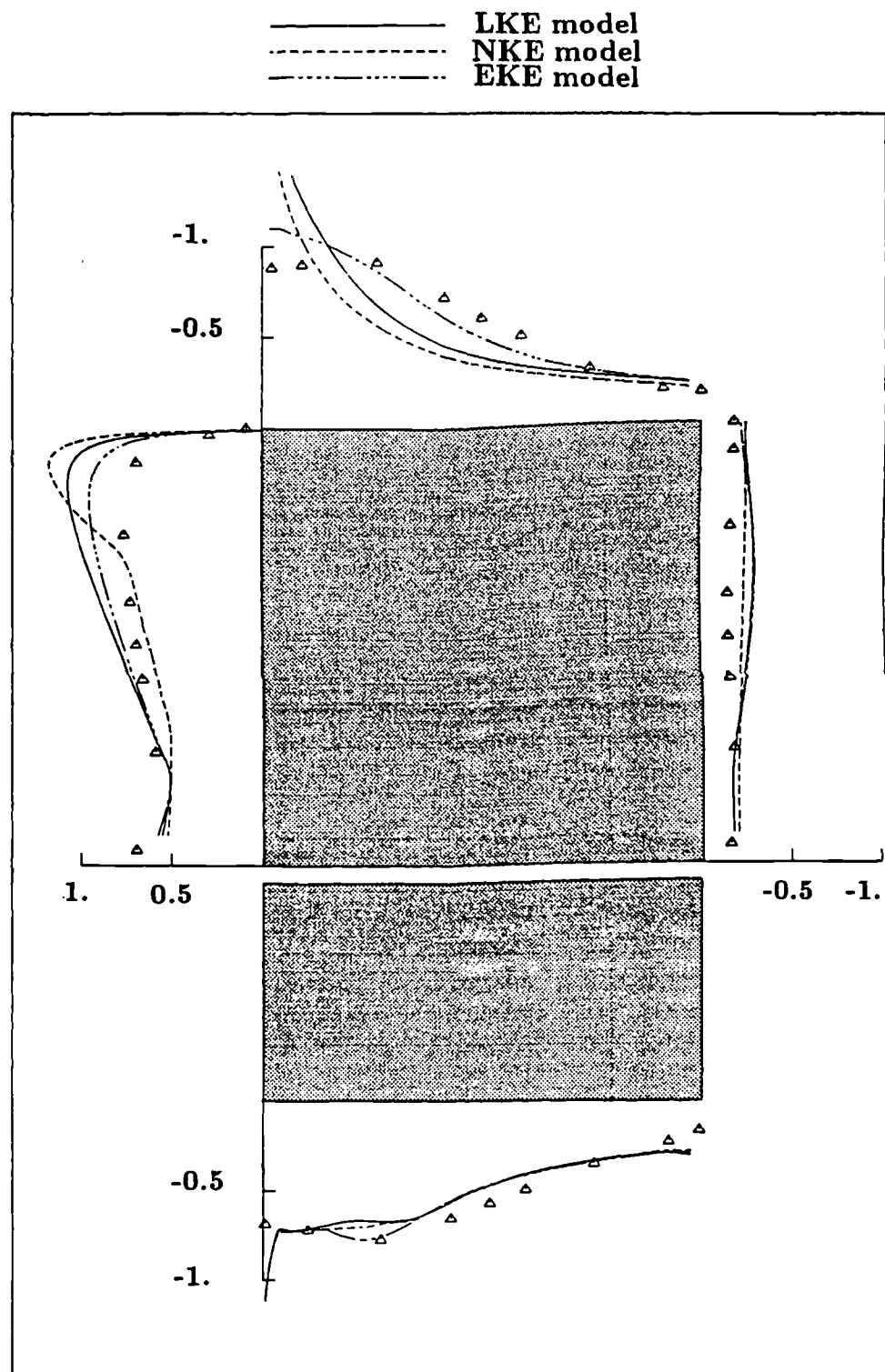


Fig. 4.31 Cube. Comparison of surface pressure coefficients at vertical and horizontal plane ( $y=H/2$ )

# Chapter 5

## COMPUTATION OF FULL-SCALE FLOWS

### 5.1 INTRODUCTION

This chapter presents the results of the numerical simulations of turbulent flows around full-scale buildings. The validity of the simulations is demonstrated by comparisons with full-scale tests conducted by the Agriculture and Food Research Council - Engineering Institute, Silsoe. Various building shapes were investigated but the ones of interest here are a two-dimensional, long, portal-framed barn designated FB16, a single span film clad building designated FB17 and a multi-span glasshouse designated GO7.

The reported measurements consist of:

- The velocity profile in the atmospheric boundary layer with roughness  $y_0 = 10\text{mm}$ , and  $y_0 = 40\text{mm}$ .
- Values of the turbulence intensity at ridge height.
- The distribution of the coefficient of pressure  $C_p$  around the mid-length section for a wind direction normal to the ridge ( $C_p = \Delta p / 0.5 \rho U_h^2$  where  $U_h$  is velocity at ridge height).
- Some flow visualization.

The remainder of this chapter is in seven sections. Section 5.2 considers the prescription of the atmospheric boundary layer by empirical relationships and by full Reynolds-stress model simulations. The predictions for buildings FB16, FB17 and G07 are presented in Sections 5.3, 5.4 and 5.5, respectively. A parametric study is presented in Section 5.6 to determine the effects of varying the height to width ratio, the shape of the eaves and the placement of a solid windbreak. A method for simulating the unsteady wind loading is presented in Section 5.7 and the chapter is concluded in Section 5.8 with a summary of the main findings.

## 5.2 SIMULATION OF THE ATMOSPHERIC BOUNDARY LAYER

The forces on a structure immersed in a boundary layer are very strongly influenced by the profiles of velocity and turbulence within this layer and hence the need for a very accurate representation of the approach flow.

Two alternative approaches were tried in the present work:

- The use of empirical correlations for the mean velocity, the turbulence kinetic energy and its dissipation rate which are based on experimental observations and assume that the atmospheric boundary layer is in equilibrium.
- The simulation of the atmospheric boundary layer with complete Reynolds-stress-transport model of turbulence.

In each case, the objective is to reproduce, as closely as possible, the conditions prevailing in the field tests. Examples of the field measurements are presented in Fig. 5.1 (a, b) (see next page) for two different roughness lengths.

The straight lines are best-fit lines to the data, passing through the  $y_0$  points, and are typically of the form:

$$U_y = U_n \frac{\log(\frac{y}{y_0})}{\log(\frac{n}{y_0})} \quad (5.1)$$

where  $U_y$  is mean velocity at height  $y$ ,  $U_n$  mean 'reference' velocity at height  $n$  (usually 10 m),  $y$  distance from the ground and  $y_0$  - ground roughness length.

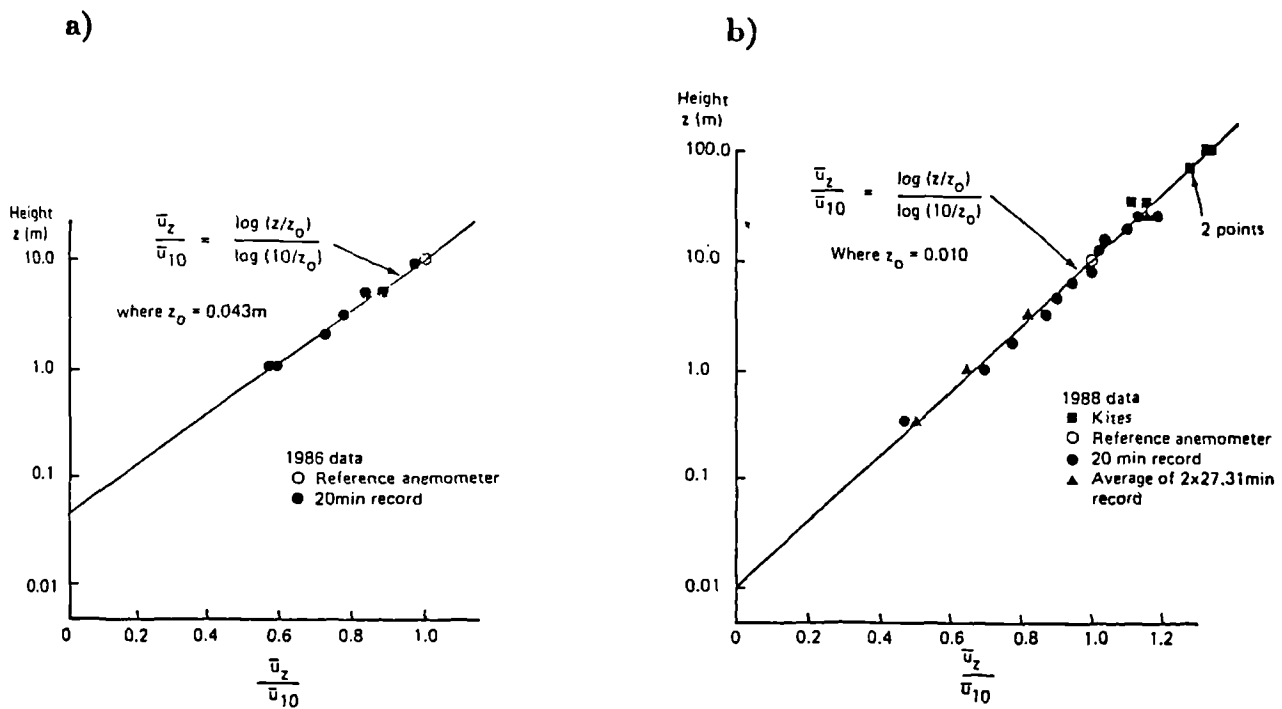


Fig. 5.1 Figure from Hoxey and Richards (1991) showing measured velocity profiles for the roughness a)  $y_0 = 40\text{mm}$  and b)  $y_0 = 10\text{ mm}$  (N.B:  $z$  above correspond to  $y$  in the present notation).

While it is relatively easy to measure the velocity or even obtain it from the above using a reference velocity from the Meteorological Office data (Section 1.1), the measurement of turbulence quantities is much more difficult and complete profiles for those quantities are almost never reported in the full-scale tests. The aim of the empirical correlations or the numerical simulations is therefore to create, from knowledge of a single measured value for the reference velocity, representative profiles of velocity and turbulence quantities that are self-sustaining (i.e. will remain

unaltered in the absence of a building).

### 5.2.1 Empirical correlations

Profiles of mean velocity and turbulence parameters in a smooth flat-plate boundary layer can be obtained from the following correlations.

The mean-velocity is assumed to follow the seventh power law, given by:

$$\frac{U}{U_\infty} = \left(\frac{y}{\delta}\right)^{\frac{1}{7}} \quad (5.2)$$

The turbulence kinetic energy is related to the turbulent shear stress by:

$$k = \frac{-\bar{uv}}{0.3} \quad (5.3)$$

The shear stress is approximated using the mixing-length relation by:

$$-\bar{uv} = l_m^2 \left( \frac{\partial U}{\partial y} \right)^2 \quad (5.4)$$

The mixing length is defined as:

$$l_m = \min(0.41y, 0.085\delta) \quad (5.5)$$

And, finally, local-equilibrium is assumed so that the dissipation rate is obtained from:

$$\epsilon = -\bar{uv} \frac{\partial U}{\partial y} \quad (5.6)$$

The Reynolds stresses (when RSM is used) may be evaluated from their respective equations as suggested in Section 3.6.5.

Some preliminary calculations were carried out based on the above assumptions. As expected, the computed results showed a great sensitivity to the choice of  $\delta$  - boundary layer thickness (Fig. 5.2). This approach was abandoned because, not surprisingly, it produced velocity profiles that were quite different from the measured ones (Fig. 5.1). The computations did nevertheless serve one important purpose: they showed that the computational domain should extend vertically to 55 building heights to obtain  $\delta$ -independent solutions. The results for  $\delta = 55H$  are shown in Fig. 5.3 where it is clear that they overestimate the measurements at the windward and leeward sides by approximately 40% .

Another approach tried here was based on the correlations of Harris and Deaves model (1981) which are the most popular of the empirical models in Wind Engineering. This model is based on asymptotic similarity theory in which velocity scaling is with the friction velocity and the length scale parameter is taken to be either the roughness length  $y_0$  or the thickness  $\delta$ , depending on position within the boundary layer:

$$U_y = \frac{U_\tau}{\kappa} \left[ \ln \frac{y}{y_0} + a_1 \frac{y}{\delta} + a_2 \left( \frac{y}{\delta} \right)^2 + a_3 \left( \frac{y}{\delta} \right)^3 + a_4 \left( \frac{y}{\delta} \right)^4 \right] \quad (5.7)$$

Note that for small distances from the ground, this expression becomes equal to equation (5.1). The constants  $a_1, a_2, a_3, a_4$  were determined from comparisons with measured wind profiles and are given the values 5.75,  $-1.875$ ,  $-4/3$ ,  $1/4$  respectively. For lower heights, expression (5.7) can be written as:

$$U_y = \frac{U_\tau}{\kappa} \left[ \ln \frac{y}{y_0} + 5.75 \frac{y}{\delta} \right] \quad (5.8)$$

from which the friction velocity is obtained in the usual way.

The shear stress  $\tau_y$  is assumed to decrease parabolically with height, thus:

$$\tau_y = \rho U_\tau^2 \left[ 1 - \left( \frac{y}{\delta} \right)^2 \right]^2 \quad (5.9)$$

The dissipation rate of turbulence kinetic energy is again obtained from

local-equilibrium assumptions while  $k$  itself is evaluated from:

$$k_y = \frac{U_\tau^2(1 - (\frac{y}{\delta}))^2}{\sqrt{C_\mu}} \quad (5.10)$$

This approach was previously adopted by Hagen, Skidmore, Miller and Kipp (1981) who took the constant  $C_\mu$  to be 0.026 instead of its usual value of 0.09 in order to obtain a better correlation with the measurements. The consequence of decreasing the constant  $C_\mu$  is that the inlet boundary layer was no longer self-sustaining (Richards, 1989). Results obtained by using this approach are presented in Section 5.2.3.

### 5.2.2 Reynolds-stress transport modelling

RSM0, one of the Reynolds-stress models discussed in Chapter 2, was used in the simulation of the atmospheric boundary layer upstream of the buildings. The solution procedure used for those calculations is a finite-volume one based on the solution of the boundary-layer equations in transformed coordinates. Details may be found in Spalding (1975) and Younis (1987) but, essentially, the solutions are now obtained in the transformed plane  $(x, \eta)$  where  $x$  is the coordinate direction aligned with the flow while  $\eta$  is a normalized cross-stream coordinate defined by:

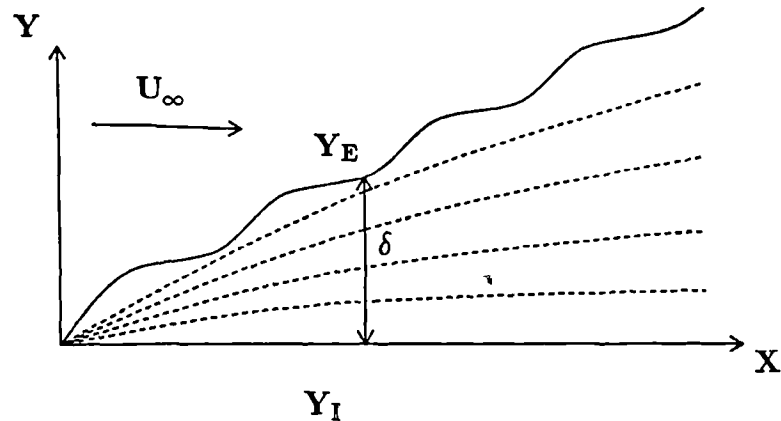
$$\eta = \frac{y - y_I}{y_E - y_I} = \frac{y - y_I}{\delta} \quad (5.11)$$

where  $y_I$  is the height of the inner boundary,  $y_E$  is the height of the external boundary and the difference between the two height defines  $\delta$ , the flow width. As can be seen, the computations are always confined in the region  $0 \leq \eta \leq 1$  irrespective of the actual physical width of the flow (see Fig. 5.4, next page).

The discretized equations are solved by marching integration which is appropriate for boundary-layer flows. The calculations start at a given point with arbitrary profiles for the dependent variables and then move

by a small interval in the main direction of flow till the whole domain is covered. Results from one plane are used for the calculation of the next plane downstream from it.

a)



b)

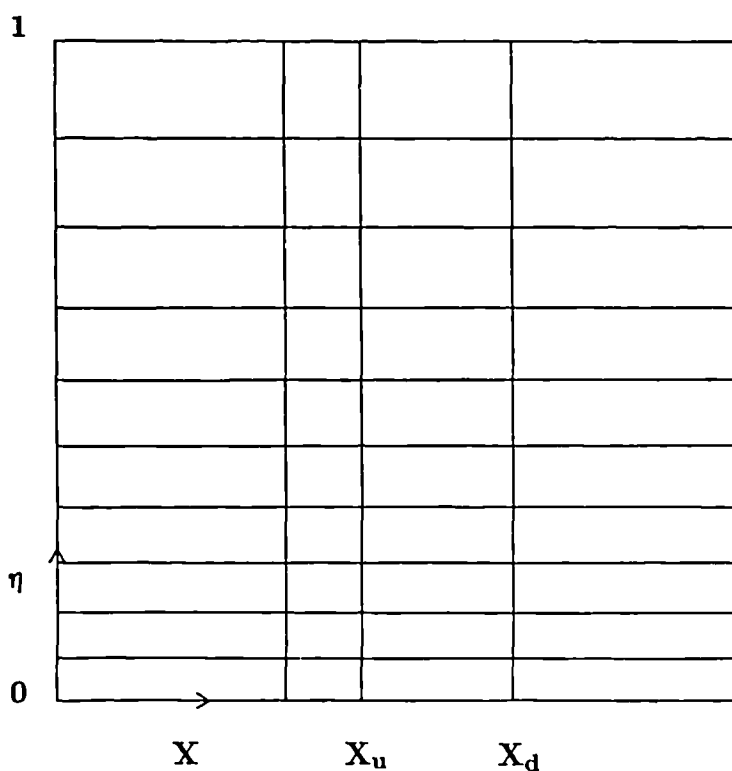


Fig. 5.4 The physical a) and transformed b) coordinate system.

In the near-wall region, it is assumed that the turbulent stresses are con-

stant and hence all their gradients normal to the wall are set to zero. The effects of surface roughness are included in the calculation procedure through a modified logarithmic relation, thus :

$$U_y = \frac{U_\tau}{\kappa} \ln \frac{y}{y_0} \quad (5.12)$$

This defines the wall shear stress value which is then used as a flux boundary-condition for the axial momentum equation.

The purpose of the calculations was to obtain an equilibrium atmospheric boundary layer where the velocity  $U$  at a given height (the reference height) was equal to the value reported in the full-scale tests.\* This was done by performing an initial calculation with guessed free-stream velocity and initial boundary-layer thickness and, once equilibrium is reached, comparing the calculated velocity at the reference height with the data. If the velocities are different, another run is performed with slightly different  $U_{\text{freestream}}$  and  $\delta$  till an acceptable match is obtained. The computed results are then stored for later use in the elliptic-flow calculations.

### 5.2.3 Effects of inlet profiles

The profiles of streamwise velocity, turbulence intensity and energy dissipation rate generated with the Harris and Deaves formula are compared in Fig. 5.5 with those obtained with the Reynolds-stress model. Ground roughness length was 10 mm and the mean velocity at 10m height was 10 m/s in each case. The profiles obtained with either method are quantitatively and qualitatively similar. The RSM0 results for the turbulence intensity are higher than those for the empirical correlations and this remains the case for the two roughness heights of  $y_0=20$  mm and  $y_0=40$  mm shown in Fig. 5.6. The full-scale results tend to be closer to RSM0: Hoxey and Richards (1991) reported turbulence intensities of 15-17% and 18% for roughnesses of  $y_0=16-25$  mm and  $y_0=40$  mm, respectively. The full-scale measurements of mean-velocity are well reproduced by either method (see Fig. 5.7).

The effects on the predicted wall static pressure distributions arising from the choice of inlet profiles can be seen in Fig. 5.8. Plotted there are the RSM0 results for  $y_0 = 0$  and 10 mm and the Harris and Deaves correlations. The differences in predicted pressures are due to the different levels of turbulence intensity obtained with either method. Those differences are not as great as might have been expected because the inlet to the computational domain was located at 13H (H is the building height) upstream of the building with the result that the inlet boundary layers developed into similar new states before interacting with the building. Had the inlet plane been located closer to the building, the Harris and Deaves profiles would still be undergoing adjustment to attain a self-sustaining state.

On the basis of those and other results, it was decided that all full-scale calculations would be carried out using inlet atmospheric boundary layer profiles generated by the Reynolds stress model. Those equilibrium and self-sustaining profiles allow the inlet boundary to be located at shorter distance from the building with obvious savings in computer time and storage. From a practical point of view, the boundary-layer code is very simple to use and complete simulations take only a few minutes on a SUN SPARC 1<sup>+</sup> machine. The practice here has been to prepare inlet profiles for a wide range of flow and roughness conditions and then to use those in later calculations.

### **5.3 RESULTS FOR BUILDING FB16**

FB16 is a low-rise building which is sufficiently long (120 m) for the flow along the mid-length section to be effectively two-dimensional. The roof is twin-pitched with a 15 degrees included angle. The geometry is shown in Fig. 5.9. In the full-scale tests, the building was situated on a flat, open, field and oriented with the ridge normal to the prevailing wind direction. Smoke visualization revealed the presence of a recirculation zone on the windward side of roof (see Fig. 5.10 and Fig. 5.11.a) while snow tracks give some indication of the position of the stagnation point (see Fig. 5.11.b). The actual sizes of the recirculation zones are therefore not known with any precision, particularly as the smoke patterns were

severely influenced by wind gusts. The anticipated pattern of pressure distribution on a building such as FB16 is positive external pressures on the windward side and suction on the roof and the leeward side.

In determining the extent of the computational domain, a compromise has to be made between the need to place the boundaries sufficiently removed from the building to ensure that their influence does not affect the computed results yet for the overall domain to remain small enough to allow for adequate grid resolution. During the course of numerous numerical experimentations, it was found that the inlet boundary plane must be placed at a minimum distance of  $8H$  from the building for the computed solutions to be completely independent of the position of the inlet. In other words, placing the inlet at distances greater than  $8H$  produced essentially identical results, but with more computational effort. The exit plane was located at  $20H$  downstream from the building, a distance shown by the two-dimensional rib calculations of Chapter 4 to be sufficient for total flow recovery. The top boundary was placed at a distance of 300 m (or 55 building heights) which is a typical depth of the atmospheric boundary layer and the minimum recommended in the Code of Practice.

The effects of grid density and distribution on the computed solutions can be very large, as can be seen in Figs. 5.12 and 5.13 where results for two grids (108x100 and 142x110) are plotted. It is immediately apparent that the discretization errors associated with the coarser grid have reduced the size of the recirculation zone on the windward side and eliminated it altogether on the roof. The absence of this roof vortex is often blamed on the use of the  $k-\epsilon$  model but this is clearly incorrect as demonstrated by the present results which were obtained with the standard model. Several other grids were tested and a quantitative comparison between them is presented in the Table 5.1 which reports the location the stagnation point obtained with each grid.

| grid                              | 78x56 | 108x100 | 142x110 | 160x125 |
|-----------------------------------|-------|---------|---------|---------|
| $\frac{y_{\text{stagnation}}}{H}$ | 0.3   | 0.4     | 0.5     | 0.5     |

Table 5.1 Grid effects on the position of the stagnation point

The same, standard,  $k-\epsilon$  model was used in all those tests. The results of this test suggest that the 142x110 grid would be suitable for all later calculations.

The effects of grid density are, of course, not easily separable from those associated with the differencing scheme. Several calculations were therefore carried out with the aim of testing the sensitivity of the computed solutions to the choice of differencing scheme. In all those tests, the 'best' grid to emerge from the last test (i.e. 142x110) was used. The differencing schemes tested were the upwind scheme, the power-law scheme, the linear-upwind scheme and, finally, the standard central-upwind (hybrid) differencing scheme. The results of these tests were in many cases indistinguishable when plotted on a normal scale. A sample result is presented in Fig. 5.14 where the (first-order accurate) upwind scheme is compared with the (second-order accurate) power-law scheme. Since the upwind scheme is relatively more robust than the others, as well as being easier to obtain converged solutions with, this scheme was to be used in the majority of subsequent calculations. The other schemes were also used from time to time, mainly to provide an independent check on the grid resolution.

Full-scale measurements were reported for two values of ground-roughness lengths,  $y_0 = 10$  mm and 40 mm. The former value corresponded to the state of the surrounding field shortly after the grass has been cut, the latter when the grass was at nearly full height (Robertson, 1989). The measurements appeared to suggest that ground roughness in those limits had very little effect on the pressure distribution on the building and calculations were therefore carried out to check this result. The effects of roughness entered the simulations through the modified log.-law discussed in Section 5.2.2. The calculations, like the measurements, appear to show that roughness effects are indeed small in this range. That is not to say they are unimportant: Fig. 5.15 (a, b) which presents the streamlines for the  $y_0 = 0$  and 40mm (the 10 mm results can be seen in Fig. 5.13), shows illustrative results obtained for a smooth ground (see also Fig. 5.8) and those are clearly very different from the rough-ground results.

Further calculations were carried out to determine the consequence of treating the surface of the building itself as being rough. The experi-

ments suggest that a roughness height for the buildings is about 0.5 mm and calculations based on this value were identical to ones obtained for a smooth wall. The building was therefore treated as smooth in all subsequent calculations.

The mean-flow streamlines obtained with the standard  $k-\epsilon$  model are shown in Fig. 5.13.b. The position of the stagnation point on the windward side is about 50% of the eaves height from the ground. There is also a separated zone on the windward side of the roof, much smaller in size, extending to only about 25% of the width. The pressure distribution predicted by the linear  $k-\epsilon$  model, presented in Fig. 5.14, shows that the largest discrepancy with the data occurs on the windward side of the roof where the model appears to underpredict the measured values as well as obtain the wrong profile shape. It will become clear from later results that the size of the separated zone on the roof and the shape of the predicted pressure distribution there are very closely linked: the correct shape being obtainable only when a sufficiently deep separated zone is predicted. The results for the windward and the leeward walls compare extremely well with the data. Those results are quite similar to those obtained with the same turbulence model for the cube (Section 4.6) which suggests that here, too, production of  $k$  is being overestimated by Boussinesq's relationship.

It was not possible to obtain results with the non-linear  $k-\epsilon$  model on the fine grid deemed necessary for grid-independent solutions. Even dropping the difficult second-order differential terms did not resolve the convergence problem and hence the results for this model, reported below, were obtained on the coarser 102x74 grid and may therefore not be entirely grid independent. The pressure distribution obtained with the non-linear model is compared with the data in Fig. 5.16. The results are not very different from those of the linear model except on the windward roof where they are somewhat worse. The downstream reattachment length is about 10% longer than obtained with the linear model, which is similar to the results obtained for the backward-facing step and the 2D square rib (Chapter 4).

The results for the 'irrotational-strain' modification to the  $\epsilon$ -equation are presented in Fig. 5.17 for the pressure coefficient and Fig. 5.18 for the mean velocities. The windward-wall stagnation point now occurs at is

60% of the eaves height and it is immediately clear that a deeper roof recirculation zone is obtained with this model and that the static pressure distribution on the windward roof is much more closely predicted. The pressure distributions on the windward and the leeward walls are also well predicted. Contours of the turbulence kinetic energy (defined as  $k/U_{ref}^2$ ) are presented in Fig. 5.19 (a, b) for the linear and the modified models respectively. Again, as for the cube, the maximum turbulence energy obtained with the linear model occurs close to the top front corner where higher levels of eddy-viscosity will be generated, leading to the small separated region observed in Fig. 5.13.b. In contrast, the use of the modified model shifts the position of maximum turbulence energy further along the windward roof and reduces the maximum levels by about 25% which is consistent with the prediction of a deeper separated zone.

Attention is now turned to the Reynolds-stress model results. All the computational details discussed above apply here as well. Numerous tests were conducted using both the upwind and the linear-upwind differencing schemes with a different grids. The outcome of those tests supported the use of the upwind scheme in conjunction with a mesh of 142x110 which is also the combination used for the  $k-\epsilon$  model tests. The conditions at inlet are more detailed than before: profiles are required for all the Reynolds-stress components and not just for the turbulence kinetic energy. Those were again obtained from the boundary-layer calculation method as described in Section 5.2.

The predicted streamlines of the two Reynolds-stress model variants RSM0 and RSM1 are presented in Fig. 5.20 (a, b), respectively. Like the  $k-\epsilon$  models before, both of the present models obtain the windward-wall stagnation point to be around 50% of the eaves height from the ground. The similarity, however, ends here. The Reynolds-stress models predict significantly deeper separated zones on the windward roof and, moreover, they predict separated flow over the leeward side which is also seen in some flow visualization tests. The pressure distributions on the building walls are presented in Figs. 5.21 (a, b) where the RSM0 and RSM1 results are compared with the data and, for illustration, with the linear  $k-\epsilon$  model. On the windward and leeward walls, the Reynolds-stress model results are virtually identical and in very close correspondence with the data. Some differences are apparent but those differences are small and do not favour either model over the other. The shapes of the pressure

profiles on the windward roof are better predicted, as could have been inferred from the deeper separated zones obtained there, but the pressures on the leeward side are somewhat underestimated due, perhaps, to prediction of detached flow there. The exact position of dividing streamline cannot be determined with any certainty from the measurements and so no comparisons are possible with this parameter. The distributions of the turbulence kinetic energy predicted with the RSM0 and RSM1 models are shown in Fig. 5.22 (a, b) where it is clear that the maximum is calculated to occur some way downstream of the top front corner, with maximum the levels being well below those obtained with the linear  $k-\epsilon$  model.

In conclusion, therefore, the results obtained with RSM1 are very close to those obtained with RSM0 with the difference mainly in the size of the separated region on the leeward roof. The computational times associated with the Reynolds-stress models are approximately three times greater than for the  $k-\epsilon$  models but the results of the former are in much better agreement with the data.

There are two further aspects of the present computations of FB16 that need to be presented: the first relates the use of the 'entraining' boundary condition to reduce the overall size of the computational domain, the second to the use of the multigrid technique to reduce the computational time.

To appreciate the physical dimensions involved in the present calculations, Fig. 5.23 shows the building and the computational domain drawn to scale. The height of the domain is initially determined by the depth of the atmospheric boundary layer (300 m). Computations were first performed with the extremely coarse grid of 37x29. In a subsequent run, the depth of the solution domain was reduced to 18 m, simply by removing the top 9 nodes in the y-direction (Fig. 5.24 a). The 'entraining' boundary conditions described in Section 3.6 were next applied at the top boundary. Now if this procedure is valid then the results for the new domain should exactly match those of the old, larger, domain since the number of nodes and their distribution remained the same within the 18 m region. This was checked and found to be the case. The remaining task was to refine the grid within the 18 m region. Two further grids were used: 75x38 and 142x74 (Fig 5.24 b and c). The effects of this grid

refinement on the predicted flow streamlines are shown in Fig. 5.25. The figure shows that there is now a net outflow through the top boundary while a comparison with the streamlines presented in Fig. 5.13 shows that patterns of separated flow are identical to those obtained with the 142x110 grid but with a 25% reduction in the computing time. This reduction in computing time is not really satisfactory considering the effort involved in attaining it and for this reason very few 'entraining' boundary calculations were obtained in the course of this work.

In contrast, the performance of the multigrid method was quite impressive as can be seen from the table below. The comparison there is between the CPU times of a single-grid calculation with a 142x110 with multigrid results obtained on three grids of 37x29, 72x56 and 142x110 (Fig. 5.26).

| Grid size | Number of grid levels | CPU time required |
|-----------|-----------------------|-------------------|
| 142x110   | 1                     | 43062.8           |
| 37x29     |                       |                   |
| 72x56     | 3                     |                   |
| 142x110   |                       | 3669.09           |

Table 5.3 CPU times for the single-grid and multigrid methods (FB16)

It is clear that the multigrid method has produced an order of magnitude reduction in the total CPU time which is very welcome considering that the real time for performing a single-grid calculation for FB16 is about 15 hours on SUN SPARC station 1+ .

The convergence limits for both methods were, of course, identical: the sum of absolute residuals, normalized by the inlet fluxes, had to fall to below 0.0002 in each case. The rates of convergence of the two methods are compared in Fig. 5.27 where the average normalized residuals for the finest grid (RES) are plotted against the actual CPU time (TIME). It can be seen that, in the multigrid results, there is a discontinuity in the residuals curve each time the corrections are extrapolated to the finest grid but that this discontinuity decreases with time and eventually disappears altogether.

#### **5.4 RESULTS FOR BUILDING FB17**

Attention is now directed to consideration of building FB17 which corresponds to a single-span, plastic-clad greenhouse of semi-cylindrical cross section. The dimensions are given in Fig. 5.28. The ratio of building length to its height is 7.1 and hence two-dimensional flow conditions may be assumed to apply at the center-plane. The building is situated on a flat open field with no obstructions to the prevailing wind and the only measurements obtained are for the wall static-pressure distribution along the center-plane and for the mean velocity at ridge height (6 m/s) (Hoxey and Richardson, 1984). Some smoke visualization tests were carried out but those proved to be of limited value due to rapid smoke dispersion and chaotic behaviour attributed to wind gusts. Nevertheless, some indication of the separation point position was obtained from those tests; the point of flow separation apparently fluctuated in the range 100° - 120° (polar angle).

In the calculations, the atmospheric boundary layer was simulated in the same way as for FB16 with the ground roughness length  $y_0$  set to 10 mm. Grid-sensitivity tests were carried out on three grids, as shown in Table 5.5.

| model | grid size     | separation point (degree) |
|-------|---------------|---------------------------|
| LKE   | 55x34         | 175.0                     |
|       | 109x67        | 160.8                     |
|       | 216x123       | 159.6                     |
|       | 109x67 (LUDS) | 159.2                     |
| RSM0  | 55x34         | 176.0                     |
|       | 109x67        | 146.5                     |
|       | 216x123       | 152.0                     |
| RSM1  | 55x34         | 176.0                     |
|       | 109x67        | 145.0                     |
|       | 216x123       | 151.0                     |

Table 5.5 Grid effects on the location of separation point (FB17)

In carrying out the grid-sensitivity tests, the Upwind Differencing scheme was used and the coarsest grid doubled in both directions and then doubled again. The grid-smoothing procedure presented in Section 4.5 was used and a sample grid (216x123) is shown in Fig. 5.29. Further calculations were also performed using the Linear-Upwind Differencing Scheme (LUDS) and those produced results that were no different from the Upwind results obtained on a finer mesh. For the  $k-\epsilon$  model, the position of the separation point, which is taken to be a sensitive flow parameter, reduces, monotonically, by about 9 % as a result of the successive grid refinement. In contrast, the Reynolds-stress model exhibit a non-monotonic behaviour with the finest-grid result about 14% smaller than the coarse-grid result. This corresponds to 24 degrees of turning angle. Clearly, the correspondence between predictions and measurements is not very close with predicted position of the separation point delayed by about  $40^\circ$  when the LKE model is used and by about  $32^\circ$  when either one of the Reynolds-stress models is used. Such discrepancy is due in part to the gusty nature of the flow, as indicated by the smoke tests.

The reasons behind the earlier separation obtained with the Reynolds-stress models can be guessed from Fig. 5.30 which compares the wall skin-friction coefficient as obtained with all the models (no data are available). It is immediately clear that the  $k-\epsilon$  model is less sensitive than the RSMs in simulating the reduction in this quantity due to stabilizing streamline curvature effects. Those are associated with the development of a boundary layer on a convex surface and lead to a reduction in the level of turbulence activity and wall-shear stress. As the  $k-\epsilon$  boundary layer possesses relatively higher wall-shear stress values, it is able to withstand greater adverse pressure gradients, and progress through larger turning angles before eventually separating from the surface.

The predicted flow streamlines are shown in Fig. 5.31 (a-c). Note the emergence, in the Reynolds-stress models results, of a small counter-rotating vortex downstream of the building. This result is quite similar to that observed in the backward-facing step case and arises from the fact that a longer separated region is now obtained by those models.

The predicted and measured wall static-pressure distributions are compared in Fig. 5.32. The closest correspondence is obtained with the Reynolds-stress models. The observed underestimation of the pressure is

due to the use in the full-scale tests of permeable walls very close to the ground: air was therefore free to flow within the structure and this is the cause of the observed pressure relief on the surface. Contour plots of the static pressure across the whole field are presented in Fig. 5.33 for the  $k-\epsilon$  model and for the RSM1. Those contours show a smooth and continuous distribution of this parameter, something which was only attainable with the use of the grid-smoothing procedure.

Contours of the turbulence kinetic energy (defined as  $k/U_{ref}^2$ ), obtained by LKE, RSM0 and RSM1, are shown in Fig. 5.34 (a-c). The two Reynolds-stress models yield very similar results which is a very encouraging result for RSM1 where no wall-damping terms were present. The  $k-\epsilon$  model, in contrast, yields much higher levels of this quantity but this is to be expected since the model is not very sensitive to convex-curvature effects.

## 5.5 RESULTS FOR BUILDING G07

The target here are the measurements of Hoxey and Moran (1991) on a long, multi-span glasshouse. The geometry is shown in Fig. 5.35 which also shows the position of the pressure tappings. The roof of this building contained 52 spans and hence, for normal flow directions, the flow was expected to become cyclical after an initial development length. In the calculations, the domain extended to cover only the first 15 spans which, as will be seen below, was sufficient to obtain this cyclic behaviour.

The atmospheric boundary layer was simulated here for a mean velocity of 8 m/s at ridge height. The ground roughness length was set equal to 10 mm. It proved difficult to simulate this flow with RSM0 due mainly to difficulties in prescribing the wall-reflections function. Therefore, all Reynolds-stress model results presented here are for RSM1.

The predicted and measured wall pressure distributions are presented in Fig. 5.36 (a). The coefficient  $C_p$  becomes well established after very few spans which justifies the truncated solution domain used in the calculations. Hoxey and Moran (1991) concluded from their measurements that only the first three or four spans of this structure are subjected to a significant wind load while the remaining spans have a very small net

wind load. This is confirmed by the present predictions.

The predicted streamlines obtained with the modified  $k-\epsilon$  and RSM1 are compared in Fig. 5.37 (a, b) and the corresponding turbulence kinetic energy are presented in Fig. 5.38.

Further computations were carried out using the multigrid method. Three grids were used: 63x29, 124x56 and 246x110 (see Fig. 5.39 a-c). The convergence characteristics are compared with those for the single grid in Fig. 5.40. In this flow, the computational effort involved with the multigrid method is 8.14 times less than that for the single-grid, as can be seen from Table 5.3.

| Grid size      | Number of grid levels | CPU time required |
|----------------|-----------------------|-------------------|
| <b>246x110</b> | <b>1</b>              | <b>56703.9</b>    |
| <b>63x29</b>   |                       |                   |
| <b>124x56</b>  | <b>3</b>              | <b>6962.59</b>    |
| <b>246x110</b> |                       |                   |

Table 5.3 CPU times for the single-grid and multigrid methods (G07)

Note that, in this flow, the reduction in CPU time is rather less than that obtained for FB16. This is probably due to the fact that the first grid-level employed is not really very coarse as many cells are needed to resolve the complex roof geometry. Nevertheless, the method is clearly suited for use for parametric studies, which is the subject treated next.

## 5.6 PARAMETRIC STUDIES

Having determined the performance of the predictive method by comparisons with field data, the task now is to exercise the method to determine, computationally, the consequences of changes to some geometric parameters. In this section, we investigate the effects on the averaged pressure loads of changes in the building's height and width, the shape of the eaves

(sharp or curved) and, finally, the consequences of placing a windbreak ahead of the building. The difficulties in designing experiments to study those effects in isolation are discussed in Hoxey, Robertson, Basara and Younis (1992). In all the calculations presented below, the extended  $k-\epsilon$  model (EKE) was used in conjunction with the multigrid method. The use of the  $k-\epsilon$  model is justified by the fact that the interest in parametric studies is confined to the relative changes in a particular parameter, rather than in its absolute value. Moreover, the computed wall-pressure values were averaged over the entire surface and hence any refined modelling of this quantity would seem unnecessary.

### 5.6.1 Effects of geometry

The purpose of the following computations is to provide information on the effects of varying the building's height and width, independently, on the averaged pressure loads. The reference building used in those tests is FB16 with the roof pitch always fixed at 15 degrees. The atmospheric boundary layer was simulated as before (Section 5.4) and the finest grid in the multigrid scheme was 142x110.

To investigate the influence of the building's height, four different heights were computed, with eaves heights set to 3m, 4.5m (FB16), 5.5m and 7m. The grids used are shown in Fig. 5.41 a-d. The predicted streamlines for each case are shown in Fig. 5.42 a-d. As expected, the size of the vortex generated on the windward wall increases with the building's height though the ratio of the reattachment length to building height appears to remain sensibly constant. There is also a separated region on the windward side of the roof and, again, its size increases with building's height till a point is reached when the flow over the entire roof becomes detached. Turning now to consideration of the averaged pressure coefficient (i.e. the quantity that enters in the Code of Practice calculations), the variation of this quantity with the building's height is shown in Fig. 5.43. In Fig. 5.43 a, the windward wall results are plotted and those are clearly insensitive to changes in height. For the roof, Fig. 5.43 b, again little variation is observed with the values being different by no more than 10% . The largest differences occur on the leeward side (Fig 5.43

c) where it is seen that changing the building's height by 60% leads to changes of the same order in the averaged pressures.

Assessing the effects of changing the building's width was by carrying out computations for four different widths: 5m, 6.7m (FB16), 8.6m, 10m. The grids are shown in Fig. 5.44. The computed streamlines (Fig. 5.45) show a largely unaffected flow upstream of the buildings and on the roofs except, perhaps, for the narrowest case where a larger portion of the roof flow is separated. The averaged pressure coefficients (Fig. 5.46) are largely insensitive to the width except on the leeward wall where a 100% increase in width is seen to cause a reduction of about 25% in the averaged pressure.

### 5.6.2 Effects of eaves shapes

Curved eaves are sometimes used on buildings both for aesthetic reasons as well as to reduce the overall pressure loading. Computations were therefore carried out to study the effects of eaves shapes. Those were performed for the Silsoe building FB28, shown in Fig. 5.47 a, for which full-scale measurements are available for both sharp and curved eaves (radius 0.635 m). The grids used were the same for both types and consisted of 168x110 nodes distributed as shown in Fig. 5.47 (b, c). The grid for the curved eaves was smoothed as already described.

The predicted streamlines are shown in Fig. 5.48 (a, b). those show patterns that are generally in line with the smoke observation shown in Fig. 5.49 (see, also, Fig. 5.7). The flow was attached around the curved eaves and detached from the sharp eaves, as can be seen from the enlarged sections shown in Fig. 5.50 (a, b). The pressure coefficients (for the mid-length line of the roof) are presented in Fig. 5.51. Those show that the curved eaves may be of benefit on the windward side of the roof where the pressures (vacuum) are about 40% smaller than for the sharp eaves. On the leeward side, the curved eaves produced pressure that are 16% greater than for the sharp eaves. Those results are in good agreement with the full-scale measurements of Robertson (1989).

In conclusion, then, the curved eaves reduce the overall loading but may

actually increase it for some region. The peak levels are, however, lower than for the sharp eaves case.

### 5.6.3 Effects of windbreaks

Windbreaks are permeable walls placed upstream of low-rise buildings in open fields for the purpose of reducing the wind loads on those buildings. There are three important parameters to consider when using a windbreak: its permeability (defined as the ratio of open to total frontal area) and its position and size relative to the building. Various computational and wind-tunnel studies were carried out to quantify the effects of permeability (e.g. Wilson, 1985, Raine and Stevenson, 1977 and Hagen, Skidmore, Miller and Kipp, 1981) and those seem to show that optimum pressure-reduction performance can be attained when the windbreak permeability is in the range 0.3 - 0.5. The purpose of this part of the work was to investigate the geometric parameters affecting the performance of the windbreak in isolation of permeability effects. For this reason, all the computations presented here were obtained with solid walls. The effects of permeability can be included simply by adding to the streamwise momentum equation some drag-related term which will contain an empirical coefficient whose value can only be deduced from experiments.

All the computations reported here were obtained with the multigrid method utilizing three grid levels, the finest being 142x110. The inlet boundary conditions were specified with the Reynolds-stress models calculations and the roughness length  $y_0$  was set to 10 mm. The extended k- $\epsilon$  (EKE) model was used.

All computations were performed for building FB16. The geometry is defined in Fig. 5.52 a and the computed streamlines corresponding to a windbreak of height  $H = 2.18$  m placed at distance  $X = 5$  m are shown in Fig. 5.52 b. For this arrangement, the presence of the windbreak generates a large region of reversed flow downstream of it. The flow does not reattach before reaching the windward wall and this is seen to reduce the size of the separated flow region on the roof. The averaged wall-pressure coefficients are the parameters of interest in this applica-

tion and the variation of these with the position of the windbreak relative to the building is shown in Fig. 5.53 (a-c). Plotted there are results for two different windbreak heights: 1.42 and 2.18 m (respectively 0.3 and 0.6 eaves height). The experimental values for FB16 (obtained without windbreaks) are also shown for reference. As expected, the pressure on the windward wall turns out to be the most affected by the presence of the windbreak. Note that the pressures on all walls asymptote to their reference levels but the rate at which this takes place varies from one wall to the other. For the leeward wall, the pressure recovery is fastest and is completed when the windbreak is placed at a distance of 30 m or more from the building. In contrast, on the windward side, the pressure remains affected by the windbreaks till the latter are at 200 m or more from the wall. With the windbreaks located so far away from the building, the disturbed flow relaxes to a new equilibrium and the effects of the disturbance are completely forgotten. In all cases, there is an optimum location for placing the windbreak to achieve maximum pressure reduction and the present results suggest that this location is almost independent of the windbreak height.

## 5.7 SIMULATION OF PEAK LOADS

The random nature of the wind mean velocity causes the pressures acting on a building to be unsteady and randomly behaved. Examples of typical recordings of wind mean velocity and pressure at a point on the roof of a house are shown in Fig. 5.54. Those plots are taken from the 1991 Code of Practice and clearly show the peak pressure value to be many times greater than the mean value. Clearly, knowledge of those peak values is essential to the safe design of buildings.

There are many proposals in the literature for taking into account the effects of the pressure peaks. A widely used one is that of Whitbread (1980) :

$$\Delta p = (C_p + g C_{prms}) q \quad (5.13)$$

where  $g$  is a 'peak factor' and  $C_{prms}$  is the standard deviation of the peak pressures from the mean which is normally obtained from wind-tunnel tests. This quantity turns out to be very sensitive to the state of the approach boundary layer such that, often, wind-tunnels tests are not repeatable and are quite different from the full-scale results. The aim of this part of the work was to investigate how best to predict the unsteady effects (e.g. peak pressure coefficients, rms values and load spectra) by using conventional turbulence modelling technique.

In all the calculations reported so far, a steady-state method was used to obtain pressure coefficients that did not vary with the time. The first step, therefore, for obtaining peak and rms loads is to extend the solution method to handle the unsteady forms of the governing equations. An additional term  $\partial\Phi/\partial t$  is now present and this is handled here by direct integration, viz.

$$\int_V \frac{\partial \rho \Phi}{\partial t} dV = (\Phi^n - \Phi^o) \frac{\rho \delta V}{\delta t} \quad (5.14)$$

where superscripts  $o$  and  $n$  refer to values of variable  $\Phi$  at the old and the new time levels respectively. The 'old' part of the integrated term is moved to the right-hand-side of the appropriate difference equation where it is then treated as a source of the quantity  $\Phi$ :

$$S_\Phi = S_\Phi^{\text{steady}} + \frac{\rho \delta V}{\delta t} \Phi_P^o \quad (5.15)$$

The 'new' part of the integrated term is retained on the left-hand-side of the difference equation which now becomes:

$$\left( \sum_{nb} A_{nb} + S''_\Phi + \frac{\rho \delta V}{\delta t} \right) \Phi_P^n \quad (5.16)$$

The remaining terms in the equation are treated fully implicitly, i.e. evaluated with reference to their new time-level value. The fully-implicit scheme has the advantage of being stable for large time steps but is only first-order accurate. A number of iterations were conducted at each time step till the normalized residuals fell below a prespecified level. All other

aspects of the steady-state approach (e.g. boundary conditions, pressure-velocity coupling etc.) remained unchanged.

The results of the first time-dependent simulations obtained for FB16 were very disappointing. Thus starting from the same boundary conditions as before and marching in time from there, the predicted pressure coefficient varied at first with time but eventually settled on a steady-state value. The drag coefficient  $C_d$  is plotted in Fig. 5.55 and the corresponding flow streamlines are shown in Fig. 5.56 for a number of time steps. In fact, the streamlines predicted by the unsteady simulations after a sufficiently long period of time were identical to those obtained iteratively by the steady-state method after convergence has been attained. The mechanism underlying the unsteady nature of the observed pressure loading on real buildings is therefore not necessarily due to the shapes of those buildings but to some other agency not accounted for in the simulations.

It was eventually concluded that the unsteady pressure loading is a consequence of the properties of the approach flow. This was not immediately obvious from the start since it is sometimes the case that unsteady loading occurs in conditions of uniform and steady approach flow (e.g. vortex shedding from a bluff body). The task now was to incorporate this into the calculation method.

Examination of a typical instantaneous velocity record (Fig. 5.54) shows that this quantity fluctuated randomly around the mean value. This can be reflected in the calculations by imposing random fluctuations on the profiles of the atmospheric boundary layer that are predicted with the Reynolds-stress model. To achieve this, a routine for generating random numbers was adapted and used to perturb the velocity profile by a certain amount within a pre-specified maximum limit. Fig. 5.57 shows a typical result for a velocity at a certain point randomly perturbed by 15%, 10%, 5% and 1% of its mean level. The turbulence quantities were simply scaled from their steady-state values.

With this modification to the inlet profiles, the computed variation of the pressure coefficient with time no longer tends to a steady-state level but fluctuates, randomly, in response to the changing input. This can be seen from Fig. 5.58 where the roof values are plotted. It is immediately clear that the method now predicts peak values that are about five

times greater than the apparent average value. The perturbation time interval specified for those predictions, i.e. the time interval over which the variables were perturbed around their steady-state values, was set equal to one second, shorter than the 3-15 second interval recommended in the Code of Practice for gust measurements. The time-step size for advancing the solution from the old time level to the new one was 0.01 (corresponding to non-dimensionalized time  $U_\infty \delta t / H$ ).

A further refinement to this technique was introduced: it involved using the full-scale measurements of wind velocity with time to perturb the inlet flow instead of the random number generator. An example of the measured velocity signal is shown in Fig. 5.59 (Hoxey, 1992, private communication). The consequences on the calculated results of using the measured velocity signal can be seen from Fig. 5.60 for the roof pressure coefficient and in Fig. 5.61 which shows the spectrum of the pressure signal. It is very encouraging to note that, now, the calculated peaks exceed the mean value by a factor of about twenty which is of the same order as the value observed in some field measurements (Hoxey, 1992, private communication).

## 5.8 CLOSURE

This chapter presented the main results of this thesis by way of comparisons between the numerical method and turbulence models described in Chapters 2 and 3 and data from many full-scale experiments conducted on buildings in open fields.

It was first found that the computations were very sensitive to the assumed distribution of velocity and turbulence in the approach atmospheric boundary layer. A Reynolds-stress model was then used, in conjunction with a boundary-layer method, to obtain this inlet boundary layer from knowledge of the velocity at a given, reference, height and an assumed boundary-layer width. The terrain roughness was also an input to those simulations. The results obtained here, namely profiles of rough boundary layers in equilibrium, proved far preferable to those obtained from empirical prescriptions.

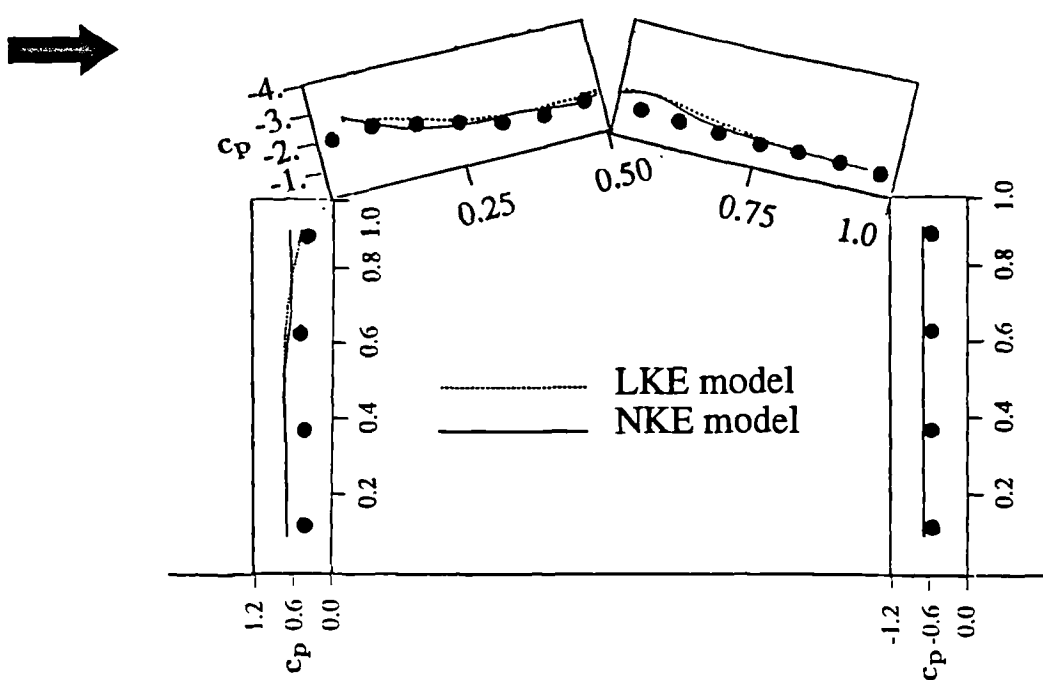
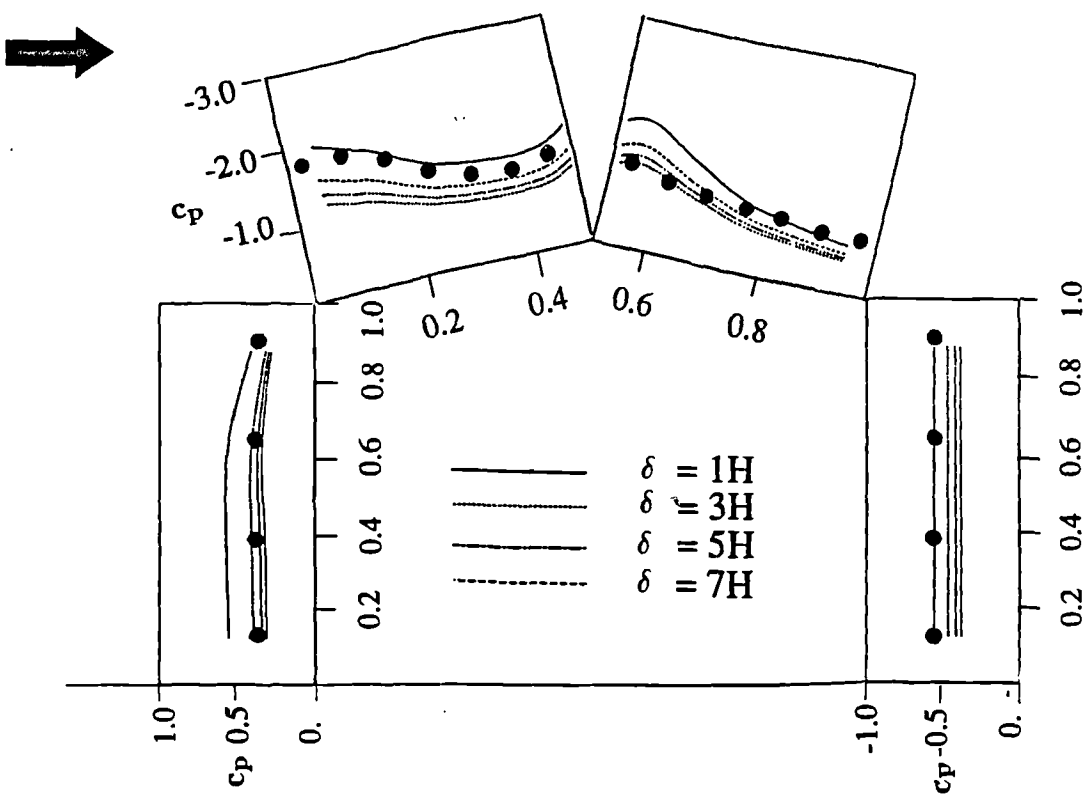
Comparisons were then obtained for the different variants of the  $k-\epsilon$  model and for the two Reynolds-stress model formulations. Those showed that the standard  $k-\epsilon$  model fails fairly badly for full-scale buildings and is not therefore recommended for practical use. In particular, it obtained a separated zone on the windward side that was much smaller than measured. The pressure distribution predicted with this model was at variance with the data on the windward side of the roof. The results of the non-linear  $k-\epsilon$  model were less conclusive. The model generally faired better than its linear counterpart but still produced incorrect roof pressure distributions. By far the best performance from the  $k-\epsilon$  model variants was obtained from the version extended to magnify the contribution to the  $\epsilon$ -sources of production. This has lead to the prediction of a small but significant region of separated flow on the windward side of the roof which, in turn, lead to much improved prediction of the wall static-pressure distribution.

As for the Reynolds-stress models, it has generally been found that the two versions tested yielded solutions that were quite similar. This argues very strongly in favour of RSM1 which does not require a 'wall-reflections' term in its formulation. The comparisons with the measurements were quite good for FB16 and G07 but the computed surface pressures tended to underestimate the measured values on FB17. As mentioned earlier, this underprediction may well have been due to the pressure relief obtained in the full-scale tests as a result of the permeability of the lower parts of the structure.

The performance of the numerical part of the method has been satisfactory. The use of grid-smoothing greatly assisted the attainment of smooth and continuous pressure field around the building and on its surface. The multigrid method yielded a consistent one order of magnitude reduction in total CPU time compared to the single-grid results.

This chapter also included some illustration of what can be achieved using a well validated predictive procedure. In particular, the consequences of using a windbreak to shield an existing structure were quantified in terms of the optimum height and position of the windbreak. Also, a parametric study was conducted to demonstrate the consequences on the averaged wall pressure values of altering the building's height and width in isolation.

Finally, a novel method for accounting for the peak loads within the context of a conventional turbulence-modelling approach was presented. The method was shown to produce results that are qualitatively in accord with full-scale measurements though the lack of any quantitative data prevented a more detailed verification. The way for simulating this type of loading has, nevertheless, been demonstrated very clearly.



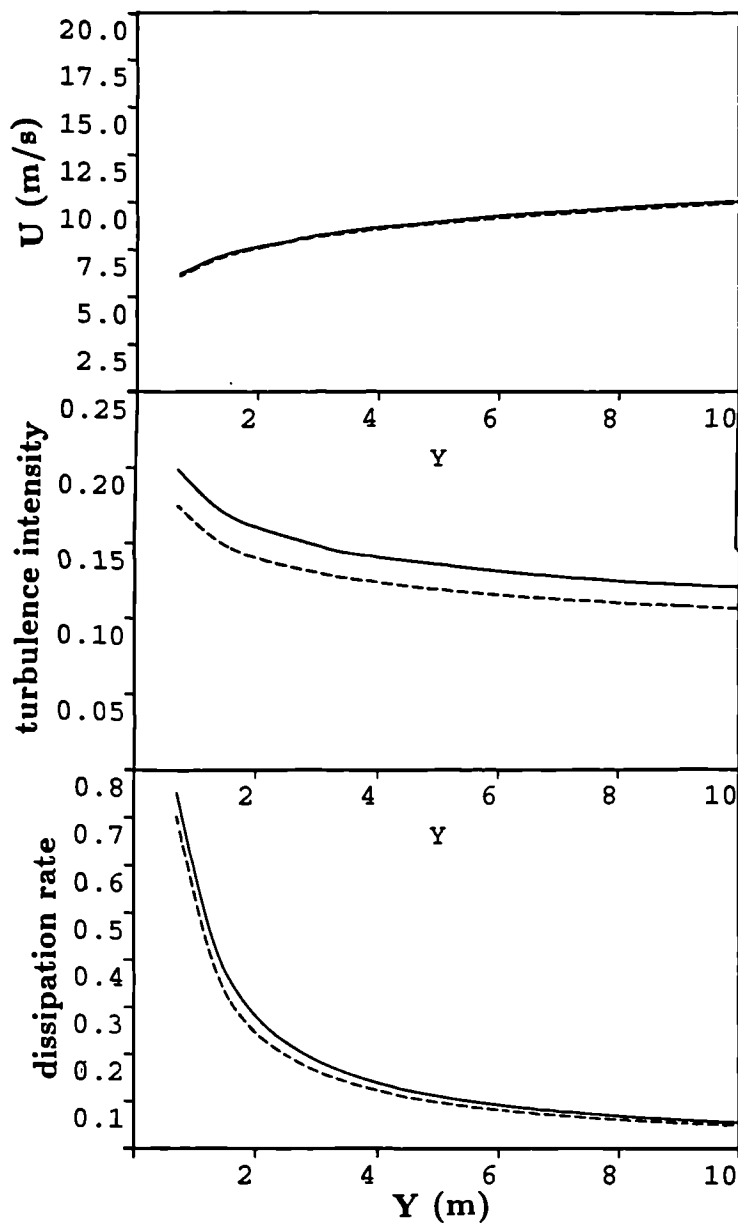


**Fig. 5.5** The streamwise velocity, turbulence intensity and dissipation rate profiles as obtained by the Harris and Deaves correlations and by the Reynolds-stress model.

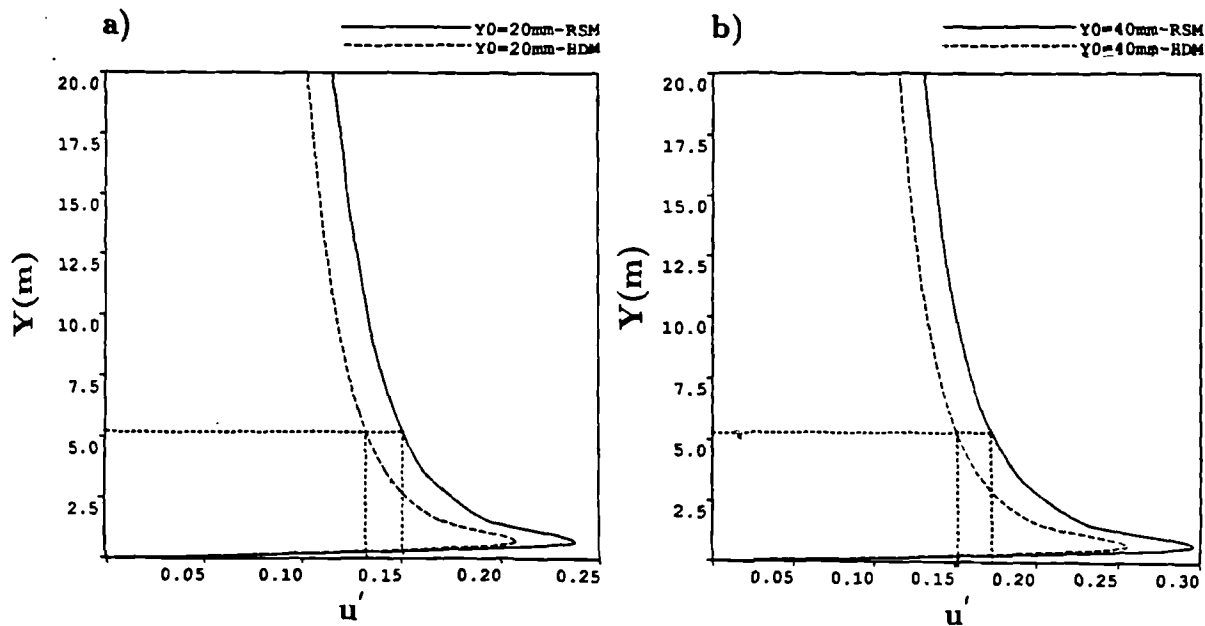


**Fig. 5.6** Turbulence intensity profiles as obtained by the Harris and Deaves correlations and by the Reynolds-stress model.  
Roughness (a)  $y_0 = 20\text{mm}$  and (b)  $y_0 = 40\text{mm}$ .

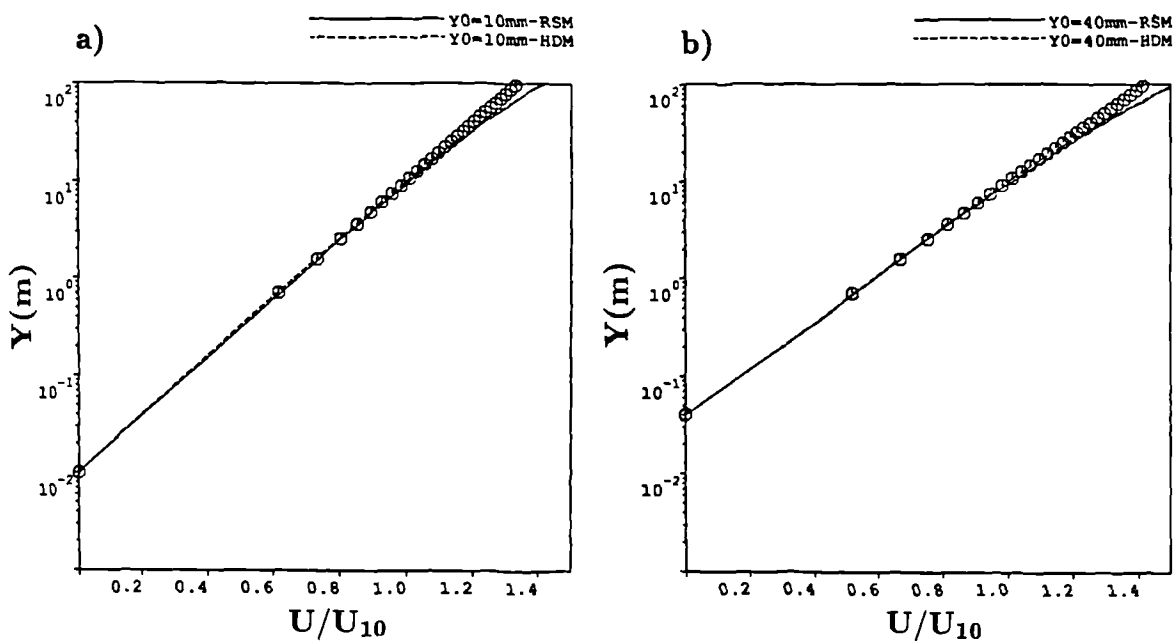


**Fig. 5.7** Measured and predicted velocity profile by the Harris and Deaves correlations and by Reynolds-stress model. Roughness (a)  $y_0 = 10\text{mm}$  and (b)  $y_0 = 40\text{mm}$ .

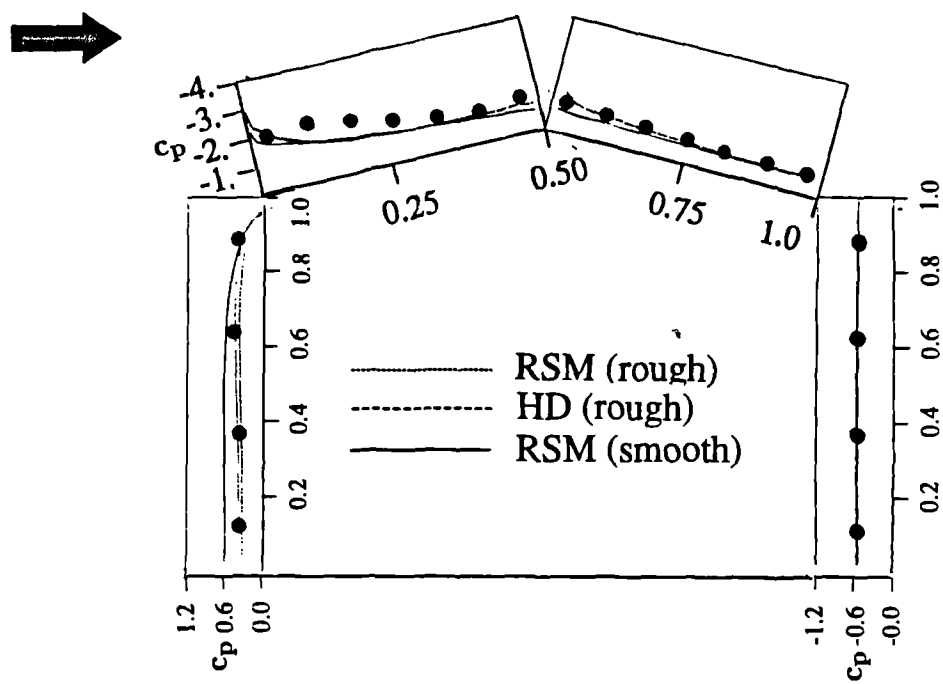


**Fig. 5.8 Predicted wall static pressure coefficient for the inlet profiles obtained by Harris and Deaves correlations and by the Reynolds-stress model.**

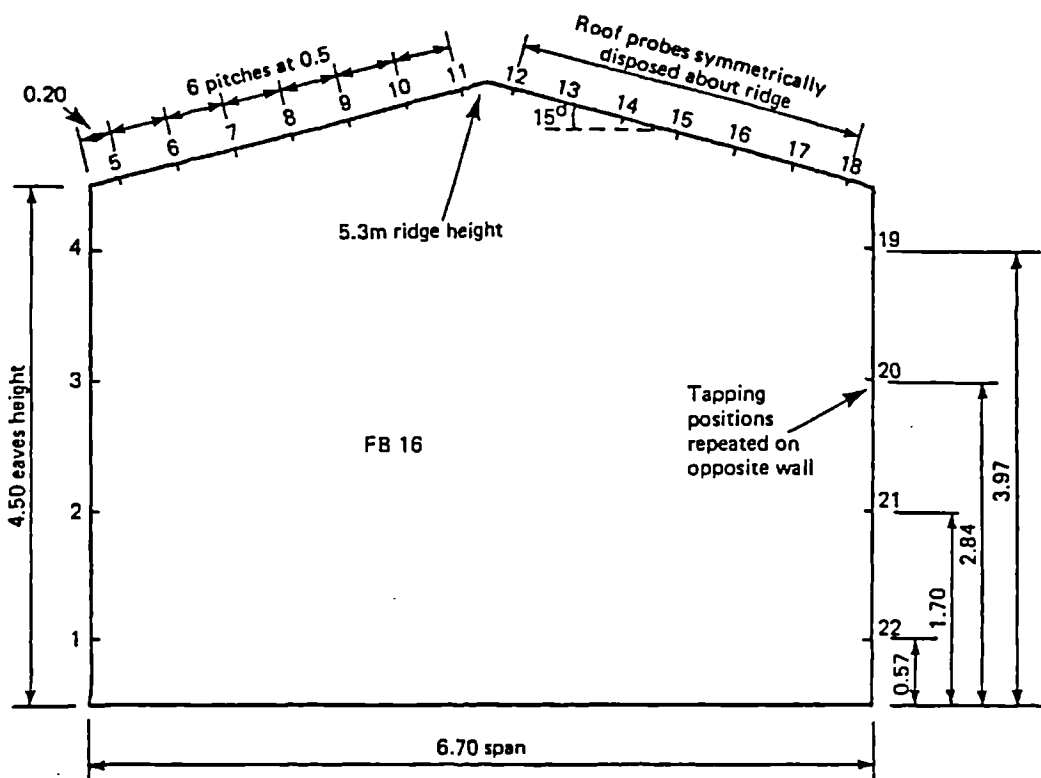


Fig. 5.9 Dimensions of the building FB16 (From Richards, 1989).

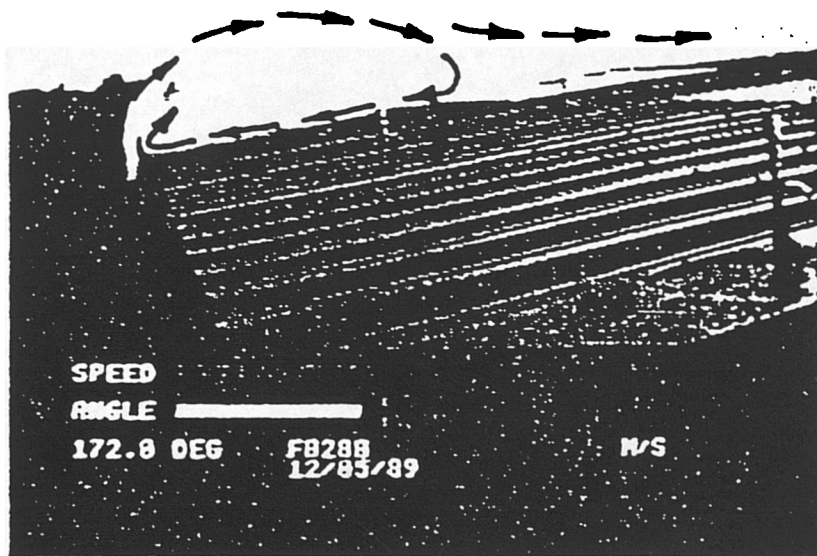
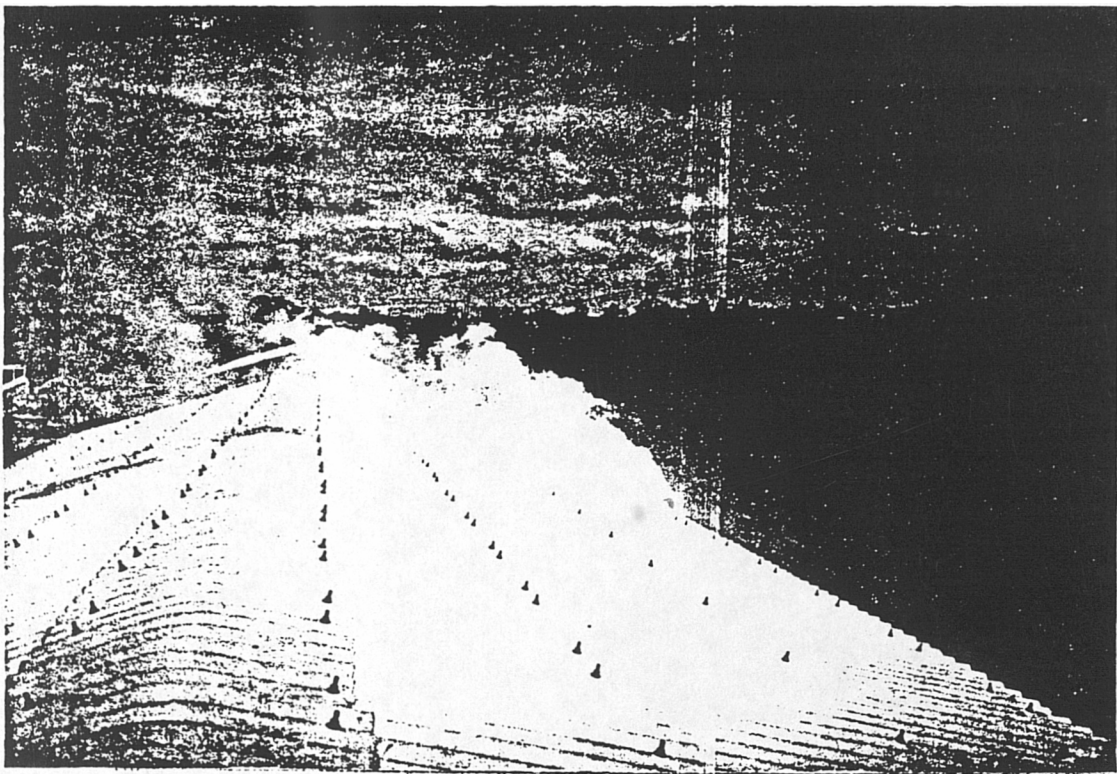
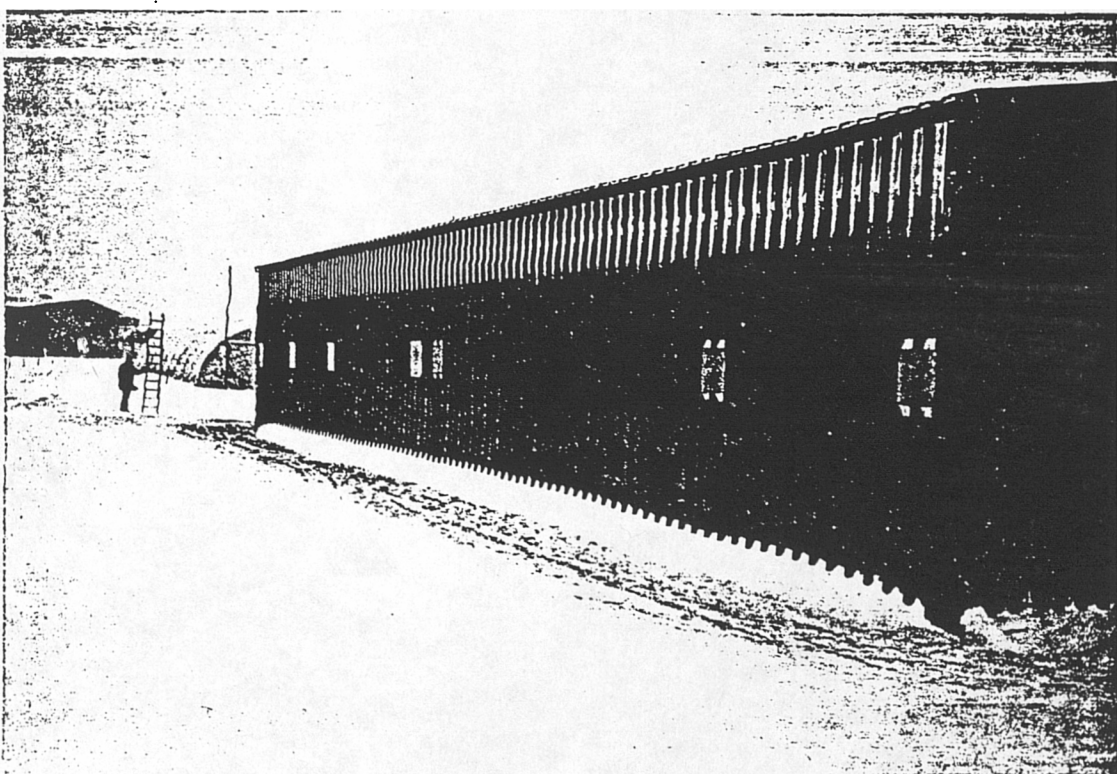


Fig. 5.10 Flow visualization on roof of FB16 (From Richards, 1989).

a)



b)



**Fig. 5.11 Smoke observations on the roof of the building (a) and snow tracks in front of the building (b).**

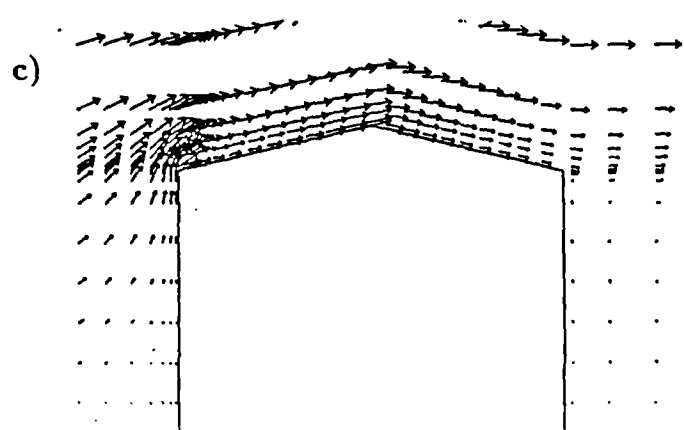
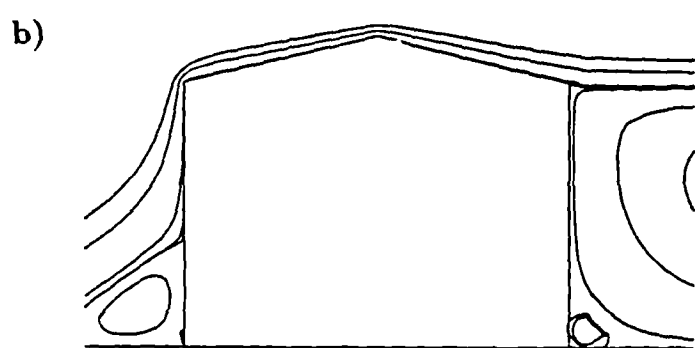
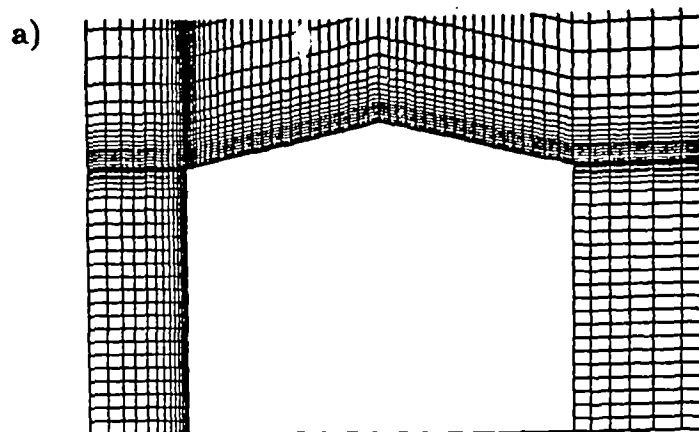


Fig. 5.12 FB16. a: Grid 108x100, b: predicted stream lines, c: velocity vectors (LKE).

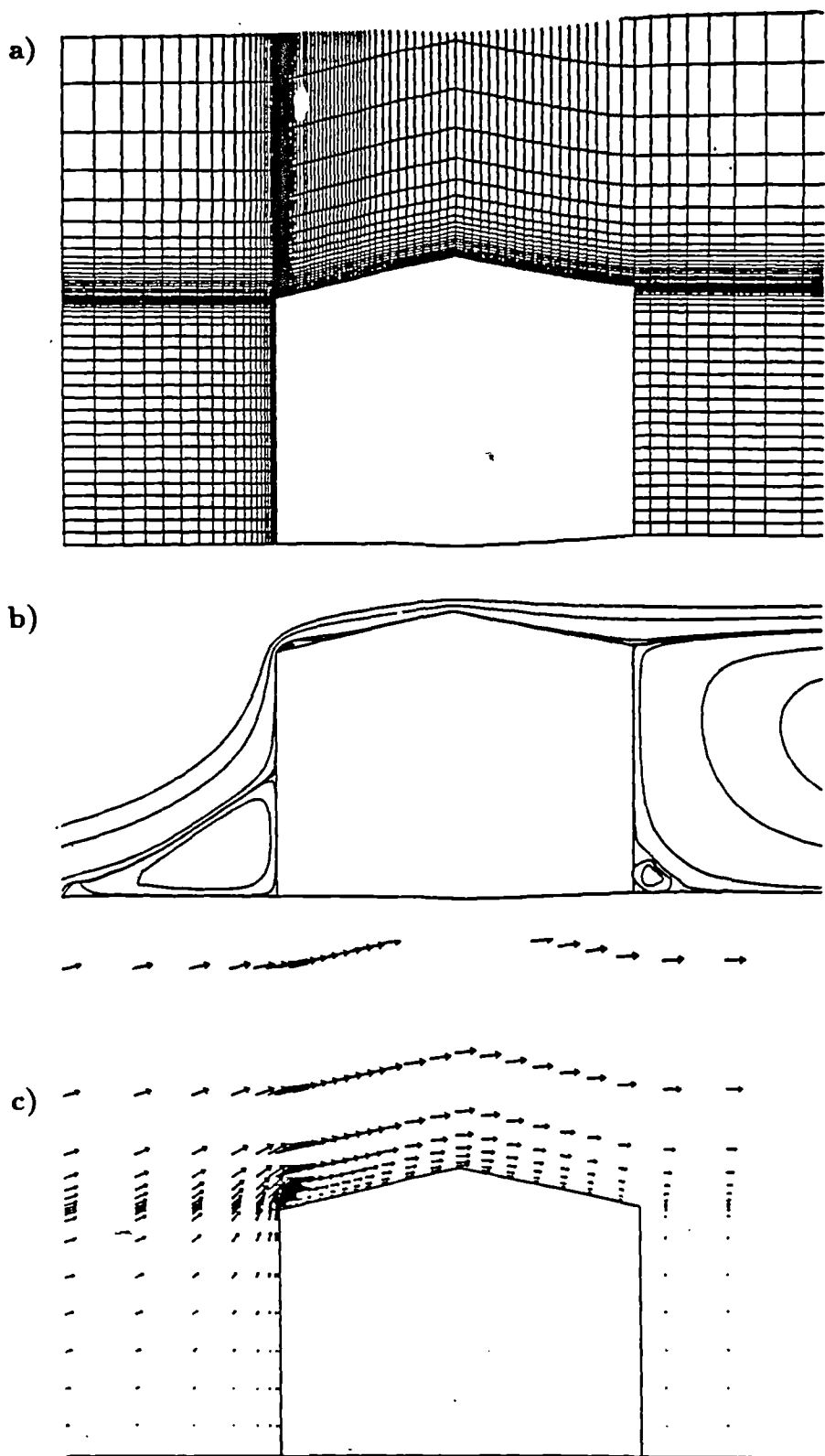


Fig. 5.13 FB16. a: Grid 142x110, b: predicted stream lines, c: velocity vectors (LKE).

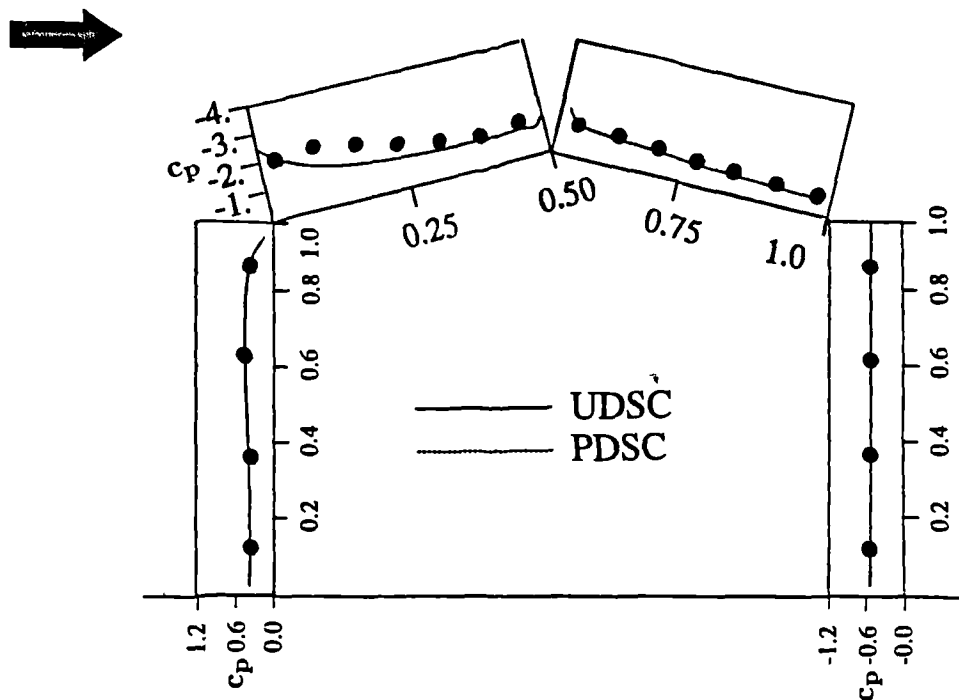
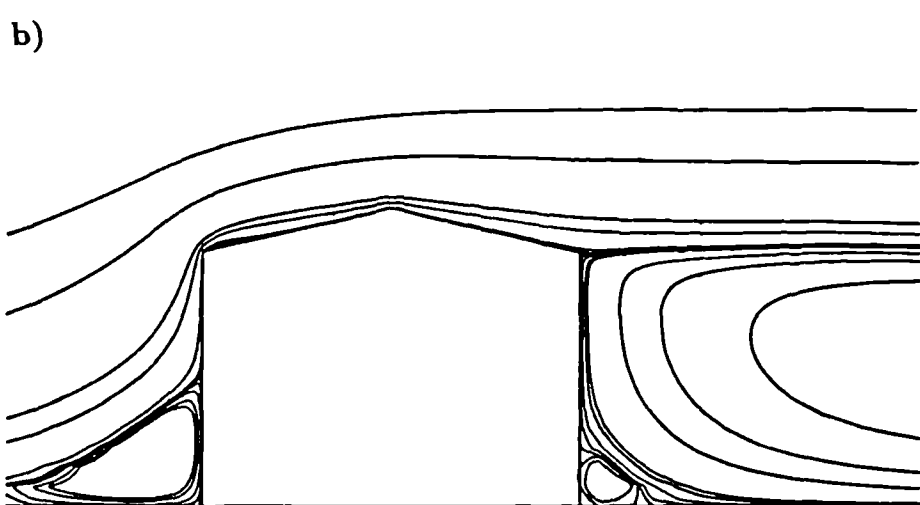
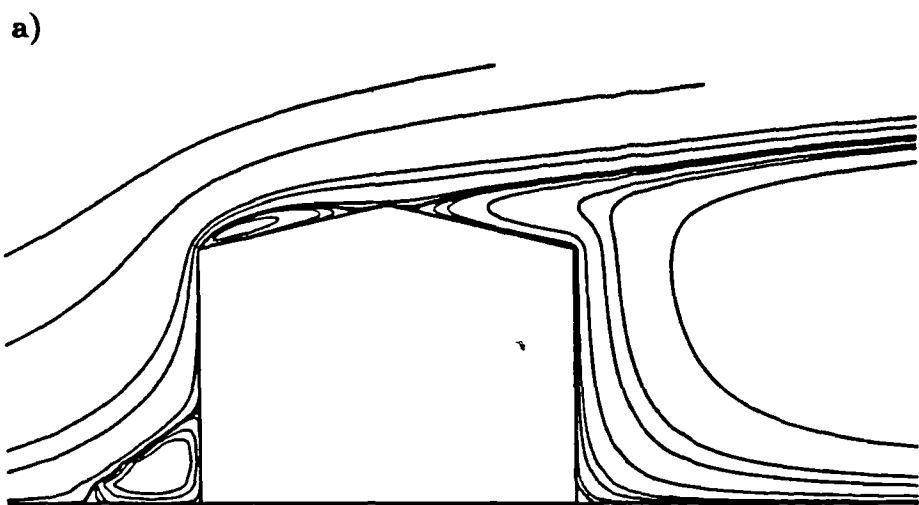


Fig. 5.14 FB16. Distribution of wall pressure coefficient obtained with the upwind and the power-law differencing schemes.



**Fig. 5.15 FB16.** Predicted streamlines for roughness lengths  $y_0 = 0$  (a) and for  $y_0 = 40\text{mm}$  (b).

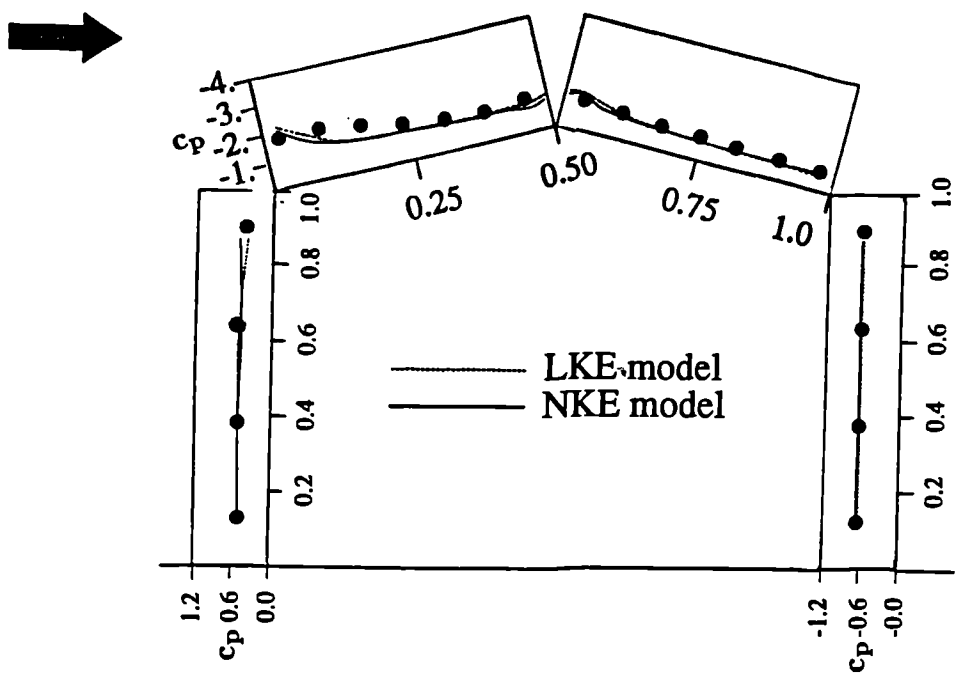


Fig. 5.16 FB16. LKE and NKE results for wall static-pressure distribution.

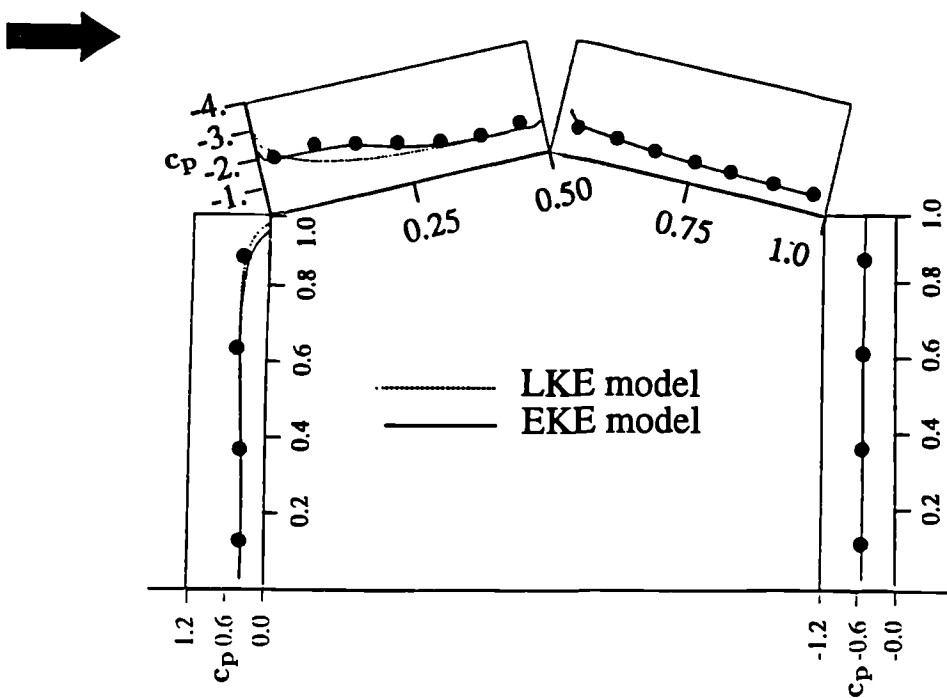
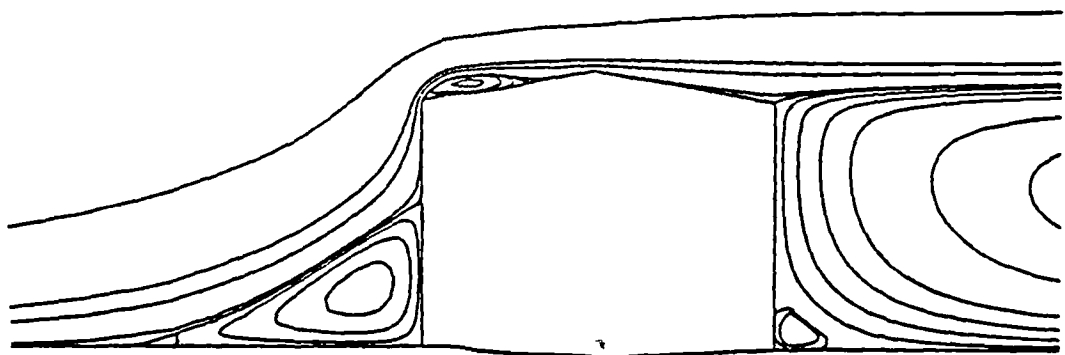


Fig. 5.17 FB16. Distribution of wall pressure coefficient predicted by LKE and EKE.

a)



b)

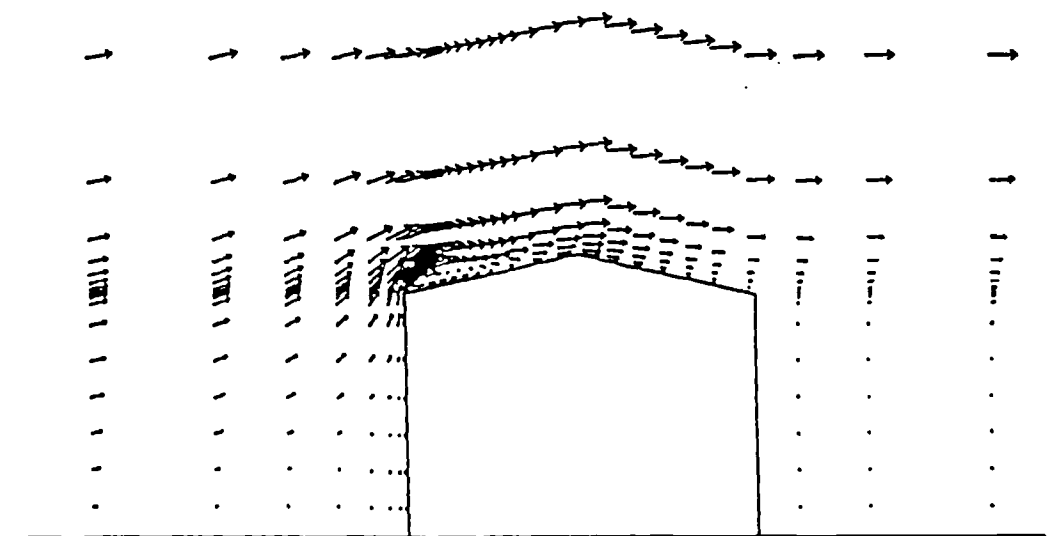


Fig. 5.18 FB16. EKE results for streamlines (a) and velocity vectors (b).

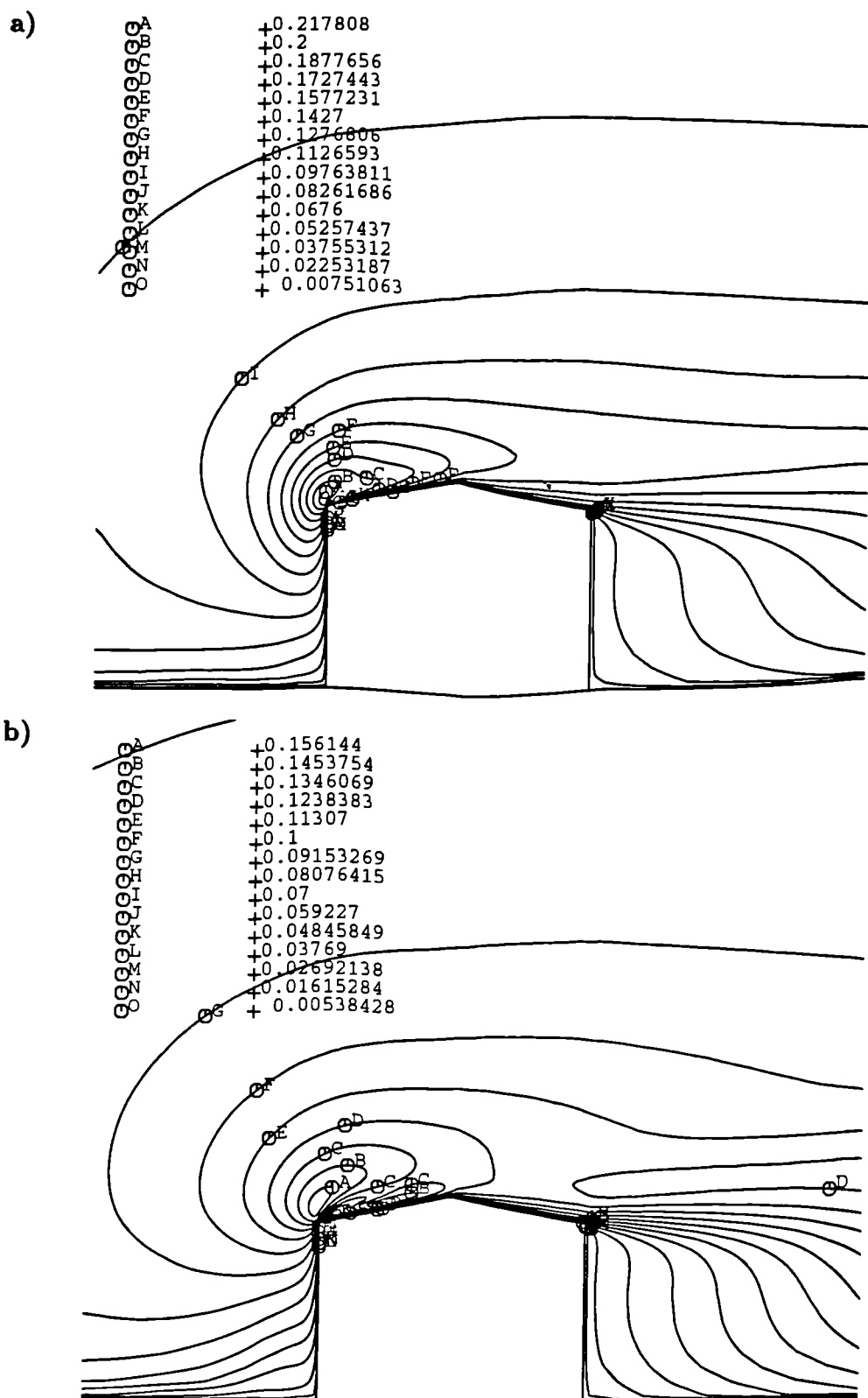
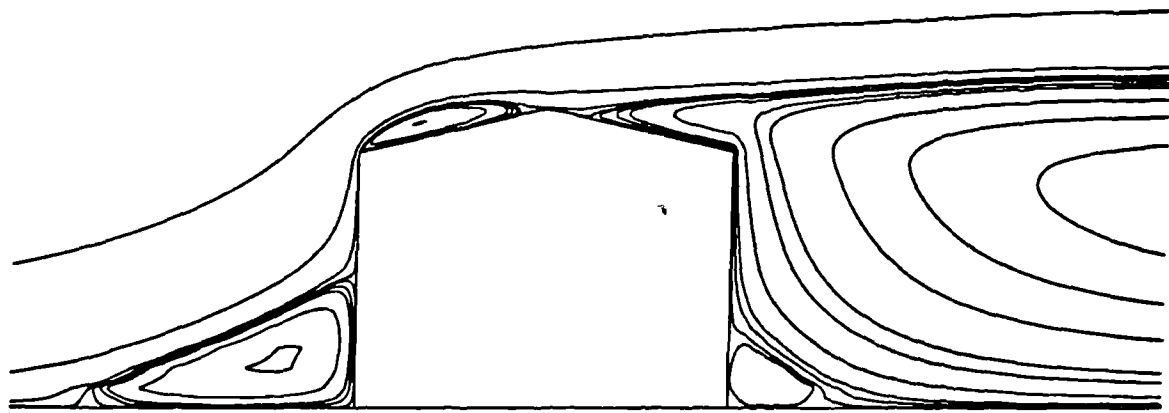


Fig. 5.19 FB16. Turbulence kinetic energy contours as obtained by LKE (a) and EKE (b).

a)



b)

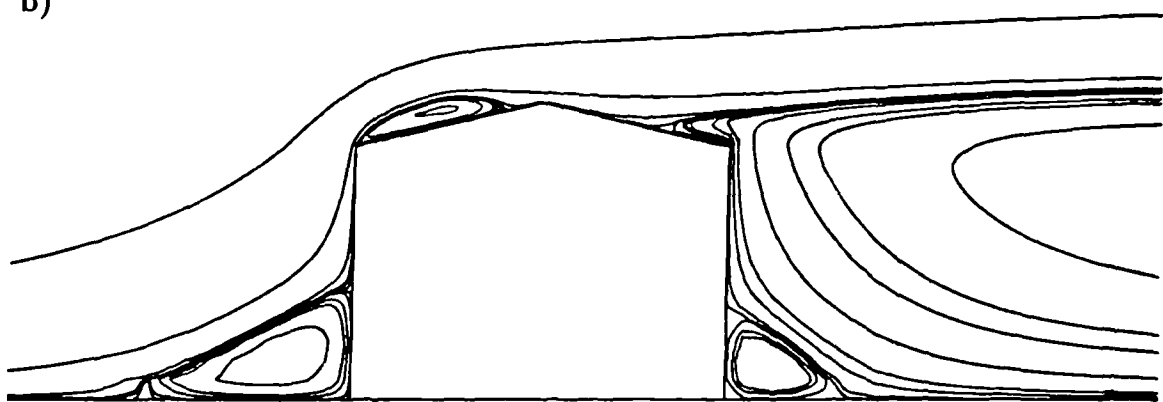


Fig. 5.20 FB16. Predicted streamlines by RSM0 (a) and RSM1 (b).

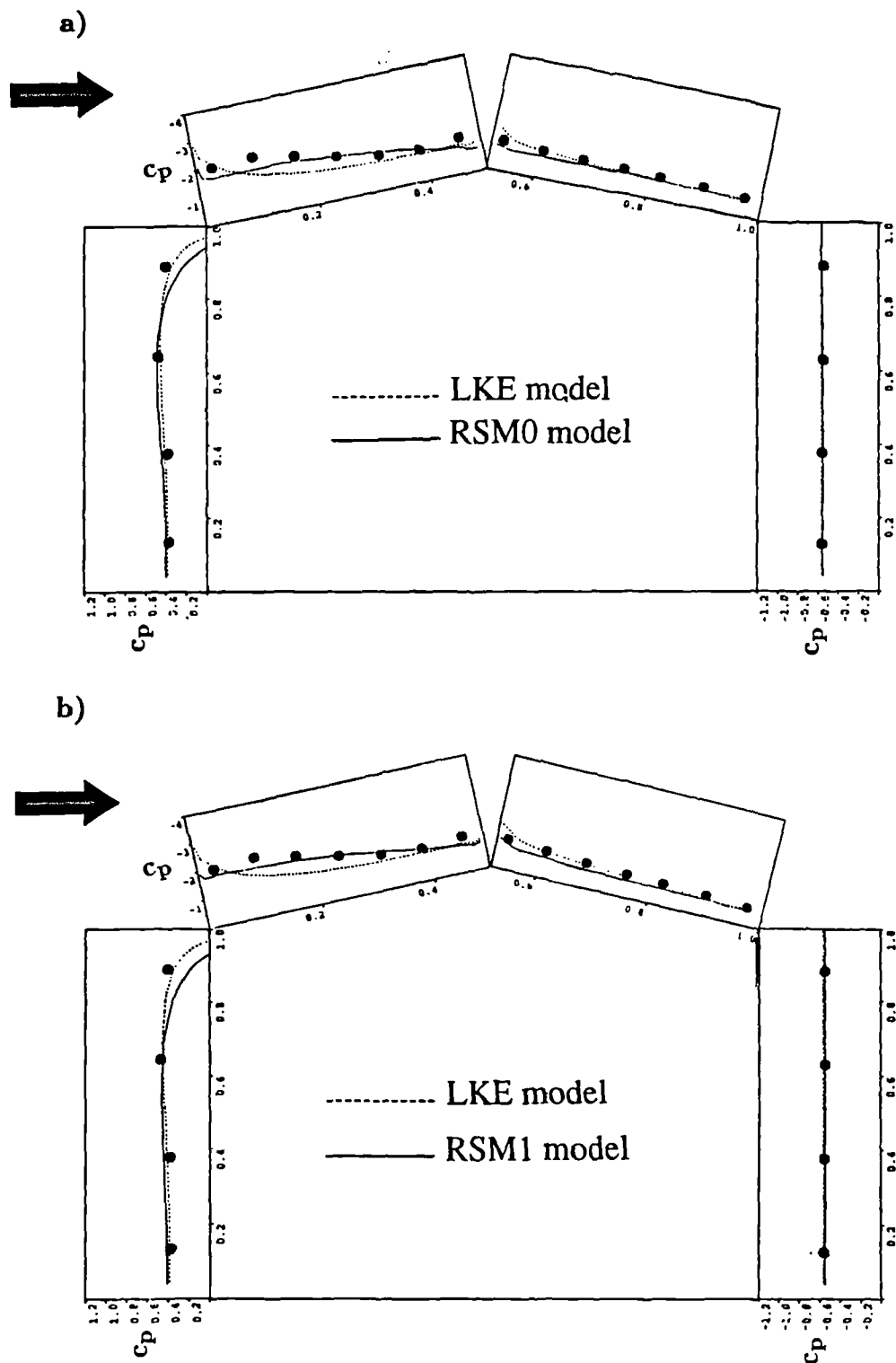
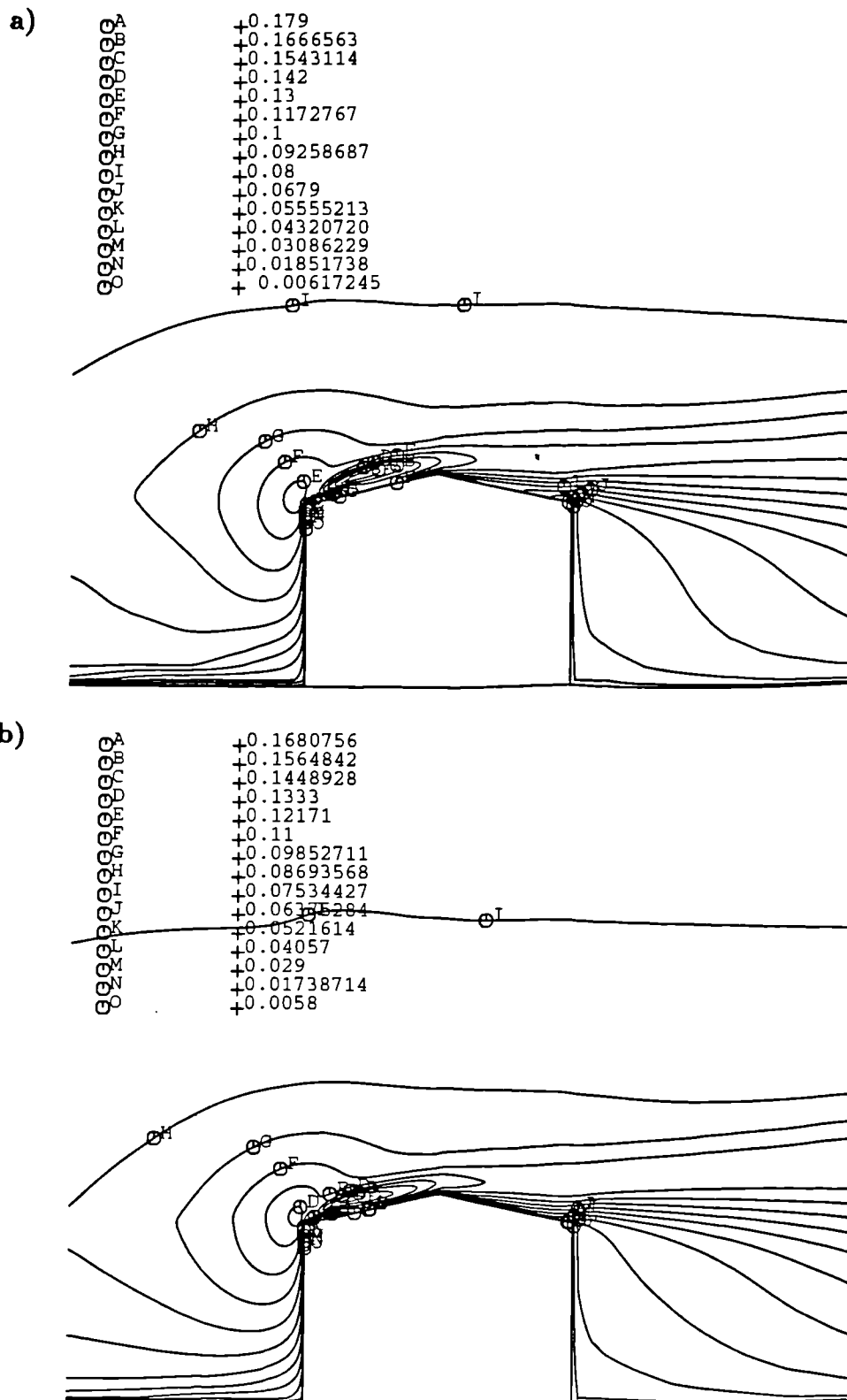
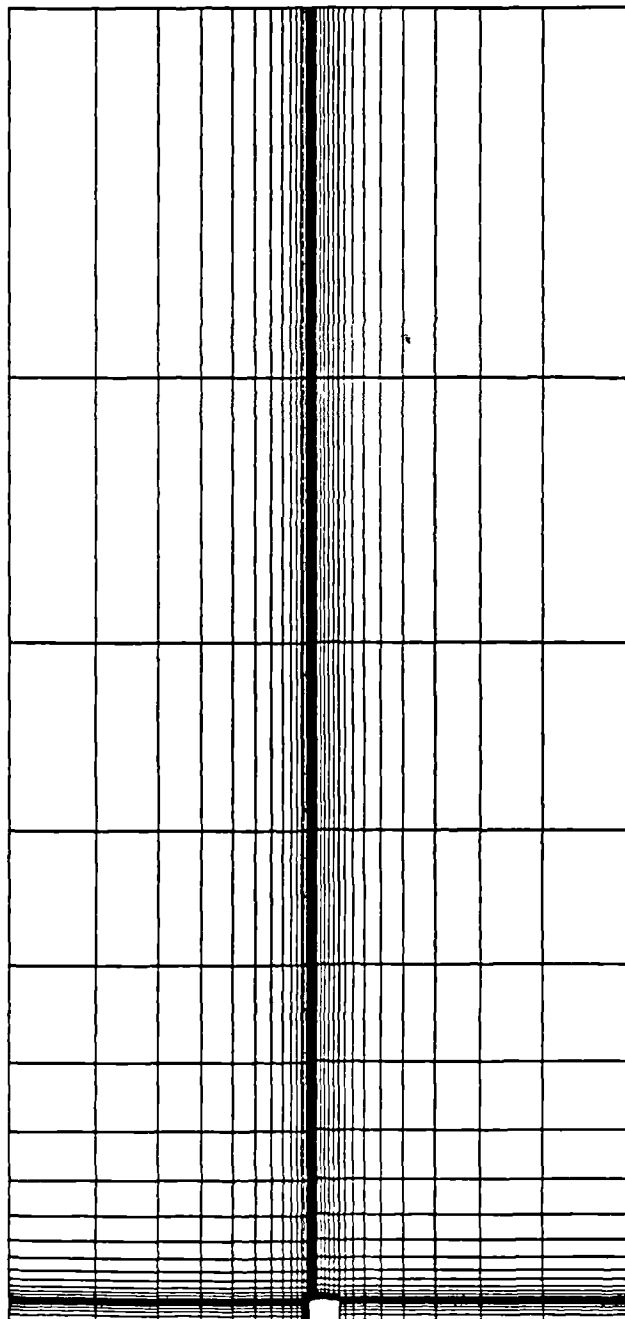


Fig. 5.21 FB16. Distribution of wall pressure coefficient predicted by LKE, RSM0 (a), and RSM1 (b).

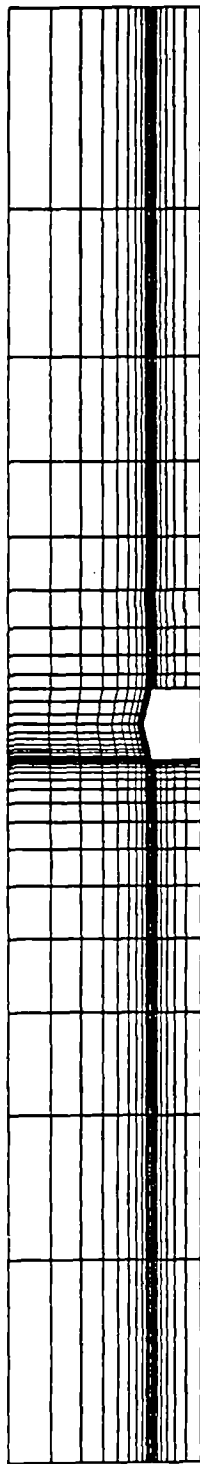


**Fig. 5.22 FB16. Predicted turbulence kinetic energy by RSM0 and RSM1.**

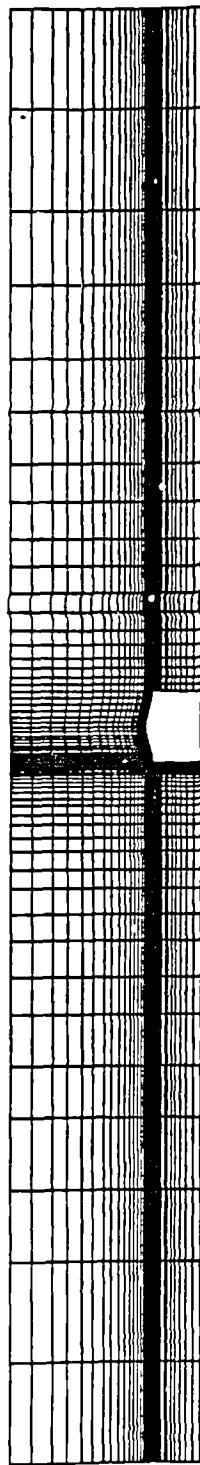


**Fig. 5.23 FB16. Computational domain (height = 300m) covered with grid 38x29.**

a)



b)



c)

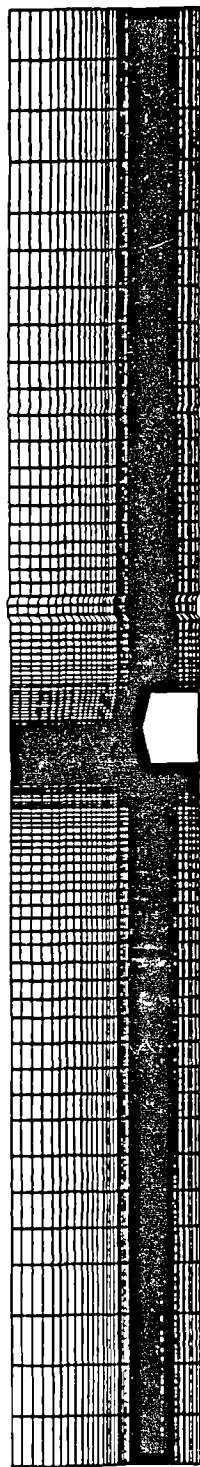


Fig. 5.24 "New" domain (height = 15m) covered with the grids  
37x20 (a), 75x38 (b) and 142x74 (c).

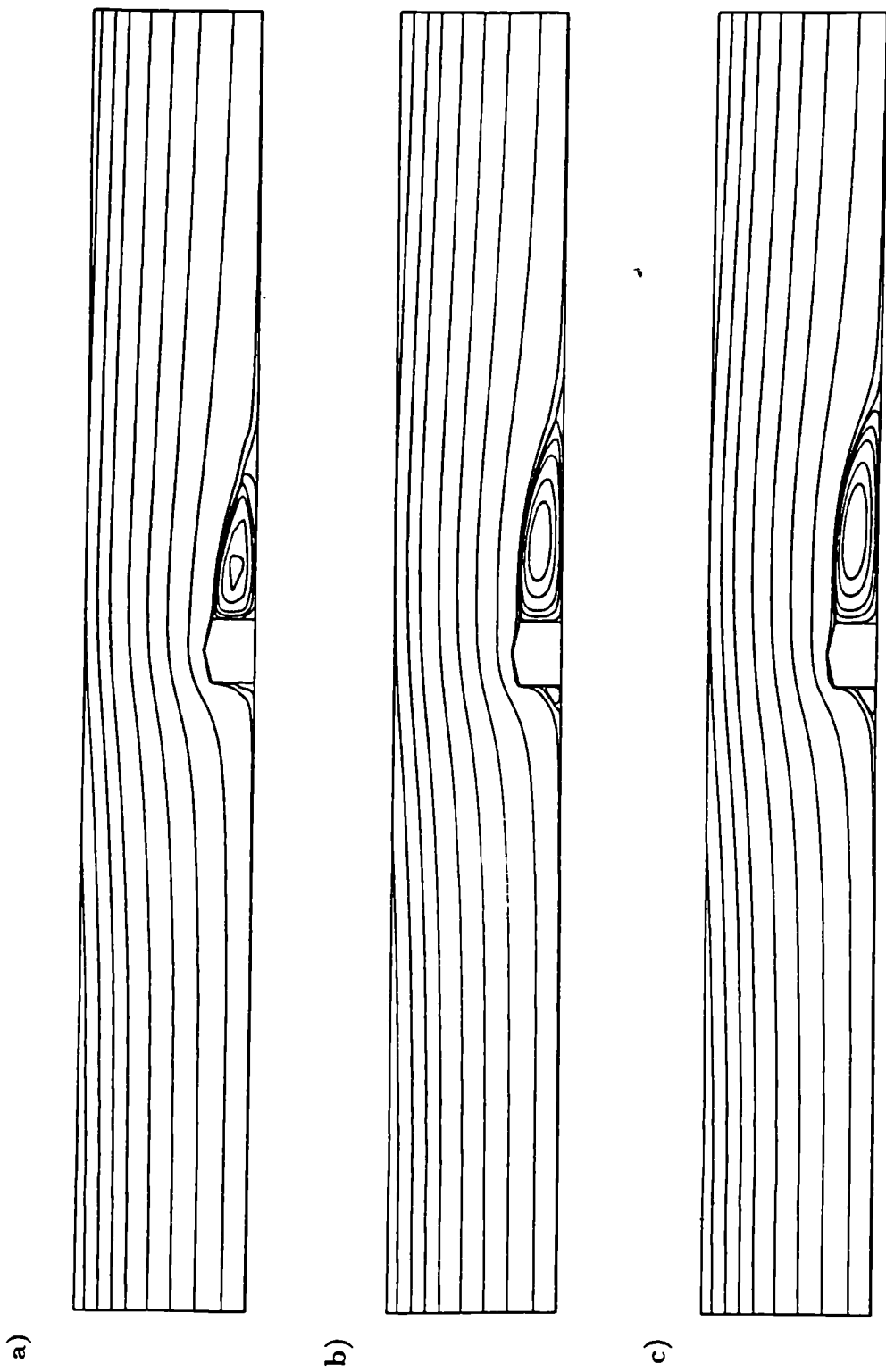
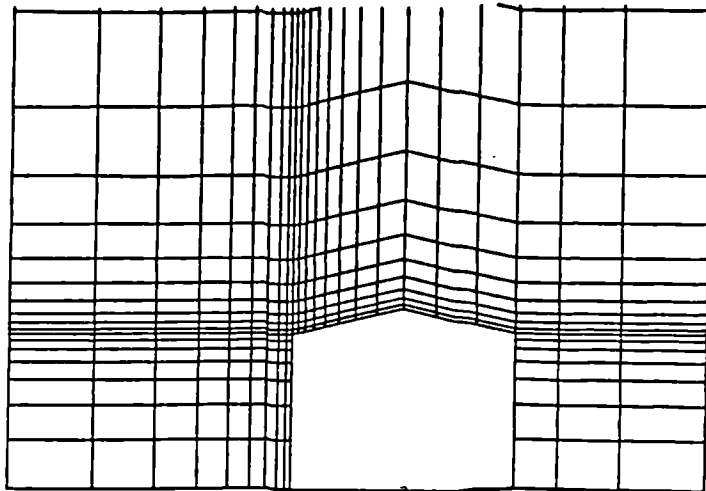
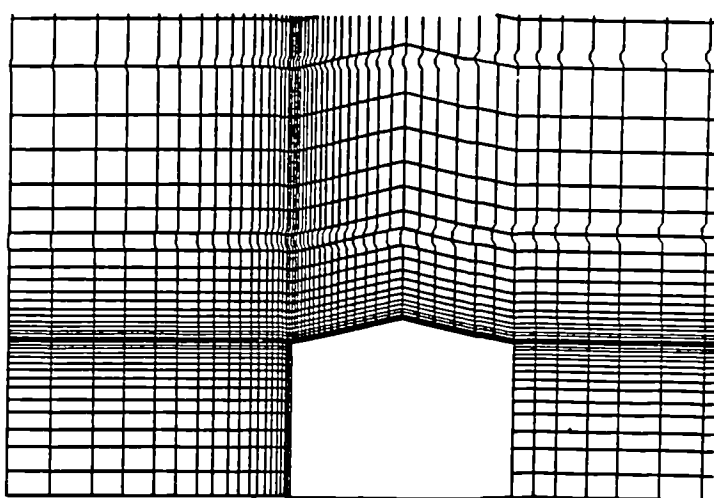


Fig. 5.25 Predicted streamlines for different grids (a), (b) and (c)  
of Fig. 5.24

a)



b)



c)

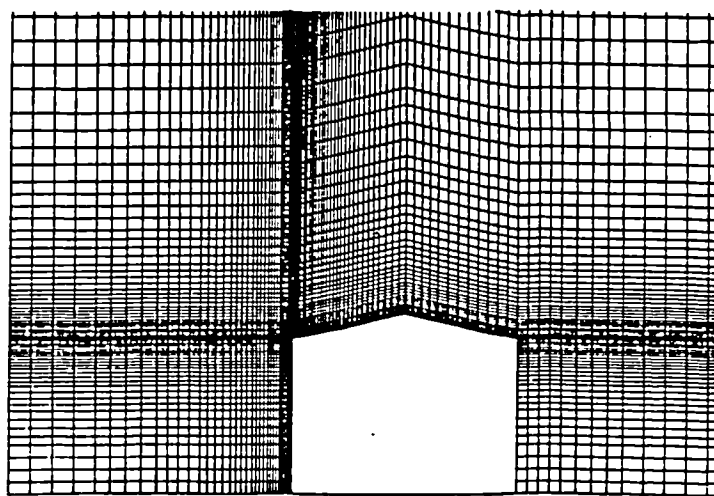


**Fig. 5.26 FB16.** Grid levels  $37 \times 29$  (a),  $72 \times 56$  (b) and  $142 \times 110$  (c) used for the multigrid method.

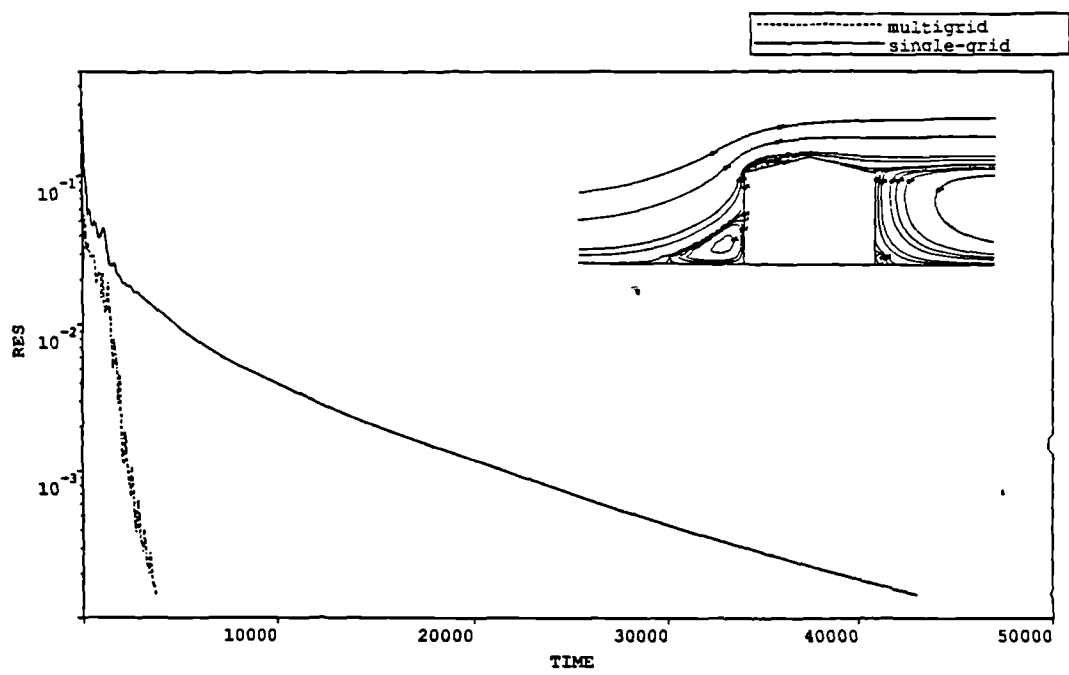


**Fig. 5.27 FB16. The convergence rate obtained with the multigrid and the single-grid methods.**

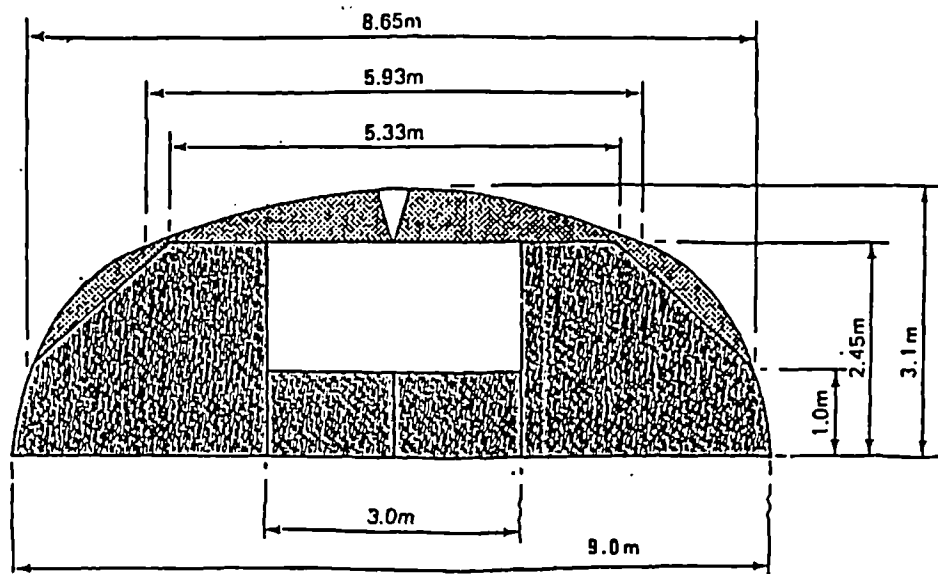


Fig. 5.28 Dimensions of Greenhouse FB17 (From Richardson, 1991).

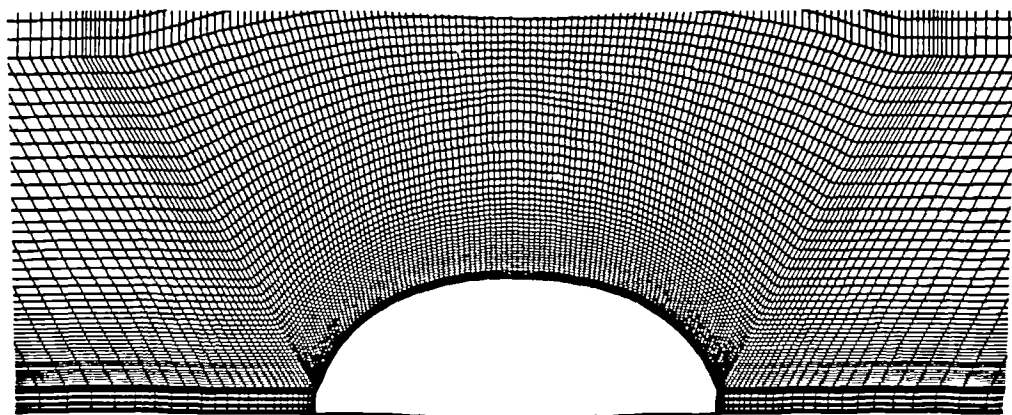


Fig. 5.29 Grid 216x123 used for FB17.

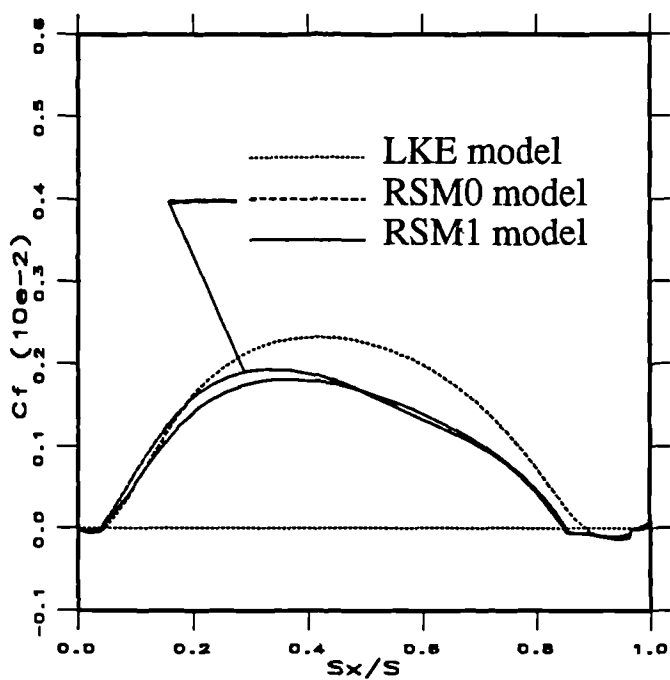
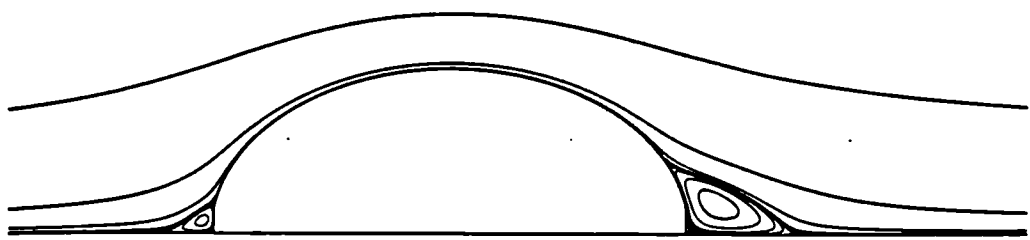
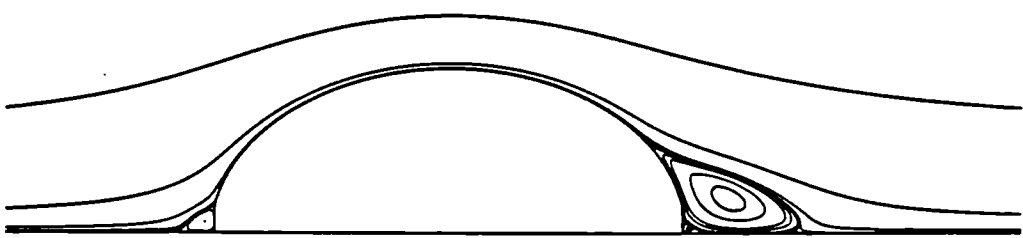


Fig. 5.30 FB17. Wall skin-friction coefficient predicted by LKE, RSM0 and RSM1.

a)



b)



c)

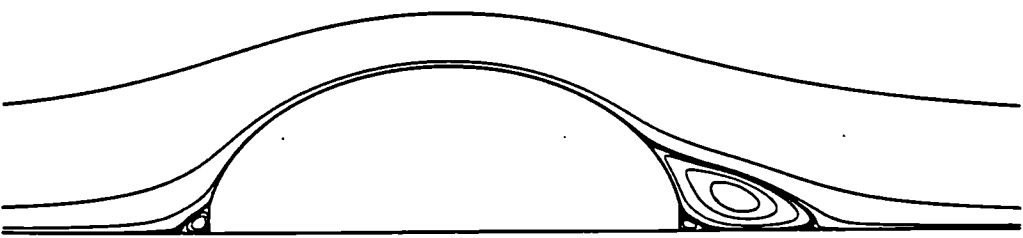


**Fig. 5.31 FB17. Predicted streamlines by LKE (a), RSM0 (b), and RSM1 (c).**

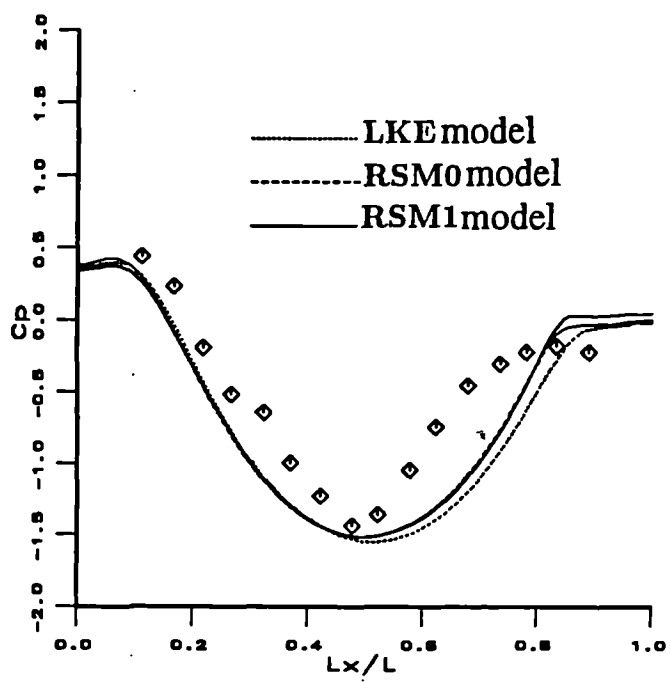


Fig. 5.32 FB17. Distribution of wall pressure coefficient predicted by LKE, RSM0 and RSM1 (FB17).

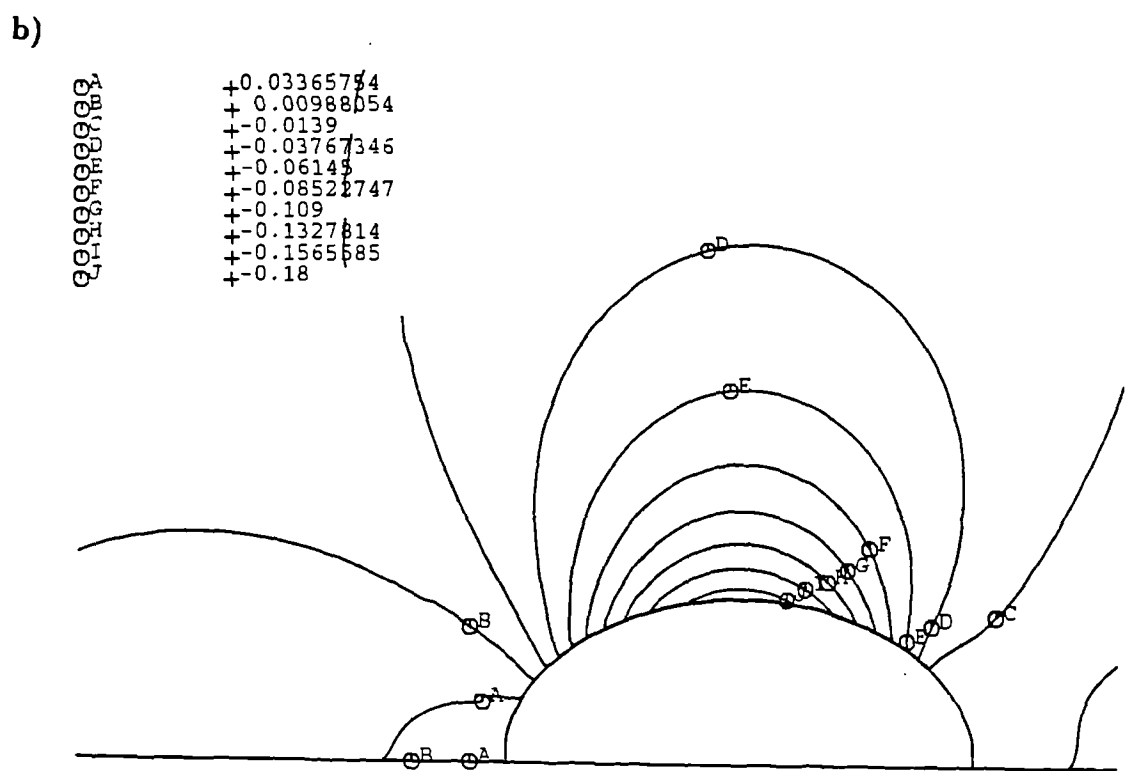
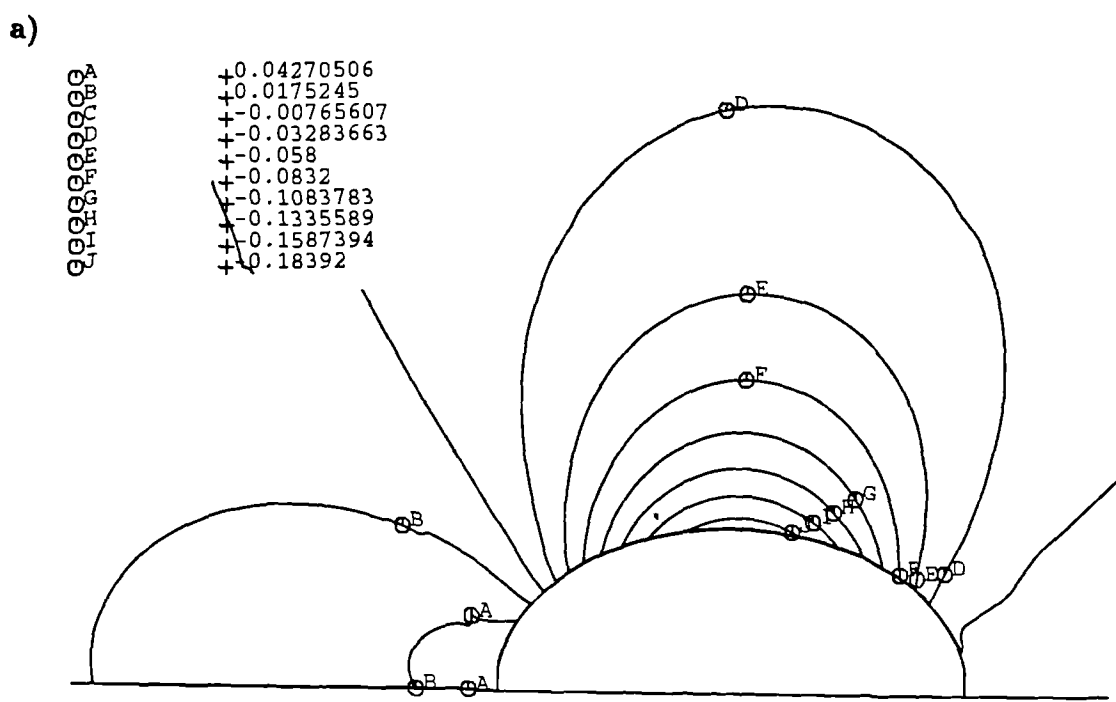
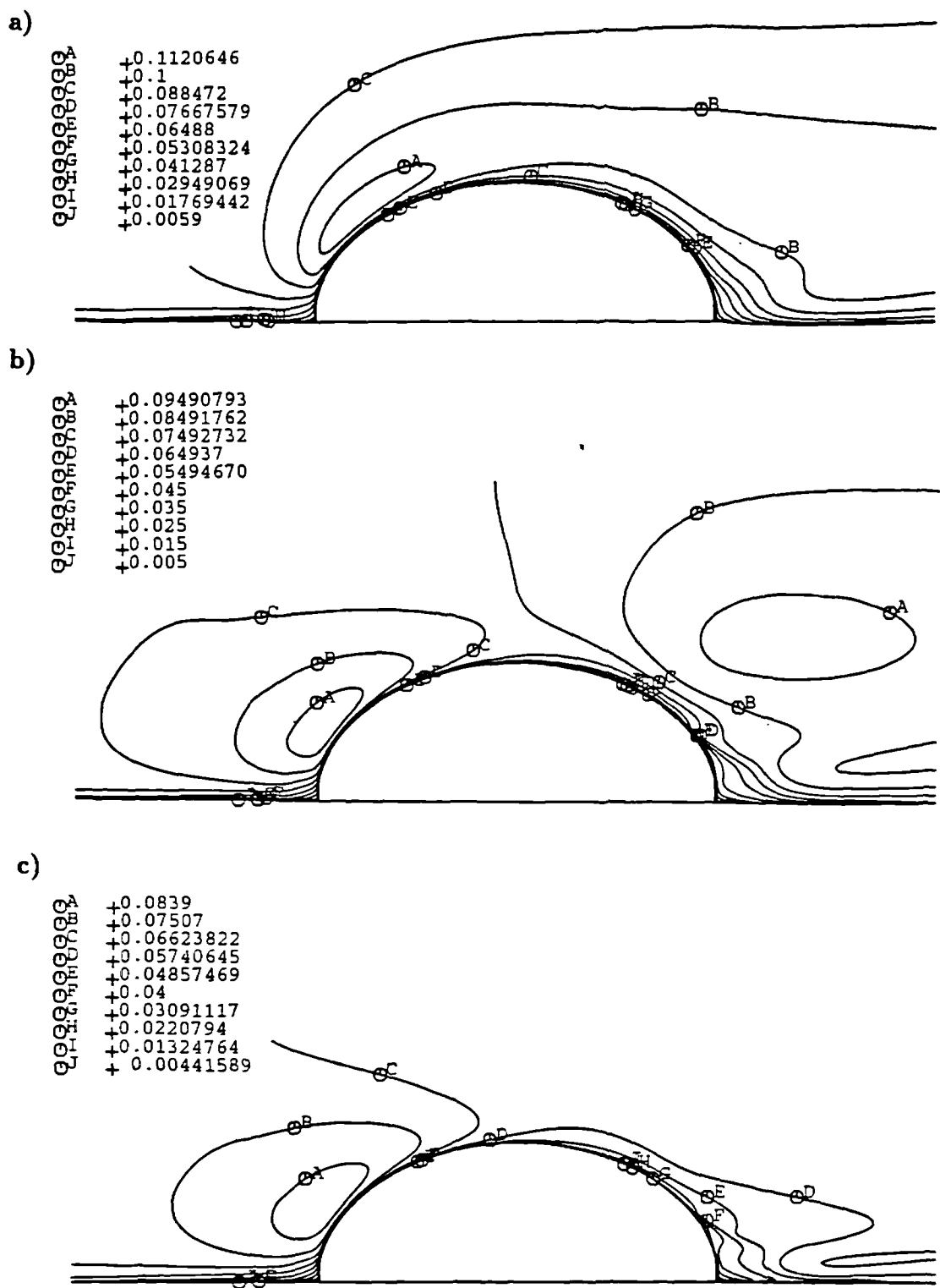
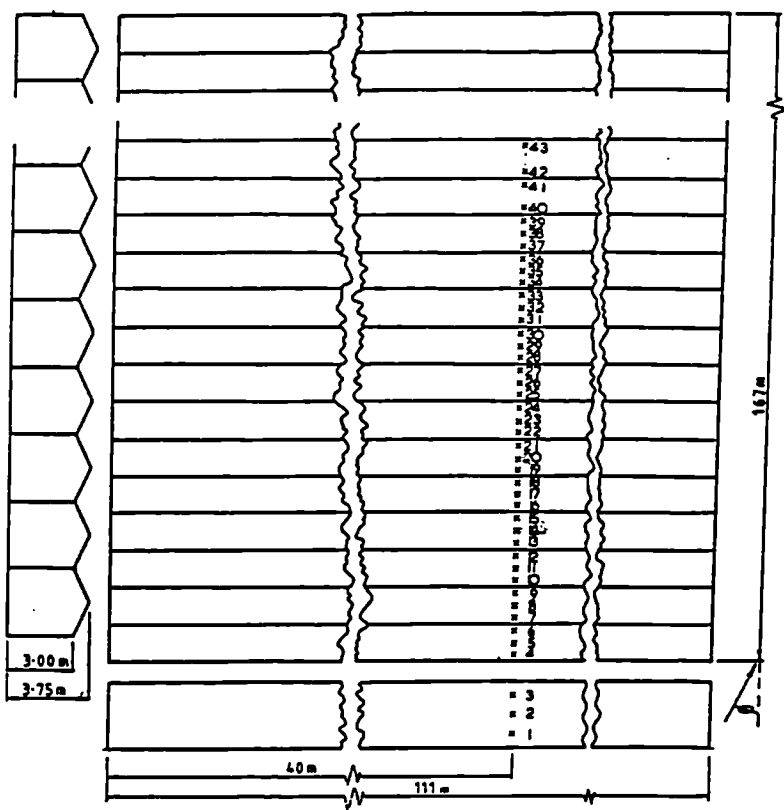


Fig. 5.33 FB17. Predicted pressure contours by LKE (a) and RSM1 (b).



**Fig. 5.34 FB17.** Predicted turbulence kinetic energy by LKE (a), RSM0 (b) and RSM1 (c).



**Fig. 5.35 Dimensions of multispan structure G07 (From Hoxey and Moran, 1991)**

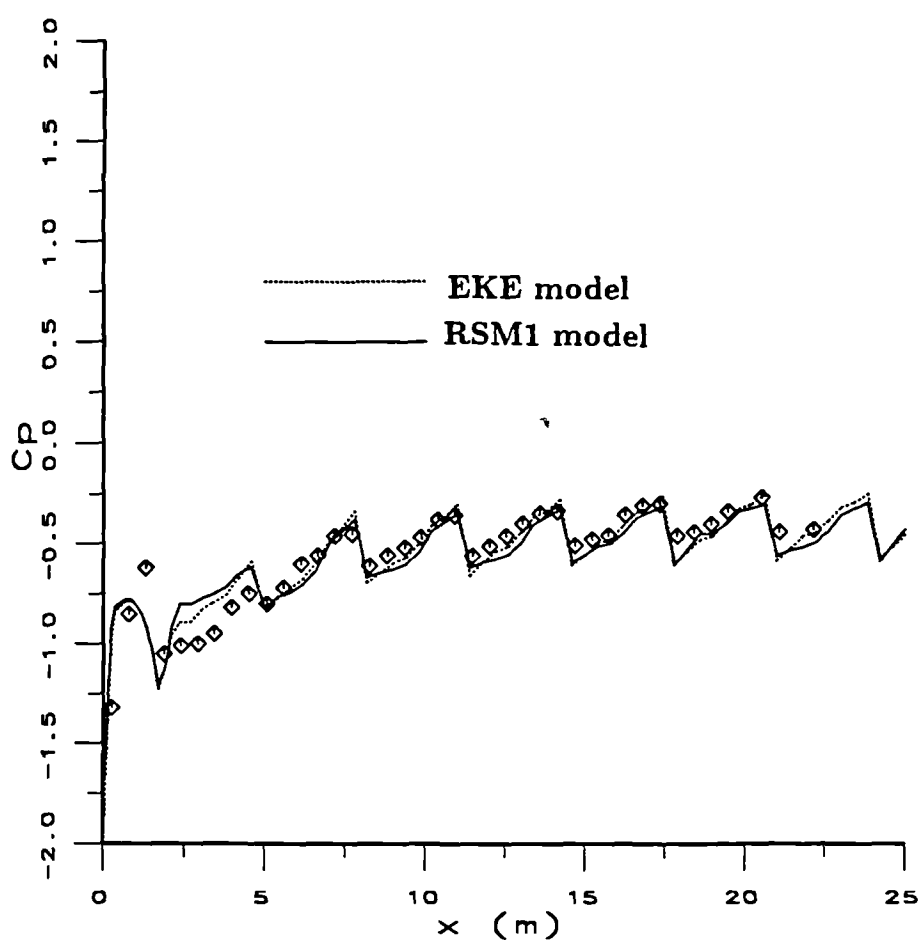
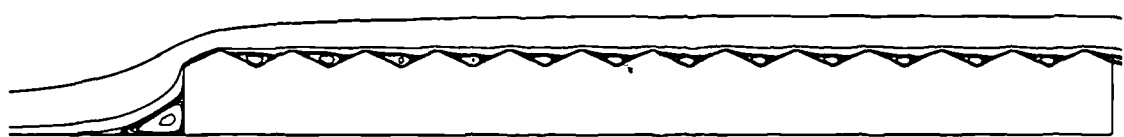


**Fig. 5.36 G07. Predicted coefficient of wall pressure distribution.**

a)



b)

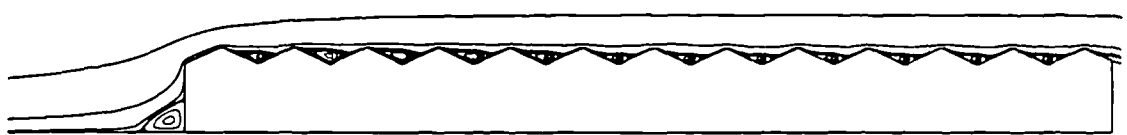
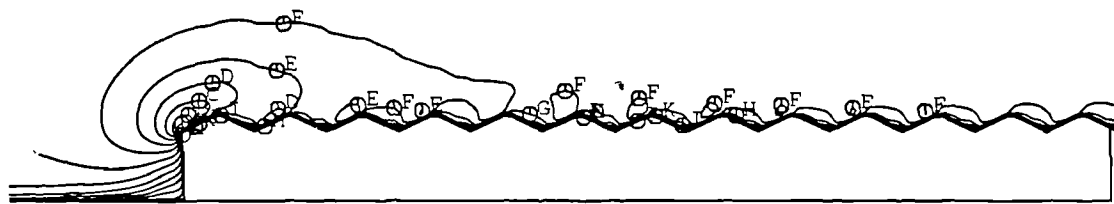


Fig. 5.37 G07. Predicted streamlines by EKE (a) and RSM1 (b).

a)

A  
+0.221  
+0.2057271  
+0.19  
+0.175249  
+0.16  
+0.1447709  
+0.13  
+0.1142928  
+0.09905378  
+0.08381475  
+0.06857570  
+0.05333665  
+0.0381  
+0.02285857  
+0.00762



b)

A  
+0.2083264  
+0.194  
+0.18  
+0.1652244  
+0.1508571  
+0.13649  
+0.1221224  
+0.1077551  
+0.0933877  
+0.079  
+0.064653  
+0.05  
+0.03591836  
+0.021551  
+ 0.00718367

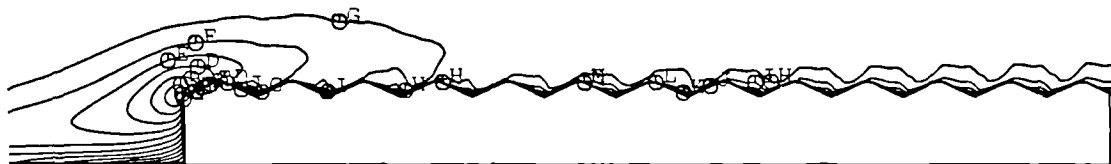
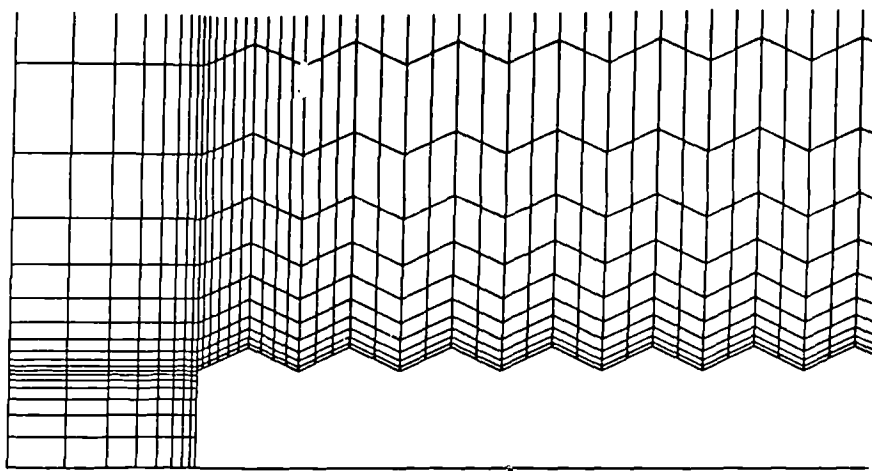
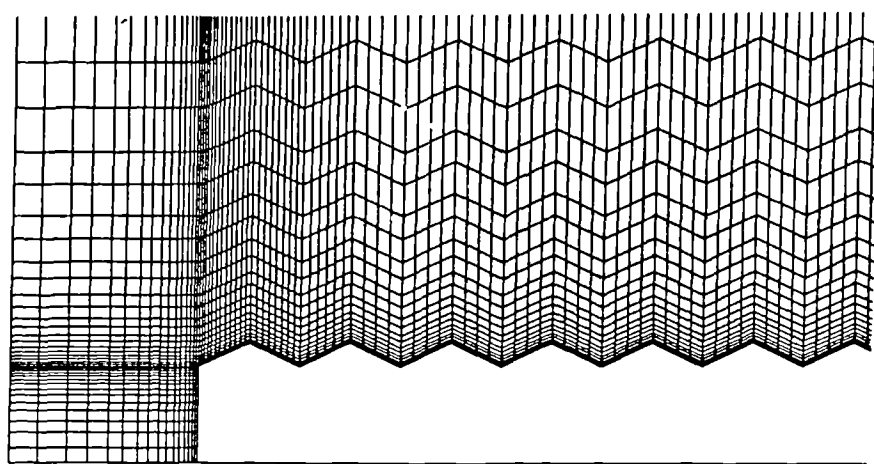


Fig. 5.38 G07. Predicted turbulence kinetic energy by EKE (a) and RSM1 (b).

a)



b)



c)

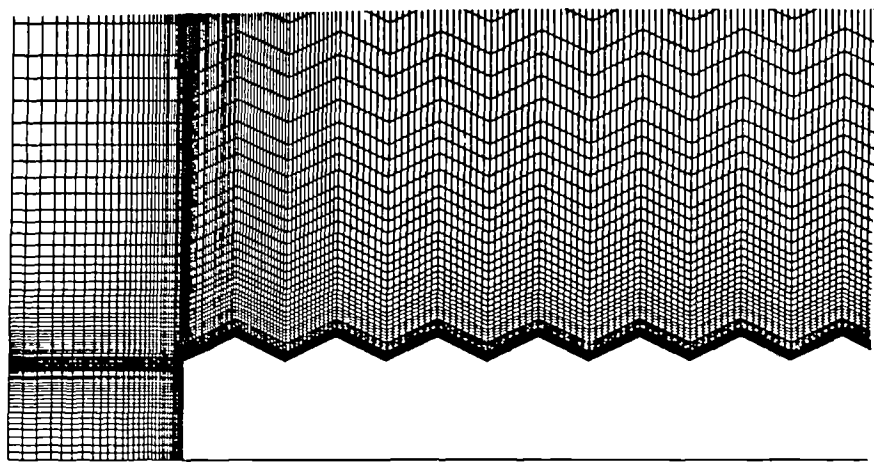
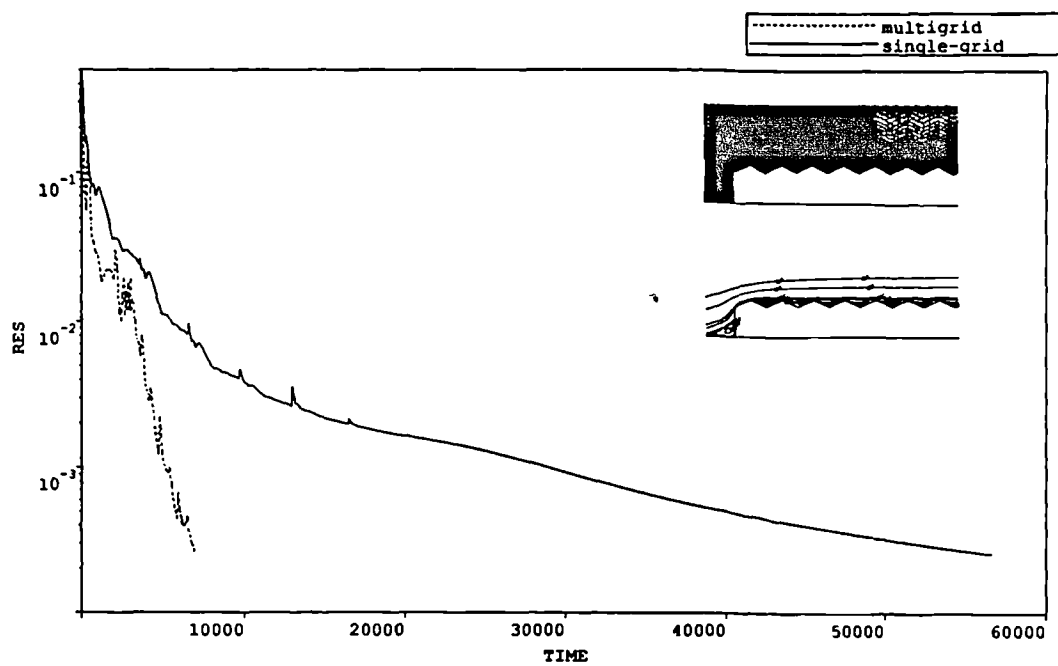
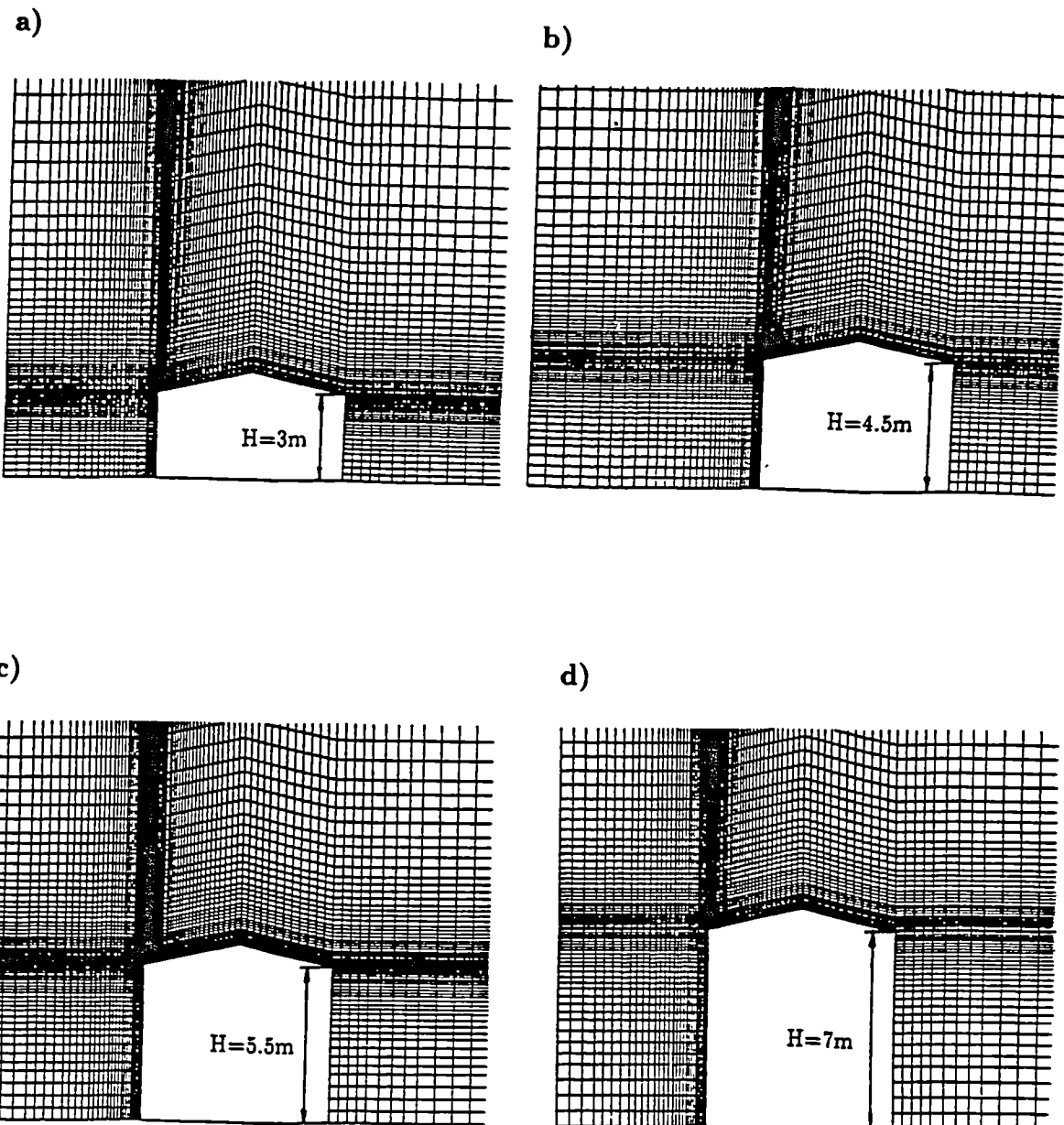


Fig. 5.39 G07. Grid levels 63x29 (a), 124x56 (b) and 256x110 (c) used for the multigrid method.



**Fig. 5.40 G07. The convergence rate obtained with the multigrid and single-grid methods.**



**Fig. 5.41 Grid distribution for buildings of same width  $W$  but different heights.  $H = 3\text{m}$  (a),  $4.5\text{m}$  (b),  $5.5\text{m}$  (c) and  $7\text{m}$  (d).**

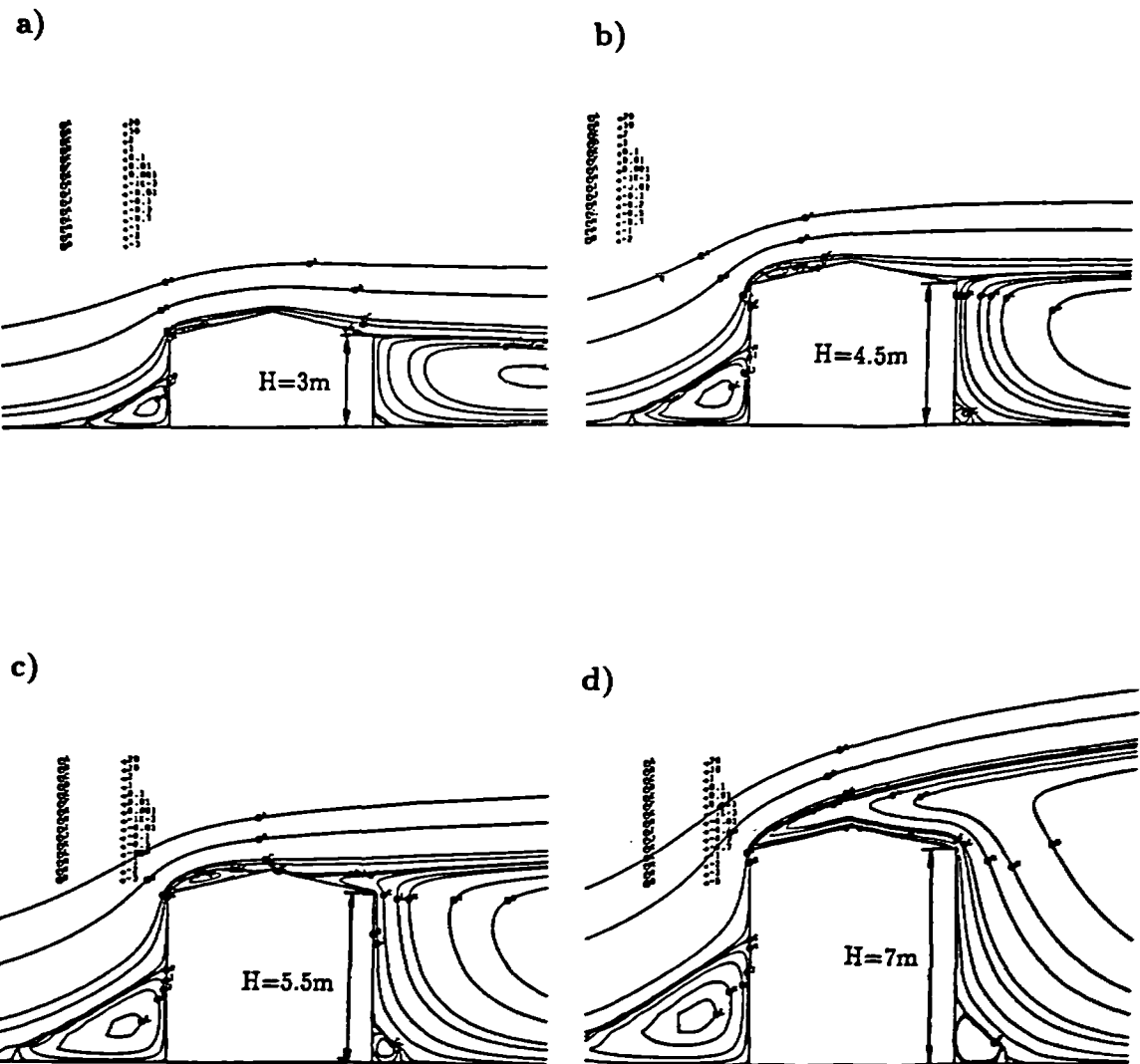
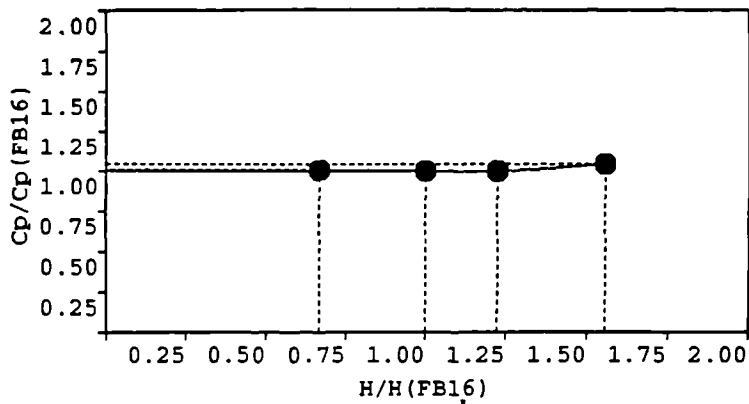


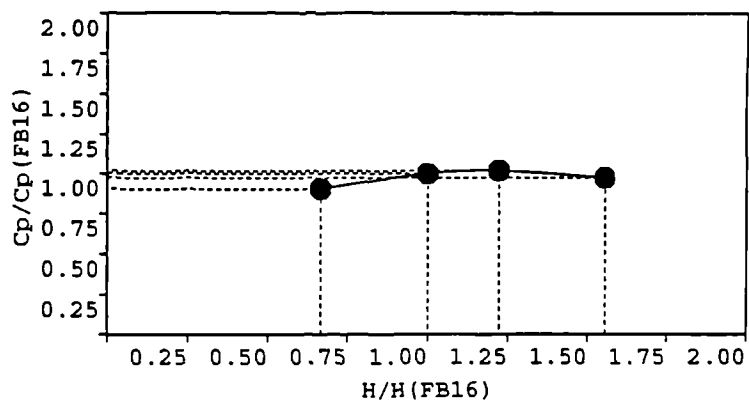
**Fig. 5.42 Predicted streamlines for heights  $H = 3\text{m}$  (a),  $4.5\text{m}$  b),  $5.5\text{m}$  c) and  $7\text{m}$  d).**

a)



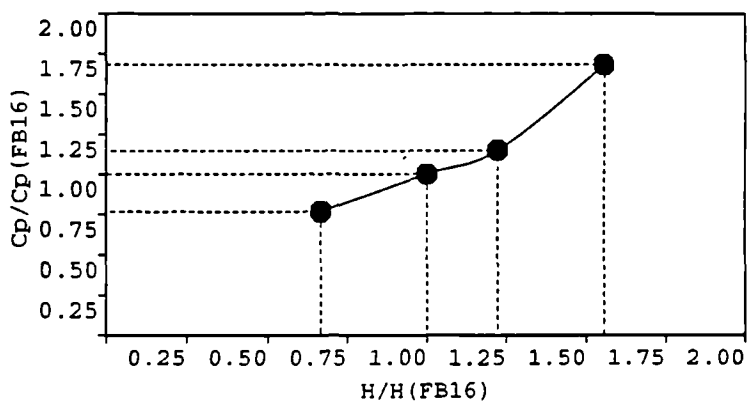
WINDWARD

b)



ROOF

c)



LEEWARD

Fig. 5.43 Predicted average pressure coefficients for buildings of different heights, on the windward (a), roof (b) and leeward (c) sides.

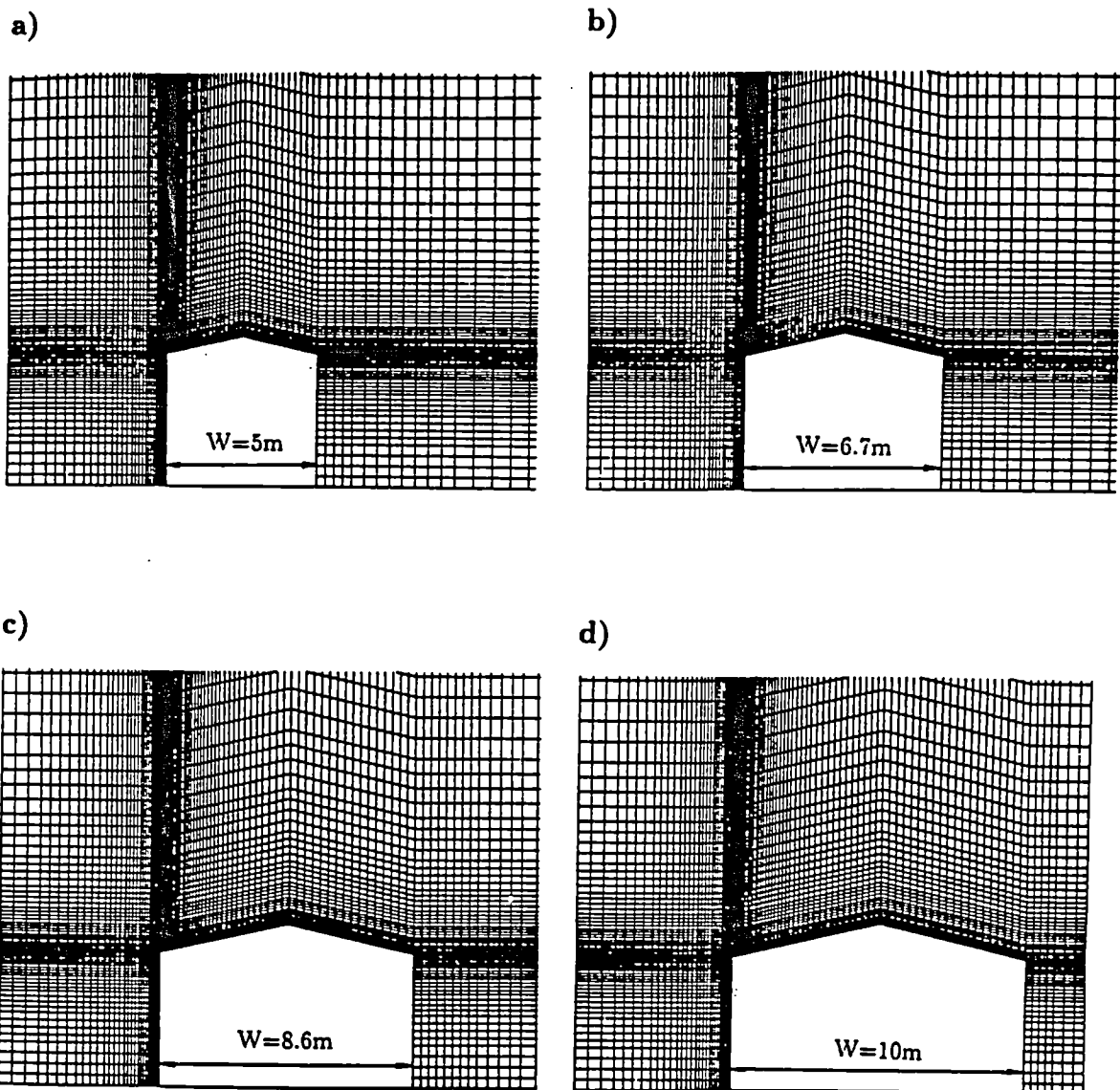


**Fig. 5.44 Computation domains for the buildings with the same height  $H$  and different widths  $W = 5\text{m}$  (a),  $6.7\text{m}$  (b),  $8.6\text{m}$  (c) and  $10\text{ m}$  (d).**

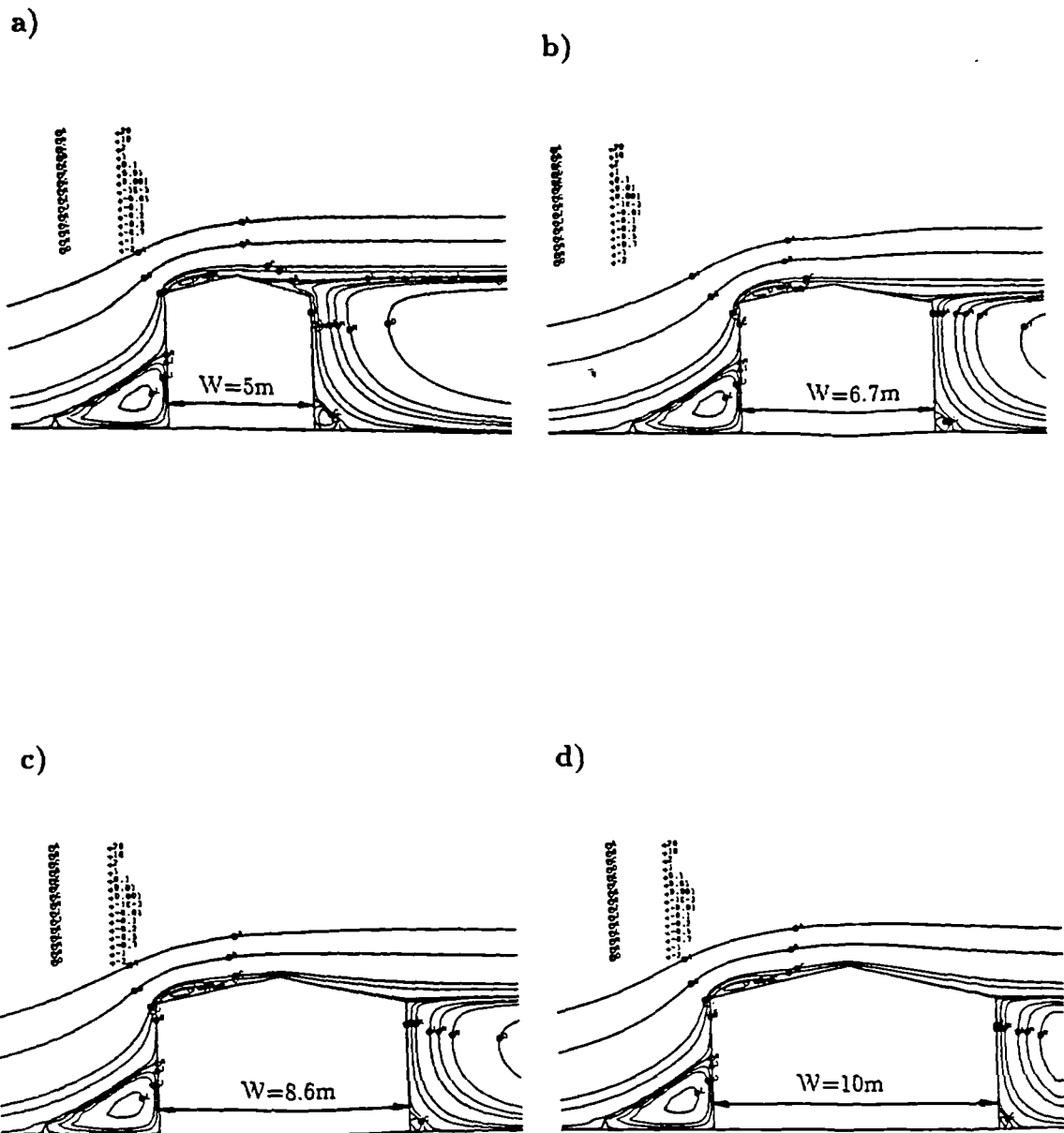


Fig. 5.45 Predicted streamlines for the different widths  $W = 5\text{m}$  a),  
 $6.7\text{m}$  b),  $8.6\text{m}$  c) and  $10\text{m}$  d).

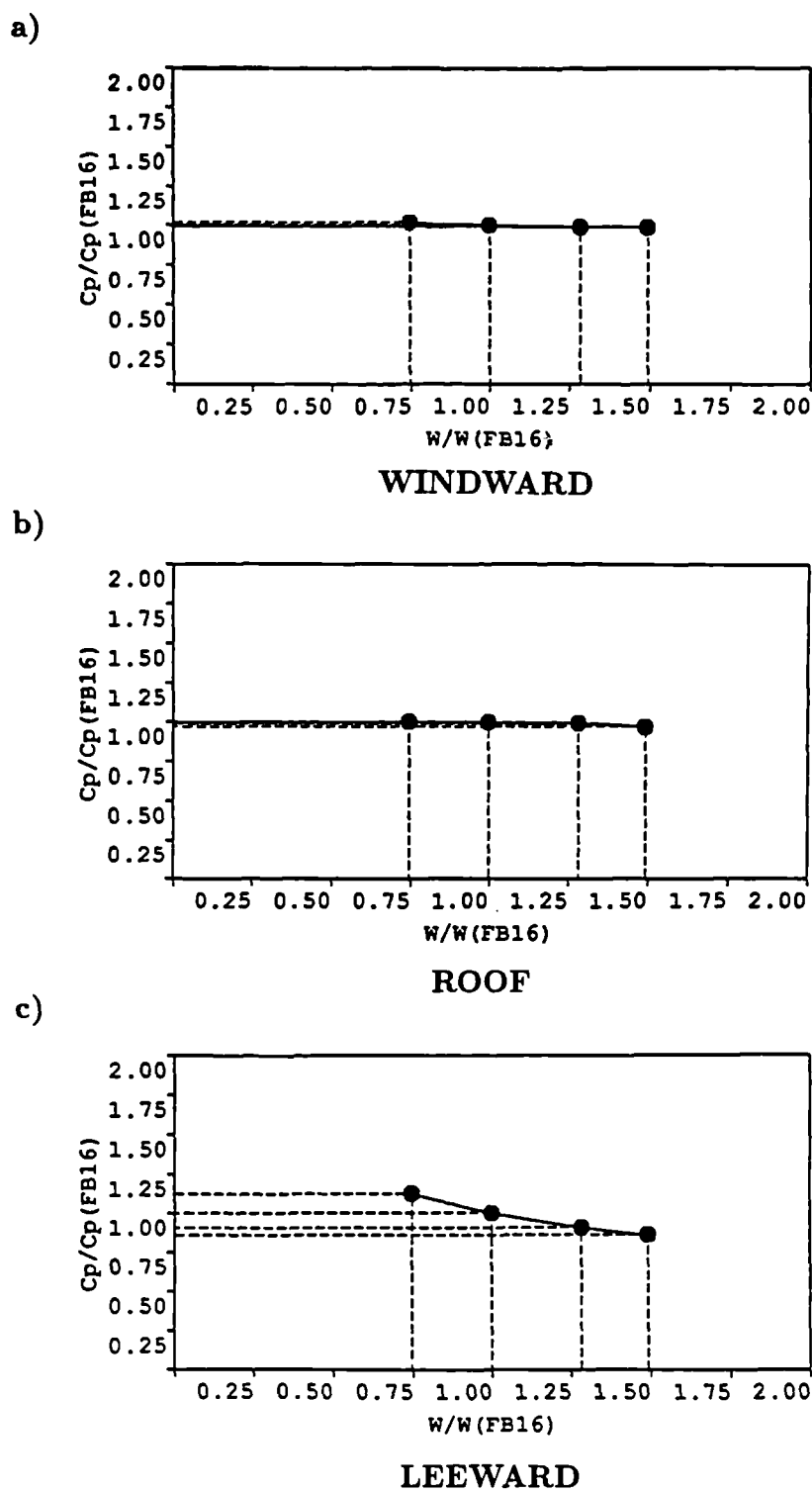
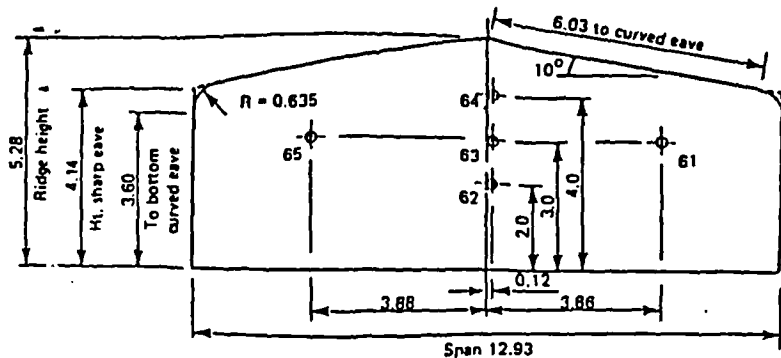
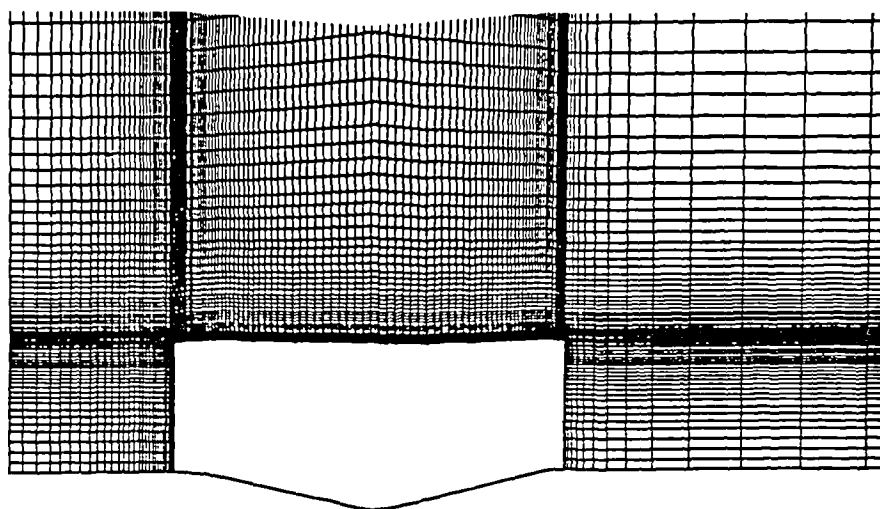


Fig. 5.46 Predicted pressure coefficients for the buildings with different widths on the windward a), roof b) and leeward c) side of building.

a)



b)



c)

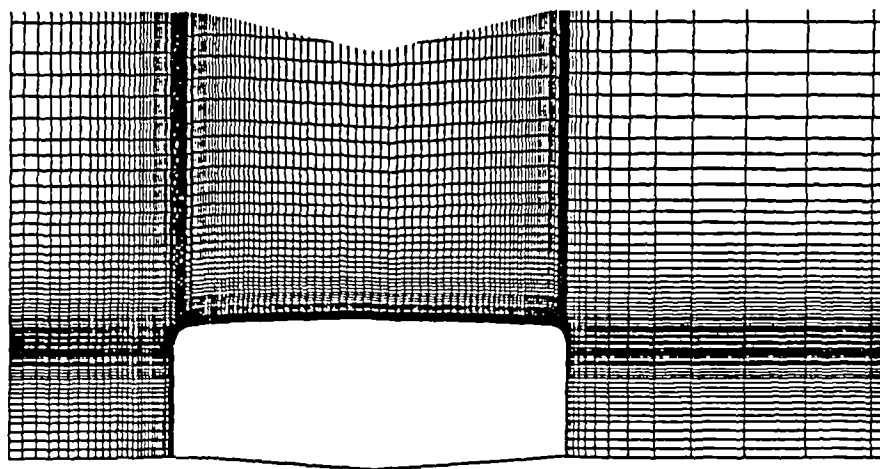
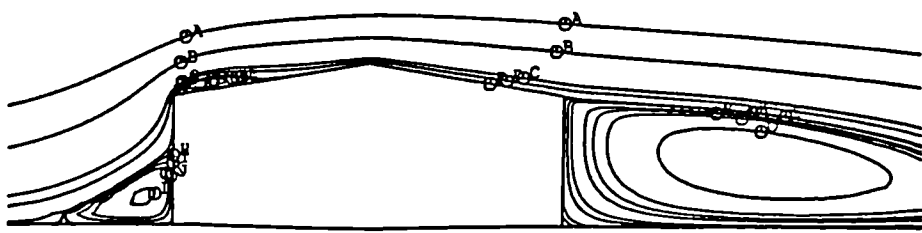
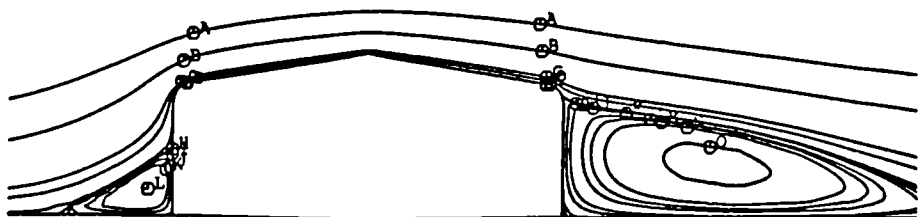


Fig. 5.47 Dimensions of building FB19 (From Robertson, 1989). Grids for sharp (b) and curved (c) eaves.

a)



b)



**Fig. 5.48 Predicted streamlines for sharp eaves a) and curved eaves b).**

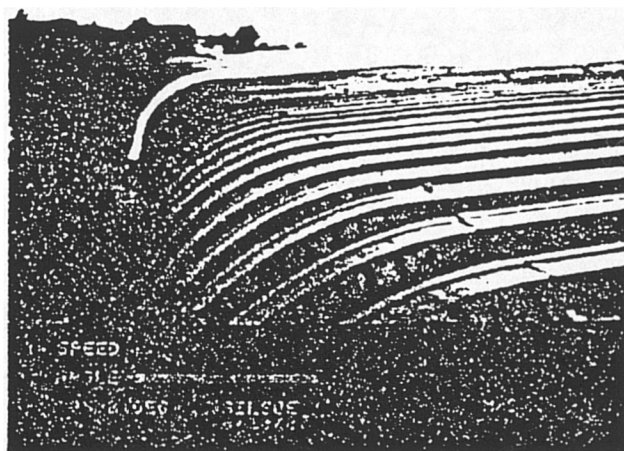


**Fig. 5.49 Flow visualization around curved eaves. (From Robertson, 1989).**

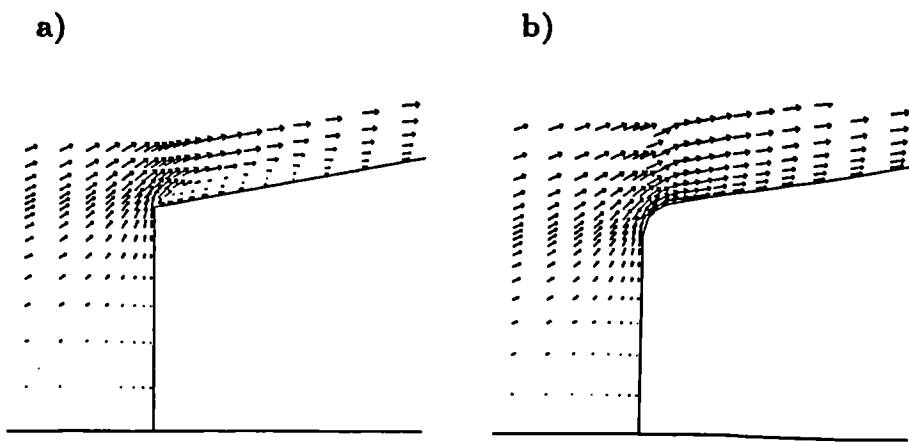


**Fig. 5.50 Velocity vectors for sharp (a) and curved (b) eaves.**

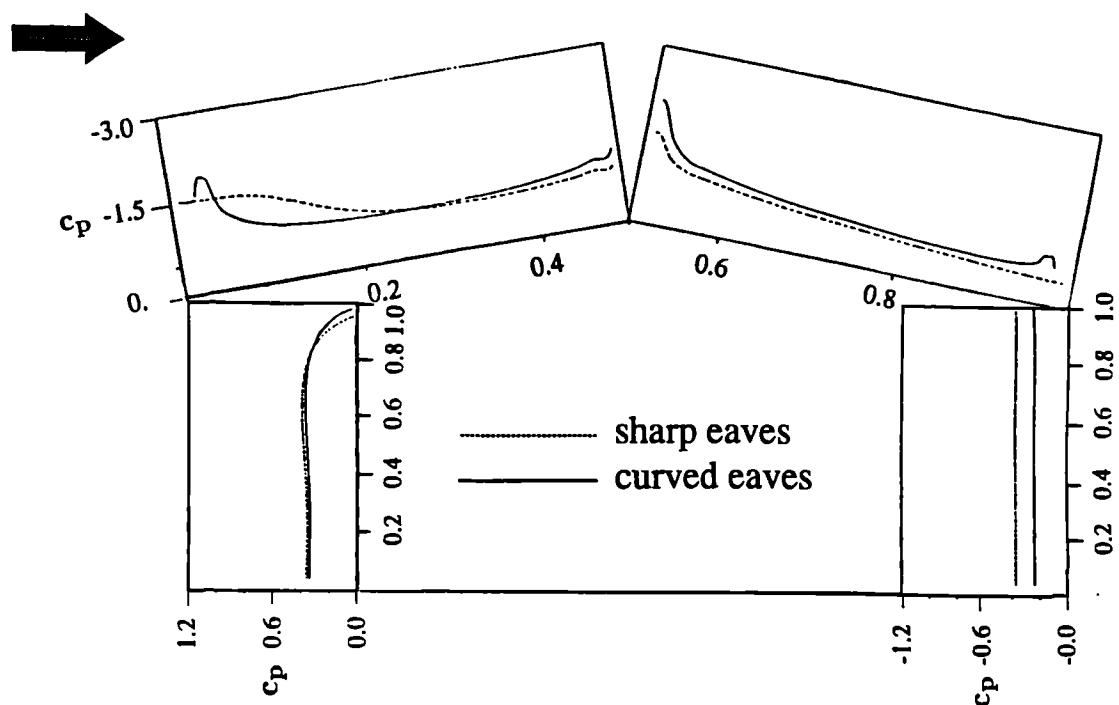
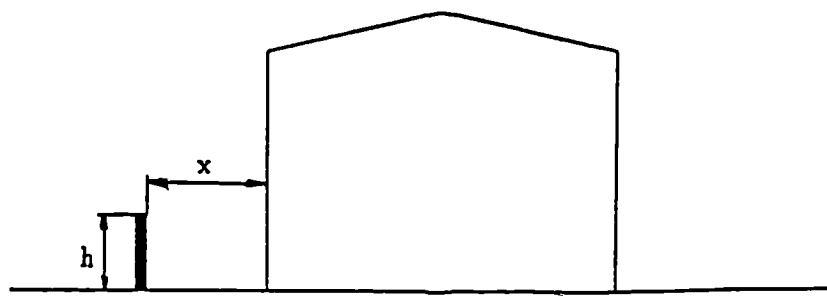


**Fig. 5.51 Predicted pressure coefficients over roof for sharp and curved eaves.**

a)



b)

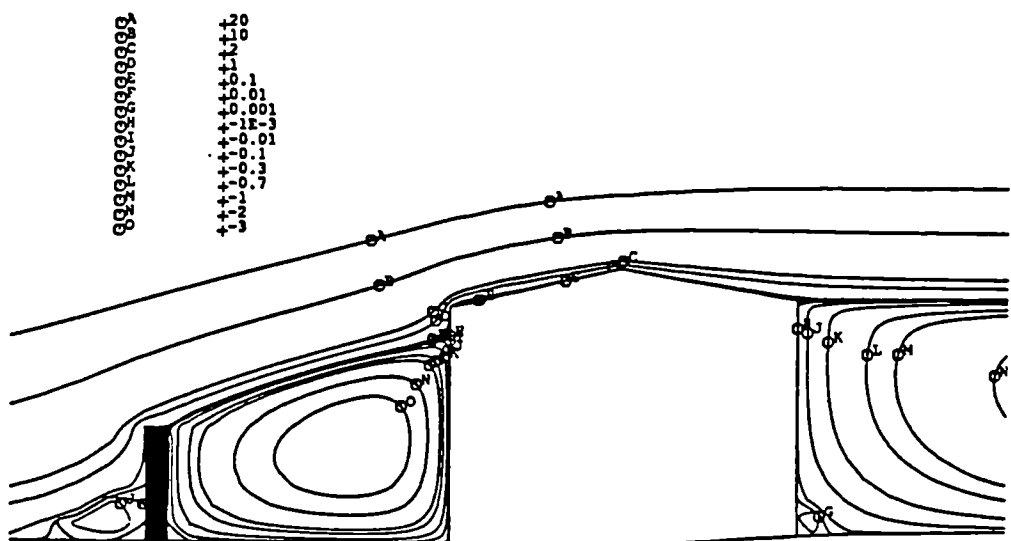


Fig. 5.52 Effects of windbreaks. (a) Notation. (b) streamlines for  $H=2.18$  and  $X=5\text{m}$  (b)

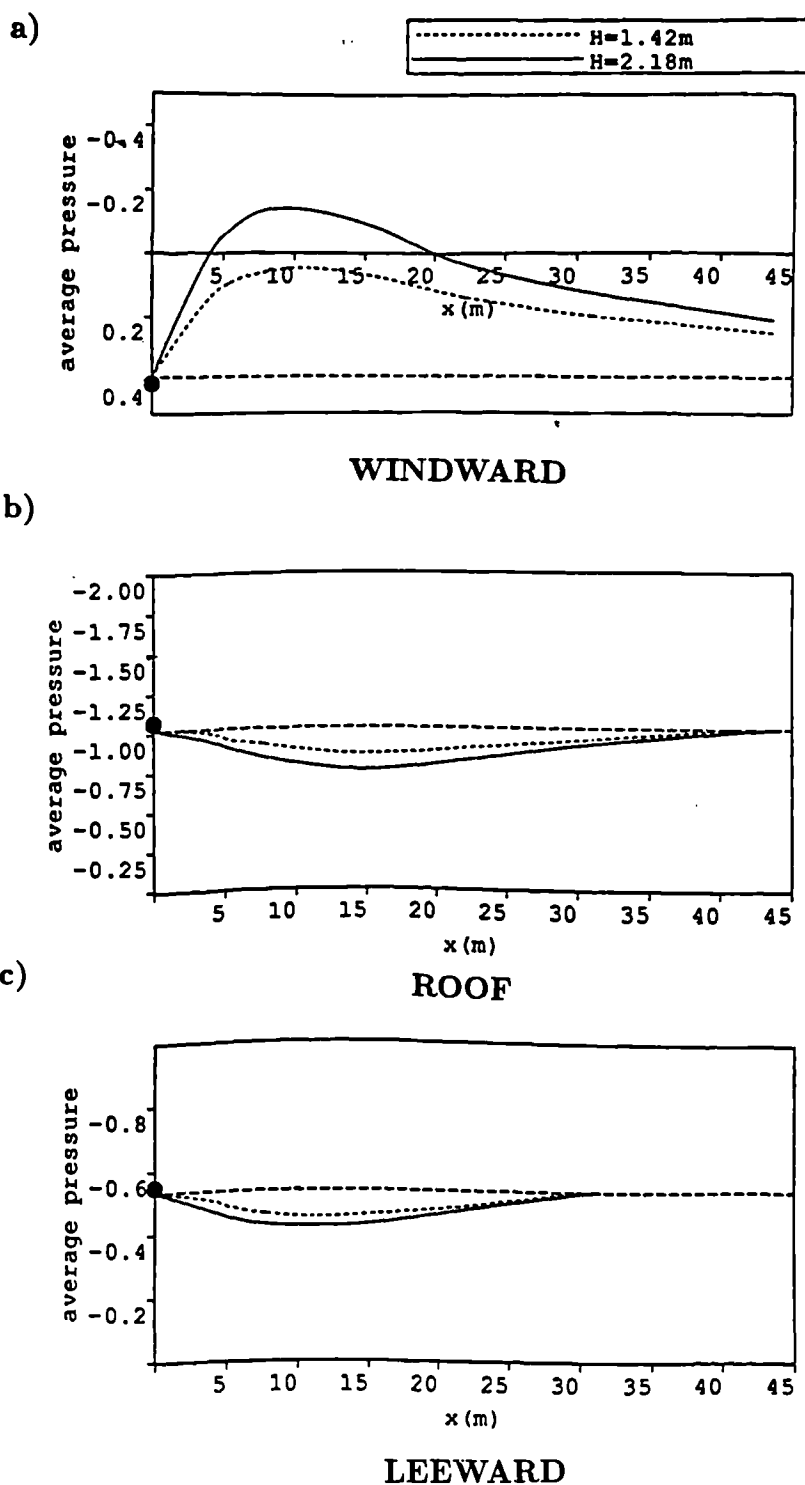
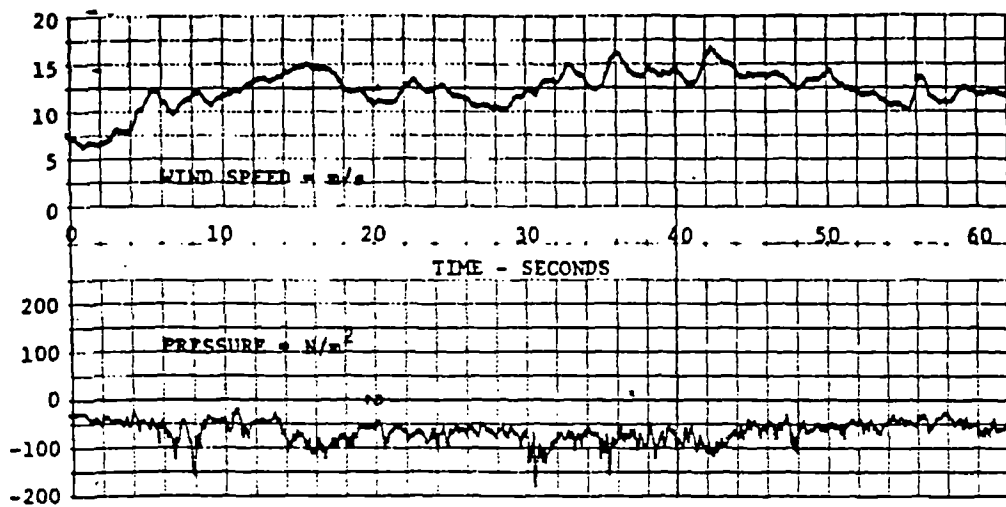
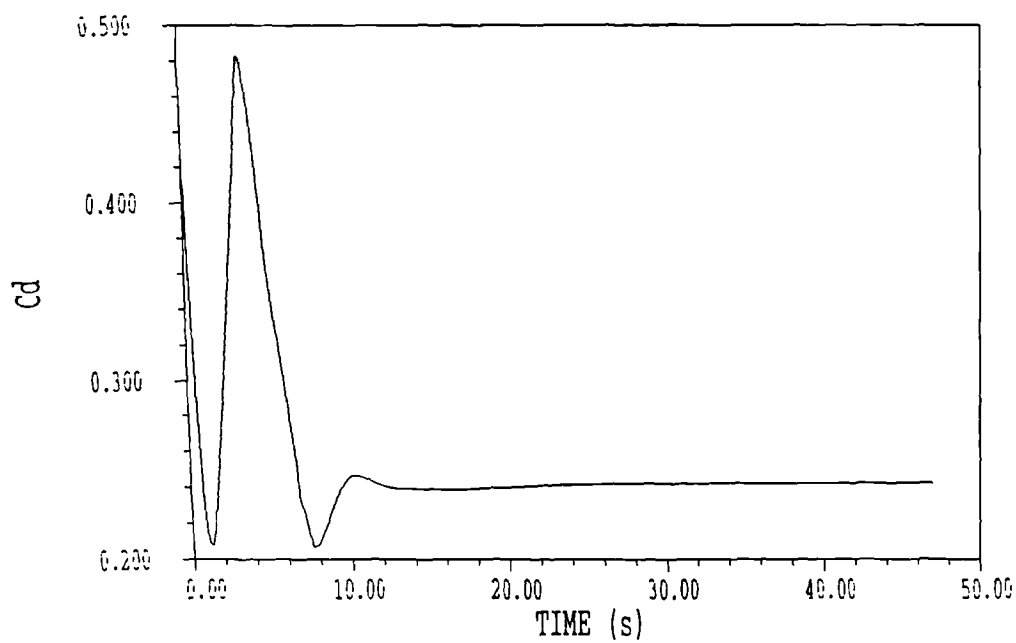


Fig. 5.53 Predicted average pressure coefficients for the windward a), roof b) and leeward (c) sides.



**Fig. 5.54 Typical records of wind mean velocity and surface pressure  
(From Part 2 Code of Practice, 1991)**



**Fig. 5.55 Unsteady results for the drag coefficient  $C_d$ .**

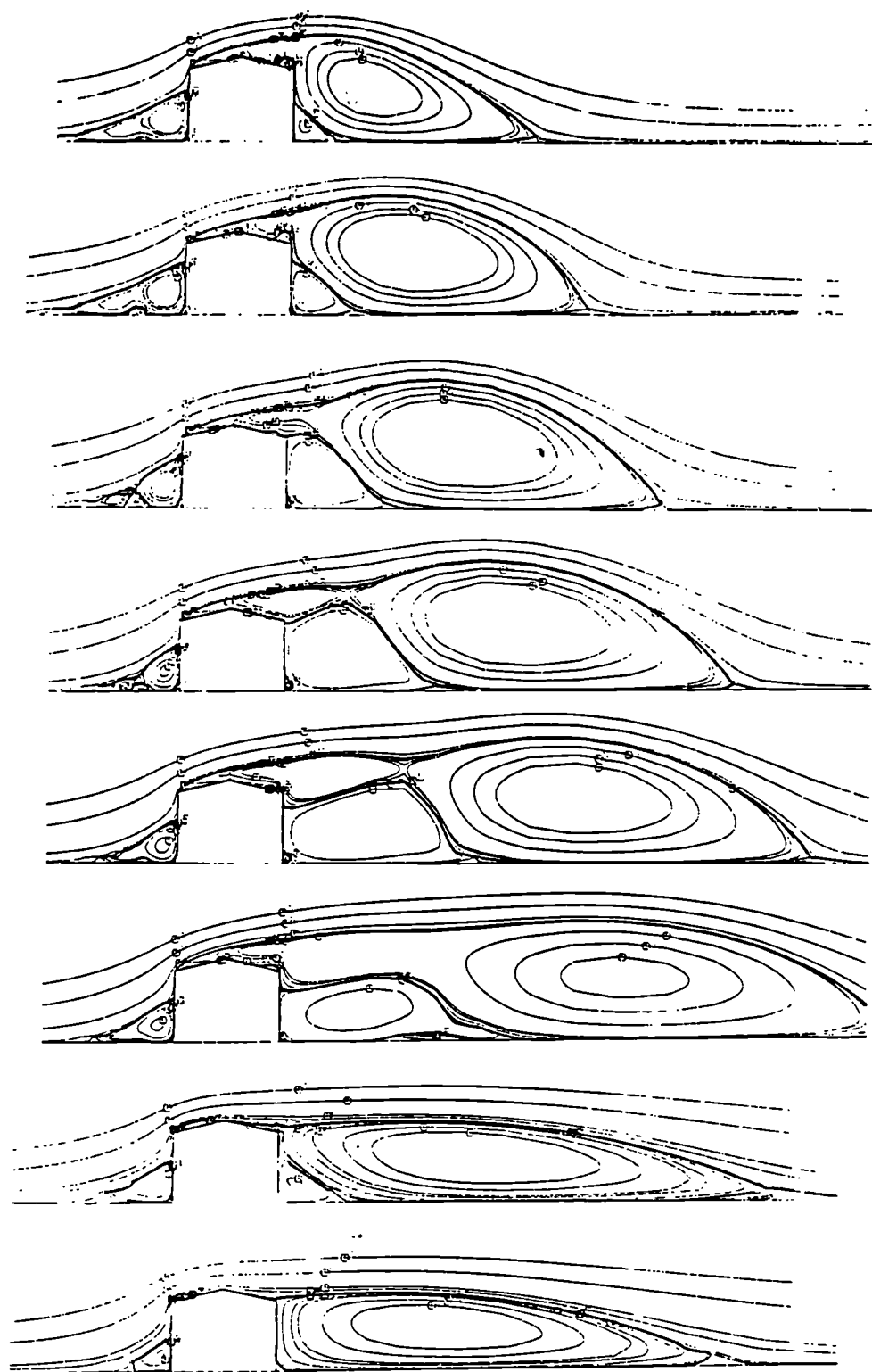
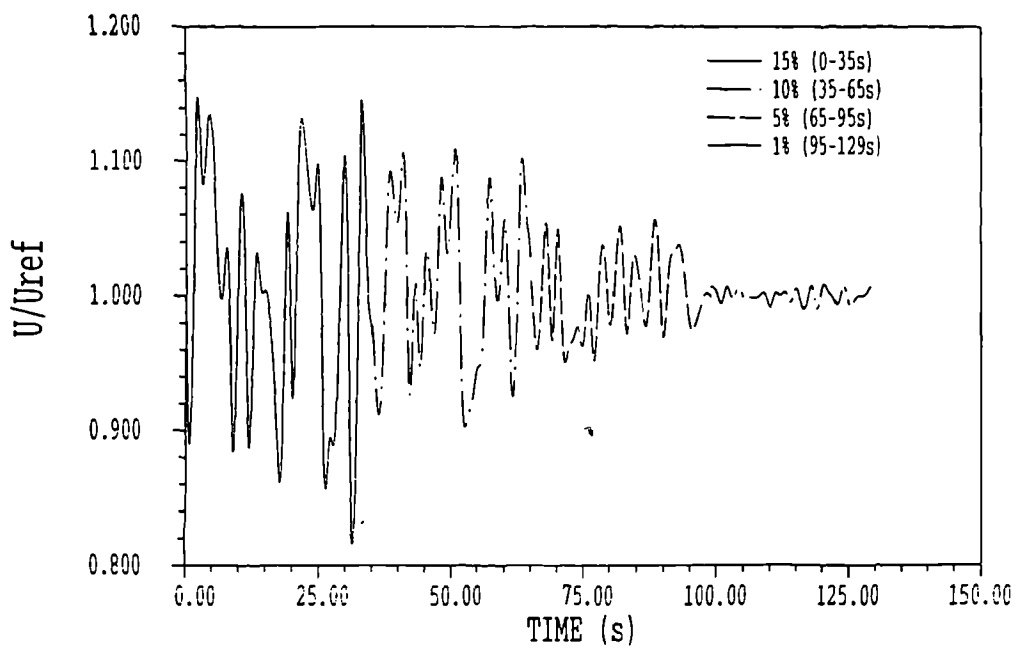
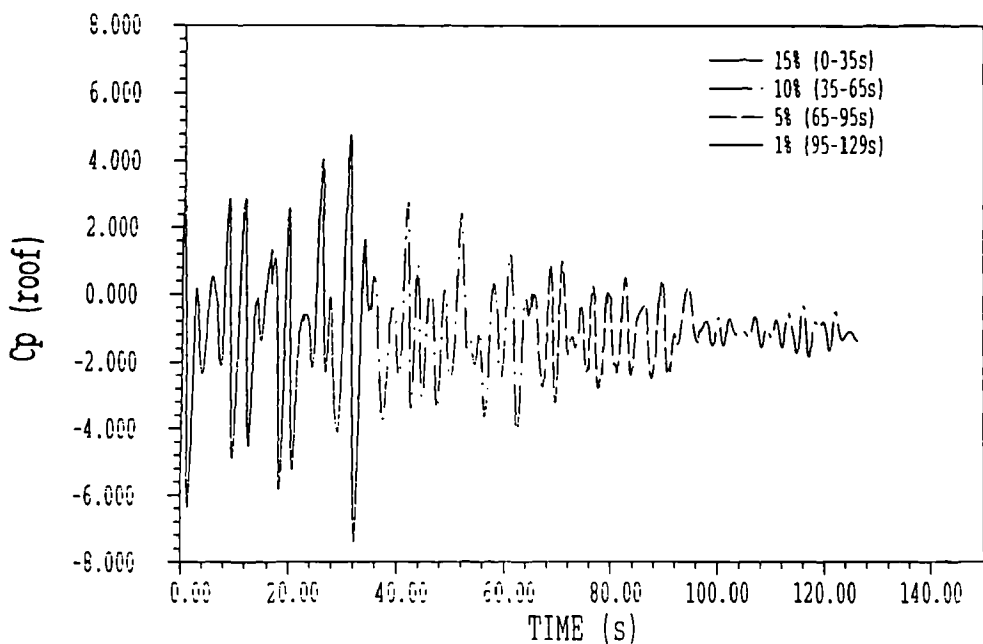


Fig. 5.56 Evolution of mean-flow streamlines with time.



**Fig. 5.57 Perturbation of velocity at inlet as a function of time and amplitude.**



**Fig. 5.58 Predicted pressure coefficient on building roof.**

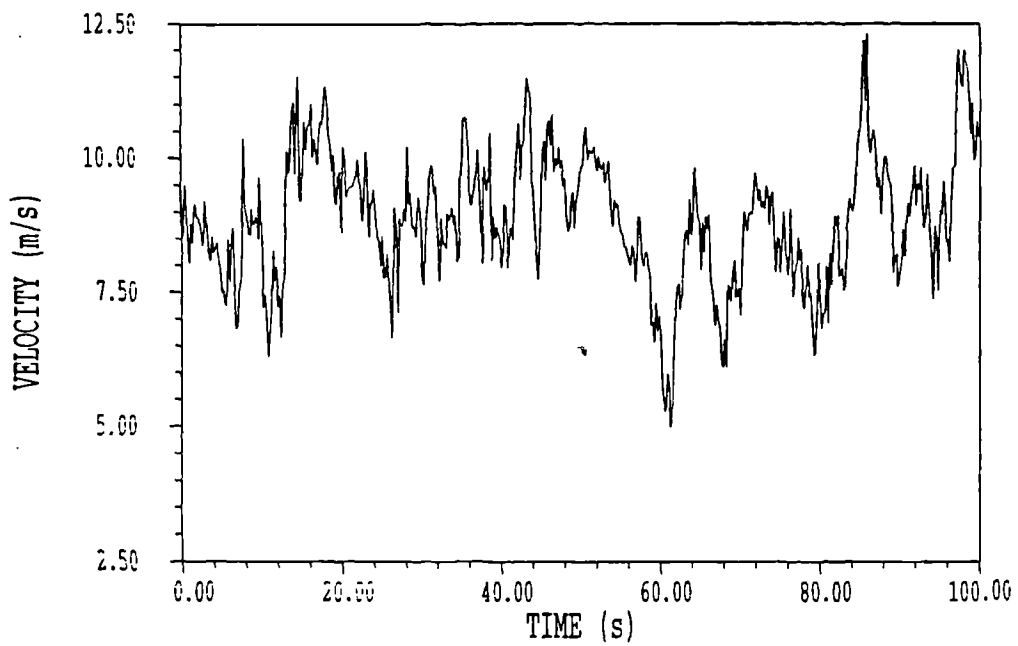


**Fig. 5.59** Field measurements of wind velocity at reference height.

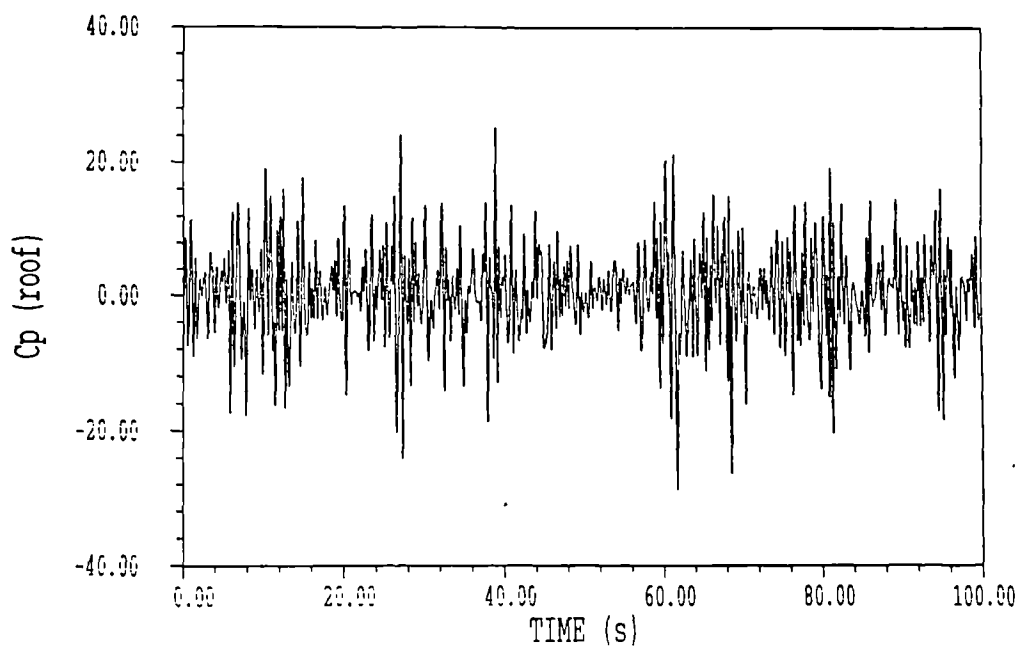


**Fig. 5.60** Predicted pressure coefficient on building roof.

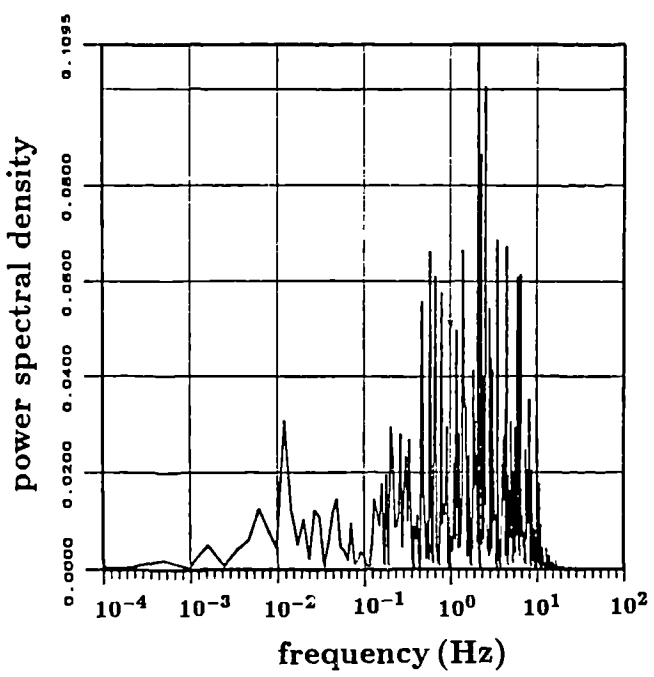


Fig. 5.61 Predicted spectra of roof pressure coefficient.

# Chapter 6

## CLOSURE

### 6.1 INTRODUCTION

The present study was intended to address some fundamental issues that are specific to the calculation of turbulent flows around full-scale buildings and to advance a predictive procedure suitable for their simulation. An existing finite-volume method was extended in a variety of ways including the implementation of a complete Reynolds-stress transport model of turbulence, the simulation of wind gusts and acceleration of the solution procedure with a multigrid technique. Two different closure methods were considered: a complete Reynolds-stress model used with two alternative proposals for the pressure-strain correlations (Section 2.4) and a  $k-\epsilon$  model used in conjunction with both linear and non-linear stress-strain relationships. A modified  $k-\epsilon$  model, emphasizing the contribution of irrotational strains, was also tested. The complete method was then verified by comparisons with data from a number of full-scale tests. The extent to which the objectives of this study have or have not been fulfilled is discussed in Section 6.2. Suggestions for future work are proposed in Section 6.3.

## **6.2 FULFILLMENT OF OBJECTIVES**

The development of a practical predictive method for turbulent flows around full-scale buildings formed a primary objective of the present study. The activities undertaken concerning this objective were as follows:

- A finite-volume procedure for solving the governing equations on body-fitted coordinates was extended by the inclusion of the non-linear  $k-\epsilon$  model and the Reynolds-stress transport model. When either model was used, it was found that distributions of the dependent variables that were both smooth and continuous in the near-wall regions were only possible by evaluating the gradients of mean velocities there from log.-law relationships. When using the Reynolds-stress model, a special interpolation practice was adopted to allow for the mean velocities and the Reynolds stresses to be stored at the same grid location without producing oscillatory solutions. Another special treatment advanced here concerned the inclusion of pseudo-diffusion terms in the momentum equations which accelerated the attainment of converged solutions.
- The pressure field was calculated using the well-known SIMPLE algorithm. The Peric (1985) procedure for pressure-velocity coupling on co-located grids was used in modified form through the inclusion of the normal stresses. This had the effect of improving the stability of the method and the attainment of converged solutions.
- A number of preferred practices were to emerge. It was found, for example, that it is preferable to use converged linear  $k-\epsilon$  model results as the starting fields for the non-linear and the Reynolds-stress models. In the case of the Reynolds-stress model, the turbulent stresses were recalculated from the converged mean-velocity and turbulence kinetic energy fields by using Boussinesq's stress-strain relationship. Furthermore, when using the Reynolds-stress model, the stresses were solved altogether, based on their values from previous iteration. In the near-wall region, it was assumed that the stresses were uniform.

The suitability of various turbulence models for wind flows around buildings was then assessed. In Section 2.3, it was suggested that the main obstacle to the use of complete Reynolds-stress-transport models of turbulence in practical engineering calculations lies in the use of those models of 'wall reflection' terms. A new pressure-strain model was published in the course of the present work, one which apparently did not require those terms, and attention was then focused on the detailed verification of this model which was here applied, for the first time, to separated flows. Detailed testing was also to be carried out for the non-linear  $k - \epsilon$  model which, for separated flows, had hitherto been applied only to a flow over a backward-facing step.

Data from a number of experiments were chosen for models verification. Those consisted of the backward-facing step in both straight and divergent channels, the two-dimensional square rib, the circular cylinder and the cube mounted on a flat surface. The main findings to emerge from these tests were as follows:

- For the backward-facing step in a straight channel, both the Reynolds stress models tested gave reattachment lengths in close accord with the data. This was also the case for the wall static pressure distribution which was predicted particularly well with RSM0. Further, those two models and the non-linear variant of the  $k-\epsilon$  model captured the small contra-rotating corner vortex whose existence is confirmed in flow-visualization tests.
- For the backward-facing step in the divergent channel, only the Reynolds-stress models were tested. Grid-independent results were obtained and those provided further confirmation that the new model for the pressure-strain correlations predicts the correct behaviour without requiring a wall-reflections term.
- For the two-dimensional square rib, the results were not very different from the backward-facing step cases: the Reynolds-stress and the non-linear  $k-\epsilon$  models obtained the right reattachment length in contrast to the linear model which underestimated this quantity quite significantly. The wall static pressures were better predicted by the Reynolds stress models.
- For the circular cylinder in uniform approach flow, all the models failed to obtain the surface pressure distribution due, perhaps, to

the use of a steady-state method in what may well be an unsteady flow.

- For the flow around a cube, only the  $k-\epsilon$  model and its variants were used since it would not have been possible to obtain grid-independent results with the Reynolds-stress models due to the limited computing resources available. Both the standard model and the non-linear variant failed around the area of the frontal corner leading to a small recirculation zone and an incorrect pressure distribution on the top of the cube. The modification introduced to amplify the contribution to the production of  $\epsilon$  of irrotational strains proved most successful here with predicted levels of turbulence kinetic energy, for example, comparing quite closely with the data.
- Compared with the CPU time for the standard  $k-\epsilon$  model, the non-linear variant's was greater by a factor of two and the RSMs' by a factor of three.

The third objective was to simulate atmospheric boundary layer to provide accurate inlet boundary conditions for the main code. A full Reynolds stress model was used in conjunction with a marching integration procedure to obtain mean-velocity and turbulence profiles appropriate to equilibrium boundary layers of given depth and for specified terrain roughness. The computed results were internally self-consistent and were quite close to the very few measurements reported in full-scale tests.

The fourth objective of the present study was to verify the predictive procedure by comparisons with data from a wide range of full-scale tests. The most important findings here were as follows:

- It was found that the computations were very sensitive to the assumed inlet conditions and that, further, the accurate simulation of the atmospheric boundary layer using the Reynolds stress model was essential for predicting the correct flow field.
- It emerged that both the linear and non-linear forms of the  $k-\epsilon$  model were incapable of reproducing the behaviour of the flow around the windward side of the roof. This result is similar to that obtained with the same model for the cube and amounts to significant under-prediction of the extent of the separated zone.

- The RSMs produced far more accurate predictions of the separated flow around a semi-cylindrical building. In particular, the position of the separation point was better predicted than with the two-equation models.
- It was found that the two models for the pressure-strain correlations yielded results that were approximately similar and this favour the use of RSM1 in future calculations.

The fifth objective was to conduct the parametric studies aimed at quantifying the influences of geometrical parameters on the pattern of wind flow. This was achieved by conducting parametric studies into the consequences on the wall pressure distribution of varying, in isolation, the height and the width of a certain building. Also, the effects of changing the eaves geometry from sharp to curved were assessed and the computations compared to full-scale data. Finally, some sample calculations were performed to illustrate how to use the prediction method to determine the optimum size and location of a solid windbreak placed upstream of the building.

The sixth objective was to advance a technique for simulating the gust loading on full-scale buildings within the context of classical turbulence modelling techniques. A method was proposed, having as its basis the use of a random-number generator to perturb the inlet atmospheric boundary layer. Sample calculations were carried out to demonstrate this technique and the results obtained were broadly in accord with expectations. Further testing against more detailed measurements is required.

The seventh objective was to improve performance of the computational method through the implementation of a multigrid procedure. This was done and the implementation checked by comparisons with a standard single-grid method. The multigrid method was found to consistently reduce the CPU time by nearly a factor of ten.

### 6.3 RECOMMENDATIONS FOR FUTURE WORK

The present study has shown that Reynolds-stress transport models of

turbulence can provide both accurate and practical means for predicting the behaviour of turbulent flows around full-scale buildings. This is especially so when used together with a particular model for the pressure-strain correlations which does not require wall-reflection terms. The recommendation, therefore, is to extend the verification of this model to the full-scale tests now available for three-dimensional buildings. The technique for simulating gust loading should be explored further, perhaps in close coordination with full-scale measurements. The overall performance of the predictive method will be enhanced by allowing for the multigrid method to be used in conjunction with local grid refinement.

## References

ACHENBACH, E., (1968), "Distribution of local pressure and skin friction around a circular cylinder in cross-flow up to  $Re=5 \times 10^6$ ", *J. Fluid Mech.*, Vol. 34, pp. 625-639.

BARCUS, M., PERIC, M. and SCHEUERER, G., (1987), "A control volume based full multigrid procedure for the prediction of two-dimensional, laminar, incompressible flows", 7th Conf. on Numerical Methods in Fluid Mechanics, Lourain-la-Neuve, Belgium.

BASARA, B., PRZULJ, V. and YOUNIS, B.A., (1992), "Steady vs. unsteady approaches to simulation of turbulent flows around full-scale buildings", Inaugural Conf. of UK Wind Eng. Soc., Cambridge U.K.

BASARA, B. and YOUNIS, B.A., (1992), "Prediction of two- and three-dimensional separated flows with a non-linear  $k-\epsilon$  model", IUTAM Symp. on Bluff-Body Wakes, Dynamics and Instabilities, Gottingen.

BASARA, B. and YOUNIS, B.A., (1992), "Progress in the prediction of turbulent wind loading on buildings", *J. of Wind Engineering and Industrial Aerodynamics*, Vol. 44, pp. 2863-2874.

BASARA, B. and YOUNIS, B.A., (1993), "Prediction of two-dimensional separated flows with second-order closure model", - in Preparation.

BASARA, B., COKLJAT, D. and YOUNIS, B.A., (1993), "Prediction of turbulent flows in dredged trenches", - in Preparation.

BASKARAN, A. and STATHOPOULOS, T., (1989), "Computational evolution of wind effects on buildings", *Building and Environment*, Vol. 24, No. 4, pp. 325-333.

BECKER, C., FERZIGER, J.H., PERIC, M. and SCHEUERER, G., (1989), "Finite Volume Multigrid Solutions of the Two-Dimensional Incompressible Navier-Stokes Equations", *Notes of Numerical Fluid Mechanics*, Vol. 22, Vieweg Verlag, Braunschweig, pp. 30-40.

BOUSSINESQ, J., (1977), "Theorie del'acoulement tourbillant", Mem. Pre. Par. Div. Sav. 23, Paris.

BRADSHAW, P., (1992), "Collaborative testing of turbulence models", Report on AFOSR 90-0154, Stanford University, California.

BRANDT, A., (1977), "Multi-level adaptive solutions to boundary-value problems", *Mathematics of Computation*, Vol. 31, pp. 333-390.

BRITISH STANDARDS INSTITUTION, (1991), "Draft BS6399 Loading for buildings Part 2 Code of practice for wind loading".

CHOU, P.Y., (1945), "On velocity correlations and solutions of the equations of turbulent fluctuations", *Quart. Appl. Math.*, Vol. 3, p. 38.

CRABB, D., DURAO, D.F.G. and WHITELAW, J.G., (1981), "Velocity characteristics in the vicinity of a two-dimensional rib", 3rd Turbulent Shear Flows Symposium, Davis.

CROSBY, C.P., MATHEWS, E.H. and PLESSIS, J.P., (1990), "The numerical prediction of air flow through and around permeable windbreaks and buildings", *J. of Wind Engineering and Industrial Aerodynamics*, Vol. 35, pp. 213-224.

DALY, B.J. and HARLOW, F.H., (1970), "Transport equations of turbulence", *Phys. Fluids*, Vol. 13, p. 2634.

DENHAM, M.K. and PATRICK, M.A., (1974), "Laminar flow over a downstream facing step in a two-dimensional flow channel", *TRANS. INSTN. CHEM. ENGRS.*, Vol. 52, pp. 361-367.

DEMIRDZIC, I., (1982), "A finite volume method for computation of fluid flow in complex geometries", Ph.D. Thesis, University of London.

DEMIRDZIC, I. and PERIC, M., (1988), "Space conservation law in finite volume calculations of fluid flow", *Int. J. for Numerical Methods in Fluids*, Vol. 8, pp. 1037-1050.

DRIVER, D.M., and SEEGMILLER., H.L, (1984), "Features of Reattaching Turbulent Shear Layer in Divergent Channel Flow", *AIAA Journal*, Vol. 23, p. 163.

DURAO, D., McGUIRK, J.J. and PALMA, J., (1982), "Measurements and numerical calculations of the flow around a two-dimensional rib", Proc. EUROMECH 163, Lisbon-Portugal.

GHIA, U., GHIA, K.N. and SHIN,C.T., (1982), "High-Re solutions for incompressible flow using the Navier-Stokes equations and a multigrid method", *J. of Computational Physics*, Vol. 48, pp. 387-411.

GIBSON, M.M. and LAUNDER, B.E., (1978), "Ground effects on pressure fluctuations in the atmospheric boundary layer", *J. Fluid Mech.*, Vol. 86, part 3, pp. 491-511.

GIBSON, M.M. and YOUNIS, B.A., (1982), "Modelling the curved turbulent wall jet", *AIAA Journal*, Vol. 20, p. 1707.

HAAGVIST, K. and TAESLER, R., (1989), "Pressure distribution on a small-scale house - numerical simulations of wind-tunnel experiments", *Building and Environment*, Vol. 24, No. 1, p. 65.

HAGEN, L.J., SKIDMORE, E.L., MILLER, P.L. and KIPP, J.E., (1981), "Simulation of effects of wind barriers on airflow", *Trans. ASAE*, Vol. 24, pp. 1002-1008.

HANJALIC, K., (1984), "Modelling of turbulence transport processes - recent advances and further research trends", Academy of Science and Art of Bosnia and Herzegovina, p. 1., Sarajevo, Bosnia and Herzegovina.

HANJALIC, K. and LAUNDER, B.E., (1972), "A Reynolds stress model of turbulence and its application to thin shear flows", *J. Fluid Mech.*, Vol. 52, pp. 609-638.

HANJALIC, K. and LAUNDER, B.E., (1980), "Senzitizing the dissipation equation to irrotational strains", *J. of Fluids Engineering*, Vol. 102, pp. 34-40.

HANSON, T., SUMMERS, D.M. and WILSON, C.B., (1984), "Numerical modelling of wind flow over buildings in two dimensions", *Int. J. for Numerical Methods in Fluids*, Vol. 4, pp. 25-41.

HARRIS, R.I, and DEAVES, D.M., (1981), "The structure of strong winds",

Paper 4, Proc. of the CIRIA Conf. on Wind Engineering in the Eighties, CIRIA, London.

HINZE, J.O., (1959), "Turbulence", McGraw-Hill Book Co., Inc., New York.

HOXEY, R.P. and MORAN, P., (1991), "Full-scale wind pressure and load experiments - Multispan 167 x 111 m glasshouse", Div. Note DN 1594, AFRC Inst. Engng Res., Silsoe.

HOXEY, R.P. and RICHARDS, P.J., (1991), "The structure of the atmospheric boundary layer below 25m", 8th Int. Conf. on Wind Engineering, London-Canada.

HOXEY, R.P. and RICHARDSON, G.M., (1984), "Measurements of wind loads on full-scale film plastic clad greenhouses" *J. of Wind Engineering and Industrial Aerodynamics*, Vol. 16, pp. 57-83.

HOXEY, R.P., ROBERTSON, A.P., BASARA, B. and YOUNIS, B.A., (1992), "Geometric parameters that affect wind loads on low-rise buildings: full scale and CFD experiments", 2nd Int. Colloquium on Bluff Body Aerodynamics, Australia.

JOHNSTON, L.J., (1984), "The calculation of turbulent boundary layer flows developing into equilibrium", Report no. A28B/304, Ministry of Defence, Bedford.

KIM, J., KLINE, S.J. and JONHSTON, J.P., (1980), "Investigation of a reattaching turbulent shear layer: flow over a backward facing step", *J. of Fluids Engineering*, Vol. 102, pp. 302-308.

LASHER, W.C., and TAULBEE, D.B., (1992), "On the computation of turbulent backstep flow", *Int. J. Heat and Fluid Flow*, Vol. 13, pp. 30-40.

LAUNDER, B.E., REECE, G.J. and RODI, W. (1975), "Progress in the development of a Reynolds stress turbulence closure", *J. Fluid Mech.*, 68, p. 537.

LESCHZINER, M.A. and RODI, W., (1981), "Calculation of Annular and Twin Parallel Jets Using Various Discretization Schemes and Turbulence-Model Variations", *J. of Fluids Engineering*, Vol. 103, pp. 352-360.

LIEN, F.S. and LESCHZINER, M.A., (1991), "Second-moment modelling of recirculating flow with a non-orthogonal collocated finite-volume algorithm", 8th Symp. on Turbulent Shear Flows, Munich.

MAJUMDAR, S. and RODI, W., (1985), "Numerical calculations of turbulent flow past circular cylinders", 3rd Symp. of Numerical and Physical Aspects of Aerodynamic Flows - Long Beach.

MATHEWS, E.H., CROSBY, C.P., VISSER, J.A. and MEYER, J.P., (1988), "Numerical prediction of wind loads on buildings", *J. of Wind Engineering and Industrial Aerodynamics*, Vol. 31, pp. 241-250.

MATHEWS, E.H. and MEYER, J.P., (1987), "Computation of wind loads on a semicircular greenhouse", Proc. 7th Int. Conf. on Wind Engineering, Aachen-Germany.

MURAKAMI, S. and MOCHIDA, A., (1989), "Three-dimensional numerical simulation of turbulent flow around buildings using the k- $\epsilon$  turbulence model", *J. of Wind Engineering and Industrial Aerodynamics*, Vol. 24, pp. 51-64.

MURAKAMI, S., MOCHIDA, A. and HAYASHI, Y., (1990), "Examining the k- $\epsilon$  model by means of a wind tunnel test and large-eddy simulation of the turbulence structure around cube", *J. of Wind Engineering and Industrial Aerodynamics*, Vol. 35, pp. 87-100.

MURAKAMI, S., MOCHIDA, A., HAYASHI, Y. and SAKAMOTO, S., (1992), "Numerical study on velocity-pressure field and wind forces for bluff bodies by k- $\epsilon$ , ASM and LES", *J. of Wind Engineering and Industrial Aerodynamics*, Vol. 43, pp. 2841-2852.

OBI, S., PERIC, M. and SCHEUERER, G., (1989), "A finite-volume calculation procedure for turbulent flows with second-order closure and colocated variable arrangement", 7th Symp. on Turbulent Shear Flows, Stanford University.

OBI, S., PERIC, M. and SCHEUERER, G., (1990), "Finite-volume computation of the flow over a square rib using a second-moment turbulence closure", 7th Symp. on Turbulent Shear Flows, Stanford University.

PATANKAR, S.V., (1980), "Numerical heat transfer and fluid flow", McGraw-

Hill.

**PATANKAR, S.V. and SPALDING, D.B. (1972)** "A calculation procedure for heat, mass and momentum transfer in three-dimensional parabolic flows", *Int. J. Heat Mass Transfer*, Vol. 15, pp. 1787.

**PATERSON, D.A. and APELT, C.J, (1986)**, "Simulation of wind flows over three-dimensional buildings", *J. of Wind Engineering and Industrial Aerodynamics*, Vol. 24, pp. 193-213.

**PATERSON, D.A. and APELT, C.J, (1990)**, "Simulation of flow past a cube in a turbulent boundary layer", *J. of Wind Engineering and Industrial Aerodynamics*, Vol. 35, pp. 149-176.

**PATERSON, D.A. and HOLMES, J.D, (1992)**, "Computation of wind-pressures on low-rise structures", *J. of Wind Engineering and Industrial Aerodynamics*, Vol. 43, pp. 1629-1640.

**PERIC, M., (1985)**, "A finite volume method for the prediction of three-dimensional fluid flow in complex ducts", Ph.D. Thesis, University of London.

**PERIC, M., RUGER, M. and SCHEUERER, G., (1989)**, "A finite volume multigrid method for calculating turbulent flows", 7th Symp. on Turbulent Shear Flows, Stanford University.

**RAINE, J.K. and STEVENSON, D.C., (1977)**, "Wind protection by model fences in a simulated atmospheric boundary layer", *J. of Industrial Aerodynamics*, Vol. 2, pp. 159-180.

**RAYNER, D., (1991)**, "Multigrid flow solutions in complex two-dimensional geometries", *Int. J. for Numerical Methods in Fluids*, Vol. 13, pp. 507-518.

**RHIE, C.M. and CHOW, W.L., (1982)**, "A numerical study of the turbulent flow past an isolated airfoil with trailing edge separation", *AIAA*, p. 998.

**RICHARDS, P.J., (1989)**, "Computational modelling of wind flow around low-rise building using PHOENICS", Div. Note DN 1508, AFRC Inst. Engng Res., Silsoe.

**RICHARDS, P.J. and HOXEY, R.P., (1992)**, "Computational and wind tun-

nel modelling of mean loads on the Silsoe Structures Building”, *J. of Wind Engineering and Industrial Aerodynamics*, Vol. 43, pp. 1641-1653.

RICHARDS, P.J. and YOUNIS, B.A., (1990), Comments on "Prediction of the wind-generated pressure distribution around buildings", *J. of Wind Engineering and Industrial Aerodynamics*, Vol. 34, pp. 107-110.

RICHARDSON, G.M., (1991), "Full-scale wind load measurements on a single-span film plastics clad livestock building: Investigating the effect of a ridge ventilation slot", Div. Note DN 1508, AFRC Inst. Engng Res., Silsoe.

ROBERTSON, A.P., (1989), "Effects of eaves detail on wind pressures over an industrial building" glasshouse", 8th Colloquim on Industrial Aerodynamics, Aachen, Germany.

ROTTA, J.C., (1951), "Statistische Theorie nichthomogener Turbulenz", *Z. Phys.*, Vol. 129, p. 547.

SELVAM, R.P., (1992), "Computation of pressures on Texas Tech building", *J. of Wind Engineering and Industrial Aerodynamics*, Vol. 43, pp. 1619-1628.

SHIR, C.C., (1973), "A preliminary study of atmospheric turbulent flow in the idealized planetary boundary layer", *J. Atmospheric Sci.*, Vol. 30, p. 1327.

SPALDING, B., (1975), GENMIX: a general computer program for 2D parabolic phenomena, Imperial Collage, London.

SPEZIALE, C.G., (1987), "On nonlinear K-l and K- $\epsilon$  models of turbulence", *J. Fluid Mech.*, Vol. 178, pp. 459-475.

SPEZIALE, C.G., (1991), "Analytical methods for the development of Reynolds-stress closures in turbulence", *Annu. Rev. Fluid Mech.*, Vol. 23, pp. 107-157.

SPEZIALE, C.G. and NGO, T., (1988), "Numerical solution of turbulent flow past a backward facing step using a nonlinear k- $\epsilon$  model", *Int. J. Engng. Sci.*, Vol. 10, pp. 1099-1112.

SPEZIALE, C.G., SARKAR, S. and GATSKI, T.B., (1991), "Modelling the pressure-strain correlation of turbulence, an invariant dynamical systems approach", *J. Fluid Mech.*, Vol. 227, pp. 245-272.

**STONE, H.L., (1968), "Iterative solution of approximations of multi-dimensional partial differential equations", *SIAM J. num. Anal.*, Vol. 5, pp. 530-558.**

**VANKA, S.P., (1986), "Block-implicit multigrid solution of Navier-Stokes equations in primitive variables", *J. of Computational Physics*, Vol. 65, pp. 138-158.**

**VANKA, S.P., (1986), "Performance of a multigrid calculation procedure in three-dimensional sudden expansion flows", *Int. J. for Numerical Methods in Fluids*, Vol. 13, pp. 507-518.**

**YOUNIS, B.A., (1987), EXPRESS: a computer program for two-dimensional turbulent boundary-layer flows, City University, London**

**WILSON, J.D., (1985), "Numerical studies of flow through a windbreak", *J. of Wind Engineering and Industrial Aerodynamics*, Vol. 21, pp. 119-154.**

**WHITBREAD, R.W., (1981), "Application of wind tunnel techniques to wind load prediction", Paper 10, Proc. of the CIRIA Conf. on Wind Engineering in the Eighties, CIRIA, London.**